

A novel digital holographic microscope (DHM) to
investigate and characterize microbial motility in extreme
aquatic environments

Thesis by
Manuel M. Bedrossian

In Partial Fulfillment of the Requirements for the
Degree of
Doctor of Philosophy in Medical Engineering

The logo for the California Institute of Technology (Caltech), featuring the word "Caltech" in a bold, orange, sans-serif font.

CALIFORNIA INSTITUTE OF TECHNOLOGY
Pasadena, California

2020
Defended April 20, 2020

© 2020

Manuel M. Bedrossian
ORCID: 0000-0003-2524-3765

All rights reserved except where otherwise noted

ACKNOWLEDGEMENTS

I would like to thank my friends and family, especially my parents, Seroj and Silvana Bedrossian. You've both made my life the purpose of yours, and have sacrificed a great deal in order for me to have the opportunities that I have had. This thesis would not be if it weren't for you two. From the very depths of my being, thank you.

ABSTRACT

Recent shifts in congressional funding have prompted the development of methods for the direct search for extant life within our solar system. In order to look for life elsewhere in our solar system, it is important to also investigate the broad spectrum of extant life on Earth. Over millions of years of evolution, life has continually adapted such that an *extreme* environment has become a relative term. What is considered extreme for one type of organism is home to another and vice versa. Very little is known about the organisms that inhabit these “extreme” environments, and even less is known about their *in situ* behavior.

Among our celestial neighbors, the moons of Jupiter and Saturn, Europa and Enceladus, are the most likely to harbor life, if it exists. If life exists, however, it must have the capability to withstand what Earth-based life would consider extreme environments. Prior to full flight missions to directly search for evidence of life on these bodies, understanding life in extreme environments on Earth would shed light on the types of life that can be expected throughout our solar system.

This thesis describes the development of a novel off-axis digital holographic microscope (DHM) for the direct *in situ* observation of microscale organisms in extreme aquatic environments. The hardware developments of this instrument are introduced and validated experimentally as well as software developments including autonomous particle detection and tracking algorithms. This instrument is then used in novel laboratory experiments involving the development of optical phase contrast agents, as well as deployed to multiple field campaigns where off-axis DHM is used to observe the *in situ* behavior of microorganisms in various extreme aquatic environments.

The primary contributions of this thesis are the achievement of a physical device that is capable of high throughput/high resolution imaging of extreme aquatic samples in remote environments, as well as successfully finding evidence of *extant* life within these extreme environments. This device shows a proof of concept instrument for future applications to Earth and flight based research involving the detection and tracking of microscale organisms.

PUBLISHED CONTENT AND CONTRIBUTIONS

- [1] Manuel Bedrossian, Casey Barr, Christian A. Lindensmith, Kenneth Nealson, and Jay L. Nadeau. Quantifying microorganisms at low concentrations using digital holographic microscopy. *Journal of Visualized Experiments*, (129): e56343, 2017. doi: 10.3791/56343. M.B participated in the conception of the project, contributed to the theoretical derivation of the equations of instrument sensitivity, collected and analyzed experimental data, as well as significantly contributed in the writing of the manuscript.
- [2] Manuel Bedrossian, Christian A. Lindensmith, and Jay L. Nadeau. Digital holographic microscopy, a method for detection of microorganisms in plume samples from enceladus and other icy worlds. *Astrobiology*, 17(9):913–925, 2017. doi: 10.1089/ast.2016.1616. M.B participated in the conception of the project, contributed to the theoretical derivation of the equations of instrument sensitivity, collected and analyzed experimental data, as well as significantly contributed in the writing of the manuscript.
- [3] Manuel Bedrossian, Jay L. Nadeau, Eugene Serabyn, and Christian A. Lindensmith. Sources and propagation of errors in quantitative phase imaging techniques using optical interferometry. In *Quantitative Phase Imaging III*, volume 10074, page 100740E. International Society for Optics and Photonics, 2017. doi: 10.1117/12.2250069. M.B participated in the conception of the project, contributed to the theoretical derivation of phase noise equations, collected and analyzed experimental data, as well as significantly contributed in the writing of the manuscript.
- [4] Manuel Bedrossian, Jody W. Deming, and Jay L. Nadeau. Methods for collection and characterization of samples from icy environments. *Methods in Microbiology*, 2018. doi: 10.1016/bs.mim.2018.05.001. M.B was invited to contribute a chapter to a journal on Experimental Microbiology, and contributed significantly to the writing of this chapter.
- [5] Manuel Bedrossian, Marwan El-Kholy, Daniel Neamati, and Jay L. Nadeau. A machine learning algorithm for identifying and tracking bacteria in three dimensions using digital holographic microscopy. *AIMS Biophysics*, 5(1):36–49, 2018. doi: 10.3934/biophy.2018.1.36. M.B participated in the conception of the project, contributed to the construction and development of the machine learning algorithm and software, collected and analyzed experimental data, as well as significantly contributed in the writing of the manuscript.
- [6] Manuel Bedrossian, J. Kent Wallace, Eugene Serabyn, Lindensmith Christian A., and Jay L. Nadeau. Enhancing final image contrast in off-axis digital holography using residual fringes. *Submitted to Optics Express*, 2020. M.B conceived, planned, and executed all research contained in this manuscript.

M.B wrote all algorithms used, as well as collected all data. M.B participated in the theoretical justification involved with this manuscript, as well as wrote the majority of the manuscript itself, including the literature review.

- [7] Arash Farhadi, Manuel Bedrossian, Justin Lee, Gabrielle H. Ho, Mikhail G. Shapiro, and Jay L. Nadeau. Genetically encoded phase contrast agents for digital holographic microscopy. *bioRxiv*, page 833830, 2019. doi: 10.1101/833830. M.B participated in the conception and planning of the research. M.B participated in conducted the DHM data collection and reconstruction. M.B carried out the generation and analysis of the salmonella hologram simulations as well as the analysis particle and salmonella image reconstruction and data analysis. M.B performed the processing and rendering of the 3D pseudo-colored phase image of CHO cells. M.B participated in the analysis of all results. M.B participated in writing the manuscript with input from all authors.
- [8] Morteza Gharib, Manuel Bedrossian, Stephanie Rider, and Jason G Beith. Systems, devices, and methods relating to the manufacture of intravascularly implantable prosthetic valves, November 14 2019. US Patent App. 16/215,376. M.B participated in the conception of this project, the design and manufacture of all prototype designs as well lead all efforts in the numerical modeling of the device.
- [9] Christian A. Lindensmith, Stephanie Rider, Manuel Bedrossian, J. Kent Wallace, Eugene Serabyn, G. Max Showalter, Jody W. Deming, and Jay L. Nadeau. A submersible, off-axis holographic microscope for detection of microbial motility and morphology in aqueous and icy environments. *PloS one*, 11(1): e0147700, 2016. doi: 10.1371/journal.pone.0147700.
- [10] Christian A. Lindensmith, Manuel Bedrossian, and Jay L. Nadeau. Approaches to distinguishing bacteria from mineral particles in microscopic imaging ieec aerospace conference. In *2018 IEEE Aerospace Conference*, pages 1–9. IEEE, 2018. doi: 10.1109/AERO.2018.8396822. M.B participated in the conception of the project, as well as participated in the writing of the manuscript.
- [11] Jay L. Nadeau and Manuel Bedrossian. Advanced topics in microscopy ii: Holographic microscopy. In *Introduction to Experimental Biophysics*, pages 305–324. CRC Press, 2017. M.B was invited to contribute a chapter to a textbook on Experimental Biophysics, and contributed significantly to the writing of this chapter.
- [12] Jay L. Nadeau, Manuel Bedrossian, and Christian A. Lindensmith. Imaging technologies and strategies for detection of extant extraterrestrial microorganisms. *Advances in Physics: X*, 3(1):1424032, 2018. doi: 10.1080/23746149.2018.1424032. M.B participated in the conception of the project, provided background research on the current state of the art in multiple optical imaging technologies, as well as participated in the writing of the manuscript.

- [13] J. Kent Wallace, Eugene Serabyn, Christian A. Lindensmith, Jay L. Nadeau, Stephanie Rider, and Manuel Bedrossian. A multiwavelength digital holographic microscope architecture for enhancing life detection. In *2019 IEEE Aerospace Conference*, pages 1–6. IEEE, 2019. doi: 10.1109/AERO.2019.8742091. M.B designed and manufactured the sample chambers that were used in all the acquisition of all data presented in this manuscript as well as participated in writing of the manuscript pertaining to his contributions.

CONTENTS

Acknowledgements	iii
Abstract	iv
Published Content and Contributions	v
Bibliography	v
Contents	viii
List of Figures	ix
List of Tables	xviii
Nomenclature	xix
Chapter I: Introduction	1
Chapter II: Theoretical Overview of Holography	8
2.1 Off-Axis Digital Holography	8
2.2 Phase Distribution of a Wave as it Travels Through Focus	14
Chapter III: Hardware Development	18
3.1 Optical Design	18
3.2 Field Instrument - Generation I	20
3.3 Field Instrument - Generation II	23
3.4 Sample Chamber Design and Fabrication	26
Chapter IV: Quantification of Performance	35
4.1 Instrument Resolution and Depth of Field	35
4.2 Phase Noise Analysis	44
4.3 Limits of Detection	51
Chapter V: Software Development	63
5.1 Machine Learning Tracking Algorithm	63
5.2 Residual Fringe Visibility as a Means of Enhanced Image Contrast	69
Chapter VI: Genetically encoded phase contrast agents for DHM	81
Chapter VII: Field Experimentation	90
7.1 Utqiagvik (Barrow), Alaska, USA	93
7.2 The Cedars, California, USA	99
Chapter VIII: Conclusions	112
Bibliography	115
Appendix A: Reference Equations and Derivations	127
Appendix B: Data Processing and Handling	140
Appendix C: Experimental Techniques	157
Appendix D: Bio-Safety and Microbiology Protocols	165
Appendix E: Technical Information	171
Appendix F: Accessing GitHub and Data Backups	187

LIST OF FIGURES

<i>Number</i>	<i>Page</i>
1.1 Performance requirements of the optical imaging device	6
2.1 Optical schematic of a Young's Double Slit Experiment. Two point sources of light located at P_1 and P_2 propagate to the image plane at the origin.	9
2.2 The Angular Spectrum Method (ASM). The electric field recorded by the digital detector U_S^+ is acted on by the transfer function of free space H in order to reconstruct the electric field at a desired axial plane z_0	12
2.3 Illustration of the Gouy Phase Shift. This is a volumetric slice (xz plane) of a single micron-sized gas vesicle cluster that has been reconstructed in phase with bounds $[-\pi, \pi]$. The particle is located at the center of the figure and the Gouy Phase Shift can be seen as a change from dark to light pixel values in the vertical direction through the center. Scale bar represents $1 \mu\text{m}$	17
3.1 An optical schematic of the Mach-Zehnder DHM instrument as well as an image of the benchtop instrument	19
3.2 An optical schematic of the Common Mode DHM instrument as well as an image of the benchtop instrument	21
3.3 The orangeBox field instrument	22
3.4 The sample chamber assembly of the orangeBox field instrument, fully assembled (left) and in use while in Nuuk, Greenland (right) (adapted from [75]).	22
3.5 Optical setup of the miniaturized DHM field instrument.	25
3.6 The second generation DHM field instrument. (A) The full working prototype of the miniaturized DHM field instrument besides the first generation DHM field instrument (orangeBox). (B) The electronics side of the miniaturized field instrument (key for scale).	26
3.7 Cross-sectional schematic of sample chamber configurations 1 through 4. The materials being investigated as well as the sample are the only objects in the light path of the instrument.	29

3.8	Interference fringes through various substrate configurations using the Zygo interferometer. Top left: AR coated solid etalon. Top middle: non-AR coated solid etalon. Top right: microscope slide. Bottom left: microscope slide and non-AR coated solid etalon. Bottom middle: polycarbonate. Bottom right: PDMS.	29
3.9	Radial PSD functions calculated from the phase images of empty sample chambers consisting of various substrate configurations . . .	32
3.10	Net phase variance calculated from the reconstructed phase images of all sample chamber configurations	32
4.1	Focus metrics for intensity images. (Left) A volumetric rendering of a resolution element with one-dimensional lateral profile lines at various points through focus. (Upper right) The intensity profiles of the lateral profile lines shown in the volumetric rendering. (Lower right) The integrated intensity profiles of the lateral profile lines of the object as a function of axial resolution. A Gaussian fit of the data shows the point of focus as the maximum of the curve.	38
4.2	Image metrics for the location of the Gouy Phase Shift in phase images. (Left) A volumetric rendering of a resolution element with a one dimensional axial profile line through the center of the element. (Upper right) The phase profile of the axial profile line shown in the volumetric rendering with a linear logistic regression fit. (Lower right) The spatial derivative of the logistic regression. The maximum of the spatial derivative corresponds to the inflection point of the plot, which is where the Gouy Phase Shift occurs.	40
4.3	USAF resolution target imaged using the Mach-Zehnder DHM. Left shows an intensity reconstruction and right shows a phase reconstruction. Scale bar represents $10\ \mu\text{m}$	40
4.4	Axial localization errors of the Mach-Zehnder instrument (50x NA0.55 objective lenses) in both phase and intensity reconstructions	41
4.5	USAF resolution target imaged using the common mode DHM. Left shows an intensity reconstruction and right shows a phase reconstruction. Scale bar represents $35\ \mu\text{m}$	42
4.6	Axial localization errors of the common mode instrument (20x NA0.3 objective lenses) in both phase and intensity reconstructions	42

4.7	Comparison of phase errors of the Four Bucket/Step, Three Bucket/Step, and Carré Methods as a function of normalized average light intensity (% well depth of pixel) (adapted from [3])	50
4.8	Comparison of phase errors of the Four Bucket/Step, Three Bucket/Step, and Carré Methods as a function of phase (adapted from [3])	51
4.9	Minimum number of required sample volumes to detect objects at various concentrations with a confidence level of 95% (adapted from [12])	53
4.10	Normalized SNR as a function of bacterial concentration in amplitude images (left) and phase images (right) (adapted from [12]).	59
4.11	Phase (left) and amplitude (right) images of <i>B. subtilis</i> at the relatively low concentration of 10^4 cells per mL (adapted from [12]).	59
4.12	Phase (left) and amplitude (right) images of <i>B. subtilis</i> at the relatively high concentration of 6×10^6 cells per mL (adapted from [12]).	60
5.1	Localization error of <i>B. subtilis</i> (left) and <i>C. psychrerythraea</i> (right) as a result of the machine learning tracking algorithm (adapted from [5]).	69
5.2	Three-dimensional trajectories of <i>B. subtilis</i> as a result of the machine learning tracking algorithm (adapted from [5]).	70
5.3	Distribution of swimming speeds of <i>B. subtilis</i> as a result of the machine learning tracking algorithm (adapted from [5]).	71
5.4	Optical Schematic of the DHM instrument used throughout this work (A), an image of the benchtop instrument (B), and fringe stability of the DHM instrument as a function of time (C). Centerline indicates the mean fringe visibility and dashed lines indicate the 95% confidence interval range.	71
5.5	Computation time of the median and mean subtraction schemes as a function of input size.	75
5.6	Raw hologram of sample containing <i>B. subtilis</i> (A), the identical hologram after background subtraction (B), and their respective Fourier spectra (C and D). Intensity reconstruction of the same <i>B. subtilis</i> bacterium without (E) and with (F) the use of the residual fringe visibility analysis, as well as vertical line plots of pixel values through the bacterium (G and H, respectively). Scale bar represents $10 \mu\text{m}$ for (A, B, E, and F).	76

- 5.7 Raw hologram of sample containing *V. alginolyticus* (A), the identical hologram after background subtraction (B), and their respective Fourier Spectra (C and D). Intensity reconstruction of the same *V. alginolyticus* bacterium without (E), and with (F) the use of the residual fringe visibility analysis, and a 3D rendering of the reconstructed intensity z-stack of the raw (G) and background subtracted hologram (H). Scale bar represents 10 μm for (A, B, E, and F). 77
- 5.8 Raw multiwavelength hologram of sample containing *E. gracilis* (A), the identical hologram after background subtraction (B), as well as their respective spectra (C and D, respectively). A pseudo-colored composite intensity reconstruction of a select *E. gracilis* using the raw hologram (E), and background fringe subtraction technique (F). Scale bar in (A) represents 50 μm for both (A and B). Scale bar in (E) represents 20 μm for both (E and F). 78
- 6.1 Gas vesicles as phase contrast agents. (A) Schematic of a single GV. (B) Schematic of the DHM used in this work, and an illustration of the inherent volumetric imaging of DHM compared to conventional microscopy. (C) Biotinylated gas vesicles purified from *Anabaena flos-aquae* can be clustered using streptavidin. Shown are a schematic and representative transmission electron micrograph of biotinylated GVs (top) and clustered GVs (bottom). Scale bars 100 nm and 500 nm, respectively. (D) Representative phase and amplitude DHM images of clustered gas vesicles and alumina beads. Scale bars represent 25 μm . (E) Phase change observed from clustered gas vesicles as a function of approximate particle size. The theoretical model comes from Equation 6.1. 84

- 6.2 (A) Clustered gas vesicles rise in solution, histogram of the z-component velocities of clustered gas vesicles, and 3D trajectory plots of tracked gas vesicles over 60 second. (B) Two example 3D tracks of clustered gas vesicles. Each trajectory is color coded with respect to time. (C) Alumina beads sink over time, histogram of the z-component velocities of alumina particles, and 3D trajectory plots of tracked alumina beads over 60 seconds. (D) Two example 3D tracks of alumina beads. Each trajectory is color-coded with respect to time. (E) Mixed population of gas vesicles and alumina beads showing two velocity histograms for gas vesicles and alumina beads, and 3D trajectory plots of the mixed population over 60 seconds. (F) Example trajectory of a rising and another of sinking particle chosen at random. (G) Phase images of the two particles from F. The buoyant particle has a positive phase contrast while the particle sinking has a negative particle. Scale bars represent $5 \mu\text{m}$. (H) Representative dynamic light scattering of the hydrodynamic diameter of pristine gas vesicles, clustered gas vesicles and alumina beads. 85
- 6.3 DHM imaging of mammalian cells labelled with engineered gas vesicles. (A) The surface of gas vesicles can be genetically decorated with R8 peptides to label mammalian cells. (B) Chinese hamster ovary (CHO) cells labelled with polyarginine modified-gas vesicles and imaged using DHM. Scale bar represents $25 \mu\text{m}$. (C) Pseudocolored 3D rendering of gas vesicles decorating CHO cells. See Appendix C for more information. (D) Phase image (scale bar represents $25 \mu\text{m}$) of CHO cells transfected with GFP labeled GVs under the high power DHM showing positive phase contrast in correspondence with (E) a high power fluorescence image (scale bar represents $25 \mu\text{m}$) of the identical CHO cells. 87

6.4	GVs as genetically encoded phase contrast agents in Salmonella. (A) Schematic of engineered gas vesicle gene cluster comprising genes from <i>Anabaena flos-aquae</i> (orange genes) and <i>Bacillus megaterium</i> (blue genes) that enable heterologous expression of gas vesicles in <i>Salmonella typhimurium</i> . (B) Representative transmission electron micrograph of <i>S. typhimurium</i> expressing gas vesicles. Scale bar represents 1 μm . (C) Numerical simulation of phase and amplitude images of a GV-expressing Salmonella cell. (D) Representative phase and amplitude images of gas vesicles-expressing <i>S. typhimurium</i> cells under DHM. Example zoomed-in images are illustrated on the right. Scale bars for full field of view are 25 μm and 5 μm for the zoomed-in images. (E) Representative phase and amplitudes images of GV-expressing <i>S. typhimurium</i> cells after collapsing GVs using 1.2 MPa of hydrostatic pressure. Scale bars for full field of view are 25 μm and 5 μm for the zoomed-in images. (F) Quantified average phase contrast from <i>S. typhimurium</i> cells with intact gas vesicles compared with collapsed gas vesicles ($n = 88$).	88
7.1	Geographic locations that have been visited by the DHM field instrument	92
7.2	Select trajectory plot (left) and histogram of turning angles from sea ice brine samples	95
7.3	Select trajectory plots of motile eukaryotic cells (left) and a histogram of turning angles of these cells (right) imaged from the ice/ocean interface	96
7.4	Amplitude image of cryopeg brine showing a cylindrical object as well as three other non-spherical objects. Scale bar represents 20 μm .	97

7.5	<i>In situ</i> results from various field sites visited in Utqiagvik (Barrow), Alaska. (A) Select trajectory of a motile microorganism found in the sea ice brine sample. This image is a composite image rendered by the minimum pixel intensity projection of 5 seconds of data. Scale bar represents 10 μm . (B) Select trajectory of a motile microorganism found in the ice/ocean interface sample. This image is a composite image rendered by the minimum pixel intensity projection of 5 seconds of data. Scale bar represents 50 μm . (C) A single plane intensity reconstruction showing a select microorganism observed at the ice/ocean interface sample. Scale bar represents 10 μm . (D) A single plane intensity reconstruction of a particle that exhibits lifelike morphological features observed in the cryopeg brine sample. Scale bar represents 10 μm . (E) Trajectories of the heterogeneous <i>in situ</i> sample taken from the ice/ocean interface. This plot shows trajectories of multiple organisms within the field of view of the DHM instrument and is color-coded with respect to time.	98
7.6	Select microbial trajectories (left) and histogram of turning angles (right) of microorganisms from samples taken directly from BS5 (Top Pool).	102
7.7	Select microbial trajectories (left) and histogram of turning angles (right) of microorganisms from samples taken directly from GPS.	103
7.8	Sample location near GPS called ‘White Calcite Pool’	103
7.9	Select microbial trajectories from the White Calcite Pool	104
7.10	Sample location near GPS called ‘Orange Calcite Pool’	105
7.11	Select trajectory plot (left) and histogram of turning angles (right) of microorganisms from samples taken from the Orange Calcite Pool	105

7.12	<i>In situ</i> results from various field sites visited in The Cedars, California. (A) A single plane intensity reconstruction of a select micron-sized organism from the BS5 spring sample. Scale bar represents 10 μm . (B) Select trajectory of a motile microorganism found in the direct GPS spring sample. This image is a composite image rendered by the minimum pixel intensity projection of 7 seconds of data. Scale bar represents 10 μm . (C) A single trajectory of a micron-sized organism from the White Calcite Pool, which was volumetrically tracked through time. The plot shown is color-coded with respect to time. (D) Trajectories of the heterogeneous <i>in situ</i> sample taken from the White Calcite Pool. This plot shows trajectories of multiple organisms within the field of view of the DHM instrument and is color-coded with respect to time. (E) Trajectories of the heterogeneous <i>in situ</i> sample taken from the Orange Calcite Pool. This plot shows trajectories of multiple organisms within the field of view of the DHM instrument and is color-coded with respect to time.	107
B.1	Initial dialog box of the automated tracking software suite	147
B.2	Plot of turning angles as a function of time.	153
C.1	The temperature along the thermal gradient generator with a linear correlation of $r = -0.73$	162
C.2	Experimental setup of the in-field pulsation dampener	164
D.1	Sampling new sea ice. (A) Using a sterile bag to collect new (hour-old) “grease ice” as it forms on the surface of freezing seawater at the edge (lower right) of young (month-old) sea ice. Ethanol-rinsed latex gloves should be worn when the sample is intended for microbiological analysis. (B) Young sea ice can support the weight of a researcher, but safety precautions include wearing an immersion suit, as shown, and a harness with tethering rope to a secure position.	169

D.2	Ice coring in Utqiagvik (formerly Barrow), Alaska. (A) The interrupted coring technique is used to drill into sea ice, while another team member clears ice chips from the drill site. A third team member has completed the process of clearing the snow cover from the planned coring area. (B) Using a weighted depth gauge to measure the sea ice thickness through a borehole drilled through the ice to underlying seawater; the gauge is designed to anchor to the underside of the ice for a taught pull upwards. (C) Using core retrieval tongs to pull a partial ice core out of the sea ice cover and establish a “sackhole” for the accumulation of sea ice brine. Photos courtesy of Anders Torstensson.	170
E.1	Fully assembled sample chamber	177
E.2	Exploded CAD view of sample chamber	177
E.3	Schematic of sample chamber	178
E.4	Mold assembly used for soft lithography of sample chambers	178
E.5	A laser cut plastic shim with double-sided adhesive tape	184
E.6	Plastic shim stock after being compressed between glass substrates	184
E.7	A fully assembled disposable sample chamber	185
E.8	Electronic schematic for the miniaturized DHM field instrument	186
F.1	Navigating the server IP address via internet browser	188
F.2	Typical warning message given by Google Chrome	188
F.3	Expanded view allowing access to the server IP address. Click ‘Proceed to 131.215.99.223 (unsafe)’ for Google Chrome, or ‘visit this website’ for Safari.	189
F.4	Server dashboard (note the ‘Options’ tab at the top right after clicking the dropdown menu attached to the username)	189
F.5	The ‘Options’ dialog box where you can change account information, including your password	190
F.6	File Station dialog box	190

LIST OF TABLES

<i>Number</i>	<i>Page</i>
3.1 Surface roughness of sample chamber substrates	30
4.1 Image performance metrics for the common mode and Mach-Zehnder instruments	43
4.2 Specifications of the off-axis DHM and comparable brightfield microscope (labeled Conventional)	54
4.3 Minimum number of required sample volumes to detect objects (detection confidence of 50%)	54
4.4 Summary of results from sensitivity verification experiments	58
5.1 Experimental parameters used in the validation of the machine learning object detection algorithm.	68
7.1 Conditions that would constitute an extreme environment	92
7.2 Field deployment summary from Utqiaġvik 2017	99
7.3 Field deployment summary from The Cedars General Survey 2017	106
7.4 Measured cell densities of ultrabasic springs at The Cedars	108
A.1 Common Mode instrument parameters	139
A.2 Mach-Zehnder instrument parameters	139
A.3 Sensor parameters used in error simulations	139
A.4 Physical properties of GV clusters, aluminum oxide, and water	139
B.1 List of configuration files in KOALA	142
E.1 Specifications of Etalon Glass	179

NOMENCLATURE

Amplitude Reconstruction. The magnitude of the complex wavefront that is determined as a result of the numerical reconstruction of a holographic image.

Angular Spectrum Method (ASM). A numerical and discrete method to predict the displacement function of a wave as it passes through a plane, while only sampling the wave as it passes through a different parallel plane. This method treats wave propagation as a linear system, where the measured wave at a plane can be convolved by an impulse function (see Transfer Function of Free Space) to calculate the displacement function of the wave at a different plane.

Background Subtraction (aka median or mean subtraction). An image processing technique where stationary artifacts from an image are removed in order to highlight aspects of an image sequence that are temporally transient.

Band-Pass Filtering. An image processing technique where certain spatial frequencies are removed from an image by multiplying the Fourier transform of the image with a mask.

Biosignature. Any substance or observation that can provide scientific proof of past or present life.

Colony Forming Unit (CFU). A unit of measure used to quantify the viability of a microbial population. See Culture Plate Counting.

Culture Plate Counting. A standard microbiological technique to quantify living bacterial concentrations in a sample. A known volume of sample is deposited on a plate containing nutrients. A sufficient amount of time is allotted for the bacteria in the volume deposited on the plate to grow into discrete colonies. These colonies are counted and divided by the original volume deposited on the plate to infer on the original sample concentration. Units are reported in colony forming units (CFU) per mL.

Data Acquisition (DAQ). The process of digitally sampling and recording a signal.

Depth of Field (DOF). The distance, in the axial dimension, between the nearest and farthest object imaged in a hologram that is capable of being resolved with sub-micron resolution.

Differential Interference Contrast (DIC) Reconstruction. A synthetic form of traditional DIC, where the DIC reconstruction is defined as the one-directional lateral (spatial) derivative of a phase reconstruction.

Field of View (FOV). The dimensions of the total observable area of an image.

Flight Qualification. Product or instrument testing in order to prove that it will withstand the physical stresses of space flight (See Technology Readiness Level (TRL)).

Fringe Visibility. The normalized contrast of an interference pattern. Fringe visibility is defined as $V = \frac{2\sqrt{I_1 I_2}}{I_1 + I_2} = \frac{I_{\max} - I_{\min}}{I_{\max} + I_{\min}}$.

Fringes (aka interference pattern). The interference of two coherent waves that manifest as wave intensity oscillations through space or time.

Gouy Phase Shift. A phase shift introduced to a converging wave as it passes through focus caused by an apparent increase in wavelength as the phase velocity of the wave surpasses the speed of propagation in the medium.

Hologram (aka interferogram). A two-dimensional image with three dimensional information, which is encoded into the image via the interference of two coherent waves.

Intensity Reconstruction. The square of the amplitude reconstruction of the complex wavefront calculated as a result of the numerical reconstruction of a holographic image.

Lysogeny Broth (LB). A nutrient-rich media used for the growth of bacterial cultures. There is no single type or recipe of LB. A typical LB recipe (per 1 L of distilled water) is as follows: 10 g bacto tryptone, 5 g bacto yeast, 10 g NaCl.

Microbial Density (aka microbial concentration). The measure of the amount of microbial life in a sample. This metric usually measured in cells/mL.

Numerical Reconstruction. The numerical analysis and extraction of three dimensional data from a hologram. Many methods for this exist, but the most common and least computationally expensive is the angular spectrum method (ASM). The information of the electric field encoded into the hologram is discretely re-propagated to determine the complex wavefront of the light before being incident onto the optical detector.

Phase Reconstruction. The phase of the complex wavefront that is determined as a result of the numerical reconstruction process. This is calculated as the arc-tangent of the imaginary components of the complex wavefront divided by the real components of the complex wavefront.

Pixel Pitch. The size of the smallest sampled 2D element in an image.

Pixel Size. The physical size of the detector's pixels.

Propagation Distance. The distance that the wave propagates in free space. This term is used in the propagator and describes the extent of diffraction of a wave from one plane to another.

Reference Beam. In a twin beam interferometer, two coherent beams of light are used to create interference. The reference beam is the beam in an interferometer that remains undisturbed and acts as a reference to create interference patterns at the detector.

Sample Beam. In a twin beam interferometer, two coherent beams of light are used to create interference. The sample beam is the beam in an interferometer that interacts with the sample being observed.

Science Traceability Matrix (STM). An organizational tool in the form of a logical flow diagram. This starts with high level mission objectives and successively deduces specific requirements of a solution to meet those high level goals.

Technology Readiness Levels (TRL). A measurement system used and implemented by NASA to quantify the maturity level of a particular technology. A technology is considered flight qualified if it is designated a TRL of 8 or above.

Transfer Function of Free Space. Analogous to an impulse function used in the numerical reconstruction of holograms when employing the angular spectrum method. This two-dimensional term describes the phase changes of a wave as it propagates in free space.

Voxel Size. The size of the smallest sampled 3D element of a z-stack.

Z-slice. (aka z-plane): A reconstruction of a hologram at a particular axial plane. Denoted by the variable z as light propagates in the positive z direction. A z-slice is an XY plane evaluated at a particular z location.

Z-stack. A collection of multiple z-slices or z-planes, that when assembled in order, represent the three dimensional information that is contained in a hologram.

Chapter 1

INTRODUCTION

Ex astris, scientia. From the stars, knowledge.

From the dawn of mankind, we've learned an unfathomable amount just from looking up at the stars. From the first astronomical observatory near the current city of Sisian in the Syunik Province of Armenia called Զորաց Քարեր (Zorats Karer), which is estimated to be about 6,000 years old, to Galileo Galilei's revelation that the Earth orbits the sun rather than the opposite, knowledge from the stars has shaped almost every aspect of our modern lives. The earliest observations of the stars led us to understand the cyclic nature of seasons, so we were able to transition from a hunter-gatherer to agricultural way of life, which has so deeply impacted the lives we live today that it is difficult to imagine a reality without this seemingly trivial bit of knowledge. And where would mankind be, if it weren't for Galileo's heresy?

In the relatively recent years, mankind has no longer been limited to observing the stars from the confines of Earth. We have put tremendous effort in reaching for the stars and learning every step of the way, not only from the scientific yield of our space missions, but also from the technological advancements and innovations that were necessary in reaching our celestial destinations. Modern global positioning satellites, for example, are a direct fruit of this labor. This technological marvel helps us navigate the chaotic streets and highways of our cities, monitor our airways to ensure safe air travel, and even enables us to find the newest and highest rated restaurants near us at any given moment.

Similarly, a recent push for the direct search for life in our solar system has resulted in the development of technologies aimed at the direct observation of liquid samples from our celestial neighbors, namely Europa and Enceladus. In the process, a myriad of questions has arisen from the highly technical to the deeply philosophical. If we observe a sample from Europa or Enceladus, would we be able to recognize life if it were staring us in the face? What do we expect it to look like? These questions are difficult to answer and are highly subjective to say the least and will be the topic of debate in the scientific community for years to come. One aspect of this question that can be answered with a high degree of confidence is that any environment that we search for life outside of Earth can be considered an *extreme* environment.

What is an extreme environment? As will be discussed throughout this thesis, *extreme* is becoming more and more of a relative term. There are a plethora of environmental parameters that can constitute an extreme environment for a particular species or ecosystem, but this extreme environment is likely home to a highly specialized ecosystem of organisms. Some environmental parameters that can constitute an extreme environment include, but are not limited to, extreme temperature, pressure, salinity, pH, liquid water availability, or oxygen availability. Table 7.1, summarizes these parameters as well as provides some qualitative values for what might be considered extreme for each environmental parameter.

As more is learned about life in extreme environments, we are realizing how truly diverse life can be. Our understanding of *life* as oppose to *life as we know it* seems to be ever changing. This is leading to the realization that a meaningful search for *extant* life around the world and eventually the solar system requires a more simplified and general approach.

This simplified and general approach can be elegantly summarized by James Lovelock in a letter to Nature in 1965, where he said, "at the present stage of technical development, a visual search [for extraterrestrial life] is probably too complex; it is nevertheless the most rapid and effective method of life recognition in terms of orderliness outside the bounds of random assembly" [78]. Of the many subjective questions related to the search for *extant* life, the most perplexing is being able to look for *life* as opposed to *life as we know it*. As an Earth-based species, there exists only a single data point of what we know life to be. James Lovelock, along with this thesis, makes the argument that searching for extraterrestrial *life* (not life as we know it) requires a much more simple and elegant solution. This solution is to simply look using a microscale optical imaging device.

Approach to Solution

Before there can be a solution, first the problem must be known. In the search for *extant* extraterrestrial life on the icy moons of Jupiter or Saturn, it is first necessary to understand the environments we expect to find there. Europa as an example, is extremely far from the sun, while experiencing large amounts of tidal heating from the gravitational pull of Jupiter. With this, we would expect a frozen outer shell of ice while the tidal heating is capable of maintaining a global sub-surface liquid water ocean. From the radiative environment of Jupiter, we can also expect high levels of high energy radiation near the surface. K. Hand, et al. provide an excellent

review of all relevant environmental parameters as well as an in-depth analysis that aims to hypothesize the size scale and abundance of any potential life in the ice or liquid ocean of Europa [55].

This report provides a very in-depth analysis of the various bio-signatures known on Earth as well as uses these bio-signatures to infer on the possible bio-signatures expected on Europa. These bio-signatures include: 1) organic indicators, 2) morphological indicators, 3) inorganic indicators, and 4) provenance. This thesis focuses on addressing the bio-signatures associated with morphological indicators. Visual observations of microscopic and macroscopic structure have aided in the detection and study of life in both active and inactive life forms [18, 40] and can be instrumental in the detection and verification of both extant *and* extinct life on extraterrestrial bodies.

Many instruments exist that are capable of studying the morphology of micro and macroscopic organisms, but this task becomes even more complex when considering variables such as the expected concentrations of life as a result of the nutrient levels in an extreme environment. To shed light on this complex question, a review article was published comparing various imaging modalities with respect to their efficacy in extraterrestrial life detection, of which I was co-author [12]. Although K. Hand, et al. provide a succinct and all-encompassing review of all space flight mission imaging technologies and their ability to image the spatial frequencies necessary for life detection, our literature review focuses on the overall state of the art in imaging technologies while attempting to address other life detection challenges such as the low biomass expected in extreme environments as well as the physical robustness needed in an instrument in order to become flight qualified.

As a result of this survey into the state of the art of micro and macroscopic imaging modalities, it was seen that there currently exists no imaging device that is capable of space flight while also being sensitive enough to detect microbial life in an average cubic meter of Earth ocean water. The modalities surveyed were recent advancements in atomic force microscopy (AFM), fluorescence microscopy, digital holographic microscopy (DHM), imaging flow cytometry, electron microscopy, lightfield microscopy, Fourier ptychographic microscopy, as well as the possible combinations of all of these imaging modalities to form a multimodal optical sensing system.

Throughout the course of this technology survey, many candidates for potential instruments were identified. These instruments either were capable of resolving the

spatial frequencies necessary for life detection of microscale life, sensitive enough to detect the low concentrations of life expected, or were physically robust enough to withstand the mechanical stresses of space flight and landing. In addition to this, it was argued that morphology alone should not be used as an unambiguous bio-signature for *extinct* life because certain minerals have been observed to self-assemble into biomimetic shapes [49], which can result in potential false positives.

Scientific and Functional Performance Requirements

The report of the Europa Lander science definition team by K. Hand, et al. [55], provides a very extensive and exhaustive science traceability matrix (STM), which is a document that establishes all high-level objectives of a proposed project and progressively defines the various factors involved with accomplishing those objectives. This document provides a deductive method of explicitly defining performance parameters that will achieve the high level science goals of a project. This logical nature of the STM provides a succinct, yet thorough introduction into the design requirements of the instrument described in this thesis as well as introducing the reasons behind these performance requirements.

The high-level task, set out in this thesis, is to develop a device to be used in the search for extraterrestrial life, but also to explore more immediate Earth-based applications as a microbiological scientific tool to conduct sophisticated and targeted experimentation. In order for this high-level objective to be brought to fruition, this goal must be broken down into its constituent parts that will address the objective as a whole. In order to infer on the presence of life based on morphological indicators, these indicators must be able to be identified and characterized. An optical imaging device is an intuitive modality for the investigation of microscale morphology, so any optical imaging device that is to accomplish this goal must be able to resolve morphological features on the spatial scales expected in microscopic life.

K. Hand, et al. [55] and J. Nadeau, et al. [12] provide an in-depth review of the spatial scales of the known life on Earth which exists on the micron scale. This involves single celled prokaryotic life which can be as small as $0.2 \mu\text{m}$ up to tens of μm in their longest dimension. In order for the morphological features of cells of this spatial scale to be identified, an optical imaging device must be able to laterally resolve particles at these spatial scales. For this reason, the optical imaging device must have a sub-micron lateral resolution ($r_{xy} \leq 0.8 \mu\text{m}$), with a field of view no less than $300 \times 300 \mu\text{m}^2$. In addition to resolving these morphological features, it is

necessary to be able to detect particle motion on these spatial scales. This requires a temporal resolution of greater than or approximately equal to 10 observations per second. This temporal resolution is sufficient to provide information of the movement of particles at the sub-micron spatial scales at speeds of 1-100 $\mu\text{m/s}$.

In addition to identifying and characterizing microscale morphological indicators of life, the variable concentration of microbial life must be taken into account. Depending on many factors, the concentrations of microbial life can vary from 10^2 objects/mL to 10^8 objects/mL. This necessitates the optical imaging device to be able to detect and identify these morphological indicators at ranges of object concentrations between 10^2 - 10^8 objects/mL. This indirectly necessitates a minimum depth of field of the instrument as this impacts the sensitivity of the instrument. This relationship between depth of field and instrument sensitivity will be explored in Chapter 4.3 as well as [13]. In order to meet the sensitivity requirements, a depth of field of no less than 600 μm is needed.

Finally, in a heterogeneous population, sub-micron scaled particles can be distinguished and discriminated based on properties related to buoyancy. The range of various mass densities of particles that are to be distinguished are particles with densities ranging from 0.8-3.0 g/cm^3 . Thus, depending on the physical orientation of the imaging instrument relative to the gravity vector, the optical imaging instrument must have an axial resolution of $r_z \leq 10 \mu\text{m}$.

Figure 1.1 shows a diagram of the progression of the general scientific goal of this thesis and traces this goal all the way down to explicit performance requirements of the optical imaging device. This explicitly defined list of functional performance requirements will serve as a basis for the quantification of the instrument's performance throughout the thesis. This will ensure that a device is designed with the most reasonable confidence of addressing the scientific goals of this thesis.

Based on these performance requirements as well as the literature review conducted on the state of the art of microscale optical imaging devices, off-axis digital holographic microscopy shows the most promise as a device to meet these explicit performance requirements. Holography is inherently a 3D imaging modality enabling the imaging of large samples simultaneously without any moving parts. This instantaneous 3D imaging provides high temporal resolution as well as a large depth of field. Furthermore, it has been previously shown that diffraction limited performance is possible with off-axis DHM. This makes off-axis DHM capable of sub-micron resolution as well as addressing all performance requirements of an

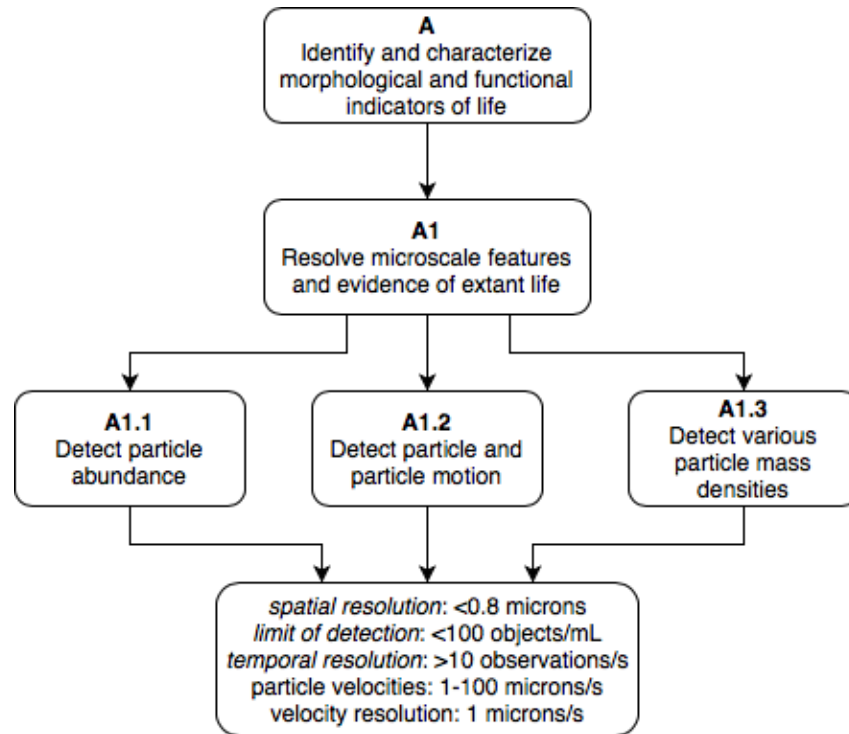


Figure 1.1 – Performance requirements of the optical imaging device

optical imaging device for the detection of life on the micron scale.

Thesis Statement

This thesis describes the development of both hardware and software techniques for an off-axis digital holographic microscope (DHM) in order to accomplish the high-level goal of one day being used in the search for extraterrestrial life, but also explores more immediate Earth-based applications as a microbiological scientific tool to conduct sophisticated and targeted experimentation. First, an in-depth analysis of the problem to be addressed was presented as well as a survey of the current state of the art in instruments that can shed light on this problem. The solution as developed in this thesis will then be introduced with explicit definitions of the expected scientific and engineering capabilities of the instrument. The instrument will be described in detail including the theoretical operating principle, hardware and software development, as well as the experimental verification of its performance. Next, laboratory experiments are introduced with the instrument involving the development of a novel optical phase contrast agent for the targeted increase in optical phase contrast of samples. Lastly, field experimentation with the instrument is to be introduced where the instrument was used for the *in situ* study of liquid

samples in multiple remote and extreme environments. The use of the DHM developed throughout this thesis to successfully search for, detect, and characterize life in various extreme environments around the world, shows its utility and value as a potential instrument for the search for life around the solar system.

Chapter 2

THEORETICAL OVERVIEW OF HOLOGRAPHY

This chapter will introduce the fundamental theory which allows off-axis digital holography to be implemented, as well as more specific theoretical information regarding the properties of the phase of a wave as it travels through a focus. Although many forms of holography exist, including but not limited to, off-axis, in-line, coherent, and incoherent holography, this work focuses on the implementation of coherent off-axis digital holography.

2.1 Off-Axis Digital Holography

Off-axis digital holographic microscopy is performed by the use of optical interferometry. This technique encodes both the amplitude and phase characteristics of an object simultaneously. It accomplishes this by the superposition of a reference and sample light beam. The reference and sample beam are recombined at the detector plane which then creates interference patterns, or an interferogram. The beams of an interferometer can be represented as plane waves of identical wavelengths, such that their displacement functions are

$$\psi_1(x, y, t) = A_1(x, y)e^{i(\phi_1(x,y)-\omega t)}, \quad (2.1a)$$

$$\psi_2(x, y, t) = A_2(x, y)e^{i(\phi_2(x,y)-\omega t)}, \quad (2.1b)$$

where A_1 and A_2 are the amplitudes of the electric field as a function of x and y , ϕ_1 and ϕ_2 are the relative phases of waves 1 and 2, respectively, and ω is the angular frequency of the wave.

The combination of these two waves at the detector plane causes the resultant wave to be expressed using the superposition principle such that

$$\Psi(x, y, t) = \psi_1 + \psi_2 = A_1(x, y)e^{i(\phi_1(x,y)-\omega t)} + A_2(x, y)e^{i(\phi_2(x,y)-\omega t)}. \quad (2.2)$$

Modern optical detector arrays' mode of operation is by the integration of the electric field incident on it over a period of time [67]. The measured electric field by the

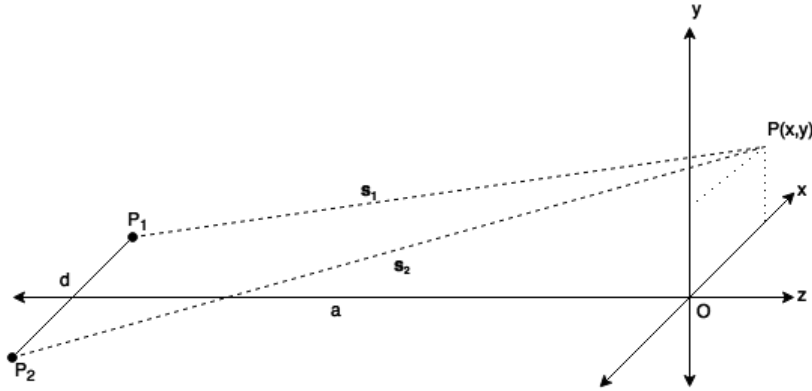


Figure 2.1 – Optical schematic of a Young's Double Slit Experiment. Two point sources of light located at P_1 and P_2 propagate to the image plane at the origin.

detector becomes

$$I(x, y) = \int_{t_1}^{t_2} \Psi \Psi^* dt = I_1 + I_2 + 2\sqrt{I_1 I_2} \cos(\Delta\phi), \quad (2.3)$$

where Ψ^* is the complex conjugate of Ψ , I_1 and I_2 are the intensities of beams 1 and 2, respectively, and $\Delta\phi$ is the phase difference between the two waves. It is within the variable $\Delta\phi$ that we can modulate the spatial frequency of the interference patterns, or fringes [21].

The two plane waves that are converging towards each other can be considered as the two converging waves in a simple Young's Double Slit Experiment. In this analogy, illustrated in Figure 2.1, two point sources of light, P_1 and P_2 , are separated by some distance d . The light from these point sources propagate in the positive z direction, and are incident to a detector located a distance a from P_1 and P_2 , such that $a \gg d$.

Modeling the DHM as a modified Young's Double Slit Experiment [20] yields a value for the phase difference between the two beams of the instrument as

$$\Delta\phi(x) = \frac{2\pi}{\lambda_0} \left(\frac{nx d}{a} \right), \quad (2.4)$$

where λ_0 is the illumination wavelength of the system, and n is the index of refraction of the medium through which the light propagates.

This variable is very influential in the practical implementation of a DHM as it dictates the spatial frequency of the fringes caused by the reference and sample

beams of light. It is important to match this variable with an appropriately sized digital detector so that one obtains proper Nyquist sampling of the fringe. For an in-depth derivation of this variable, see Appendix A.

Numerical Reconstruction of a Hologram

A process of numerical reconstruction is used to digitally propagate the electric field recorded in the hologram to a desired focal plane. This allows the real time 3D imaging of dynamic samples in both amplitude and phase. An amplitude image is analogous to a traditional brightfield microscopy image, while a phase image has no conventional counterpart.

Multiple methods of holographic reconstructions exist based on various optical assumptions. The most common are known as the Fresnel Transform Method (FTM), the Huygens Convolution Method (HCM), and the Angular Spectrum Method (ASM). Throughout this thesis, only the ASM was implemented for reasons that are to be discussed. Here, a brief overview of the FTM and HCM are provided while the ASM is described in greater detail.

The FTM involves the use of the Fresnel Transform to reconstruct the electric field recorded in a hologram. This transform combines the recorded hologram with Fresnel point spread function (PSF). The reconstructed wavefront (Γ_{FTM}) as a result of the FTM is

$$U_{\text{FTM}}(x_0, y_0, z_0) = 2\pi e^{\frac{ik}{2z}(x^2+y^2)} \mathfrak{F}[I(x_S, y_S) * S_F(x_S, y_S, z_0)], \quad (2.5)$$

where U is the reconstructed electric field and S_F is the Fresnel PSF.

The Fresnel PSF is the optical point spread function using the paraxial approximation. This approximation is also known as the 'small angle approximation.' For more on the FTM, see [66].

The HCM involves the convolution of the hologram with the Huygens PSF. The Huygens PSF is the optical point spread function using the Huygens wavelet principle. The reconstructed electric field as a result of the HCM is

$$U_{\text{HCM}}(x_0, y_0, z_0) = \mathfrak{F}^{-1}[\mathfrak{F}[I(x_S, y_S)] * \mathfrak{F}[S_H(x_S, y_S, z_0)]], \quad (2.6)$$

where S_H is the Huygens PSF. For more on the HCM, see [66].

The ASM describes the propagation of a wave by decomposing the wave into its angular spectrum (Fourier Transform). This is accomplished by using the convolution theorem along with the fact that wave propagation is a linear process. This method, along with other methods for the reconstruction of holographic data are well reviewed in [66].

If an electric field is sampled by a detector and represented as $I(x, y)$, then the numerical reconstruction process of the ASM would be able to numerically propagate this electric field by some axial distance z such that the reconstructed electric field is

$$U_{\text{ASM}}(x_0, y_0, z_0) = \mathfrak{F}^{-1}[\mathfrak{F}(I(x_S, y_S)) * H(f_x, f_y, z_0)], \quad (2.7)$$

where $I(x, y)$ is the hologram, H is the transfer function of free space, and \mathfrak{F} is the Fourier Transform operator.

To understand the function and form of the transfer function of free space, we first must know a bit about our optical system. Off-axis DHM uses a plane wave to illuminate a sample. Because of this, as well as the fact that the samples we are interested in imaging are transmissive and relatively sparse, we can assume that we are to numerically reconstruct a plane wave that has been disturbed slightly by the sample.

Let's consider a plane wave propagating in free space in the z direction such that the plane wave can be expressed by the displacement function

$$U(\mathbf{r}) = Ae^{-i\mathbf{k}\mathbf{r}} = Ae^{-i(k_x x + k_y y + k_z z)} \quad (2.8)$$

where A is the plane wave's amplitude, and \mathbf{k} is the wave number that can be decomposed into its three spatial components k_x , k_y , and k_z .

The wave number k is defined as

$$\mathbf{k} = \frac{2\pi}{\lambda} = 2\pi\nu = \sqrt{k_x^2 + k_y^2 + k_z^2} \quad (2.9a)$$

$$k_x = \frac{2\pi}{\lambda_x} = 2\pi\nu_x \quad (2.9b)$$

$$k_y = \frac{2\pi}{\lambda_y} = 2\pi\nu_y \quad (2.9c)$$

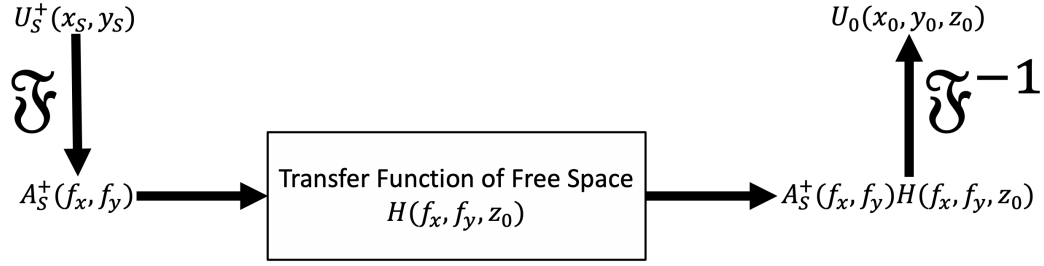


Figure 2.2 – The Angular Spectrum Method (ASM). The electric field recorded by the digital detector U_S^+ is acted on by the transfer function of free space H in order to reconstruct the electric field at a desired axial plane z_0

$$k_z = \frac{2\pi}{\lambda_z} = 2\pi\nu_z = \sqrt{\mathbf{k}^2 - k_x^2 - k_y^2} \quad (2.9d)$$

where λ is the wavelength, and ν is the spatial frequency of the plane wave.

In reality, the plane wave that we are reconstructing is off-axis, so we employ the paraxial approximation such that we assume that $\mathbf{k} \gg k_{x,y}$ and the direction of the wave propagation is predominantly in the z direction.

Let us assume that a plane wave is considered at $z = 0$ such that $U(x, y, 0) = Ae^{-i(k_x x + k_y y)}$. At some distance $z \neq 0$, the wave will take the form $U(x, y, z) = Ae^{-i(k_x x + k_y y + k_z z)} = U(x, y, 0)e^{-ik_z z}$.

Because the propagation of a wave through free space is a linear process, we can consider this a linear system with an input and an output that is created as a result of a transfer function.

Let $U_S^+(x, y)$ be the electric field recorded by the digital detector, and let $U_0(x_0, y_0, z_0)$ be the numerically reconstructed electric field at some axial plane z_0 , as illustrated in Figure 2.2.

The transfer function for this system is known as the transfer function of free space as it describes the propagation of a wave in free space.

Employing the ASM, we know that

$$H(f_x, f_y, z_0) = \frac{A_0(f_x, f_y, z_0)}{A_S^+(f_x, f_y)} \quad (2.10)$$

where $A_0(f_x, f_y, z_0)$ and $A_S^+(f_x, f_y)$ are the Fourier transforms (also known as the angular spectrum) of U_0 and U_S^+ , respectively expressed in units of spatial frequency f_x and f_y .

Combining our definitions of $U_S^+(x, y)$, $U_0(x_0, y_0, z_0)$, as well as Equation 2.9d, we find the transfer function of free space to take the form

$$H(f_x, f_y, z) = e^{-ik_z z} \quad (2.11)$$

where $k_z = \frac{2\pi}{\lambda} \sqrt{1 - (\lambda f_x)^2 - (\lambda f_y)^2}$.

Thus, the transfer function of free space at a given axial distance z is

$$H(f_x, f_y, z) = \exp\left(\frac{-2\pi z i}{\lambda} \sqrt{1 - (\lambda f_x)^2 - (\lambda f_y)^2}\right). \quad (2.12)$$

Using this definition of the transfer function of free space with the ASM shown in Equation 2.7, the amplitude, intensity, and phase of the incident light at the plane z are calculated as

$$A(x_0, y_0, z_0) = |U_0|, \quad (2.13a)$$

$$I(x_0, y_0, z_0) = A^2 = |U_0|^2, \quad (2.13b)$$

$$\phi(x_0, y_0, z_0) = \arctan\left(\frac{\Im(U_0)}{\Re(U_0)}\right), \quad (2.13c)$$

where $\Im(\Gamma)$ and $\Re(\Gamma)$ are the imaginary and real components of Γ , respectively. The expressions in Equation 2.13 describe the fully reconstructed electric field of a holographic image at a desired focal plane z .

There are multiple reasons why the ASM is used in the numerical reconstruction of holograms throughout this thesis over the other two methods. The FTM is a numerical reconstruction method that has the advantage of only needing a single Fourier Transform. This makes it less computationally expensive, but this method is difficult to implement for microscopy applications as the paraxial approximation in concert with the Fresnel PSF breaks down for high numerical aperture optical systems. The HCM involves the propagation of spherical waves. This causes the fringe spacing on the optical detector to become non-uniform and depending on

the size of the detector, the fringe spacing according to the HCM will exceed the Nyquist sampling limit that the detector is capable of imaging. The ASM involves the propagation of a plane wave which does not suffer from these limitations. This plane wave approximation is valid because we design our optical systems such that $a \gg d$ as seen in Figure 2.1. Furthermore, the ASM involves the use of two Fourier Transforms as opposed to the three Fourier Transforms needed in the HCM. For these reasons, the ASM is more advantageous for the particular implementation of DHM discussed throughout this thesis.

2.2 Phase Distribution of a Wave as it Travels Through Focus

The intensity of light is very well studied and characterized by the Airy function (laterally) as well as the point spread function (PSF) in three dimensions. Intensity, however, only describes one aspect of a wave's propagation. As off-axis holography is capable of not only imaging and reconstructing the intensity of an electric field as it interacts with a sample, but is also capable of reconstructing the phase of the wave, an understanding of the phase distribution of light as it passes through focus is necessary.

In 1890, the French physicist Louis Georges Gouy directly observed that a converging beam of light experiences an axial phase advance as it travels through focus. Gouy also discovered that this was not a property of light exclusively, but that this is a property of all converging waves including acoustic waves [52]. Since this first observation made by Gouy, many theoretical analyses have led to the verification of this axial phase shift. In 1909, Peter Debye found an exact analytical solution to the wave equation which also encapsulated the phase shift observed by Gouy [36]. In 1938, Wojciech Rubinowicz explained this phase shift by treating light using the boundary diffraction theory [101]. In addition, Edward H. Linfoot and Emil Wolf observed this phase shift while analyzing the phase distribution of light using the Kirchoff diffraction theory [76]. Since its discovery, the Gouy phase shift has been observed, both theoretically and experimentally, in many different beam types including, but not limited to, Gaussian beams, Bessel beams, and photonic nanojets. An extensive review of the state of the art in research and application of the Gouy phase shift can be found in Volume 58 of *Progress in Optics* [64].

Although this phenomenon has been discovered for 130 years now, there is still much debate in the scientific community as to its origins and even the reason it occurs. Intuitive explanations of the Gouy phase shift have been provided with respect to a

spherical converging Gaussian beam, but is only capable of providing an explanation for the case of a converging *spherical* wave [24]. In an attempt to provide a general explanation for one, two, and three-dimensional converging waves, light was theoretically modelled as an adiabatic propagation through space [25, 54, 112, 117]. Treatments of optical propagation involving the quantum mechanical principle of Heisenberg's uncertainty principle were also used in an attempt to explain this anomaly [35, 45]. The Gouy phase shift has also been characterized as a geometric quantum effect arising from the uncertainty principle due to the constraints in physical space available for the propagation of photons through focus [57]. Although these explanations were successful at capturing the Gouy phase shift, a quantum mechanical approach is unnecessary as the Gouy phase shift occurs for all waves, including acoustic waves, which are well characterized by classical mechanics.

Most optical imaging modalities are oblivious to this phenomenon due to the fact that current optical detectors are only capable of measuring the time integrated electric field intensity of an incident wavefront. Certain imaging modalities benefit from the Gouy phase shift, however, either directly or indirectly. Certain methods of measuring the optical resonance frequency of laser cavities exploit the Gouy phase shift [21, 111]. Other disciplines that have benefited from imaging devices that exploit the Gouy phase shift include generic optical metrology [69], coherence tomography [74], terahertz spectroscopy [44], optical trapping [46, 50, 100], as well as research into surface plasmon polaritons [130]. Developments in astronomical interferometry have made it possible to employ this effect in the development of certain astronomical nulling interferometric instruments such as the achromatic interfero coronagraph (AIC) [8, 9].

As mentioned above, there is no consensus on a single satisfactory theoretical origin for its existence. Because of this, in the following section, a brief overview of a heuristic theoretical approach is offered. This derivation is based on the convergence/divergence of a spherical wave with Gaussian cross section and sheds light on the existence of the Gouy phase shift without making claim to its origin.

If a converging/diverging wave of Gaussian cross-section is considered such that the wave is propagating in the positive z direction and comes into focus at $z = 0$, the function $\Phi(z)$ can be used to describes the phase distribution of the wave of light

along the optical axis and is defined as

$$\Phi(z) = \arctan\left(\frac{\lambda z}{\pi\omega_0^2}\right), \quad (2.14)$$

where λ is the wavelength of the light, and ω_0 is the beam waist at focus ($z = 0$). The coordinate system employed here places the point of focus of the Gaussian beam at $z = 0$. Thus, by calculating the phase change as light passes through focus ($\Phi|_{z=\pm\infty}$), we see a phase difference of exactly π , which corresponds precisely to the predicted phase shift by Gouy [24, 111]. For an in-depth derivation of this expression, see Appendix A. Figure 2.3 shows an axial slice through a particle that has been reconstructed in phase. This volumetric slice illustrates the Gouy Phase Shift as a jump from dark to light pixel values can be seen in the vertical direction at the center of the particle (located at the center of the slice).

Concluding Remarks

This chapter offered a theoretical background into the basic optical theory which allows for the implementation of off-axis digital holography. This chapter presented no new material, but rather introduced the relevant theory as a means of providing context for the remainder of the thesis. Furthermore, due to off-axis holography's ability to image the phase of the electric field, a brief description of the volumetric phase distribution of light at a focus was described. In the following chapter, this optical theory will be applied experimentally in the development of bench-top and field DHM instruments.

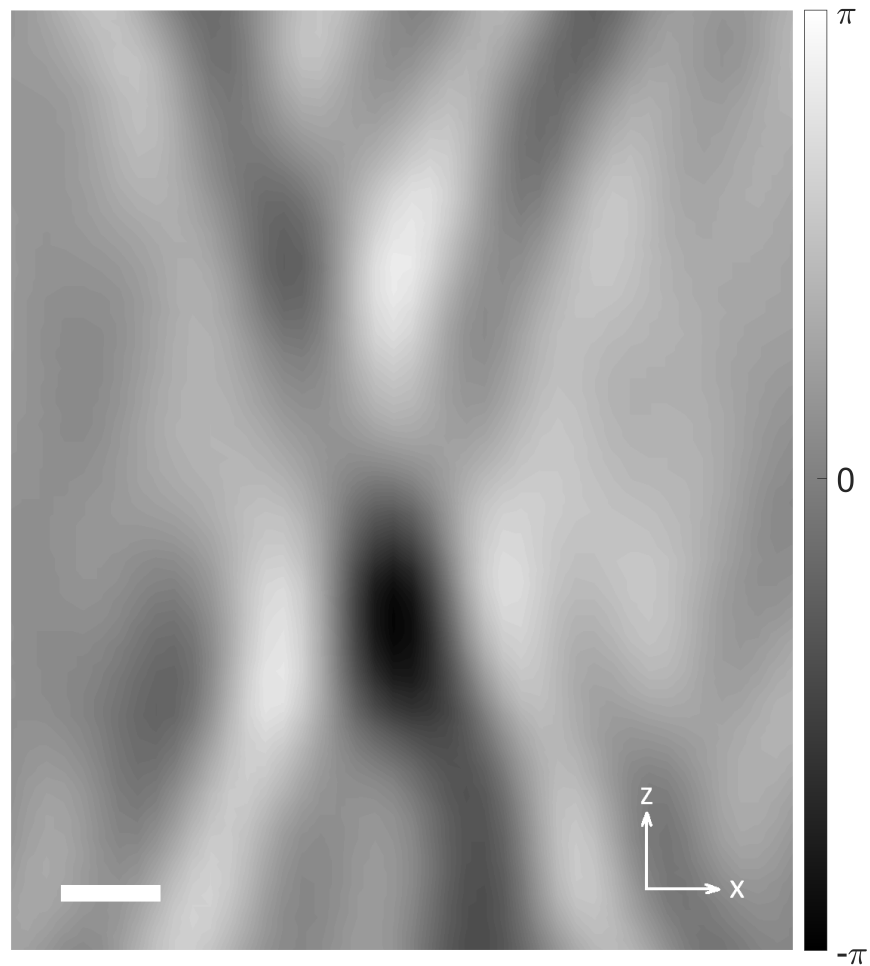


Figure 2.3 – Illustration of the Gouy Phase Shift. This is a volumetric slice (xz plane) of a single micron-sized gas vesicle cluster that has been reconstructed in phase with bounds $[-\pi, \pi]$. The particle is located at the center of the figure and the Gouy Phase Shift can be seen as a change from dark to light pixel values in the vertical direction through the center. Scale bar represents $1 \mu\text{m}$.

Chapter 3

HARDWARE DEVELOPMENT

The previous chapter introduced an overview of the theoretical background that allows holography to encode 3D information of a sample simultaneously in a 2D image. Here, the practical implementation of this theory will be introduced. This chapter describes the hardware development for the DHM instruments used throughout this thesis. Select instruments described in this chapter were designed prior to my involvement with this project, so the optical schematics and performances of the instruments are only introduced here with their respective publications referenced. Details of my involvement and contribution to each instrument will be explicitly outlined throughout the chapter as the instruments are introduced. Using the optical architecture called the common-mode, a ruggedized field instrument was built for *in situ* experimentation of remote and extreme environments. The details as well as my contributions to this instrument will be introduced. This field instrument motivated the development of a miniaturized instrument that would have identical optical performance, but with a smaller form factor and power consumption. The design details of this instrument will also be introduced. Due to the complex wavefront sensing nature of holography, the quality of sample chamber substrates was also considered in the design of custom sample chambers. The details of the effects of substrate types on image quality as well as general sample chamber design information will be provided in detail in this chapter.

3.1 Optical Design

Throughout this thesis, two optical architectures were used for all subsequent hardware and software development as well as data acquisition. The first architecture is a traditional Mach-Zehnder interferometer architecture and the second is informally referred to as the common mode architecture. Each of these operating modes present various advantages and disadvantages, making one more suitable for certain situations than the other, as will be discussed further.

The Mach-Zehnder interferometer architecture was originally developed and verified in 2014 [71]. The operating principle behind this instrument involves the splitting of an originally monochromatic and coherent light source via a 50/50 beam-splitter. The two spatially separated beams of light are then redirected via mirrors where

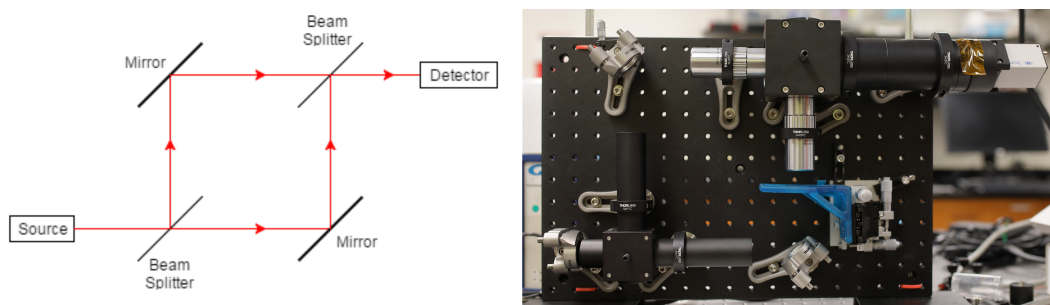


Figure 3.1 – An optical schematic of the Mach-Zehnder DHM instrument as well as an image of the benchtop instrument

one beam (the sample beam) interacts with the sample being imaged while the reference beam remains undisturbed. The two beams then travel through separate, but identical, infinity corrected microscope objective lenses that provide magnification. The infinity corrected light from the two separate beams then get recombined via a second 50/50 beam-splitter such that the two beams are incident to a digital detector at an angle relative to each other. The bench-top instrument of the Mach-Zehnder DHM is shown in Figure 3.1.

This instrument provides many advantages as well as disadvantages for in-lab and field use. The main advantage of this instrument is that it provides a spatially separated reference and sample beam. This physical separation allows for robust experimentation that may involve bulky sample chamber components. Bulky sample chamber components can include, but are not limited to, sample temperature controllers, electronic equipment, and magnetic field sources, all of which can be used to investigate the behavior of a sample under various conditions. Another noteworthy advantage is the modular design of the instrument, which allows for the relatively easy changing of objective lenses in order to suit the needs of the particular experiment being performed. This instrument has successfully been developed using four different types of objective lenses and can be adapted to be compatible with other lenses of different magnification and numerical aperture. See Appendix E for more details on the specific compatible parameters of an objective lens.

The disadvantages of this instrument stem from the very qualities that provide its advantages. Because the reference and sample beams are spatially separated by tens of centimeters, the instrument is incredibly sensitive to misalignment between the two beams. Events such as physical vibrations or convection in the air can cause misalignment in the instrument that is time consuming to rectify. In addition to this

sensitivity, the instrument itself is difficult to align in the first place. The multiple optical components necessary in its construction (beam-splitters, mirrors, objective lenses, etc.) all must be precisely aligned, which can be very difficult to establish and maintain in practice.

In order to address these disadvantages, a novel optical architecture was designed, which is referred to as the common mode architecture/instrument because although it has two spatially separated beams of light, it forces the two beams of light to travel through common optical components. This instrument was originally developed, built, and verified in 2015 [123]. The operating principle behind this instrument involves the input of a monochromatic and coherent light source that first travels through a collimator lens, which produces parallel light from the diverging light source. This parallel light must then travel through a custom sample chamber containing two channels that are spatially separated and isolated from each other (more about these sample chambers later in this section). A custom sample chamber is necessary to hold the sample that is to be imaged, but also contain an identically sized channel that can contain reference liquid in order to match optical path lengths with the sample. Matching optical path lengths is vital to this instrument as it maintains the coherence of the two beams of light. Once the parallel light has interacted with the sample and reference liquids, they pass through two, spatially separated aspheric lenses. After these lenses, a relay lens is used to recombine the light at a digital detector. The aspheric lenses, in addition to the relay lens, provide the image magnification and interference created at the digital detector. Figure 3.2 shows an optical schematic of the instrument as well as an image of the bench-top instrument.

3.2 Field Instrument - Generation I

In 2015, the common mode optical instrument was fitted in a ruggedized and water-resistant case in addition to a processor, hard drive and all other electronics necessary for its stand alone operation. This DHM field instrument was informally named the orangeBox due to its distinct orange color. This instrument was designed and built in 2015 and had its initial field test, which took place in Nuuk, Greenland in March of that year.

The details of this instrument as well as the scientific yield of the field campaign to Nuuk, Greenland have been published in the peer-reviewed journal *PLOS One* [75], of which I am third author.

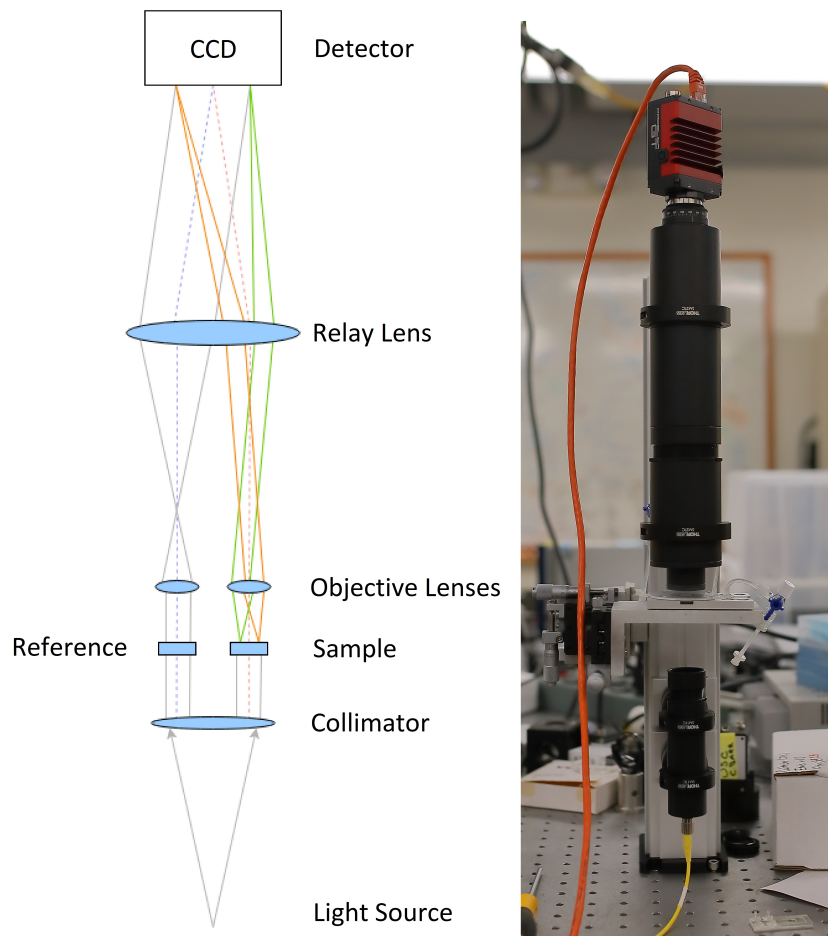


Figure 3.2 – An optical schematic of the Common Mode DHM instrument as well as an image of the benchtop instrument

The development of the optical architecture of this instrument was done prior to my graduate career at the California Institute of Technology. At the time, I was an undergraduate at the University of California, Riverside and contributed to this instrument's development as a research technician. My responsibilities on this project included the design and fabrication of the sample handling subsystem. This involved everything that interacted with the sample being imaged by the instrument as well as all hardware that the human user would interact with.

Figure 3.3 shows the orangeBox instrument and Figure 3.4 shows the microfluidic sample chambers of the device.

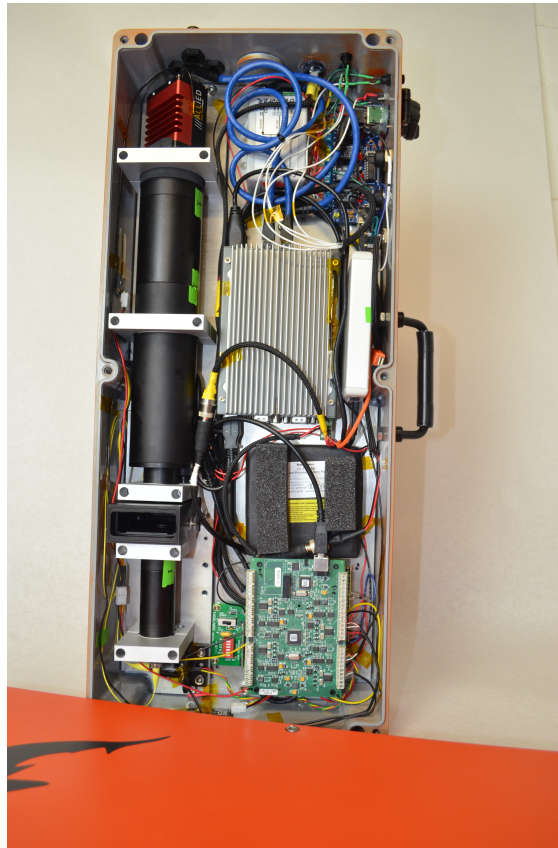


Figure 3.3 – The orangeBox field instrument

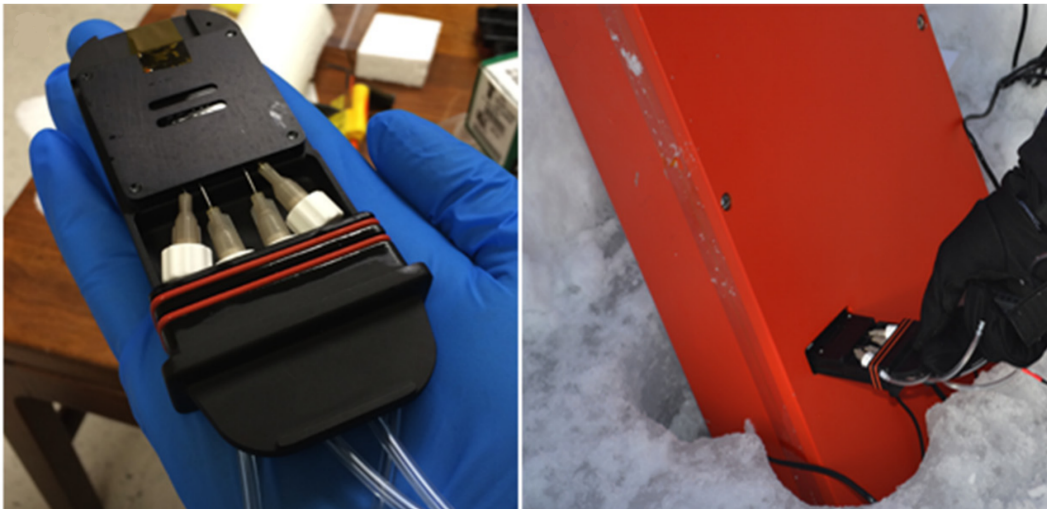


Figure 3.4 – The sample chamber assembly of the orangeBox field instrument, fully assembled (left) and in use while in Nuuk, Greenland (right) (adapted from [75]).

3.3 Field Instrument - Generation II

The miniaturization of the orangeBox was motivated by the limitations the size and mass of the instrument placed on the types of field work possible. The mass of the orangeBox is about 10 kg, which along with its size qualifies it to be carried on as baggage on a typical commercial airplane, but presents difficulty in actual field work that involves carrying the instrument across long distances/rugged terrain. For these reasons, Stephanie Rider (Caltech) and I, as well as Felipe Fregoso and J. Kent Wallace at JPL/NASA worked together to redesign the orangeBox field instrument in order to incorporate hardware and software enhancements based on feedback from the instrument's users, as well as technological advances made in computer electronics and optical detectors.

Stephanie Rider and I worked together to design the entire instrument. Her roles included the mechanical design of the instrument including the sample handling subsystem, while my role included the design and fabrication of the electrical hardware and software of the instrument. We worked together on the optical design with help from J. Kent Wallace, an optical engineer at JPL/NASA. Technical drawings for this instrument are provided in Appendix E. The electrical schematics for the custom printed circuit board (PCB) are also described in Appendix E.

The electronics package of the instrument includes a compact computer (UDOO x86 ULTRA), a 128 GB M2 solid-state hard drive, a USB 3.0 powered CMOS camera (Allied Vision MAKO U-503B), and a custom PCB, which interfaces the computer with all peripheral devices such as the laser driver (Thorlabs EK1102), thermistors, moisture sensors, as well as status indicating LED's.

The electronics of the instrument are controlled by a commercially available computer (UDOO x86 ULTRA). The computer is equipped with one Gigabit Ethernet port, three USB 3.0 ports, an HDMI output, as well as 16 GPIO pins and a fully embedded Arduino Leonardo. The computer has a rated nominal power consumption of about 11 W and a maximum consumption (CPU, GPU, and GigE at 100%) of 36 W. The instrument described in this work is normally operated without a display or constant use of the GigE port, reducing its operating power consumption below its reported values (<11 W). A 128 GB solid-state hard drive is used for data and metadata storage. The operating software is Linux Ubuntu 18.04, which is well supported by data acquisition hardware and allows the user to limit the background activity of the CPU, further decreasing power consumption and interruptions of data acquisition.

The laser driver (Thorlabs EK1102) provides power to the 405 nm pigtailed laser (Thorlabs LP405-SF10) used as the illumination source in the instrument. The optical power output of the laser is dictated by a voltage input to the laser driver (0-2.5 V) that is provided by a PWM-enabled pin of the Arduino Leonardo. This PWM pin is wired to a low-pass filter on the custom PCB to attenuate the high frequency oscillations of the PWM prior to interfacing with the laser driver.

The laser driver is provided an excitation voltage of 12 V that is controlled by a TTL SPDT relay circuit on the custom PCB. This board is signaled using the GPIO pins of the computer.

Voltage divider circuits are used to read temperatures provided by a thermistor. The voltage divider circuit is designed to be used with any PT1000 compliant thermistor.

The CMOS camera (Allied Vision Technology Mako U-503B) is powered via USB 3.0 and has a power consumption of 1.9 W. This camera was used due to its compact form factor, low power consumption, low cost, and small pixel size of the detector ($2.2 \mu\text{m}$ by $2.2 \mu\text{m}$). The data acquisition speed of the instrument is ≤ 14 frames per second. The original DHM field instrument was built with a digital detector whose pixel size is $3.45 \mu\text{m}$. The Mako U-503B has a detector with a 36.2% smaller pixel size. According to Equation A.30, this allows the overall length of the DHM instrument to shrink proportionately. This size reduction, in addition to a pair of optical mirrors, allows a dramatically smaller optical form factor without any sacrifice of optical performance of the instrument. Figure 3.5 shows a CAD model of the optical setup of the field instrument indicating the laser driver, laser diode, collimating lens, objective lenses, folding mirrors, relay lens, and CMOS detector.

The DHM operating software is written in a combination of Python and C++. A shell script is used to launch a main python wrapper function at initial startup of the computer. The software architecture is based on a publish-subscribe pattern where each module of the software is both a publisher of information and/or a subscriber to information from other modules. This scheme allows for the software to remain flexible in order to accommodate expansion, which is expected as the instrument usage and capabilities grow. Felipe Fregoso, a software engineer at JPL/Caltech led the main effort of this software development. The communication between the python publisher(s) and subscriber(s) occurs through TCP ports, which allows for wireless transfer of live data. A host computer (user operated laptop), can connect to the instrument's on-board UDOO computer and stream live data via TCP port, rather than use a hard-wired Ethernet connection. Felipe wrote the

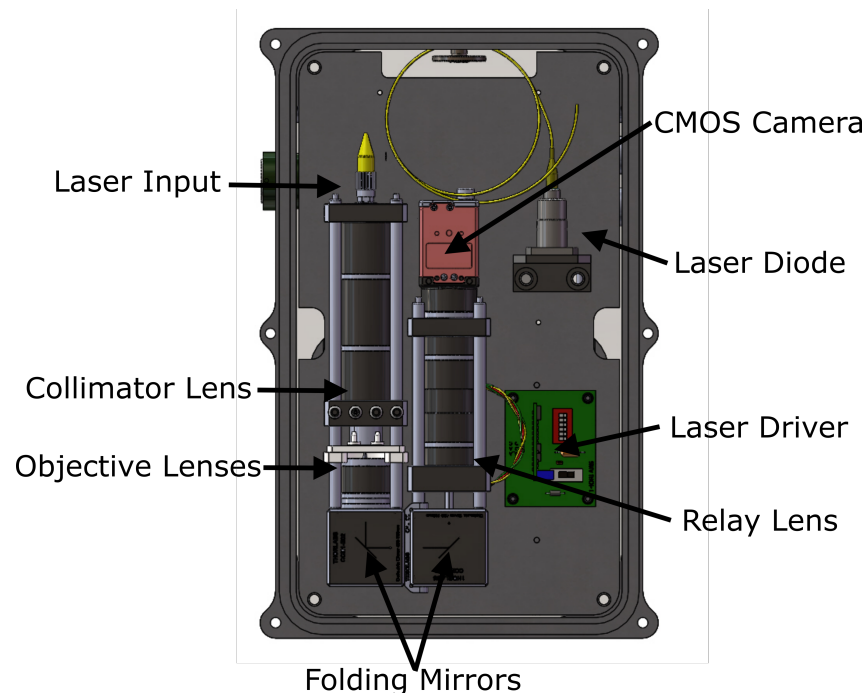


Figure 3.5 – Optical setup of the miniaturized DHM field instrument.

functional software to interface with the camera as well as display data, but I along with a summer intern, developed the software architecture that allows for real time data streaming. In addition to this, because the peripheral electronic hardware of the device is controlled by a combination of the UDOO's native GPIO pins as well as the embedded Arduino Leonardo, I developed a python-based virtual server that subscribes both the UDOO and Arduino as virtual clients in order to facilitate communication to and from both.

Metadata of the instrument is periodically monitored and recorded to a diagnostic file as well as sent to the host server via UDP port.

The system as a whole consumes roughly 15 W and requires an excitation voltage of 12 Vdc.

Figure 3.6 shows the fully functional miniaturized DHM field instrument next to the first generation field instrument (orangeBox). Showing them next to each other highlights the reduction in size between the two generations. It is important to note that because of the smaller pixel camera used, the size of the instrument was reduced drastically, while still maintaining sub-micron resolution (no loss of optical performance). At the time of the writing of this thesis, the exact instrument shown in Figure 3.6 is on a field deployment to a roughly 2 km deep salt mine

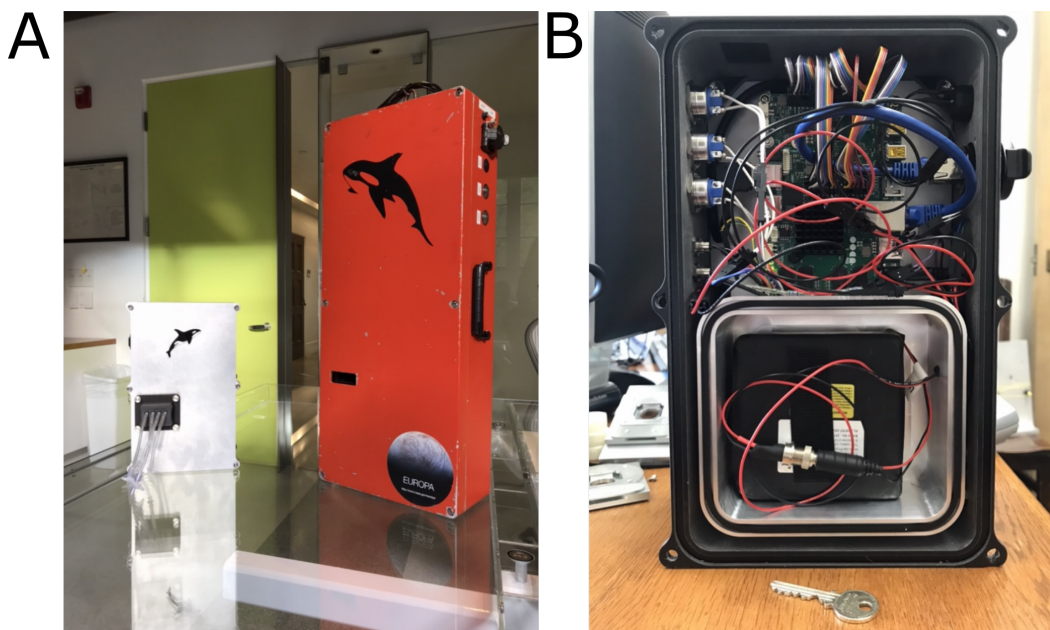


Figure 3.6 – The second generation DHM field instrument. (A) The full working prototype of the miniaturized DHM field instrument besides the first generation DHM field instrument (orangeBox). (B) The electronics side of the miniaturized field instrument (key for scale).

in Ireland for a two-week field campaign. This prototype also helped secure a collaboration with Britney Schmidt of the Georgia Institute of Technology and her work with the ICEFIN Autonomous Underwater Vehicle (AUV). This work is in close collaboration with the Schmidt Lab as well as Andy Mullen, a NASA Astrobiological post-doctoral scholar, and involves a multi-year campaign to develop a submersible DHM instrument to be integrated into ICEFIN in order to explore sub-glacial seawater in Antarctica.

3.4 Sample Chamber Design and Fabrication

In the use of off-axis DHM to image liquid samples, much attention must be paid to the design and fabrication of the sample chambers that contain these sample liquids. Many factors are involved with the design of such sample chambers. In the design of sample chambers for off-axis DHM, optical quality, flow physics, reusability/disposability, and general user experience considerations must be made.

In addition to these considerations, custom sample chambers are necessary for the common mode instrument due to its novel design which places the reference and sample beam of the instrument parallel and in close proximity to each other. In the

particular implementation of the common mode instrument that was used throughout this thesis, the reference and sample beams are spatially separated by 6 mm.

This section discusses in detail the optical considerations that have been made in ensuring high image quality of holographic images obtained using the common mode instrument. This consideration involved the experimental quantification of errors introduced by various sample chamber substrates. The relevant flow physics involved with the design of these microfluidic sample chambers as well as more practical considerations including efforts in designing higher quality/reusable sample chambers versus lower quality/disposable sample chambers are discussed in detail in Appendix E. In addition, Appendix E contains all technical drawings for the sample chambers discussed in this section as well as all sample chamber design iterations with references to digital CAD files.

Optical Considerations for Sample Chamber Design

In designing an instrument to readily image thick biological samples that do not appreciably absorb or scatter light such as microorganisms [37, 89], much attention must be paid to various sources of noise in the system that can otherwise attenuate the signal of the sample. In the case of sample chambers, a large source of noise is from the substrates that are used to construct the sample chamber itself.

Currently for traditional light microscopy, which is only concerned with the intensity of light passing through a sample, microfluidic sample chambers are routinely constructed out of moldable polymers such as polydimethylsiloxane (PDMS) [2, 51]. Although the effects of polymers on the optical quality of a traditional light microscope are negligible, off-axis holography is capable of not only imaging the intensity of light passing through a sample, but can also provide information on the quantitative phase contrast of the light passing through the sample as well. This ability of off-axis DHM prevents the use of polymers such as PDMS as an optical substrate due to the complex scattering events that polymers induce on light as it travels through the substrate. This destroys the optical coherence in the light rendering it useless for the retrieval of phase information from an off-axis hologram. Work has been previously published involving the use of PDMS substrates with DHM, but no results were shown involving the phase retrieval from these holographic images for this reason [87].

This necessitates that any substrate in the optical path of the DHM instrument is of high enough optical quality such that the quantitative phase imaging capabilities

of the technique are not lost. In the analysis of DHM image quality's sensitivity to various optical substrates, phase images were reconstructed from holographic images obtained with sample chambers constructed with various types of glass. These types of glass include high optical quality solid etalons (with and without an anti-reflective (AR) coating), conventional microscope slides, polycarbonate microscope cover slips, as well as custom fabricated PDMS sample chambers. A total of four glass sample chamber configurations were tested using these substrates. These sample chambers were constructed using:

1. Two non-AR coated solid etalons
2. Two AR coated solid etalons
3. One non-AR coated solid etalon and one conventional microscope slide
4. Two conventional microscope slides

Figure 3.7 shows a cross-sectional schematic of these four sample chamber configurations.

The microfluidic channel geometries for configurations 1 & 2 were established by the soft lithography of PDMS, which was compressed, via aluminum frames, between two AR coated or non-AR coated solid etalons. The PDMS establishes flow channel geometries as well as secures hypodermic needles, which provide fluid transport to and from the flow channels. These sample chambers use PDMS solely to establish flow channel geometry and thus contain no PDMS in the optical path of the instrument. For more detailed information on the manufacturing methods and properties of these sample chambers, see Appendix E.

Configurations 3 & 4 were constructed by ALine, Inc. (www.alineinc.com). Using acrylic sheets that contain the flow channel geometries, non-AR coated solid etalons and microscope slides or only microscope slides were attached via adhesive to create the desired sample chambers.

The quality of the glass surfaces was first quantified using a Zygo laser interferometer. This interferometer measures the surface quality of substrates by the double pass transmission of light through the medium. The instrument's mode of operation is by the establishment of linear interference patterns, or fringes across the sample being analyzed. It then measures the surface roughness of a substrate based on the curvature of the fringes caused by the wavefront errors introduced by the substrate's surfaces.

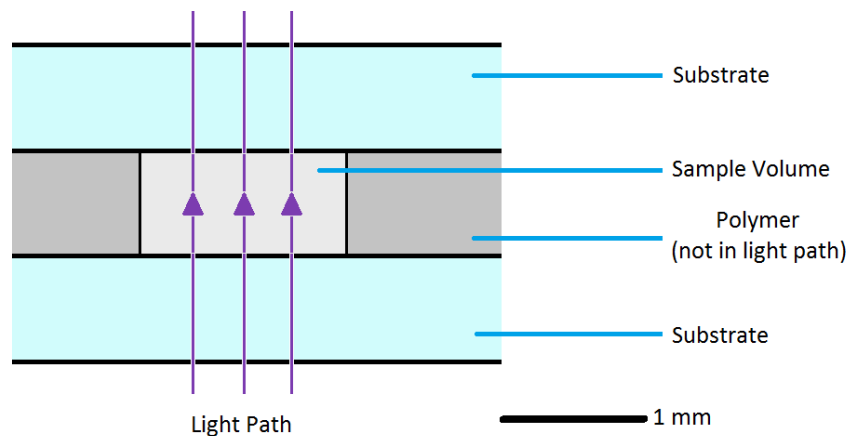


Figure 3.7 – Cross-sectional schematic of sample chamber configurations 1 through 4. The materials being investigated as well as the sample are the only objects in the light path of the instrument.

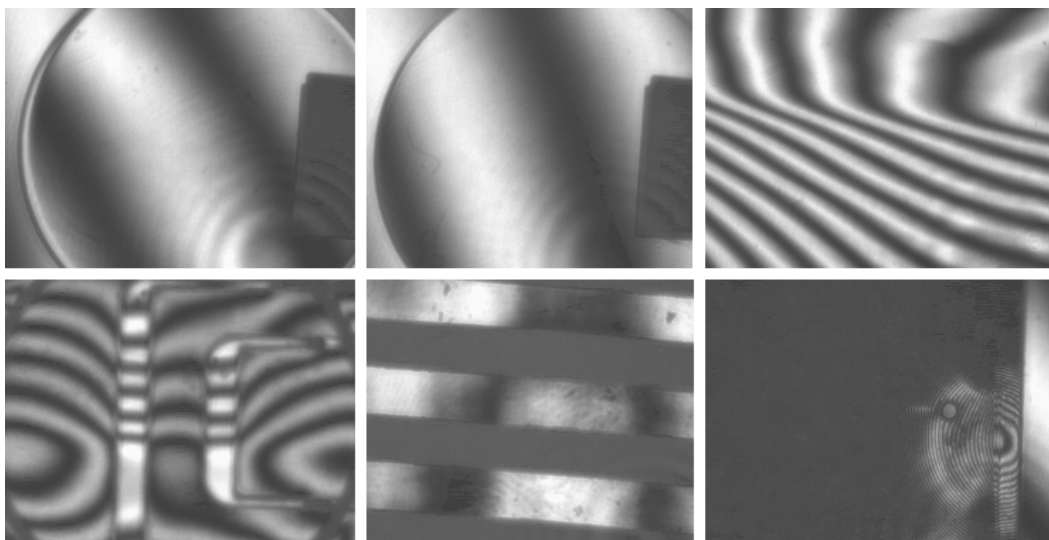


Figure 3.8 – Interference fringes through various substrate configurations using the Zygo interferometer. Top left: AR coated solid etalon. Top middle: non-AR coated solid etalon. Top right: microscope slide. Bottom left: microscope slide and non-AR coated solid etalon. Bottom middle: polycarbonate. Bottom right: PDMS.

Figure 3.8 shows the qualitative output from the Zygo interferometer of the various sample chamber substrates and configurations. Table 3.1 summarizes the quantitative results from this analysis.

The measurement of the surface quality of the various glass substrates confirmed that solid etalons had a superior surface quality to all other substrates. The AR coating of the solid etalons resulted in a slightly higher RMS value as opposed to

Table 3.1 – Surface roughness of sample chamber substrates

Type	RMS [nm] (% λ)	Peak-Valley [nm]
<i>AR coated etalons</i>	3.9 (1.0%)	23.7
<i>Non-AR coated etalons</i>	2.7 (0.7%)	18.6
<i>Microscope slides</i>	92.7 (22.9%)	563.2
<i>Microscope slide and non-AR coated etalon</i>	99.4 (24.5%)	928.1
<i>Polycarbonate</i>	44.3 (10.9%)	178.2
<i>PDMS</i>	-	-

non-AR coated solid etalons caused by the AR coating itself. Both types of solid etalons introduce far less wavefront error in the form of surface roughness than all other types of glass or polymer tested.

It was seen that conventional microscope slide glass exhibited high amplitude, low spatial frequency wavefront errors that varied greatly across its surface. This can be seen in the large difference between RMS and Peak-Valley values measured by the Zygo interferometer. In addition to this high amplitude, low spatial frequency surface roughness, the degree of these artifacts varied from one microscope slide to another. Indeed, a discouraging fact about conventional microscope slide glass as a sample chamber substrate is not necessarily the degree of wavefront error it introduces to a phase image, but the variation of that phase error from one sample chamber to the next.

The polycarbonate sample chambers yielded results showing higher wavefront error compared to solid etalons, but with errors on the same order of magnitude as microscope slides.

In measuring the surface quality of PDMS, the Zygo interferometer was unable to register any light traveling through it. This is to be expected as thick polymer substrates are known to attenuate the coherence of light as it travels through it. It is believed that the polycarbonate sample chambers performed relatively well because the polycarbonate layer is only 250 μm thick as opposed to the 1 mm thick PDMS substrate.

In addition to measuring the surface properties of these substrates, sample chambers were constructed and loaded with filter sterilized water to obtain blank holographic images. These blank images contained no biological sample, only the sample chamber configurations previously mentioned with sterile liquid in the fluidic channels. These holographic images were reconstructed in phase and the noise in these subsequent images were quantified by the calculation of the images' radially averaged

power spectra density function (PSD).

The PSD was calculated by obtaining the squared normalized Fourier Transform [108, 120] of phase images, such that

$$P(\omega_x, \omega_y) = \frac{|\mathfrak{F}(S(x, y))|^2}{f_s N_x N_y}, \quad (3.1)$$

where $P(\omega_x, \omega_y)$ is the PSD as a function of spatial frequency in the x and y directions, \mathfrak{F} is the Fourier Transform operator, $S(x, y)$ is the phase image, f_s is the spatial sampling frequency at the focal plane, and N_x and N_y are the number of pixels in the x and y directions, respectively.

With the PSD for each sample chamber configuration, radial averaging condenses the PSD into a one-dimensional function. The radially averaged PSD function is calculated as

$$\bar{P}_r(\omega_r) = \frac{\int_0^{2\pi} P(\omega_r, \omega_\theta) d\theta}{\int_0^{2\pi} \omega_r d\theta}, \quad (3.2)$$

where $P(\omega_r, \omega_\theta)$ is the PSD function from Equation 3.1 expressed in polar coordinates. Integrating $\bar{P}_r(\omega_r)$ across all spatial frequencies results in the variance, or net power, of the image

$$\sigma^2 = 2 \int_0^{\omega_m} \bar{P}_r(\omega_r) d\omega, \quad (3.3)$$

where ω_m is the maximum spatial frequency that can be imaged by the camera, dictated by the Nyquist-Shannon sampling theorem. The expression in Equation 3.3 provides a metric for variations in an image that is representative of a broad range of spatial frequencies.

Figure 3.9 illustrates the radially averaged PSD functions of the phase images obtained by all sample chamber configurations as well as a ‘control’ which corresponds to an empty hologram with no sample chamber in the optical path.

Figure 3.10 illustrates the variance of these phase images obtained by all sample chamber configurations.

These figures show that both AR and non-AR coated solid etalons add a negligible amount of noise to phase images. Microscope slides add a statistically significant

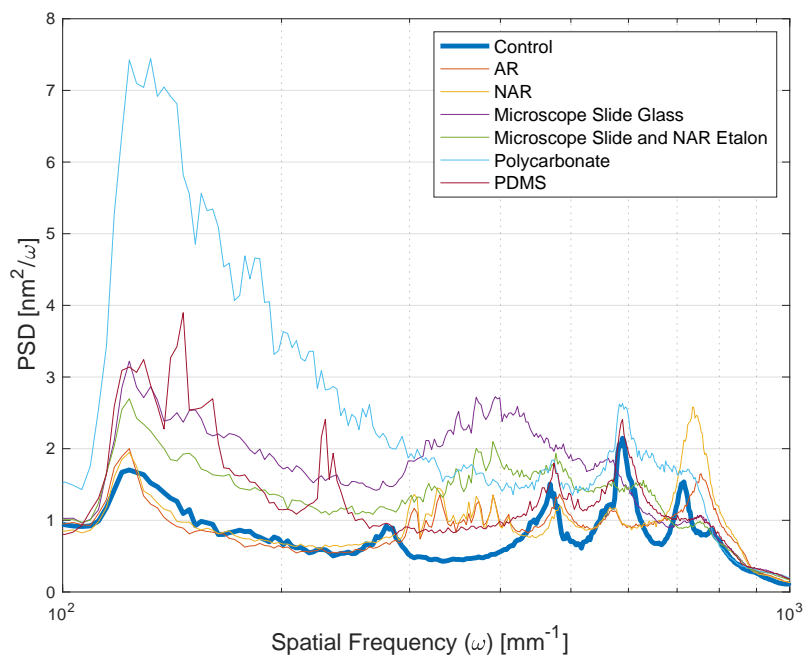


Figure 3.9 – Radial PSD functions calculated from the phase images of empty sample chambers consisting of various substrate configurations

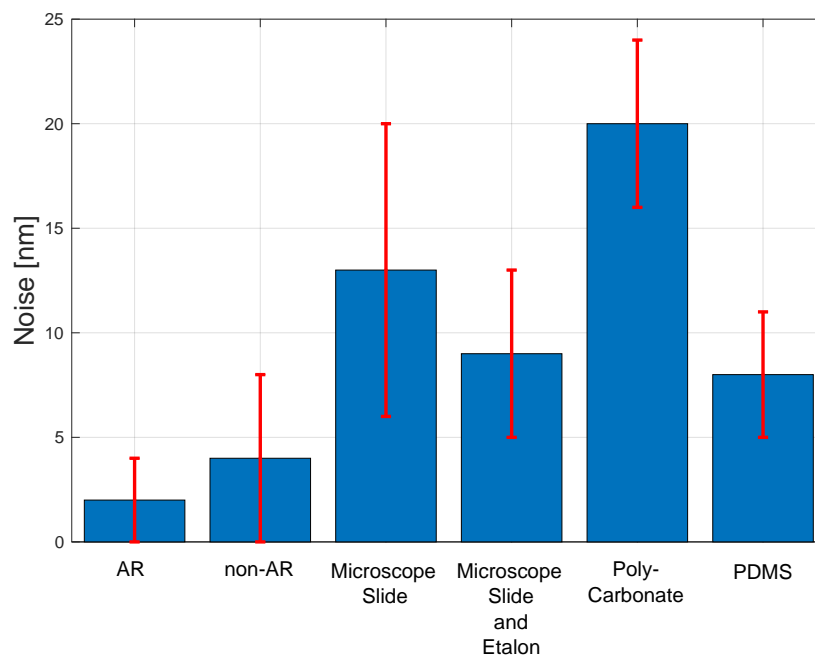


Figure 3.10 – Net phase variance calculated from the reconstructed phase images of all sample chamber configurations

amount of noise, but also a larger variation of noise, which was seen in the Zygo surface quality analysis. A combination of microscope slide glass and non-AR coated solid etalon, although still added a significant amount of noise, maintained a low level of variability in noise. Polycarbonate sample chambers added the highest amount of phase noise with 14% higher variance compared to conventional microscope slide glass, while PDMS yielded 10% less variance than that of microscope slide glass. Although PDMS introduced less noise compared to microscope slide glass, its shortcomings for its use in holographic imaging are seen by the low transmission of signal through the substrate.

In summary, this series of experimentation aimed to investigate the DHM's sensitivity to errors introduced by the substrates that are used in the manufacturing of the sample chambers of the instrument. Multiple substrates were investigated with various configurations. As expected, the exceptional optical quality of solid etalons proved to provide superior quality in phase images followed by microscope slide glass and polycarbonate. In Section 4.2, a theoretical model of phase noise is derived where other sources of noise are considered.

Sample chambers are the devices that are interacted with by any human operator of the instrument. Because of this user experience aspect, other qualitative and subjective matters must be considered in the design of a sample chamber. These considerations as well as general fluid mechanical considerations are discussed in detail in Appendix E.

Concluding Remarks

This chapter discussed the many areas of hardware development that have taken place to either directly or indirectly implement off-axis DHM for the investigation of microbial motility in extreme environments.

The optical designs used in the implementation of DHM throughout this thesis were developed prior to my involvement with the project, but a general overview of the optical designs of two instruments were presented and their respective journal articles were referenced. These two instruments were the Mach-Zehnder and common mode instruments.

Using the optical design of the common mode DHM instrument, a field instrument was constructed and packaged in a water-resistant ruggedized box. This instrument consisted of all optical components for the DHM instrument, as well as all electronic equipment necessary for its standalone operation. These electronics include a

processor, solid state hard drive, battery, as well as diagnostic sensors such as temperature and moisture sensors to monitor the status and health of the instrument. My contributions to the development of this instrument involved the design and fabrication of the entire sample handling subsystem. The instrument, as well as my contributions are well outlined in [75].

The results and user feedback from this first-generation field instrument's initial deployment to Nuuk, Greenland in 2015 led to the development of a prototype miniaturized field instrument. This instrument was designed by Stephanie Rider and myself. I was responsible for the design of all electronic hardware and software for the instrument, which included a custom PCB, as well as the writing of software components to interface with the peripheral electronic hardware through the PCB.

Lastly, the unique optical and physical constraints of the common mode DHM instrument necessitated the development of custom microfluidic sample chambers. The optical constraints involved the analysis of the optical quality of various sample chamber substrates as well as the careful design of the sample chambers from a microfluidic standpoint. The optical analysis and sample chamber design was carried out by myself with guidance from optical engineers at JPL.

The hardware developments described in the chapter lay the groundwork for the rest of this thesis in where software techniques are developed to enhance the usability of the DHM instruments as well as their implementation in conducting research both in an out of the laboratory.

Chapter 4

QUANTIFICATION OF PERFORMANCE

In the design and prototyping of any device, it is important to establish clear performance metrics in order to ensure that the desired outcome is reached. Furthermore, it is important to investigate sources of error that might hinder the instruments' performance or sensitivity. In this chapter, the resolution of the DHM instruments are quantified, error analyses are conducted on common phase calculation algorithms, a theoretical model is introduced that estimates the sensitivity of the DHM instrument, as well as an experimental verification of this sensitivity model, which ensures that the common mode instrument meets the sensitivity requirements set out in the Introductory Chapter. The theoretical analysis of phase noise was presented and published in the proceedings of the Photonics West Conference of the International Society of Optics and Photonics (SPIE) in February of 2017 in San Francisco, CA [3]. The theoretical model of sensitivity was published in a special edition of the peer-reviewed scientific journal *Astrobiology* in 2017 [12]. The experimental verification of this theoretical model was published in the peer-reviewed scientific *Journal of Visualized Experiments* in 2017 [11]. I was first author for all three of these works.

4.1 Instrument Resolution and Depth of Field

This section describes both the theoretical diffraction limited resolution (lateral and axial) that one can hope for in an imaging modality as well as experimental verification of the achieved resolution of the DHM instruments. This comparison shows that the DHM instruments developed and described throughout this thesis operate at the diffraction limit of light. Furthermore, an experimental definition of depth of field is defined as well as a verification of the depth of field in the two DHM instruments.

The lateral resolution and the depth of field of the Mach-Zehnder and common mode instruments were theoretically derived and experimentally verified in each of the instruments' respective peer-reviewed articles [71, 123]. The work in this section describing the *axial* resolution and variance of the two DHM instruments was conducted by myself.

Lateral Resolution

The theoretical diffraction limited lateral resolution is defined as

$$r_{xy} \propto f\lambda, \quad (4.1a)$$

$$r_{xy} = \frac{1.22\lambda}{2NA}, \quad (4.1b)$$

where f is the F-number of the optical system ($f \approx (2NA)^{-1}$), λ is the wavelength of the illumination light source, and NA is the numerical aperture of the imaging system [19].

It is important to note that multiple definitions of optical resolution exist. The expression used in Equation 4.1b is an expression for lateral resolution which meets the Rayleigh criterion for resolution. This criterion specifies two diffracted points in an image as resolved if the central maximum of one of the point's diffraction pattern overlaps the central local minimum value of the other point's diffraction pattern [97].

With this definition of the lateral resolution as well as the optical parameters of the common mode and Mach-Zehnder instrument, which are tabulated in Tables A.1 and A.2, the theoretical diffraction limited resolution can be quantified.

The common mode instrument has a theoretical diffraction limited lateral resolution of $r_{xy} \approx 800$ nm (using a 405 nm laser illumination source), and was experimentally verified to achieve diffraction limited performance by having a sub-micron ($0.78 \mu\text{m}$) lateral resolution. This was verified by imaging an optical US Air Force (USAF) Resolution Target.

The Mach-Zehnder instrument was experimentally verified to achieve sub-micron resolution although was not verified to operate at the diffraction limit. This is due to the relatively high numerical aperture of the system ($NA \geq 0.55$). According to Equation 4.1b, a 405 nm illumination source would provide a diffraction limited lateral resolution of $0.49 \mu\text{m}$. The smallest elements available in the high resolution US Air Force Target used in the development of the instrument was $0.78 \mu\text{m}$, which the instrument was able to resolve well.

Axial Resolution

Experimental quantification of axial resolution is difficult as there exists no standardized or readily available three-dimensional optical resolution target on the micron

scale. There are however, theoretical models of diffraction limited resolution [65] that are derived from the ability to resolve the point spread function (PSF) of a diffraction limited particle in the axial direction. As with lateral resolution, many definitions of axial resolution exist, but all theoretical expressions for the axial resolution of an optical system dictate that the axial resolution be proportional to the square of the F-number of the imaging system, such that

$$r_z \propto f^2 \lambda, \quad (4.2a)$$

$$r_z = \frac{2\lambda}{\text{NA}^2} \quad (4.2b)$$

where f is the F-number of the imaging system and λ is the illuminating wavelength.

As with lateral resolution, multiple definitions exist to explicitly define the theoretical diffraction limited axial resolution of an optical system. Equation 4.2b defines the theoretical diffraction limited axial resolution as defined by German physicist Ernst Abbe in 1873.

This theoretical definition of axial resolution predicts that the diffraction limited axial resolution of the Mach-Zehnder instrument is $0.33 \mu\text{m}$, while the diffraction limited axial resolution of the common mode instrument is $1.1 \mu\text{m}$.

Axial Variance

Previous work regarding the development and verification of DHM instruments have led to the development of experimental methods of quantifying axial resolution in DHM instruments. This method, described in detail in [5, 29, 59, 127] establishes a metric for the quantification of focus, applies this metric of focus, programmatically, to successive images of a stationary resolvable particle, and considers the variance of these axial localization measurements to be the axial resolution of the instrument. The aforementioned work described the focus metric of *intensity* images only. This is due to the fact that in the previously mentioned work, development was done with an *in-line* DHM, which is only capable of intensity reconstructions. Because of this, a custom focus metric was also derived for phase images, so that axial resolution of off-axis DHM can be quantified in both intensity and phase images.

The metric for focus of intensity images is done via local-intensity-maxima searching of the integrated intensities of reconstructed lateral images along the axial direction

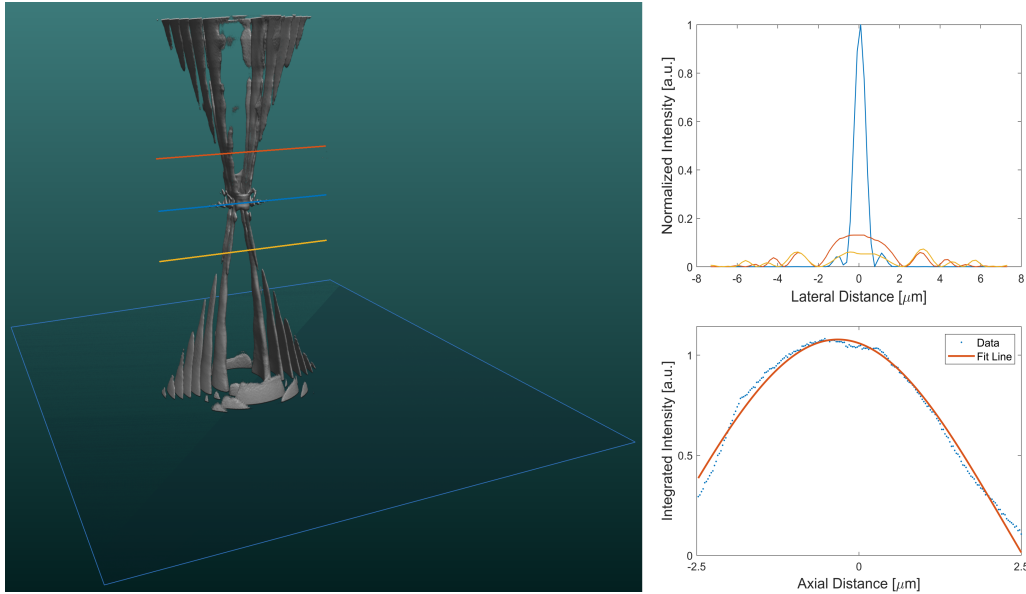


Figure 4.1 – Focus metrics for intensity images. (Left) A volumetric rendering of a resolution element with one-dimensional lateral profile lines at various points through focus. (Upper right) The intensity profiles of the lateral profile lines shown in the volumetric rendering. (Lower right) The integrated intensity profiles of the lateral profile lines of the object as a function of axial resolution. A Gaussian fit of the data shows the point of focus as the maximum of the curve.

[59]. By knowing the lateral position of a resolvable particle, numerical reconstruction of intensity images at various axial locations about the particle are constructed into a z-stack. Plotting the integrated lateral intensity profiles of the individual z-slices as a function of axial direction results in a Gaussian distribution of integrated intensity values. By finding the maximum value of this Gaussian distribution, focus can be calculated. The maximum of this Gaussian fit is the axial location of focus for this particle. Figure 4.1 shows a 3D z-stack of intensity reconstructions of a single resolvable particle, as well as a series of one dimensional lateral intensity line plots of the particle at various axial locations. This figure also shows a plot of the integrated intensity profiles as a function of axial distance (z). This plot of integrated intensity as a function of axial position is known to follow a Gaussian distribution [59]. A Gaussian fit to this experimental data shows the point of focus to be the maxima of the Gaussian curve. This process is repeated for multiple holographic reconstructions until a sufficiently large sample size is obtained. The RMS error of the localization measurements results in the axial variance of the DHM instrument in intensity reconstructions.

A similar approach is applied to the quantification of focus in phase images. In phase imaging, a phenomenon known as the Gouy Phase Shift causes a sudden phase advance through a particle in the axial direction. This phase step *can* be modeled as a logistic regression. By knowing the lateral position of a particle, the axial profile can be analyzed by fitting it to a logistic regression. The point of focus is defined as the inflection point of this logistic regression. To implement this, the derivative of the logistic regression is calculated and the axial position of the inflection point is quantified by finding the maximum of this spatial derivative. Figure 4.2 shows a 3D z-stack of phase reconstructions of a single resolvable particle, as well as a one-dimensional axial plot of phase values through the lateral position of the particle along with a logistic regression fit line. This figure also shows the spatial derivative of the logistic regression fit. The axial location of the maxima of the spatial derivative defines the inflection point of the phase profile and is thus the location of the Gouy Phase Shift. This process is repeated for multiple holographic reconstructions until a sufficiently large sample size is obtained. The RMS error of the localization measurements results in the axial variance of the DHM instrument in phase reconstructions.

In order to quantify the axial variance of the Mach-Zehnder instrument, a series of holographic images were obtained of a high resolution USAF target. The holograms of the USAF target were then numerically reconstructed into intensity and phase z-stacks with an axial interval of 2.78 nm. Figure 4.3 shows representative intensity and phase images of the USAF resolution target imaged using the Mach-Zehnder DHM instrument equipped with 50x NA= 0.55 Mitutoyo long working distance dry objective lenses.

Implementing this method results in an axial variance of the Mach-Zehnder instrument of 163 nm in intensity reconstructions and 368 nm in phase reconstructions, with a combined axial variance (root sum squared) of 402 nm.

Figure 4.4 shows the axial localization errors of the Mach-Zehnder instrument with 50x NA= 0.55 objective lenses as a function of time (103 total holograms at 5 fps). The plot shows the localization errors made in phase and intensity reconstructions.

In order to quantify the axial resolution of the common mode instrument, a series of holographic images were obtained of a high resolution USAF target. The holograms of the USAF target were then numerically reconstructed into intensity and phase z-stacks with an axial interval of 25 nm. Figure 4.5 shows representative intensity and phase images of the USAF resolution target imaged using the common mode

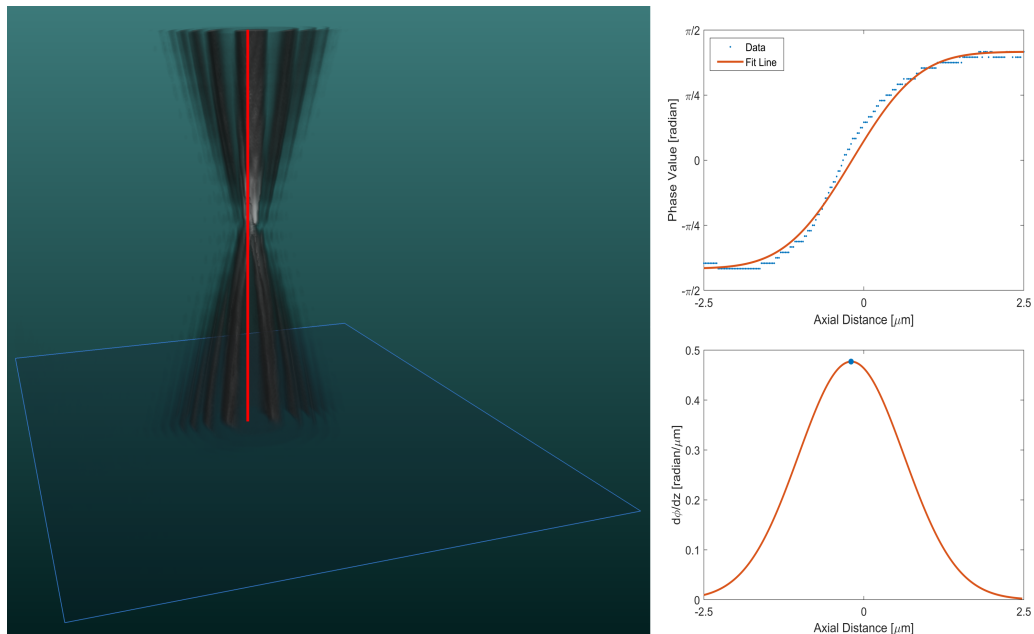


Figure 4.2 – Image metrics for the location of the Gouy Phase Shift in phase images. (Left) A volumetric rendering of a resolution element with a one dimensional axial profile line through the center of the element. (Upper right) The phase profile of the axial profile line shown in the volumetric rendering with a linear logistic regression fit. (Lower right) The spatial derivative of the logistic regression. The maximum of the spatial derivative corresponds to the inflection point of the plot, which is where the Gouy Phase Shift occurs.

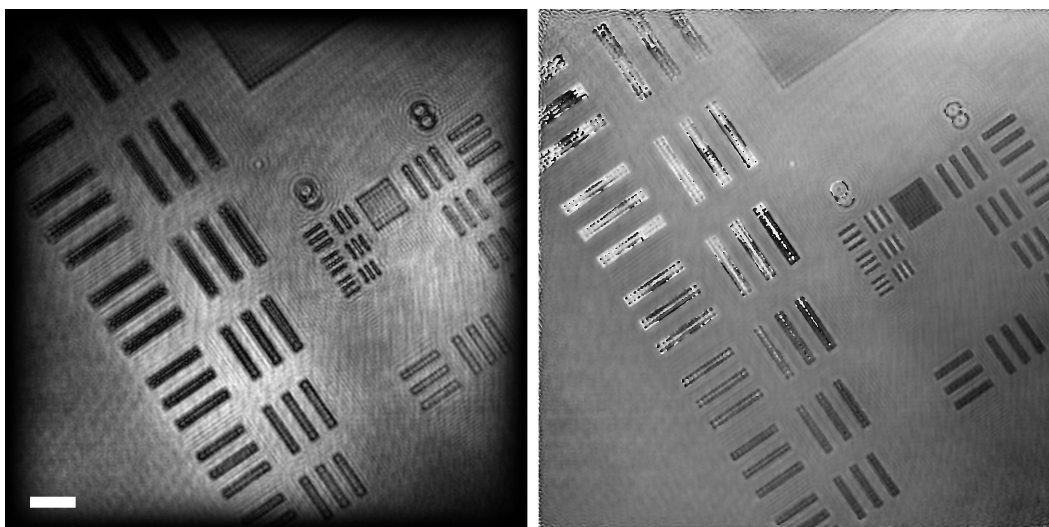


Figure 4.3 – USAF resolution target imaged using the Mach-Zehnder DHM. Left shows an intensity reconstruction and right shows a phase reconstruction. Scale bar represents $10 \mu\text{m}$.

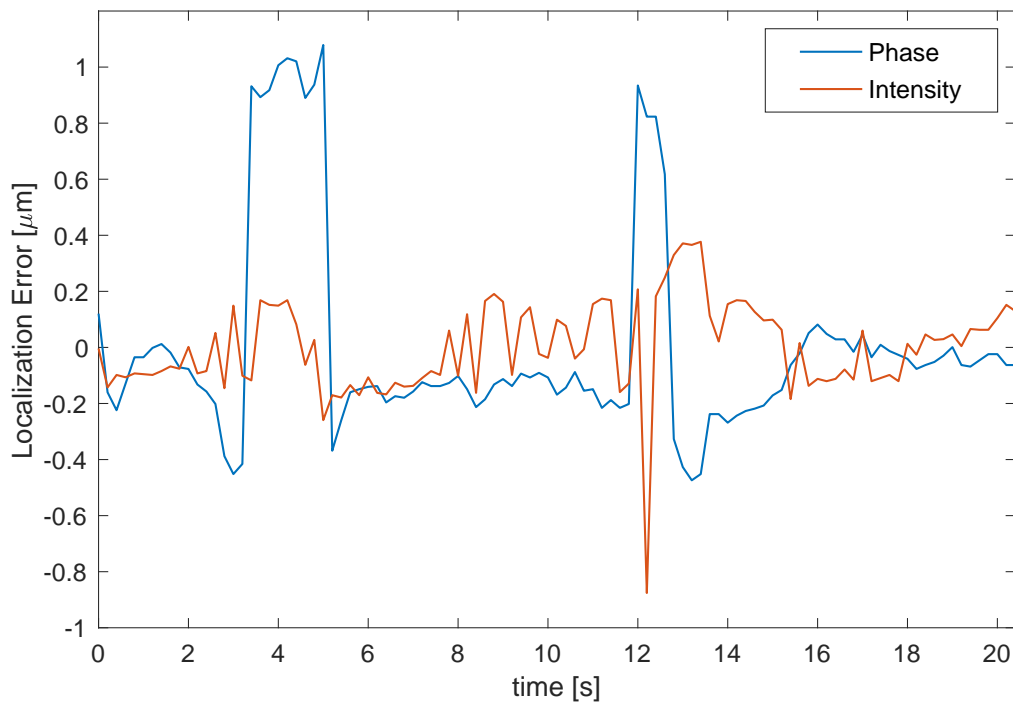


Figure 4.4 – Axial localization errors of the Mach-Zehnder instrument (50x NA0.55 objective lenses) in both phase and intensity reconstructions

DHM.

Implementing this method results in an axial variance of the common mode instrument of 87 nm in intensity images and an axial variance of 71 nm in phase, with a combined axial variance of 112 nm.

Figure 4.6 shows the axial localization errors of the common mode instrument as a function of time (89 total holograms at 5 fps). The plot shows the localization errors made in phase and intensity reconstructions.

Table 4.1 summarizes the results of the analysis in the variance of focus in both the common mode and Mach-Zehnder DHM instruments.

Both instruments demonstrate sub-micron axial variances of focus, but as mentioned earlier in this chapter, a major advantage of the common mode instrument over the Mach-Zehnder instrument is the insensitivity it inherently has to uncorrelated shifts in the two beams of the instrument caused by stochastic events including, but not limited to, convection in the air and physical vibrations. This advantage can be seen when comparing Figures 4.4 and 4.6 as there exist large swings in localization errors made by the Mach-Zehnder instrument that are non-existent in the localization

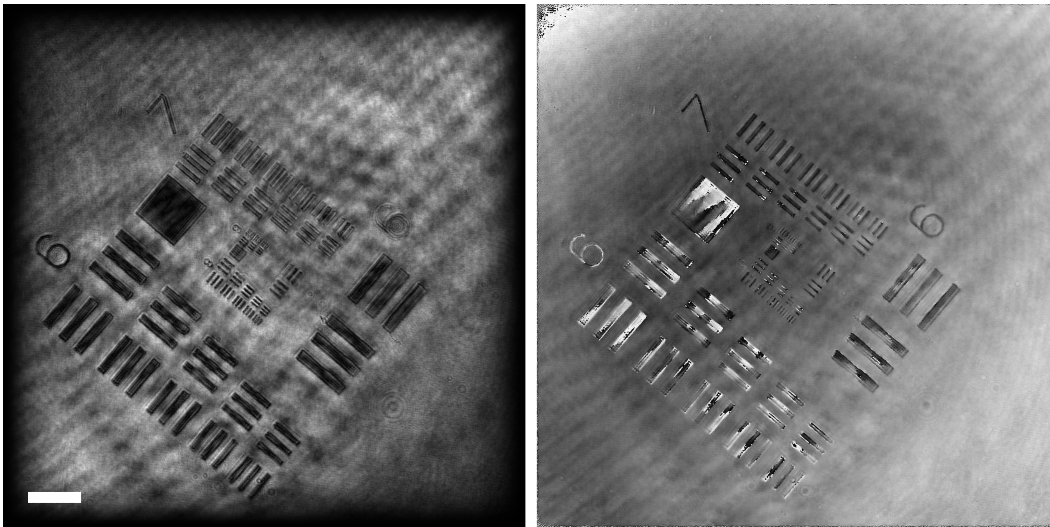


Figure 4.5 – USAF resolution target imaged using the common mode DHM. Left shows an intensity reconstruction and right shows a phase reconstruction. Scale bar represents $35 \mu\text{m}$.

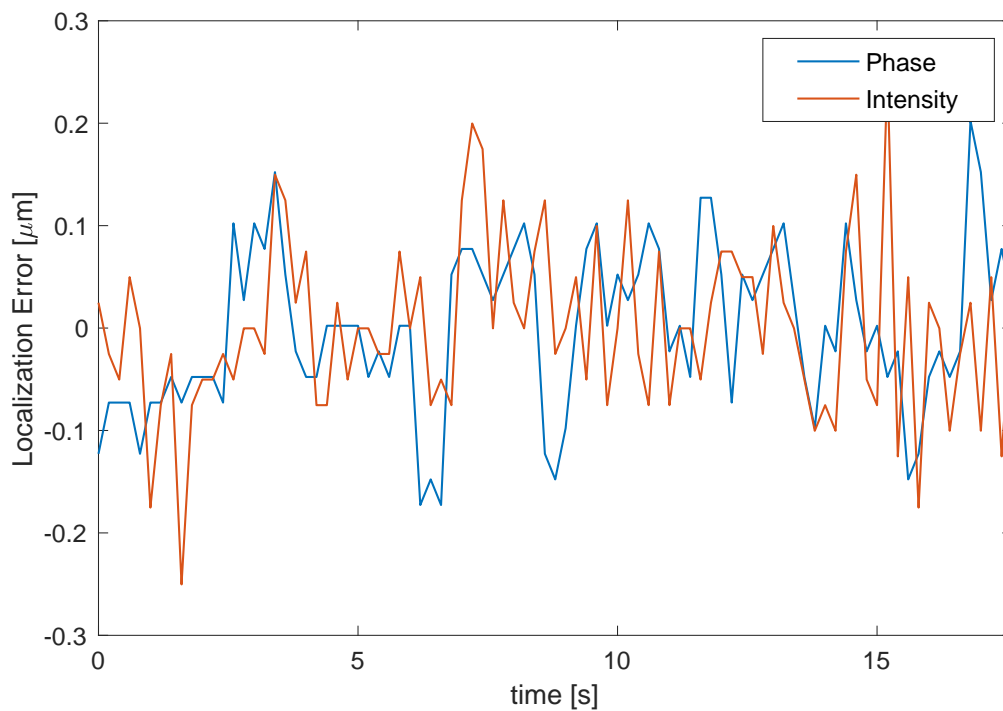


Figure 4.6 – Axial localization errors of the common mode instrument (20x NA0.3 objective lenses) in both phase and intensity reconstructions

Table 4.1 – Image performance metrics for the common mode and Mach-Zehnder instruments

<i>Property</i>	<i>Common Mode (20x NA=0.3)</i>	<i>Mach-Zehnder (50x NA=0.55)</i>
<i>Theoretical Lateral Resolution</i>	0.82 μm	0.45 μm
<i>Experimental Lateral Resolution</i>	0.78 μm	<0.78 μm
<i>Theoretical Axial Resolution</i>	1.1 μm	0.33 μm
<i>Variance of Focus in Phase (with outliers removed)</i>	0.079 (0.079) μm	0.368 (0.037) μm
<i>Variance of Focus in Intensity (with outliers removed)</i>	0.084 (0.084) μm	0.163 (0.126) μm
<i>Total Axial Variance (RSS)</i>	0.115 (0.115) μm	0.402 (0.131) μm
<i>Depth of Field [μm]</i>	900 μm	600 μm

errors of the common mode instrument. This is believed to be due to random convection cells in the ambient air of the laboratory while data was being collected. The common mode instrument contains a majority of its optical components in sealed lens tubes that do not allow ambient air to flow through the optical path of the instrument. The Mach-Zehnder instrument, however, contains sections where the optical path of the instrument is open to ambient air and is thus susceptible to convection that may be present in the laboratory by such things as ventilation and even the breath of the instrument's operator. During the data acquisition that comprised the data presented in this analysis, both instruments were secured on a pneumatically isolated optical table (Newport Smart Table UT2 equipped with I-2000 Series Laminar Flow Isolators), which isolates the table from any physical vibrations from the floor. Because of this, it is believed that the large variation in localization errors seen in the Mach-Zehnder instrument are due to uncorrelated changes in laser coherence between the two beams of the instrument caused by convection in the ambient air of the laboratory.

Table 4.1 shows the RMS values of localization errors in both phase and intensity reconstructions for the common mode and Mach-Zehnder DHM instruments. Due to the large spikes in localization errors present in the Mach-Zehnder instrument, two values are reported, the first being the total RMS value of localization error, and the second corresponding to the localization errors after statistical outliers have been removed.

Depth of Field

The depth of field of the common mode instrument was defined as the axial distance around the focal plane in which sub-micron lateral resolution can be maintained. This was experimentally found to be a depth of $900 \mu\text{m}$ [123].

The US Air Force Target was used to verify the axial distance where sub-micron lateral resolution could be maintained in the Mach-Zehnder DHM instrument and was experimentally found to maintain sub-micron resolution across a depth of $600 \mu\text{m}$ [71].

The lateral/axial resolution and depth of field of these instruments provide a very practical method of imaging the unconstrained motility of sub-micron sized prokaryotic single-celled organisms. As will be discussed in the coming sections, the depth of field of the common mode and Mach-Zehnder instrument out-match that of other conventional microscopy instruments by orders of magnitude. This allows DHM to not only be more sensitive to lower biomass samples, but to also be capable of imaging dynamic biological processes in three dimensions.

4.2 Phase Noise Analysis

Many techniques exist for the extraction of phase information from optical interferograms and have been well reviewed by Katherine Creath [?]. Prior to this work, however, no thorough error analysis had been done on phase retrieval schemes. In this section, a select few of the most common phase calculation techniques are described in detail. Error analyses are conducted on these common techniques to shed light on how sensitive each technique can be to the various sources of error and noise that are introduced during optical phase measurements. The contents of this section were presented and published in the proceedings of the Photonics West Conference of SPIE in February of 2017 in San Francisco, CA [3]. I was first author of this manuscript and conducted all theoretical derivations and experimental verification of this work.

The Four Bucket/Step Method

A common algorithm for the extraction of quantitative phase information from such interferograms, or fringes, is called the 'Four Step' or 'Four Bucket' Method, where a single fringe is sampled four times along its length. These four points can be sampled at discrete points in space or time, corresponding to a Four Bucket or Four Step method, respectively.

In the Four Bucket method, a time invariant interference pattern is sampled across four adjacent pixels that have a phase offset of $\pi/2$ from each other. Similarly, in a Four Step method, an identical pixel experiences a phase step as a function of time such that the light incident on it from exposure i to $i + 1$ carries a phase offset of $\pi/2$.

In this phase measurement technique, the equation for phase retrieval becomes

$$\phi = \arctan\left(\frac{I_d - I_b}{I_a - I_c}\right), \quad (4.3)$$

where I_i is the intensity of pixel i . For an in-depth derivation of this expression, see Appendix A.

The Three Bucket/Step Method

Similarly to the Four Bucket/Step Method, the Three Bucket/Step Method involves the extraction of phase information from an interference pattern that has been sampled only three times along its length at an even spacing. A common phase spacing between sample points is $\pi/2$, although others have been used [33]. In this phase measurement technique, the equation for phase retrieval becomes

$$\phi = \arctan\left(\frac{I_c - I_b}{I_a - I_b}\right), \quad (4.4)$$

where I_i is the intensity of pixel i . For an in-depth derivation of this expression, see Appendix A.

The Carré Method

Unlike the Four or Three Bucket/Step Methods that use a fixed and predefined phase offset between exposures, the Carré Method allows for phase calculations where the phase offset between exposures can vary linearly. This requires four measurements along the length of an interference pattern, each with a phase offset of α between each sample, where $\alpha \in (0, \pi]$.

In this phase measurement technique, the equation for phase retrieval becomes

$$\phi = \arctan\left(\frac{\sqrt{3(I_b - I_c)(I_a - I_c)}}{(I_b + I_c) - (I_a + I_d)}\right), \quad (4.5)$$

where I_i is the intensity of pixel i . For an in-depth derivation of this expression, see Appendix A.

Phase Errors and Sources of Noise

As with any digital measurement, there are errors and noise that must be accounted for. In the application of quantitative phase imaging, digital sensors that measure the intensity of incident light are subject to multiple sources of error. These sources of error include photon noise, dark noise, read noise, quantization noise, pixel non-uniformity, as well as electronic interference. Such errors as pixel non-uniformity and electronic interference are difficult to quantify due to their dependence on factors that are independent of the optical system. As a result, they will only be mentioned here.

Photon noise is a fundamental trait of light and is caused by the discrete nature of photons. This noise is modeled as a Poisson process where the noise is equal to the square root of the intensity of photons incident on the pixel (\sqrt{I}).

Dark noise is the false reading of photons by the sensor due to thermally generated electrons on the sensor array. Dark noise is typically specified by the manufacturer of the sensor array and is reported in units of electrons (RMS) per pixel per second of integration.

Read noise is the combinations of all ‘on chip’ sources of error. In many cameras, on chip processes occur prior to the image data being sent to a computer. The errors introduced as a result of this processing are quantified and combined by sensor and camera manufacturers and reported in units of electrons (RMS) per read.

Quantization noise arises from any analog to digital conversion. In the case of an optical detector, photons are used to generate electrons in each pixel. These electrons build up voltage, which is then counted and converted to a digital number to be stored by the computer. The error of a digitization process has a mean of zero and extrema of $\pm 0.5L_{\text{SB}}$, where L_{SB} is the least significant bit of the analog to digital converter (ADC). The standard deviation of this error is $L_{\text{SB}}/\sqrt{12}$ and is commonly used to quantify errors introduced as a result of digitization of an analog signal.

The manufacturing of sensor arrays is a highly controlled and repeatable process but there are inevitable irregularities in the manufacturing process. Pixel non-uniformity is the error introduced as a result of non-uniform sensitivity to light from one pixel to another on a detector array.

Other errors can be introduced into the measurement of light in the form of electronic interference from nearby uninsulated devices. If a strong enough electronic interference is present prior to the signal amplifiers of the optical sensor, the interference noise will be proportionally amplified and corrupt the signal being measured.

For the following analyses, the error in the measurement of the light intensity incident on a particular pixel will be the root sum square (RSS) of all the contributing noise sources, and will be considered equal between all pixels. Thus, the error of an electric field intensity measurement is

$$\delta I_i = \sqrt{I_i + (\Delta t \delta D)^2 + M(\delta R)^2 + \frac{L_{\text{SB}}^2}{12}}, \quad (4.6)$$

where I_i is the intensity of photons incident on pixel i , Δt is the integration time of the pixel, δD is dark noise, δR is read noise, and M is the number of reads taken to make the measurement.

Error Associated with the Four Bucket/Step Method

Using the expression for the propagation of error on the definition of phase from the Four Bucket/Step Method (Equation 4.3) yields a phase error of

$$\delta \phi = \sqrt{\frac{1}{2V^2 \bar{I}} + \frac{(\Delta t \delta D)^2 + M(\delta R)^2 + \frac{L_{\text{SB}}^2}{12}}{2V^2 \bar{I}^2}}, \quad (4.7)$$

where V is fringe visibility and $\bar{I} = I_1 + I_2$. For an in-depth derivation of this expression, see Appendix A.

Equation 4.7, provides an expression for the error propagated by the Four Bucket/Step Method as a result of photon, detector, and quantization noise. Note that the above expression consists of two terms. The left most corresponds to errors as a result of photon noise, which will be present in any optical system due to the discrete nature of light, and the right corresponds to errors that are propagated into the phase measurement as a result of the detector used in making intensity measurements.

Error Associated with the Three Bucket/Step Method

Using the expression for the propagation of error on the definition of phase from the Three Bucket/Step Method (Equation 4.4) yields a phase error of

$$\delta\phi = \sqrt{\frac{1 + 2 \cos^2 \phi - 2V \sin \phi \cos^2 \phi}{4V^2 \bar{I}} + \frac{3 \left((\Delta t \delta D)^2 + M(\delta R)^2 + \frac{L_{SB}^2}{12} \right) (1 - \sin 2\phi)}{16V^2 \bar{I}^2}}. \quad (4.8)$$

For an in-depth derivation of this expression, see Appendix A.

Equation 4.8, provides an expression for the error propagated by the Three Bucket/Step Method as a result of photon, detector, and quantization noise. Note that the above expression consists of two terms. The left most corresponds to errors as a result of photon noise, which will be present in any optical system due to the discrete nature of light, and the right corresponds to errors that are propagated into the phase measurement as a result of the detector used to make intensity measurements.

Error Associated with the Carré Method

Using the expression for the propagation of error on the definition of phase from the Carré Method (Equation 4.5) yields a phase variance of

$$\begin{aligned} \delta\phi^2 = & \frac{A \left(\frac{3D(B-A)}{2\sqrt{3CD}} + \sqrt{3CD} \right) + B \left(\frac{3C(B-A)}{2\sqrt{3CD}} + \sqrt{3CD} \right)}{(B-A)^2 + 3CD} \\ & + 2\delta I_i^2 \left(\frac{(3D(B-A) + 6CD)^2 + (3C(B-A) + 6CD)^2}{12CD((B-A) + 6CD)^2} \right), \end{aligned} \quad (4.9)$$

where

$$A = I_a + I_d, \quad (4.10a)$$

$$B = I_b + I_c, \quad (4.10b)$$

$$C = I_a - I_d, \quad (4.10c)$$

$$D = I_b - I_c, \quad (4.10d)$$

and δI_i is defined in Equation 4.6. For an in-depth derivation of this expression, see Appendix A.

Comparisons between Phase Calculation Methods

In order to compare the noise characteristics of the Four Bucket/Step, Three Bucket/Step, and Carré Methods, performance metrics from a readily available optical detector were used (Sony ICX625 CCD). The properties of this detector are tabulated in Table A.3.

The propagation of error of the Four Bucket/Step Method in Equation 4.7 shows that this phase calculation algorithm introduces random errors. The phase variance as a result of photon, dark, read, and quantization noise is independent of the phase being measured and are thus random for any phase measurement. From this equation, we can also see that the expression for the propagation of the error is inversely proportional to fringe visibility as well as average incident light intensity.

The propagation of error of the Three Bucket/Step Method in Equation 4.8 shows that this phase calculation algorithm introduces systematic errors due to the fact that the phase variance is a function of the phase being measured. Similarly to the Four Bucket/Step Method, the expression for error in the Three Bucket/Step Method is inversely proportional to fringe visibility and average light intensity.

The Carré Method introduces a relatively complex expression for the propagation of error due to the fact that the algorithm is based on an interferogram with unknown sample frequency across a fringe. By first having to infer on this sample frequency based on direct fringe measurements, errors are compounded. Not only the errors of the intensity measurements of the fringe have to be considered in the calculation of the unknown sample frequency (α), but these errors in the calculation of α also propagate to the expression for phase error in Equation 4.9.

All three of the aforementioned phase calculation methods are inversely proportional to both fringe visibility and average electric field intensity recorded by the pixel(s). For digital detectors, such as the Sony ICX625 CCD, with finite pixel well depths, there is a finite number of photons that a pixel can detect before becoming saturated. This imposes an upper limit on the value of the average electric field intensity recorded by the detector (\bar{I}) and thus imposes an upper limit on fringe visibility as pixels begin to saturate. As the average pixel intensity becomes more than 50% saturated, fringe visibility begins to decrease. As the pixel(s) become fully saturated, the fringe visibility approaches zero making any calculation of phase impossible.

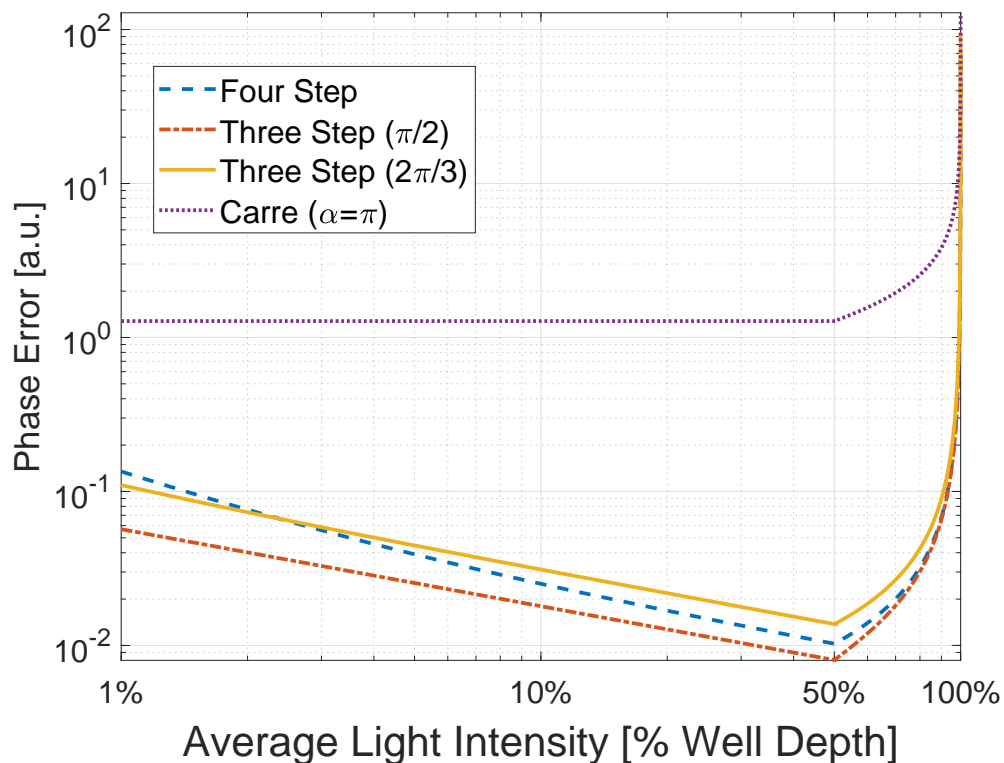


Figure 4.7 – Comparison of phase errors of the Four Bucket/Step, Three Bucket/Step, and Carré Methods as a function of normalized average light intensity (% well depth of pixel) (adapted from [3])

Figures 4.7 and 4.8 illustrate the performance of each phase calculation method as a function of normalized average electric field intensity recorded by the detector (Figure 4.7), and a function of the phase that is being measured (Figure 4.8). As mentioned earlier, the Three Bucket/Step Method can be employed using various known sample frequencies across a fringe. The figures depict the phase errors associated with the Three Bucket/Step Method that samples the fringe at spacing of $\pi/2$ and $2\pi/3$, while the Carré Method is employed while sampling the fringe every $\alpha = \pi$.

As seen in Figures 4.7 and 4.8, as well as Equations 4.7, 4.8, and 4.9, the Four Bucket/Step Method is the only method among the three that introduces random as opposed to systematic error in the calculation of phase from a fringe measurement.

When comparing these three phase calculation techniques, it becomes evident that the four bucket/step or three bucket/step methods are preferable over the Carré method due to their relatively low phase errors. However, the advantage of the

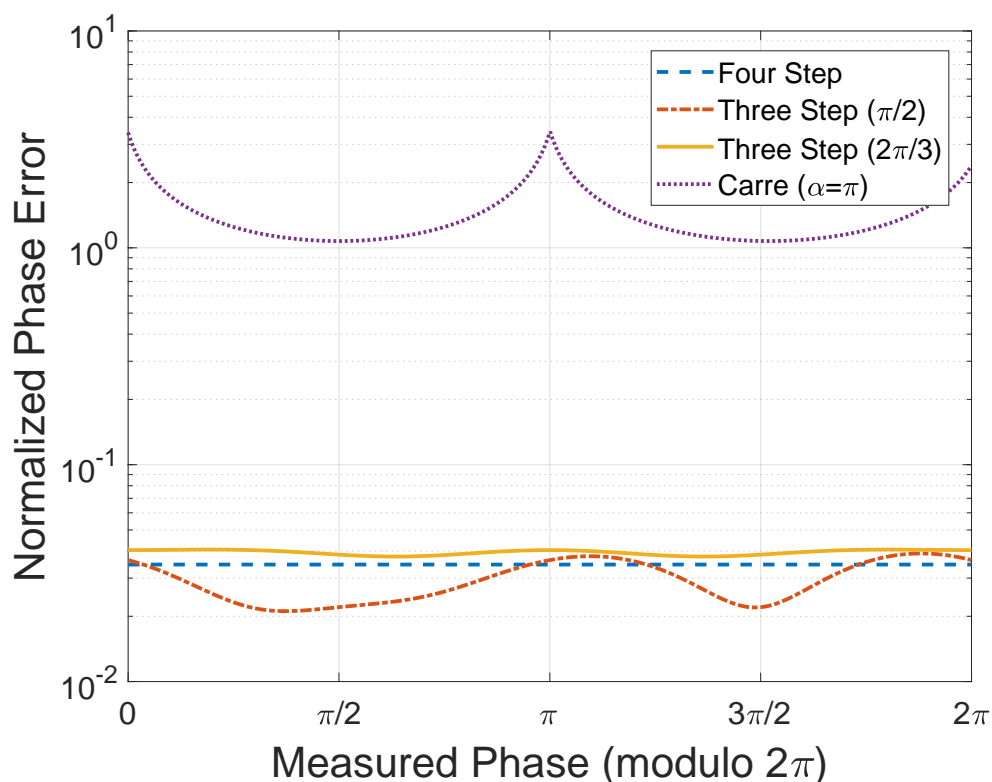


Figure 4.8 – Comparison of phase errors of the Four Bucket/Step, Three Bucket/Step, and Carré Methods as a function of phase (adapted from [3])

Carré Method is that a phase measurement can be made without knowledge of the spatial or temporal sampling frequency of the interference pattern (i.e. if $\Delta\phi$ of Equation 2.4 is unknown).

The propagation of errors between the Four Bucket/Step Method and Three Bucket/Step Method are comparable to each other, however, the Four Bucket/Step Method was shown to introduce random errors which is desirable in applications where a wide range of phases are to be measured. This ensures more consistent performance across all measurements, and was influential in the design process of the DHM instrument.

4.3 Limits of Detection

One of the design requirements of this optical system was that it be a high sensitivity imaging system. This implies that the instrument should be able to detect objects at lower microbial concentrations than other state-of-the-art optical devices. In order

to quantify sensitivities of this DHM instrument as well as other imaging systems, a statistical model was derived to theoretically calculate each instrument's ideal sensitivity. This theoretical model was then verified experimentally. The work presented in this section resulted in two publications. The theoretical derivation of sensitivity was published in a special edition issue of *Astrobiology* [12], while the experimental verification was published in the *Journal of Visualized Experiments* [11]. The work presented here pertaining to the theoretical model of sensitivity was conceived and development by myself.

Theoretical Model of Sensitivity

First, a statistical model based on Bernoulli statistics was used to derive an expression for the theoretical limits of detection of any microscopy instrument based on its optical characteristics. The general assumption for this model is that the bacterium (or object of interest) needs only be in the field of view (FOV) of the instrument to be detected. Most biological samples are transparent, but due to developments in label-free imaging techniques such as phase contrast microscopy, it is possible to image them without dyes or stains, thus making this a valid assumption.

Assuming that the sample is thoroughly mixed such that the objects are uniformly dispersed throughout the medium, the probability that a single object will be in the FOV of the image is given by $p = V\rho_b$, where V is the sample volume (FOV \times depth of field) in mL and ρ_b is the particle concentration of the sample in objects/mL.

Applying the assumption of Bernoulli statistics, the law of total probability states that $p + p_{\text{not}} = 1$, where p_{not} is the probability that an object is not in the FOV of the instrument.

If this sampling is repeated x number of times, the law of total probability becomes $p_{\text{eff}} + p_{\text{not}}^x = 1$, where p_{eff} is the effective probability that at least one object will be imaged after x samples. This results in an expression that estimates the number of sample volumes to image in order to detect an object as a function of concentration at a given confidence level (p_{eff}) such that

$$x = \frac{\ln(1 - p_{\text{eff}})}{\ln(1 - V\rho_b)}. \quad (4.11)$$

Equation 4.11 shows that the number of samples that must be recorded is inversely proportional to the image volume of the instrument. An advantage of off-axis DHM is that it is not only capable of high resolution imaging, but it is capable of this

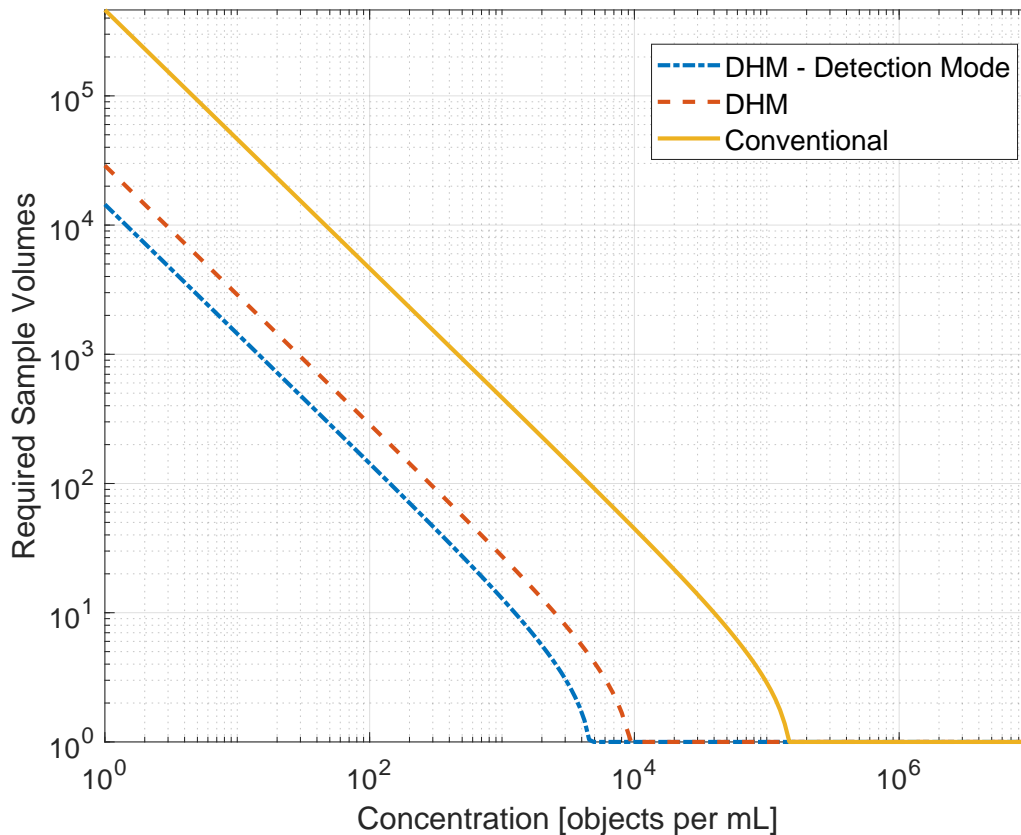


Figure 4.9 – Minimum number of required sample volumes to detect objects at various concentrations with a confidence level of 95% (adapted from [12])

high resolution imaging through a large depth of field allowing its effective image volume to be orders of magnitude larger than traditional microscopy techniques of comparable magnification and resolution.

A specific advantage of the common mode instrument is the fact that it requires two liquid channels that are imaged simultaneously. For sparse samples, it is possible to load sample in both channels as opposed to just one, which effectively doubles the sample volume capability of the instrument. Imaging done with the common mode instrument with sample in both channels of the sample chamber is referred to as operating in Detection Mode throughout this section.

Figure 4.9 plots the number of sample volumes that must be imaged as a function of concentration in order to have a detection confidence level of 95% ($p_{\text{eff}} = 0.95$). In the figure, the same calculation is shown for a conventional light microscope (parameters in Table 4.2).

Table 4.2 – Specifications of the off-axis DHM and comparable brightfield microscope (labeled Conventional)

Property [unit]	DHM	Conventional
<i>Illumination wavelength [nm]</i>	405	White light
<i>Objective numerical aperture [-]</i>	0.3	0.4
<i>Magnification [-]</i>	20	20
<i>Field of view [$\mu\text{m} \times \mu\text{m}$]</i>	360×360	400×400
<i>Depth of field [μm]</i>	800	6
<i>Lateral resolution [μm]</i>	<1	<1

Table 4.3 – Minimum number of required sample volumes to detect objects (detection confidence of 50%)

Concentration [objects per mL]	DHM	Conventional
10^0	6,686	106,967
10^1	669	10,697
10^2	67	1,070
10^3	7	107
10^4	1	11
10^5	1	1

Table 4.3 shows the number of sample volumes that must be imaged when using off-axis DHM as well as a conventional light microscope in order to have a detection confidence level of 50%. This shows the minimum number of samples that must be imaged in order to have a sufficiently large possibility of detecting bacteria.

The aforementioned analysis assumes the FOV to be instantaneous and constant; however, the ability to acquire image sequences allows for larger FOVs to be imaged. The increase in the instantaneous FOV to an effective FOV is proportional to the length of the image sequence recorded as well as the level of motility of the sample. Because this is difficult to quantify in a general case for such samples as bacteria, only a simple estimation is discussed here.

For the purposes of estimating the effective FOV, bacterial motility can be modeled as a one-dimensional random walk where each step of a bacterium has an equal probability of being forward or backward. This results in an averaged traveled distance by the bacterium of

$$|\mathbf{d}| = v\sqrt{k}, \quad (4.12)$$

where v is the magnitude of the bacterium's physical movement per step and k is the total number of steps taken. For an in-depth derivation of this expression, see Appendix A. For any given sample chamber, bacteria are only free to move in and out of the FOV of the instrument across four boundaries of the sample volume because the other two are bounded by glass (top and bottom surfaces). Thus, the effective sample volume as a function of image sequence duration (t) is $V_{\text{eff}} = V + 2zv(x + y)\sqrt{t}$, where x , y , and z are the length, width, and height of the sample volume, respectively.

Experimental Verification of Sensitivity

With a theoretical background and expectation of the sensitivity of the DHM instrument, a series of experiments were conducted to verify the model created in the previous section. It is important to note that the quantification of bacterial concentrations on the order of even 10^4 cells per mL is difficult. At these low concentrations much care must be taken to avoid false positives from various sources of contamination. For the experiments described in this section, a collaboration with the Kenneth Neilson Laboratory at the University of Southern California was crucial as they were able to provide the equipment and support necessary to ensure that these experiments were done in a highly controlled and sterile manner.

These experiments were conducted by creating samples of highly controlled concentrations of bacteria, and flowing them through the FOV of the DHM instrument using a syringe pump. The camera frame rate was chosen such that a particle would be imaged at least twice as it flowed across the FOV of the common mode instrument. Many flow characteristics must be considered when conducting an experiment of this sort and are documented in Section E. By counting the instances of bacteria as they travel past the FOV of the instrument, it is possible to deduce the concentration of the sample given information on the sample chamber geometry and flow rate of the syringe pump. Furthermore, the theoretical model from Equation 4.11, predicts detection of particles as a function of imaged sample volumes. If the flow rate of the syringe pump is chosen such that every particle is imaged at least twice from the time it enters and exits the FOV of the instrument, then a new sample volume is imaged after every two images. Because of this, it is possible to predict that within a certain amount of time, a bacteria would be imaged at a given concentration.

The biological concerns with such an experiment include contamination as well as bacterial growth throughout the experiment. Contamination can introduce tremen-

dous and confounding errors into the experiment. If unsterile objects come into contact with the sample, the apparent bacterial concentration of the sample will change as a result of the contamination. It is also possible for contamination to cause false negatives because the contaminant might exhibit a predator-prey relationship with the bacterial strain being imaged, thus artificially decreasing the apparent bacterial concentration of the sample. Furthermore, as these bacterial samples contain living things, much care must be taken in planning the experiment such that imaging can occur as soon as the serial dilutions are made to ensure that the bacteria have as little time to multiply as possible.

To address these concerns, standard biological safety protocols were followed including the use of pre-sterilized equipment, sterile personal protective equipment, as well as conducting all biological cell handling in a sterile laminar flow hood. These bio-safety procedures are described in Appendix D.

The contents of this section are part of a peer-reviewed scientific publication and video in the *Journal of Visualized Experiments* [11]. This work included a collaboration with The Kenneth Neilson Group at the University of Southern California. A graduate student from the Neilson Group, Casey Barr, and myself contributed equally to this effort. I was responsible for the experimental setup related to the DHM instrument and downstream data analysis. Casey Barr contributed by the design and implementation of the microbiological aspect of this experimental technique.

In this series of experiments, cultures of *Serratia marcescens* and *Shewanella oneidensis* were used. These particular strains of bacteria were chosen for their distinct size, shape, and color. Both strains have a distinct rod shape, while *S. marcescens* has a very distinct red color. These physical traits help prevent against false positives as their sizes and shapes can be used as distinguishing features in DHM images, while the distinct red color of *S. marcescens* can be used as a distinguishing feature when quantifying cell concentrations using traditional methods like spectrophotometric readings or culture plate counting.

The night before these experiments, about 5-6 mL of sterile lysogony broth was seeded with a sample of master culture medium (e.g. from a glycerol stock) and incubated at 23°C overnight.

The day of the experiment, a spectrophotometric reading (OD_{600}) of the bacterial master culture was taken. By conducting a growth curve analysis, it is possible to correlate the spectrophotometric reading of a sample to its concentration, but due

to the exponential growth of bacteria, this method alone is not reliable. As a result, a sample of the master culture was hand counted using a Petroff-Hauser counting chamber [11].

With the concentration of the master culture known, serial dilutions were done to achieve samples with concentrations of 10^5 , 10^4 , 10^3 , and 10^2 cells per mL. These dilutions were done into sterile 0.9% saline solutions to hinder any further cell growth by depriving the bacteria of nutrients. Prior to imaging, a sample from these dilutions were culture-plated in triplicate and allowed to incubate for further validation of cell concentration. Sample was then loaded into a sterile syringe and placed onto a syringe pump. The microfluidic system was then primed by running the syringe pump for an appropriate amount of time. This time allowed for any air bubbles or microscopic debris from the fluidic tubing to be washed out.

With the system primed and the syringe pump running, images were taken at a constant frame rate of 5 fps for each of the two bacteria strains at each of the four concentrations tested.

The hologram sequences from all eight data sets were processed and de-noised to aid in the manual detection of particles. Because this experiment involved only the detection of bacteria, no numerical reconstruction was required. Each hologram was background subtracted in order to eliminate any stationary artifacts from the image. This image processing technique is outlined in Appendix B. By cycling through the hologram sequences and counting bacteria as a function of time, it is possible to converge on an estimate of bacterial concentration. For the purposes of this experiment, a statistically significant estimate of bacterial concentration is considered when at least 30 individual bacterium have been imaged. Given the flow rate of the syringe pump, a camera frame rate of 5 fps, and Equation 4.11, a theoretical time limit can be calculated which predicts the time necessary to arrive at a statistically significant concentration estimate.

Table 4.4 summarizes the experiments performed including the theoretically predicted detection times and experimental detection time. As mentioned earlier, the target concentrations were 10^5 , 10^4 , 10^3 , and 10^2 , but culture plate counting (before and after imaging) in triplicate was done to provide more accurate measurements of concentration. Concentrations are reported with a 95% confidence interval.

Table 4.4 – Summary of results from sensitivity verification experiments

Target Concentration [cells/mL]	Theoretical Detection [s]	<i>S. marcescens</i>			<i>S. oneidensis</i>		
		Plate Counted Conc. [cells/mL]	Estimate Conc. [cells/mL]	Experimental Detection [s]	Plate Counted Conc. [cells/mL]	Estimate Conc. [cells/mL]	Experimental Detection [s]
10^5	<15	$1.08 \times 10^5 \pm 782$	$1.08 \times 10^5 \pm 234$	16.23	$1.12 \times 10^5 \pm 847$	$1.12 \times 10^5 \pm 346$	15.46
10^4	<15	$0.97 \times 10^4 \pm 576$	$0.97 \times 10^5 \pm 289$	15.89	$1.04 \times 10^4 \pm 762$	$1.04 \times 10^4 \pm 283$	16.06
10^3	84	$1.21 \times 10^3 \pm 372$	$1.17 \times 10^3 \pm 224$	68.58	$1.51 \times 10^3 \pm 468$	$1.53 \times 10^3 \pm 213$	54.73
10^2	804	356 ± 256	589 ± 204	574.87	487 ± 228	531 ± 197	465.09

Upper Limit of Detection

Because DHM is an instantaneous and volumetric imaging system, there exists an *upper* limit of detection. This is to say that there exists an upper limit of concentration where the sample becomes too dense such that the recorded image suffers from a shadowing effect where particles cannot be imaged because there are other particles that block light from interacting with them. This can have deleterious effects on image quality and resolution due to multiple optical scattering events that occur in the dense sample (the sample becomes optically opaque).

This upper limit of detection was quantified experimentally in both amplitude and phase reconstructions. A sample of *Bacillus subtilis* was grown overnight in Lysogony Broth to an optical density of $OD_{600} = 0.8$, which corresponds to a concentration on the order of 10^8 cells per mL. By serial dilution, concentrations of 10^5 , 10^6 , and 10^7 cells per mL were prepared. These concentrations were verified via culture plate counting.

Separate and sterile sample chambers were used to image each concentration using the common mode DHM instrument. The holograms were then subsequently reconstructed in both amplitude and phase. From the amplitude and phase reconstructions, bacteria were selected one at a time and their respective signal-to-noise ratios (SNR) quantified. See Appendix B for more information on these calculations.

Figure 4.10 shows the normalized SNR as a function of bacterial concentration. Experimental data is shown with straddle bars indicating the 95% confidence interval, with a solid fit line. The fit line found to straddle the experimental data with the lowest error was a logistic regression. The upper limit of detection is defined as the point at which the SNR has decreased by 3 dB. With this definition of the upper limit of detection, the logistic regression suggests that the upper limit of detection for the DHM instrument is $\approx 6 \times 10^6$ cells per mL. Note that phase images, although experience a decreased SNR in the same manner as amplitude images, they do not decrease by 3 dB.

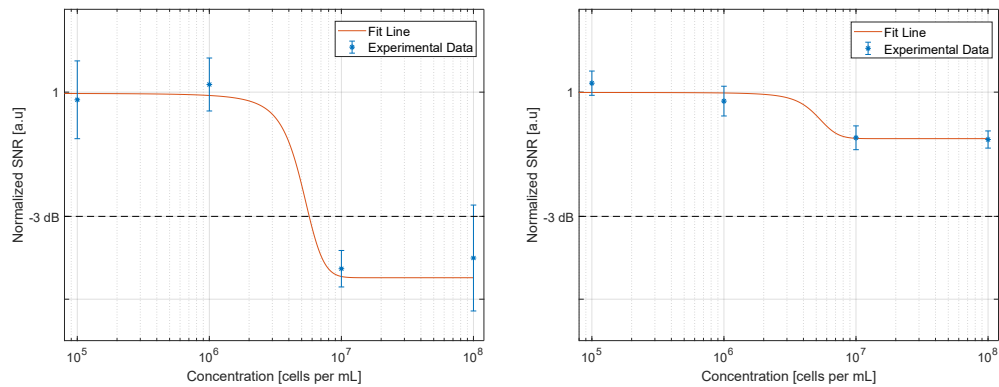


Figure 4.10 – Normalized SNR as a function of bacterial concentration in amplitude images (left) and phase images (right) (adapted from [12]).

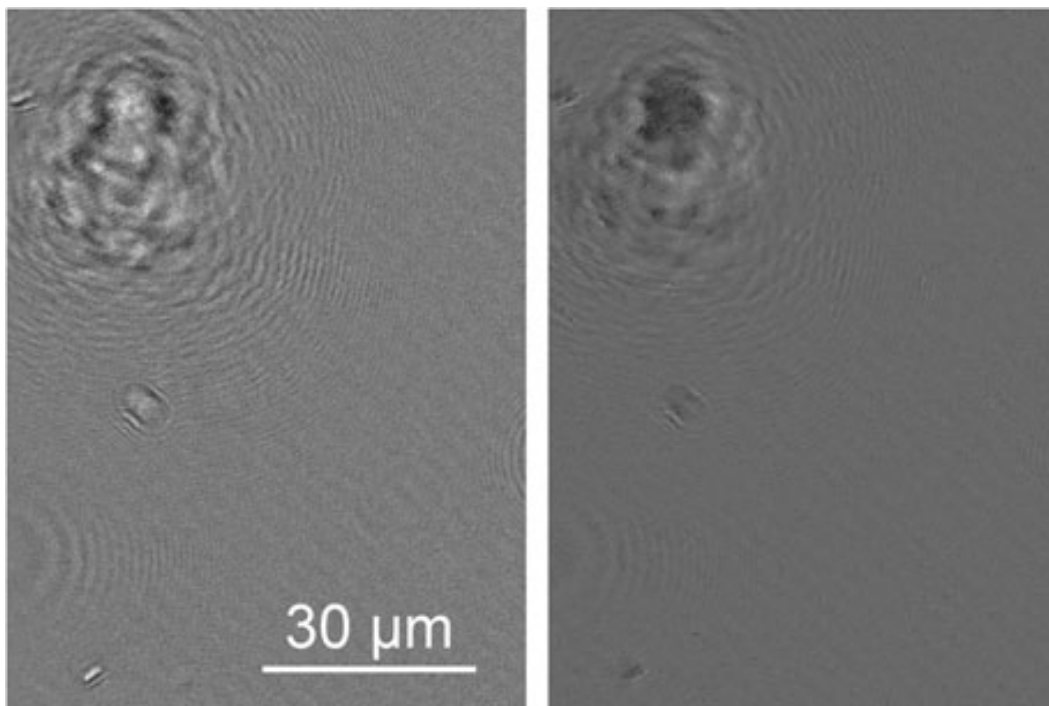


Figure 4.11 – Phase (left) and amplitude (right) images of *B. subtilis* at the relatively low concentration of 10^4 cells per mL (adapted from [12]).

Figures 4.11 and 4.12 show select phase and amplitude reconstructions of low and high concentrations of *B. subtilis*. At the relatively low concentration of 10^4 cells per mL in Figure 4.11, there is no overlap in the diffraction patterns of the bacteria. However, at the relatively high concentration of 6×10^6 cells per mL of Figure 4.12, we can notice that the diffraction patterns of one bacterium interfere with its neighboring bacterium, thus degrading the quality and resolution of the image.

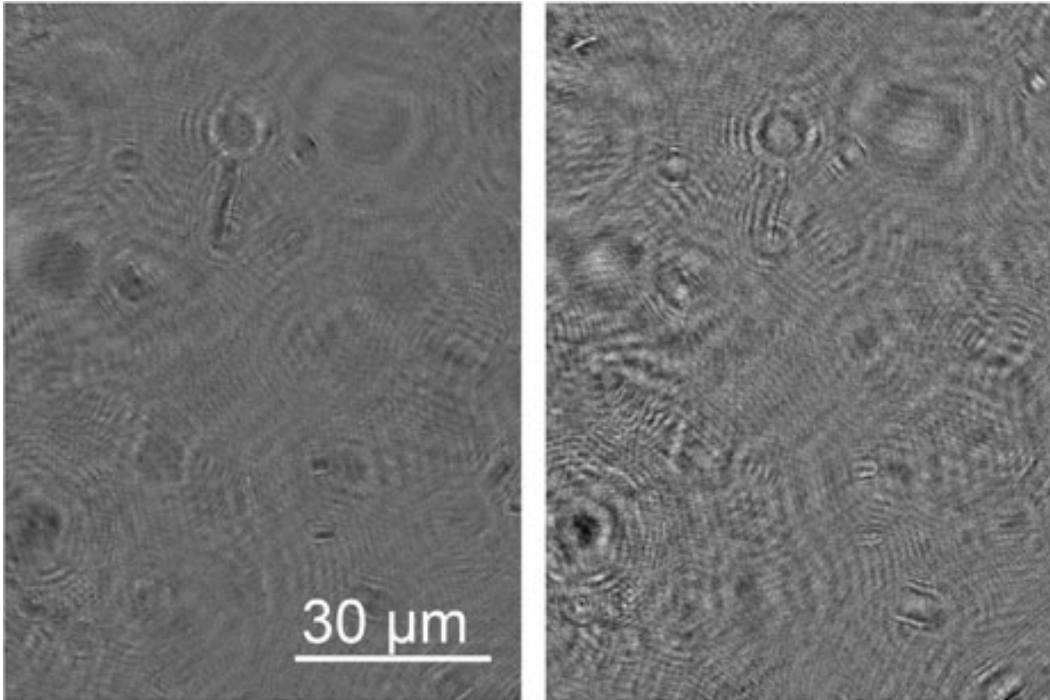


Figure 4.12 – Phase (left) and amplitude (right) images of *B. subtilis* at the relatively high concentration of 6×10^6 cells per mL (adapted from [12]).

Concluding Remarks

This chapter explored the various metrics commonly employed in the quantification of performance for many optical imaging devices. These metrics include resolution, depth of field, error analysis, and sensitivity of detection.

In the quantification of resolution, the resolution of both DHM instruments were quantified in the lateral and axial dimensions. The common mode instrument was verified to operate at the diffraction limit, while the Mach-Zehnder instrument was verified to operate with sub-micron lateral resolution. The Mach-Zehnder instrument was not experimentally verified to operate at the diffraction limit simply because the resolution target available during the analysis did not have small enough elements. The smallest element of the resolution target has a width of $0.78 \mu\text{m}$, while the theoretical diffraction limited resolution of the Mach-Zehnder instrument is $0.49 \mu\text{m}$.

The depth of field was defined as the axial distance about focus, where sub-micron lateral resolution can be maintained by the imaging device. Implementing this definition of depth of field resulted in the depth of field of the common mode instrument being $900 \mu\text{m}$, while the Mach-Zehnder instrument demonstrated a

depth of field of 600 μm .

In optical interferometry, many phase retrieval algorithms exist. Three of the most common are the Four Bucket/Step Method, the Three Bucket/Step Method, and the Carré Method. These methods were introduced and an error analysis was conducted employing the expression for the propagation of error. Aspects of each phase retrieval method were compared and the advantages/disadvantages of each method were presented. The contents of this analysis were presented and published as a conference proceeding at the 2017 SPIE Photonics West conference [3]. The method that must be employed in the phase retrieval from an interferogram depends on the fringe sample frequency of the optical detector and whether the phase difference between fringe samples are known. Having an understanding of the error characteristics of each of these algorithms aids in the design of DHM instruments as one can choose the proper optical sensor in order to suit the specific needs of the instrument.

Lastly, a design metric of great importance is the detection sensitivity of the DHM instrument. Verifying this involved the development of a statistical model of the expected sensitivity as well as an experimental verification of this sensitivity. The statistical method developed was published in a special issue in the peer-reviewed scientific journal *Astrobiology*, and the experimental verification was published in the peer-reviewed scientific journal *Journal of Visualized Experiments (JoVE)*. These analyses showed that the common mode DHM has a detection sensitivity that is roughly two orders of magnitude higher than conventional confocal microscopy of the same optical resolution and field of view. This can be interpreted in multiple and equally appealing ways. Given a certain amount of sample with a low microbial concentration, the common mode DHM can detect microbial presence in the sample roughly two orders of magnitude quicker than traditional optical methods. Additionally, this means that the common mode DHM can detect microbial life while using roughly two orders of magnitude less sample volume than traditional methods. This capability is appealing because the DHM is capable of conducting detecting life in a given sample while using two orders of magnitude less resources, whether that resource is either the sample itself (which can be very scarce), or computational resources (which can also be very scarce).

This chapter experimentally validated the hardware developments described in the previous chapter. The work presented here represents an invaluable verification that we indeed have achieved the performance metrics we have set in the Introductory

chapter. With two DHM instruments operational, with known performance and capabilities, further development, experimentation, and even field deployment is possible to investigate microbial motility and other characteristics of microbiological importance.

SOFTWARE DEVELOPMENT

In the design of novel microscopic instruments, the development of software techniques to handle and analyze data can prove just as useful as hardware development. In this section various software techniques are introduced that were developed to aid in the processing and analysis of holographic data. This section will introduce a novel application of a machine learning algorithm for the 3D tracking of particles in numerically reconstructed data, which was published in the peer-reviewed scientific journal *AIMS Biophysics*, of which I was first author [5]. This machine learning algorithm, being very computationally heavy, prompted the development of a low computational overhead algorithm to increase the image contrast of volumetric reconstructions to aid in the 3D tracking of particles. Both of these algorithms can not only be used for object detection, but object tracking as well. This section will discuss the operating principles of each method, as well as a verification of their performance.

5.1 Machine Learning Tracking Algorithm

Current techniques for observing bacterial motility are effectively two-dimensional because of the small depth of field provided by high numerical aperture objectives. Measurement of 3D trajectories is performed by approximating the third dimension from measured 2D trajectories, or by inferring the organisms' z positions as they travel in and out of focus. This severe limitation gives an incomplete image of the motility patterns observed. For example, a bacterium travelling vertically, parallel to the optical axis, will appear stationary using conventional techniques. A 2015 paper [119] calculated the systematic errors associated with observing bacterial motility when using conventional microscopic techniques and found that in addition to the effects of localization errors, 2D projection of the same volume introduce systematic errors in speed and turning angle measurements, compared to the correct speed and turning angle measurements found in 3D tracking. Similarly, observations obtained from 2D slicing are constrained to a thin focal plane thickness and ignore the vast majority of turning events; a bias against turning angles near 90° is also introduced. Finally, the boundaries of the sample chambers required for high-resolution imaging constrain motion in the z direction and affect the hydrodynamics of motility and the

organisms' possible swimming ranges. Because of this, 2D methods do not capture the entire complexity of bacterial motility and shed doubt upon models of motility such as "run and tumble" or "flick" [87, 116]. As a result, the swimming patterns of most bacteria in an unconstrained 3D volume remain largely unknown.

DHM has been used to study distribution and swimming patterns of microorganisms on the scale of 10 μm : algae in the laboratory [68], plankton in the open ocean [27], dinoflagellate feeding behavior [109, 110], algal zoospores [122] and cultured cells in the laboratory [77]. Nevertheless, papers on DHM imaging of micron-sized bacteria are few. Although the common mode instrument is capable of 3D sub-micron imaging of bacterial cells, obtaining automated 3D tracks of bacterial cells with this instrument is still very challenging. Low contrast does not allow images to be thresholded and the presence of out-of-focus airy rings confuses detection algorithms. Amplitude images show a large amount of laser speckle noise, which is inherent to any imaging technique using coherent light sources. Some solutions have been presented in the literature. One paper successfully tracked bacteria using denoising algorithms [86, 116], but this approach is computationally intensive as well as labor-intensive. Holographic microscopy using incoherent light can eliminate speckle [16], but at the expense of depth of field, such that it is less useful for 3D tracking than coherent DHM. Synthetic aperture techniques can also improve resolution [27], but are used to improve the resolution of non-diffraction limited instruments. Instruments operating at the diffraction limit, such as the common mode DHM, render such techniques futile. Other super-resolution techniques, such as angular or wavelength multiplexing [94, 129], require the sample to be stationary. Because studies of live bacteria require imaging at the order of the size of the wavelength of illumination light in a large volume, and because they move at tens to hundreds of microns per second, identifying and tracking them remains a challenge.

Automated particle tracking can generally be divided into two steps: Particle identification/detection (the spatial aspect), followed by particle tracking/linking (the temporal aspect). In 2014, Chenouard et al. [28] provided an objective comparative study of the most common particle tracking methods used in bioimaging. First, the authors identified three main factors that affect tracking performance: dynamics (type of motion), density (number of particles per field of view), and signal-to-noise ratio (SNR). Second, they simulated a set of 2D and 3D image data based on these different factors. They then sent these image data sets to fourteen separate research groups who took up the challenge of identifying and tracking the particles using

state-of-the-art methods. The teams then sent back their results, which showed that no one particle tracking method performed best for all data sets. The best identification methods were based on careful implementation and parameter tuning of any algorithm. The best tracking methods were the ones that used multiframe/multitrack optimization instead of the simpler nearest-neighbor linking. In addition, methods that made explicit use of the prior knowledge about the particle motion in each scenario were more successful than methods that did not.

In this section, a novel application of a machine-learning particle identification/detection algorithm based on linear logistic regressions is implemented for tracking of two test bacterial strains: *Bacillus subtilis* and *Collwellia psychrerythraea* [58]. The core functions of this algorithm are readily available in MATLAB as part of the Statistics and Machine Learning toolbox. This algorithm was used as a proof of concept, however, and other machine learning algorithms such as decision tree models, support vector machines, or k-nearest neighbor classification models can also be implemented. The strains were chosen to represent relative extremes of prokaryotic size and motility. *B. subtilis* is large (5 μm long) and shows slow ($\approx 20 \mu\text{m/s}$) undulating motility. *C. psychrerythraea* is a marine psychrophile that is relatively small ($< 1 \mu\text{m}$) and swims at rapid speeds (over 40 $\mu\text{m/s}$ even at subzero temperatures) [61]. The algorithm requires an expert user to identify bacteria from a training data set, which is a small subset of the recorded data. Once trained with a sufficient number of examples, the algorithm is able to automatically detect organisms from the entire data set. Performance is compared to manual tracking and found to give a statistical precision of 91%. Once identified, bacteria may be tracked by using a simple 'nearest-neighbor' Hungarian linking algorithm [121]. This represents the first demonstration of an automated algorithm for tracking of bacteria using DHM. While much work on the subject remains to be done, this is a promising area of inquiry for anyone studying 3D bacterial motility.

The contents of this section were published in the peer-reviewed scientific journal *AIMS Biophysics* in 2017 [5]. I was first author of this publication and contributed by writing the final version of the software which was publicly released with the publication. Furthermore, I was responsible for the data collection, parameter tuning, training, tracking, and data visualization of the high microbial density data set of this work.

Training

The linear logistic regression pixel classifier is a supervised learning algorithm that was implemented using MATLAB's Statistics and Machine Learning Toolbox. In order to train this classifier, a sample data set is used to generate a classifier, $h_w(x)$, as well as a pixel features matrix, X_t . This algorithm was written such that the data set it is to be trained on and eventually track is a four-dimensional image stack composed of many two-dimensional images at various z-planes and time. Prior to training, the data must be reconstructed and processed. All data structure/handling protocols prior to training are detailed in Appendix B.

The pixel features that are used to construct the pixel feature matrix are (in descending order of importance):

1. Absolute difference of pixel values $|I_{ij} - \bar{I}|$
2. Image gradient (in all three spatial directions)
3. Local standard deviation
4. Absolute difference of pixel values (in z) $|I_k - \bar{I}|$
5. Local median pixel value
6. Image standard deviation

For a given sample data set, (x, y, z, t) coordinates are provided to the algorithm by an expert user, corresponding to the location of particles of interest. Pixel feature matrices are constructed near these coordinates along with a binary probability matrix f_t , where $f_t \in \{0, 1\}$. Because absolute particle coordinates are known, this probability matrix contains zeros everywhere except for the pixels where a particle is located. Both the pixel feature matrix and the binary probability matrix are used to calculate the classifier, which is defined as

$$h_w(x) = \left(1 + e^{w^T}\right)^{-1}, \quad (5.1)$$

where w^T is the transpose of a linear weighting matrix. There is no closed form solution for w , and as a result, a gradient descent iterative minimization approach is used such that

$$w_{m+1}^k = w_m^{k-1} + \alpha \sum_{i+1}^m \left(f_{t,i} - h_w^{k-1}(x_i)\right) x_i, \quad (5.2)$$

where w_{m+1}^k is the $(m + 1)^{\text{th}}$ element of the k^{th} iteration of the linear weighting matrix and α is gradient descent learning parameter. This learning parameter must be predefined and was chosen as $\alpha = -0.1$. The resulting pixel classifier is the logistic model that is then used to analyze data in order to determine the probability of the presence of a particle of interest.

Particle Detection

With the classifier trained, data sets are analyzed and their respective pixel feature matrices (X) are constructed. These matrices are then subsequently multiplied by the classifier to yield the probability matrix

$$f_{i,j} = Xh_w(x), \quad (5.3)$$

where $f_{i,j} : f \in [0, 1]$ is a probability matrix corresponding to the probability that pixel (i, j) contains a particle of interest. A minimum probability threshold can then be employed to decide whether or not a pixel is indeed a particle of interest.

More sophisticated schemes can be employed to interpret this probability matrix f , such as agglomerative hierarchical clustering and weighted centroid clustering.

Statistical Validation Metric for Particle Detection

To quantify the performance of the automated tracking algorithm, manually obtained bacterial tracks were used in order to calculate an F_β score (F-score). The F-score is defined as

$$F_\beta = \frac{(1 + \beta^2)PR}{\beta^2P + R}, \quad (5.4)$$

where β is a weighting factor, P is the statistical precision, and R is the statistical recall. Statistical precision is defined as

$$P = \frac{T_p}{T_p + F_p}, \quad (5.5)$$

and statistical recall is

$$R = \frac{T_p}{T_p + F_n}, \quad (5.6)$$

Table 5.1 – Experimental parameters used in the validation of the machine learning object detection algorithm.

Property	Data Set 1	Data Set 2	Data Set 3
Sample Volume [μm^3]	360×360×252	360×360×392	360×360×500
Bacteria Species	<i>Bacillus subtilis</i>	<i>Colwellia psychrerythraea</i>	<i>Bacillus subtilis</i>
Concentration [cells per mL]	$\approx 10^2$	$\approx 10^2$	$\approx 10^6$
Cell volume and shape [μm^3]	$\approx 8\mu\text{m}^3$, elongated	$\approx 2\mu\text{m}^3$, comma-shaped	$\approx 8\mu\text{m}^3$, elongated
Number of z-planes	201	157	201
Number of time frames	84	18	85
Total number of bacteria in FOV	8	6	149

where T_p is the number of true positives, F_p is the number of false positives, and F_n is the number of false negatives.

The weighting factor β is used to weigh the importance of either statistical precision or recall. Because the motivations that led to the development of this algorithm were to be able to extract statistically relevant motility characteristics of bacteria from a given data set and not necessarily identify all bacteria present in the field of view, precision is weighted higher than recall by defining $\beta = 0.5$.

Results

Table 5.1 summarizes the experimental parameters of all three data sets used in the validation of the machine learning tracking algorithm. The first two data sets contained a very sparse concentration of bacteria and were used as a means of a proof of concept for the machine learning algorithm. The third data set contained a much higher concentration of bacteria, which is more representative of the concentrations expected throughout the instrument’s use.

With the manually tracked bacteria in Data Sets 1 and 2, the results from the machine learning tracking algorithm were evaluated by calculating the absolute spatial localization difference between the manually obtained tracks and the autonomously obtained tracks. These absolute differences are illustrated in Figure 5.1.

The tracking algorithm was also employed to track a data set with a higher concentration of *B. subtilis* (on the order of 10^6 cells per mL). At such a concentration, there are expected to be approximately 100 to 200 cells in the field of view of the DHM instrument at any one time. The tracking algorithm was able to identify 149 unique bacteria in this data set, while a human observer was only able to identify 127 bacteria. The remaining 22 bacteria were noticed by the human observer only after they knew there were bacteria there. Figure 5.2 shows the three dimensional

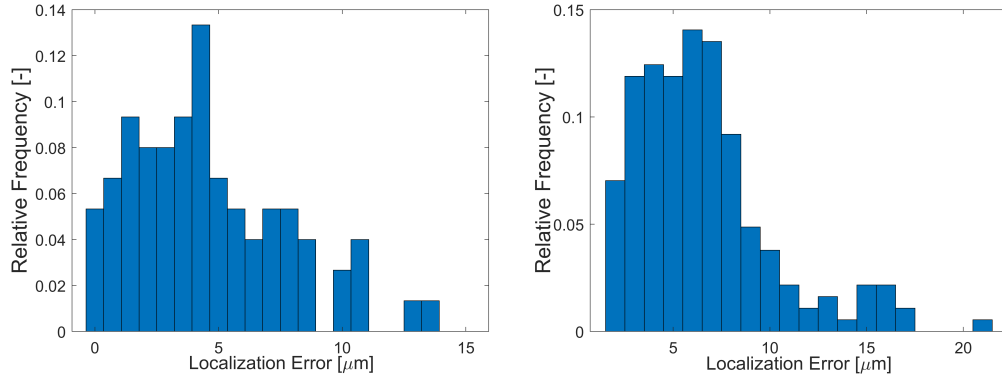


Figure 5.1 – Localization error of *B. subtilis* (left) and *C. psychrerythraea* (right) as a result of the machine learning tracking algorithm (adapted from [5]).

trajectories of Data Set 3 obtained autonomously from the machine learning tracking algorithm. This plot is color-coded with respect to time.

The average swimming speed observed from Data Set 3 is $23 \pm 17 \mu\text{m/s}$ (standard deviation, $n = 149$), with a median swimming speed of $10 \mu\text{m/s}$. These values are in agreement with the literature on wild-type *B. subtilis*. Not only the average and median speeds are in agreement with literature, but the relatively large variation in these values are also expected due to the heterogeneous swimming characteristics of bacteria, even of the same species. Figure 5.3 illustrates the distribution of swimming speeds of the *B. subtilis* tracked in Data Set 3.

5.2 Residual Fringe Visibility as a Means of Enhanced Image Contrast

As discussed in the previous section, it is possible with the help of a logistic regression statistical method, to detect and track sub-micron sized particles in three dimensions using DHM. However, this tracking ability comes at a large computational cost. The reconstruction and tracking of Data Set 3 in the previous section involved roughly 8 hours of computation using an Intel 6-core i7 processor at 3.50 GHz. This amount of computation is impractical in a field setting where computational resources are scarce. To provide useful information of the sample being imaged by the DHM while at the same time using reasonable amounts of computational resources, a novel object detection scheme was developed that is capable of detecting the lateral position of a particle within an off-axis hologram itself. This scheme involves the background subtraction of holograms prior to reconstruction. The work presented in this section is a modified version of a manuscript that was submitted to the peer-reviewed journal *Optics Express* [14]. I am first author of

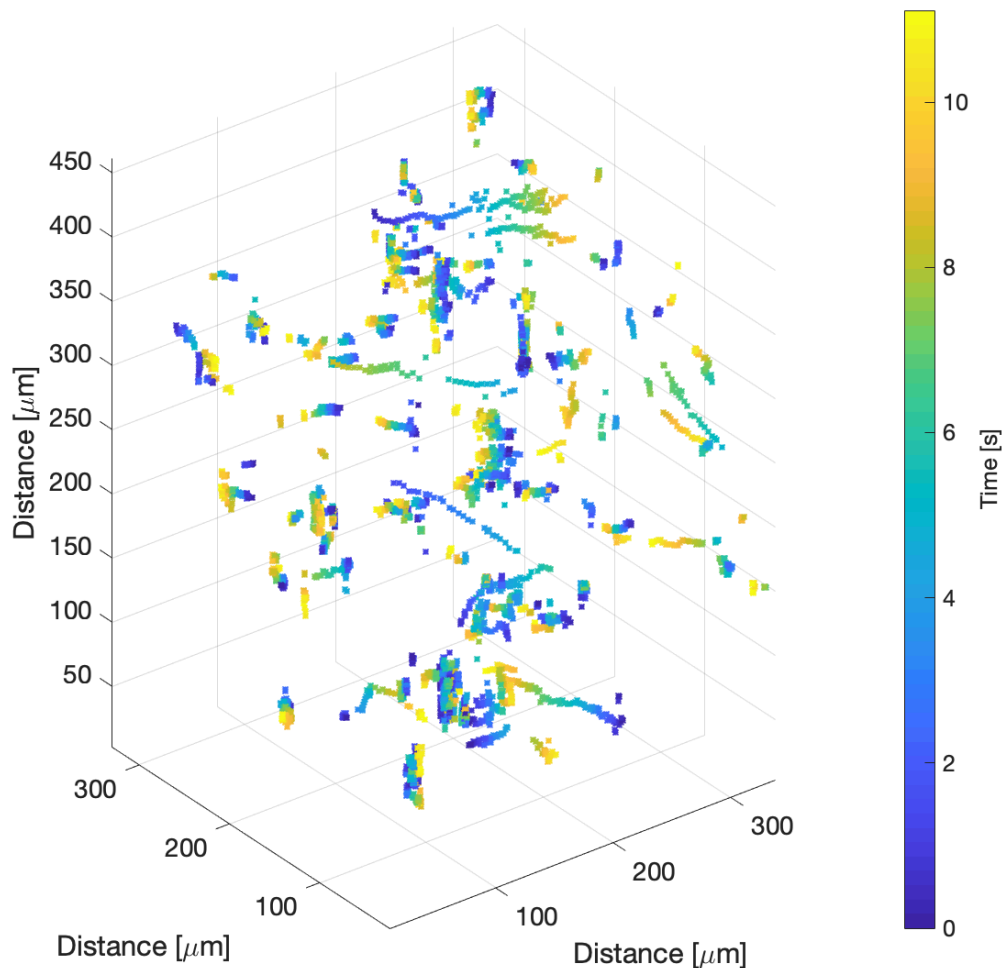


Figure 5.2 – Three-dimensional trajectories of *B. subtilis* as a result of the machine learning tracking algorithm (adapted from [5]).

this work as I conceived the research idea, collected and analyzed the necessary data for its verification, as well as wrote the entire manuscript. Supporting authors aided in guiding the research as well as aided in the development of the theoretical verification of the method.

In this section, a computationally inexpensive method of removing the dominant static noise terms from off-axis holographic images is presented. This method involves the background subtraction of raw holograms prior to numerical reconstruction. By only reconstructing the residual localized fringe packets remaining after subtraction of the background fringe pattern, noise contributions such as speckle are removed prior to propagation through the reconstruction process. A theoretical

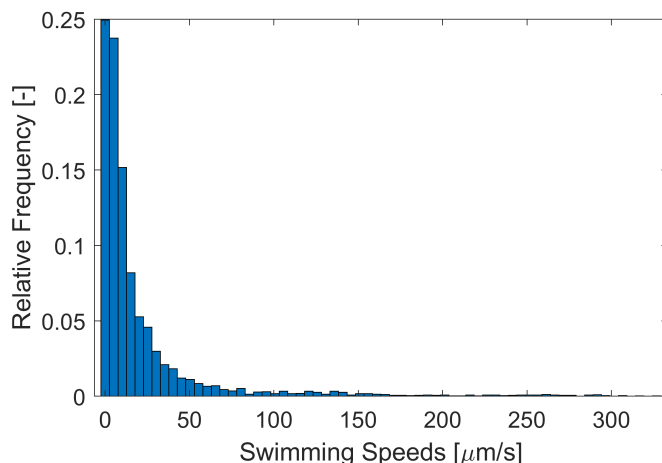


Figure 5.3 – Distribution of swimming speeds of *B. subtilis* as a result of the machine learning tracking algorithm (adapted from [5]).

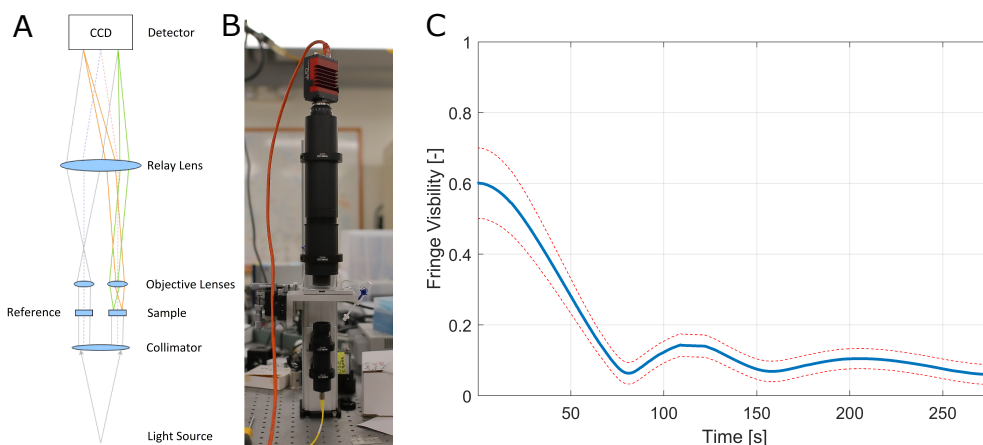


Figure 5.4 – Optical Schematic of the DHM instrument used throughout this work (A), an image of the benchtop instrument (B), and fringe stability of the DHM instrument as a function of time (C). Centerline indicates the mean fringe visibility and dashed lines indicate the 95% confidence interval range.

explanation of the approach is presented, as well as practical considerations when implementing this technique. Finally, processing of experimental data from cultures of bacterial and protozoa cells near the resolution limit of the instrument is shown, highlighting this technique's utility.

Theory of Operation

Figure 5.4A and 5.4B show the optical schematic and laboratory image of a common path DHM instrument used throughout this section. A coherent light source is

collimated and passed through two identically sized microfluidic wells. One contains the object of interest while the other contains a reference liquid in order to match optical path lengths with the sample well. The sample and reference beams are then passed through two separate but identical objective lenses. Finally, a relay lens recombines the beams at a detector plane, creating an interferogram (hologram).

Let two monochromatic and coherent beams, $O(x, y, t)$ and $R(x, y)$, corresponding to the object and reference beam, respectively, be incident on an optical detector, such that the resulting interference pattern recorded by the digital detector is

$$I(x, y, t) = (O + R)(O + R)^* = |O|^2 + |R|^2 + RO^* + R^*O, \quad (5.7)$$

where x, y are spatial coordinates within the hologram, and t is time.

The object beam can be expressed as the superposition of a static beam $O_S(x, y)$ and spatiotemporal deviations from that static beam $\epsilon(x, y, t)$, such that $O = O_S + \epsilon$. Thus, the hologram can be expressed as

$$I(x, y, t) = |O_S|^2 + |\epsilon|^2 + |R|^2 + RO_S^* + R^*O_S + (O_S + R)\epsilon^* + (O_S + R)^*\epsilon. \quad (5.8)$$

The temporally averaged hologram is defined as

$$\bar{I}(x, y, t) = |O_S|^2 + |\bar{\epsilon}|^2 + |R|^2 + RO_S^* + R^*O_S + (O_S + R)\bar{\epsilon}^* + (O_S + R)^*\bar{\epsilon}. \quad (5.9)$$

For a sufficiently large timescale, it can be assumed that $\epsilon = 0$, thus $|\epsilon|^2 = 0$. The residual hologram is defined as $I_R = I - \bar{I}$, such that

$$I_R(x, y, t) = I(x, y, t) - \bar{I}(x, y) = O_S\epsilon^* + O_S^*\epsilon + R\epsilon^* + R^*\epsilon. \quad (5.10)$$

The O_S and ϵ beams are on-axis with each other and thus their interference terms only contribute to the zero-order term of the temporally averaged hologram. With this residual hologram, numerical reconstruction techniques can be employed in combination with spatial filtering, which removes zero-order and twin image artifacts from the reconstructed images [34]. Finally, the spatially filtered hologram that becomes reconstructed can be expressed as $I_R^F = R^*\epsilon$.

Practical Considerations

Background subtraction of holograms is useful because any stationary artifacts in the image become attenuated, leaving only dynamic objects. If the background fringes of the hologram are stable, these fringes would be effectively removed from the resulting image, except for localized fringe ‘packets’ associated with any particle that has moved through the field of view of the hologram. This background subtraction technique vastly increases the SNR of any dynamic particle in an image sequence, making it much easier for automated particle detection algorithm to detect particles of interest in space and time. We show here that rapid motion is not necessary for the method to work; movement as small as bacterial Brownian motion will suffice.

Such a background subtraction technique requires a stable interferometer. Many sources of noise can introduce shifts in DHM fringes, causing them to shift across the field of view of the detector. These noise sources include but are not limited to photon (shot and speckle) noise, temporal phase noise caused by uncorrelated variations between the two beams of the instrument, as well as noise introduced by the detector and associated electronics. These sources of noise introduce an upper limit on the timescales where the proposed background subtraction scheme is useful. As the background fringes shift, they will by definition become dynamic objects in the image, thus no longer being removed by the background subtraction scheme.

The valid timescales of this background subtraction technique were quantified by collecting holographic images as a function of time without a sample in the field of view of the common mode instrument. Temporally averaged holograms were calculated at various timescales through the hologram sequence. Fringe stability was inferred by calculating the average fringe visibility of the temporally averaged hologram. This is possible due to the fact that if the fringes are absolutely stable (static), the temporally averaged hologram would equal the fringe pattern of each hologram in the sequence. As the fringe pattern begins to shift, they will by definition become dynamic artifacts in the image and thus not appear in the temporally averaged hologram. Figure 5.4C shows a plot of fringe stability as a function of time for the DHM instrument used throughout this work. The center line in the plot signifies the mean fringe visibility value while the dotted lines signify the 95% confidence interval value range. By defining the point of fringe decorrelation as the point in time where the fringe correlation decreases by -3 dB, the upper timescale that should be used for this background subtraction scheme is roughly 40 seconds of real time data.

Software Implementation

Although this algorithm shows promise as a real time particle detection algorithm, software was developed to analyze pre-recorded data for the purposes of verifying the algorithm's efficacy as this scheme is oblivious to whether the data is from a live feed or if it is from pre-recorded data.

The software was written completely in MATLAB (2017b) using standard toolboxes and features. The software as well as instructions on how to implement it are available in Appendix B, along with reference to a GitHub repository containing the MATLAB files [82].

Initially this algorithm expects as an input from the user a file path containing the data to be analyzed. From this file path, it imports all holograms and sorts them into a three-dimensional matrix (x, y, t) . With this 3D matrix, background (mean) subtraction is conducted along the third (time) dimension of the matrix in order to remove any stationary artifacts from the images. Mean subtraction is used instead of median subtraction because the computational overhead of a mean calculation is far lower than that of a median calculation (see Figure 5.5). This step requires taking note of the data type of the 3D matrix. Hologram images are in unsigned 8-bit format and must be converted to double precision prior to mean subtraction. After mean subtraction, each image is spatially filtered to remove any low and high spatial frequency noise. Because the optical parameters of the DHM are known, the spatial frequencies in which we expect fringes to be are well known, so all other spatial frequencies can be filtered.

Figure 5.5 plots the computation time required to run this algorithm as a function of input size for both a median and mean subtraction scheme. As can be seen from the plot, the mean subtraction scheme requires much less computational resources than the median subtraction scheme without any measurable sacrifice in accuracy or performance. It is worth noting that both operations are linear with respect to input size, so they are both scalable to larger applications.

Experimental Verification and Procedure

The DHM was used to image two strains of bacteria (*Bacillus subtilis* and *Vibrio alginolyticus*), as well as the protozoan *Euglena gracilis*. A 1 mm deep well was filled with a dilution of the biological sample in minimal media. A motility medium was used for *B. subtilis* which would not harm the organisms but hinder their growth (10 mM phosphate buffer pH 7.4, 10 mM NaCl, 0.1 mM EDTA, 0.1 mM glucose).

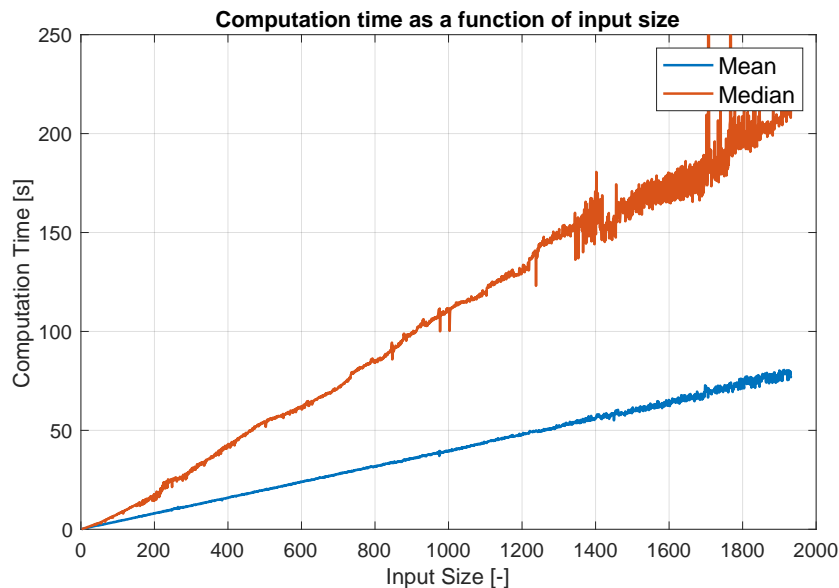


Figure 5.5 – Computation time of the median and mean subtraction schemes as a function of input size.

Due to the marine origins of *V. alginolyticus*, a different minimal media recipe was used (50 mM Tris buffer, 300 mM NaCl, 5 mM MgCl₂, 5 mM glucose). *E. gracilis* was diluted in spring water. Holographic images were recorded at a frame rate of 15 frames per second. Background image subtraction was performed with a timescale of 10 seconds (150 holograms). Both the raw holograms and background subtracted holograms were then spatially filtered and reconstructed via the angular spectrum method using either the commercial software KOALA (Lyncee Tec SA, www.lynceetec.com) or a Fiji-based plug-in developed by our group [31, 102]. All bacterial data were recorded using a monochromatic 405 nm laser illumination source. DHM images of *E. gracilis* were acquired using the multi-wavelength implementation of the common path DHM instrument [124], using a 405, 520, and 625 nm laser illumination sources simultaneously.

Results

Figure 5.6 shows a raw hologram and background-subtracted hologram of a single *B. subtilis* bacterium (5.6A and 5.6B, respectively) and their respective Fourier spectra (5.6C and 5.6D). Figure 5.6E and 5.6F show the intensity reconstruction of the same bacterium using the raw hologram and background subtracted hologram, respectively, as well as vertical line plots of pixel values through the bacterium for both the raw and background subtracted reconstruction (5.6G and 5.6H, respectively).

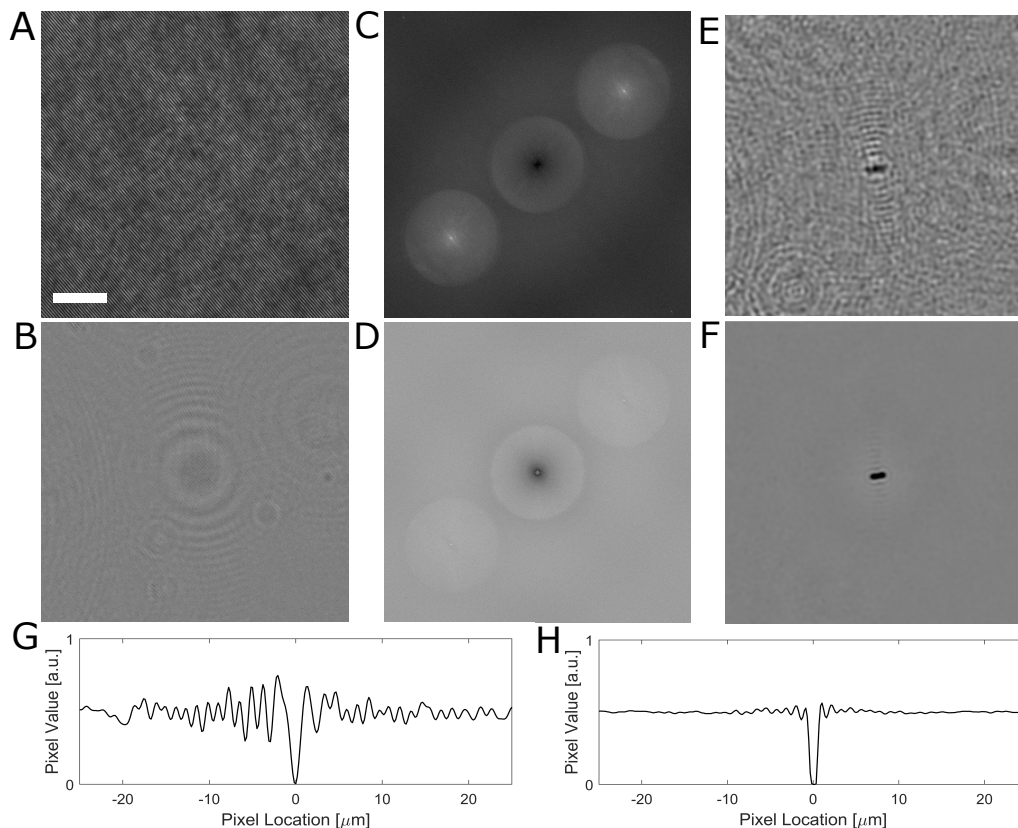


Figure 5.6 – Raw hologram of sample containing *B. subtilis* (A), the identical hologram after background subtraction (B), and their respective Fourier spectra (C and D). Intensity reconstruction of the same *B. subtilis* bacterium without (E) and with (F) the use of the residual fringe visibility analysis, as well as vertical line plots of pixel values through the bacterium (G and H, respectively). Scale bar represents 10 μm for (A, B, E, and F).

Employing the background subtraction technique on data sets containing *B. subtilis* saw an increase in SNR of roughly an order of magnitude (11x improvement in SNR).

Figure 5.7 shows a raw and background subtracted hologram of a select *V. alginolyticus* bacterium (Figure 5.7A and 5.7B, respectively), and their respective Fourier spectra (Figure 5.7C and 5.7D). Figure 5.7E and 5.7F show a single plane intensity reconstruction of the same hologram from 5.7A and 5.7B, respectively. These intensity reconstructions also demonstrate an order of magnitude increase in SNR. Figures 5.7G and 5.7H show a volumetric rendering of intensity reconstructions using the raw and background subtracted holograms, respectively. These volumetric renderings have been thresholded to the same value for comparison. The implementation of the background subtraction technique can be seen to increase the

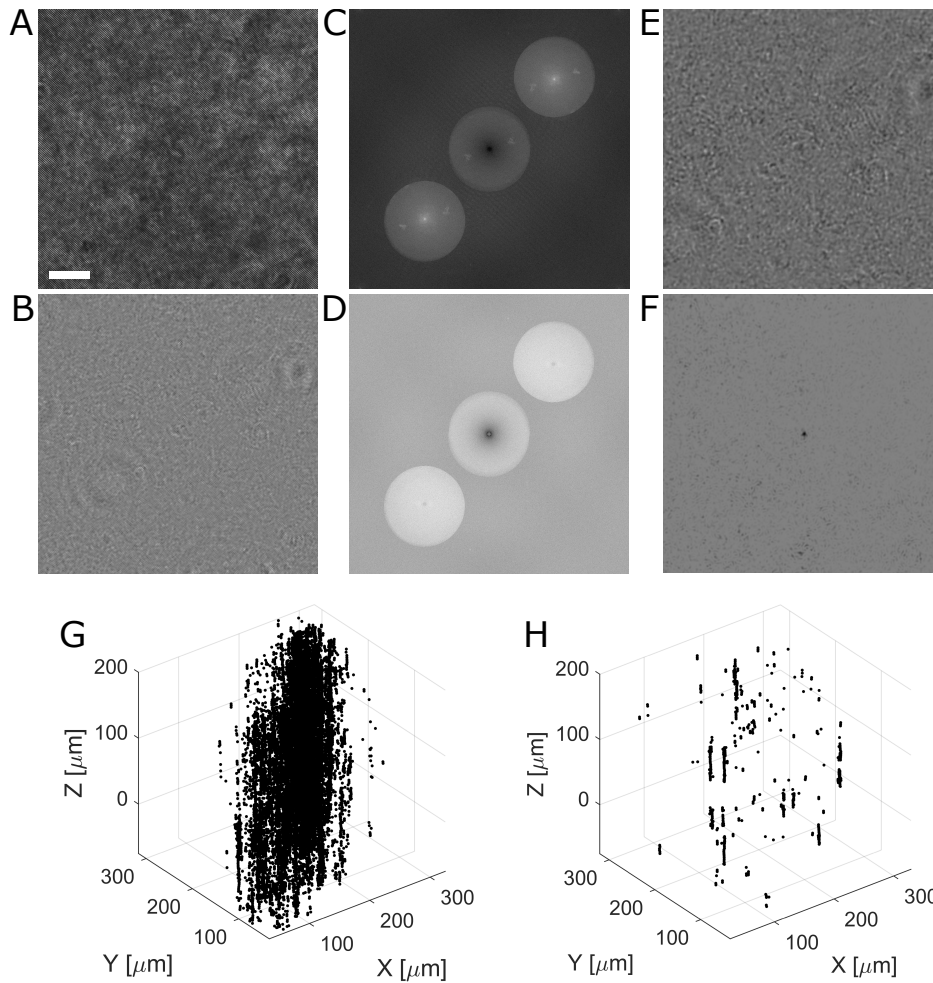


Figure 5.7 – Raw hologram of sample containing *V. alginolyticus* (A), the identical hologram after background subtraction (B), and their respective Fourier Spectra (C and D). Intensity reconstruction of the same *V. alginolyticus* bacterium without (E), and with (F) the use of the residual fringe visibility analysis, and a 3D rendering of the reconstructed intensity z-stack of the raw (G) and background subtracted hologram (H). Scale bar represents $10 \mu\text{m}$ for (A, B, E, and F).

SNR of volumetric intensity reconstructions to allow for the 3D localization of near diffraction limited objects such as *V. alginolyticus*. Due to the standard thresholding used in the volumetric renderings of 5.7G and 5.7H, vertical lines can be seen in Figure 5.7G, which are the residual artifacts of the point spread function of the *V. alginolyticus*. Downstream processing techniques, such as deconvolution, would be effective in removing such artifacts.

Figure 5.8 shows a raw and background subtracted hologram of multi-wavelength DHM data containing *E. gracilis* (5.8A and 5.8B), and their respective Fourier spec-

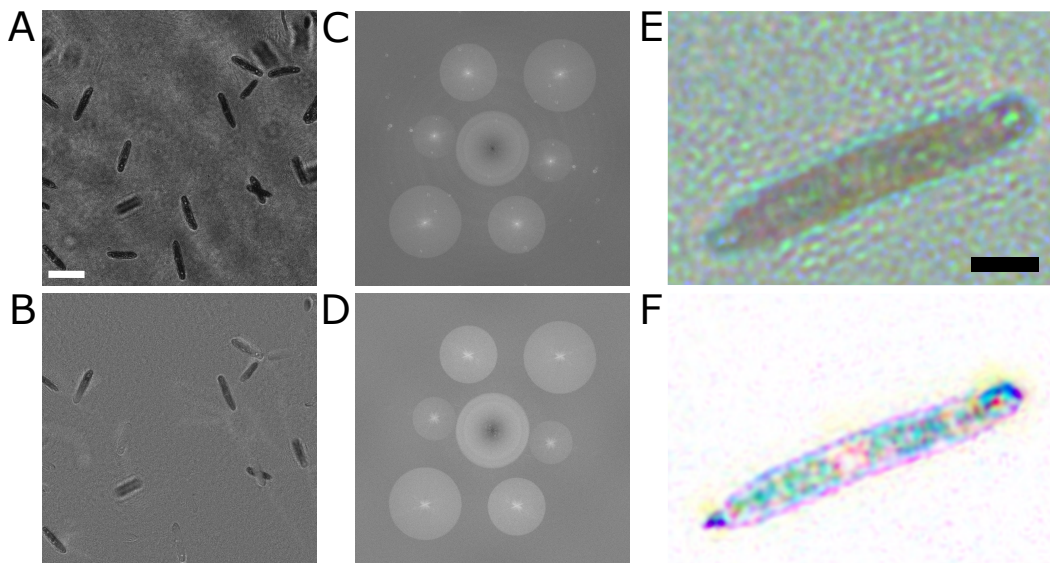


Figure 5.8 – Raw multiwavelength hologram of sample containing *E. gracilis* (A), the identical hologram after background subtraction (B), as well as their respective spectra (C and D, respectively). A pseudo-colored composite intensity reconstruction of a select *E. gracilis* using the raw hologram (E), and background fringe subtraction technique (F). Scale bar in (A) represents $50 \mu\text{m}$ for both (A and B). Scale bar in (E) represents $20 \mu\text{m}$ for both (E and F).

tra (Figure 5.8C and 5.8D). Figure 5.8E and 5.8F show a pseudo-colored composite intensity reconstructed image of a select *E. gracilis* using the raw and background subtracted hologram, respectively. The use of background subtracted holograms for multi-wavelength DHM data dramatically reduces the need for other post-processing unique to multi-wavelength data such as white balancing. Furthermore, the reduction in noise enables sub-cellular features of the *E. gracilis* to be much more visible, namely, the stigma (eyespot) and nucleus.

Concluding Remarks

This chapter discussed multiple software developments aimed at increasing the usability of DHM for both laboratory and field implementation. A major bottleneck of DHM has been the computational demands involved with numerically reconstructing the 3D information contained in a hologram. As DHM is capable of encoding 3D information within a 2D image, numerical reconstruction is required to extract the 3D information within a hologram, which is very computationally demanding. A single hologram is roughly 4 MB, and when reconstructed into a full 3D volume, becomes roughly 1.2 GB of data. Furthermore, this large data set size is difficult and time consuming to analyze manually. For these reasons, software methods were

developed to analyze these large data volumes autonomously.

A supervised machine learning-based tracking algorithm was developed and described in details which is capable of detecting and tracking diffraction limited particles through a large field of view of holographic data. This work was published in *AIMS Biophysics* [5]. This algorithm, once trained by an expert user, is capable of detecting and tracking micron sized bacteria through time, resulting in three-dimensional trajectories. This capability proves useful in the analysis of the motility characteristics of organisms on the micron scale in 3D, which is currently not well studied but of great interest to the microbiological community.

This machine learning algorithm, although autonomous, requires a great deal of computational resources, making it difficult to implement on field deployments, or any application where computational resources are limited. A novel method of enhancing image contrast of intensity reconstructions of digital off-axis holographic images is presented, including a theoretical justification, practical considerations in its implementation, and an experimental verification using biological samples. With roughly an order of magnitude of increased contrast provided by this method, standard image thresholding and clustering techniques become possible and enable high throughput and low computational overhead volumetric tracking. Furthermore, by conducting background subtraction on the raw holograms as opposed to the volumetric reconstruction, computational overhead is reduced proportionally to the number of axial planes reconstructed, potentially significantly decreasing computation times. It is critical to note that fringe stability is necessary for this approach to work. We implemented it using a common-path off-axis DHM designed to be stable against vibrations. With a traditional Mach-Zehnder interferometer, the fringes may not be stable on the timescales reported in this work. Thus, the fringe stability and resultant number of frames used for background fringe subtraction will need to be determined for each instrument and light source combination.

The software developments described in this chapter provide further enhancements of the capabilities of DHM for use in laboratory and field experimentation. The development of a machine learning tracking algorithm provides a seminal work in the application of machine learning in the tracking of micron-sized particles in three dimensions and further expands the applications of DHM for microbiological research. Furthermore, the development of a computationally light image contrast enhancement algorithm provides a reasonable path forward towards the ultimate goal of autonomous analysis of DHM data for field experimentation, or in any

application requiring quick analysis with minimal computational resources.

Chapter 6

GENETICALLY ENCODED PHASE CONTRAST AGENTS FOR
DHM

The following chapter describes work that was done in collaboration with the Mikhail G. Shapiro Group at the California Institute of Technology regarding the development and verification of gas vesicles (GV) as an optical phase contrast agent for targeted imaging in QPI. This work was submitted for publication in the peer-reviewed scientific journal PNAS [7] at the end of 2019, and was rejected in early 2020. After careful interpretation of the reviewer feedback, no fault was found with the fundamental science of the paper, only that it was not a good fit for the PNAS community. At the time of the writing of this thesis, the manuscript is being formatted for submission to the peer-reviewed journal Nano Letters, which I, along with the authors believe to be a better fit for this work. An explicit list of author contributions is provided in Appendix C.

First, the origins of GVs are introduced as well as the methods used to isolate them, their morphology, and the mechanisms involved with their ability of being optical phase contrast agents. GVs were then engineered to be expressed in salmonella cells. The phase contrast added to salmonella cells that express GVs are quantified and the usefulness of GVs as a phase contrast is verified.

Off-axis digital holographic microscopy offers many advantages to both in lab and field experimentation. A considerable advantage of off-axis DHM is its ability to conduct quantitative phase imaging (QPI). This imaging modality involves quantifying the phase value of the illuminating wavefront across the sample. This QPI image is directly proportional to the optical path length of the illuminating light source through the sample that is being imaged. This correlation has been verified by [96] and found to follow the trend

$$\Delta\phi = \frac{2\pi}{\lambda} h\Delta n, \quad (6.1)$$

where λ is the wavelength of the illuminating light source, h is the thickness of the object in the axial dimension, and Δn is the difference in index of refraction between the object and its surrounding medium.

DHM, along with other imaging techniques that are capable of QPI have been used in the study of microbial motility, chemotaxis, the flow of ions through ion channels, as well as the migration of cancer cells [41, 60, 63, 85, 92, 96, 109]. QPI is a relatively new, but very promising technique with applications in fundamental microbiological research as well as diagnostic medical imaging.

Equation 6.1 provides an expression for directly measuring the optical path differences introduced by an object of thickness h . In the case of imaging a microbial cell in an aqueous solution, $\Delta n = n_c - n_m$, where n_c is the index of refraction of the cell and n_m is the index of refraction of the aqueous solution (medium). Because typical values of n_c for the cytoplasm are ≈ 1.38 , or only 0.05 different from H₂O, a 1 μm -thick cell imaged at 405 nm is expected to show a phase shift of $\Delta\phi = 0.25\pi$, which can be difficult to resolve when considering the various sources of noise that are present in phase images [3].

Phase contrast agents and reporter genes could make smaller organisms visible or highlight subcellular features and processes, analogous to the role played by targeted small-molecule dyes and fluorescent proteins in fluorescence microscopy. Fluorescent molecules are part of every biologist's toolkit, with new agents continually being described to push the limits of specificity, resolution, and multiplexing [3, 80, 91, 128]. Unfortunately, these molecules are poor phase contrast agents due to their small and positive refractive index difference relative to water, which requires their loading at high concentration and contrast that is not easily distinguished from organelles or other dry material [30, 48, 90, 95]. An ideal phase contrast agent should have a more dramatically different index of refraction, and preferably one that is lower than that of H₂O in order to be categorically distinguishable from other cellular components.

Here, genetically encodable contrast agents for DHM, and QPI more broadly, are introduced. These genetically encodable contrast agents are based on a unique class of hollow protein nanostructures called gas vesicles (GVs). GV's are all-protein nanostructures natively expressed in a number of waterborne microorganisms as a means to regulate their buoyancy [93, 125]. GV's are gas compartments with dimensions on the order of 200 nm, enclosed by a 2 nm-thick protein shell (Figure 6.1A), which is permeable to dissolved gas, but prevents water from condensing into a liquid in the GV core. GV's have previously been described as contrast agents for ultrasound [106] and magnetic resonance imaging [43, 79, 107], but have not been applied to optical microscopy. Recently, the genes encoding GV's have been

heterologously expressed in commensal bacteria (e.g. *Escherichia coli* Nissle 1917 and *Salmonella typhimurium*) [22, 79].

In this work, we hypothesized that the large difference in the index of refraction of GVs' gaseous cores ($n = 1.0$) to that of water and cytoplasm ($n = 1.33$, $n = 1.38-1.42$) should produce excellent phase contrast for QPI. Unlike dyes or fluorescent proteins, GVs result in phase advancement producing positive phase contrast. We show that purified and clustered GVs result in the expected contrast under DHM. Using electron micrographs as a guide, we compared the predicted contrast in GV-expressing *S. typhimurium* with quantitative amplitude and phase reconstructions. GVs lead to a consistent subcellular pattern of positive contrast surrounded by bands of higher-index cell material. The GVs also create amplitude contrast. GV-expressing cells are readily distinguished from control cells, making GVs the first genetically encoded phase contrast agent. We also demonstrate contrast in mammalian cells by incubating cultured Chinese hamster ovary (CHO) cells with polyarginine-tagged GVs purified from *E. coli*. The cells take up GVs with a resulting membrane and endosomal labeling pattern.

This work provides a general tool for creating contrast in DHM in both amplitude and phase. GVs may be genetically expressed or purified with localization and/or affinity tags and incubated with the target cells. The availability of contrast agents will greatly expand the utility of QPI in cell biology and microbiology.

Results

Gas vesicles produce positive phase contrast

GVs purified from *Anabaena flos-aqua* are approximately 120-140 nm wide and 200-800 nm long (Figure 6.1A). Individually, purified GVs were too small to image on the common mode DHM, which uses $NA = 0.3$ aspheric lenses to achieve a spatial resolution of $0.6 \mu\text{m}$ (Figure 6.1B). In order to evaluate GVs as phase contrast agents, they were assembled into clusters by biotinylation followed by the addition of streptavidin. This yielded irregular clusters of 690 ± 56 nm in hydrodynamic diameter (Figure 6.1C). Holograms were collected of GV clusters and of comparably sized alumina beads (1524 ± 470 nm) suspended in phosphate-buffered saline (PBS). Holograms were reconstructed into amplitude and phase images using the commercially available software KOALA (See Appendix B). Both GVs and alumina beads appeared dark in amplitude images, while the phase shifts from the two samples were opposite in sign (Figure 6.1D). Measured phase shifts of GV

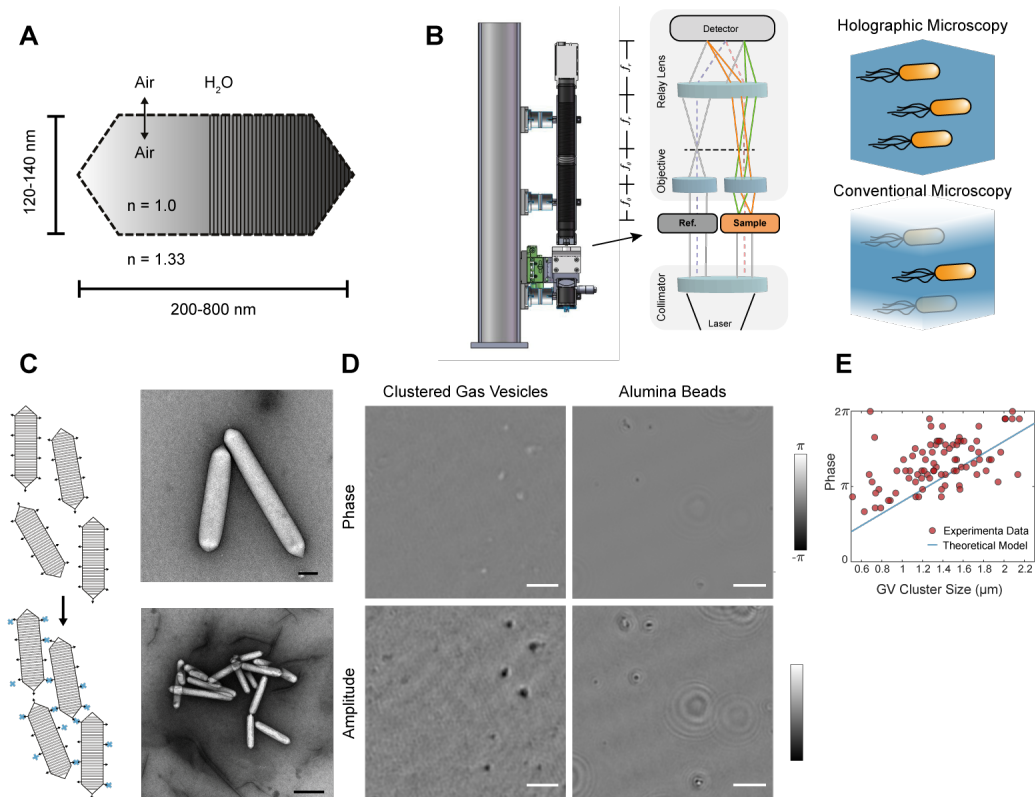


Figure 6.1 – Gas vesicles as phase contrast agents. (A) Schematic of a single GV. (B) Schematic of the DHM used in this work, and an illustration of the inherent volumetric imaging of DHM compared to conventional microscopy. (C) Biotinylated gas vesicles purified from *Anabaena flos-aquae* can be clustered using streptavidin. Shown are a schematic and representative transmission electron micrograph of biotinylated GVs (top) and clustered GVs (bottom). Scale bars 100 nm and 500 nm, respectively. (D) Representative phase and amplitude DHM images of clustered gas vesicles and alumina beads. Scale bars represent 25 μm . (E) Phase change observed from clustered gas vesicles as a function of approximate particle size. The theoretical model comes from Equation 6.1.

clusters were plotted against expected phase shifts for an equivalent air-filled bubble as calculated from Equation 6.1 (Figure 6.1E), showing good agreement. GV phase contrast can be erased by hydrostatically collapsing the gas vesicles, serving as a convenient internal control. This can be achieved by presenting gas vesicles to a pressure beyond their threshold [72], which open up their protein shelling and allow the gaseous core to rapidly dissolve in the solution.

Having identified gas vesicles as phase contrast agents, we sought to determine if phase contrast, in addition to a particle's fluid dynamics, can be used to detect them

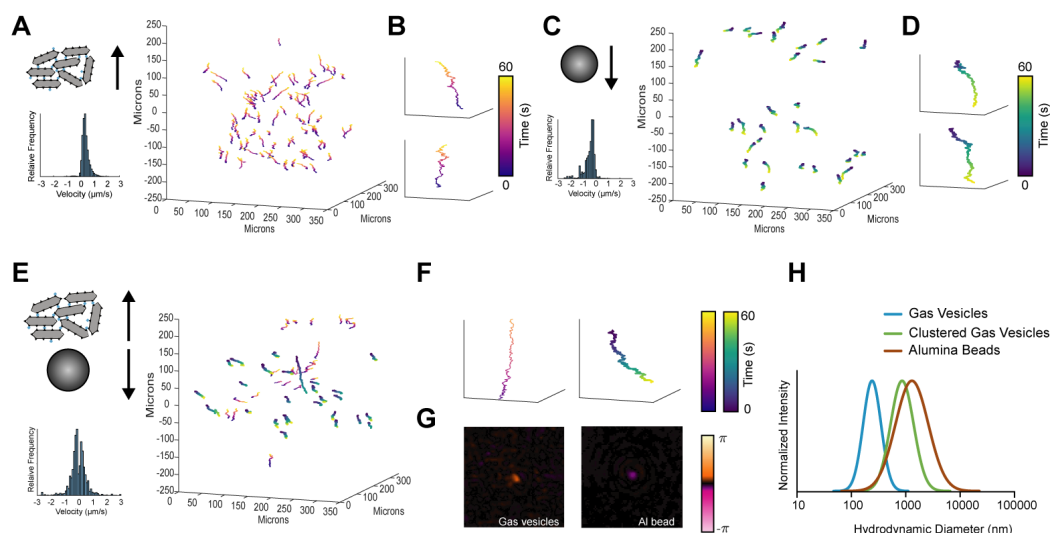


Figure 6.2 – (A) Clustered gas vesicles rise in solution, histogram of the z-component velocities of clustered gas vesicles, and 3D trajectory plots of tracked gas vesicles over 60 second. (B) Two example 3D tracks of clustered gas vesicles. Each trajectory is color coded with respect to time. (C) Alumina beads sink over time, histogram of the z-component velocities of alumina particles, and 3D trajectory plots of tracked alumina beads over 60 seconds. (D) Two example 3D tracks of alumina beads. Each trajectory is color-coded with respect to time. (E) Mixed population of gas vesicles and alumina beads showing two velocity histograms for gas vesicles and alumina beads, and 3D trajectory plots of the mixed population over 60 seconds. (F) Example trajectory of a rising and another of a sinking particle chosen at random. (G) Phase images of the two particles from F. The buoyant particle has a positive phase contrast while the particle sinking has a negative particle. Scale bars represent $5 \mu\text{m}$. (H) Representative dynamic light scattering of the hydrodynamic diameter of pristine gas vesicles, clustered gas vesicles and alumina beads.

in a mixed population. First, using QPI, we tracked the motion of both GV clusters and alumina beads in a 1 mm deep well. The average speed of GV clusters along the z-axis was $0.43 \pm 0.58 \mu\text{m/s}$ (95% C.I.) (Figure 6.2A) while alumina beads sank with an average speed (along the z-axis) of $-0.47 \pm 1.02 \mu\text{m/s}$ (95% C.I.) (Figure 6.2B). Next, both GV clusters and alumina beads were mixed together and tracked using DHM. In a mixed population, the GV clusters and alumina beads were readily distinguished (Figure 6.2C) with the particles that were rising having positive phase contrast and the particles that were sinking having negative phase contrast.

The measured rising and sinking velocities may be compared with values predicted

by balancing buoyant forces and Stokes drag. The net effect of buoyancy is

$$\mathbf{F}_B = \frac{4}{3}(\rho_p - \rho_m)\pi r^3 \mathbf{g}, \quad (6.2)$$

where ρ_p and ρ_m are the densities of the particle and the surrounding medium, respectively, r is the particle's radius, and \mathbf{g} ($\mathbf{g} < 0$) is the acceleration due to gravity. Here, the particle is assumed to be spherical and dominated by viscous forces. As a result, its Reynolds Number is expected to be far less than unity ($Re \ll 1$).

This assumption causes the effects of drag on the particle to be in a linear regime (Stokes drag) where the resistive force due to drag is $\mathbf{F}_d = 6\pi\mu r \mathbf{v}$, where μ is the dynamic viscosity of the medium and \mathbf{v} is the particle's velocity. Equating these two expressions allows for the settling velocity of a particle to be calculated as

$$\mathbf{v} = \frac{2(\rho_p - \rho_m)\pi r^2 \mathbf{g}}{9\mu}. \quad (6.3)$$

Using this equation, along with typical physical properties of air, water, and aluminum oxide (see Table A.4), the predicted velocities of GV clusters and alumina beads along the z axis are 0.29 ± 0.05 and -2.65 ± 1.50 $\mu\text{m/s}$, respectively. It is assumed here that both the GV clusters and alumina beads are spherical and that the alumina beads are solid and pure aluminum oxide, which are assumptions that are not necessarily true. From the electron micrographs depicted in Figure 6.1C, it can be seen that GV clusters are highly non-spherical. Similarly, the manufacturer of the alumina beads was not able to provide quantitative information on the quality or purity of their product. Furthermore, this model does not include stochastic events that effect settling velocities including but not limited to Brownian Motion.

GVs in mammalian cells

In order to label mammalian cells, the surface of GVs purified from *A. flos-aquae* were modified to include polyarginine (R8) sequences [72, 73]. This sequence is a mimic of the human immunodeficiency virus 1 trans-activating (HIV-1 TAT) peptide and allows tagged proteins to penetrate into cells (Fig. 6.3A) [26]. Polyarginine-modified GVs were purified and added to Chinese hamster ovary (CHO) cells at 114 pM for 45 minutes, washed and imaged by DHM. This allowed for rapid 3-dimensional reconstruction of GV location on the surface of and within the cells

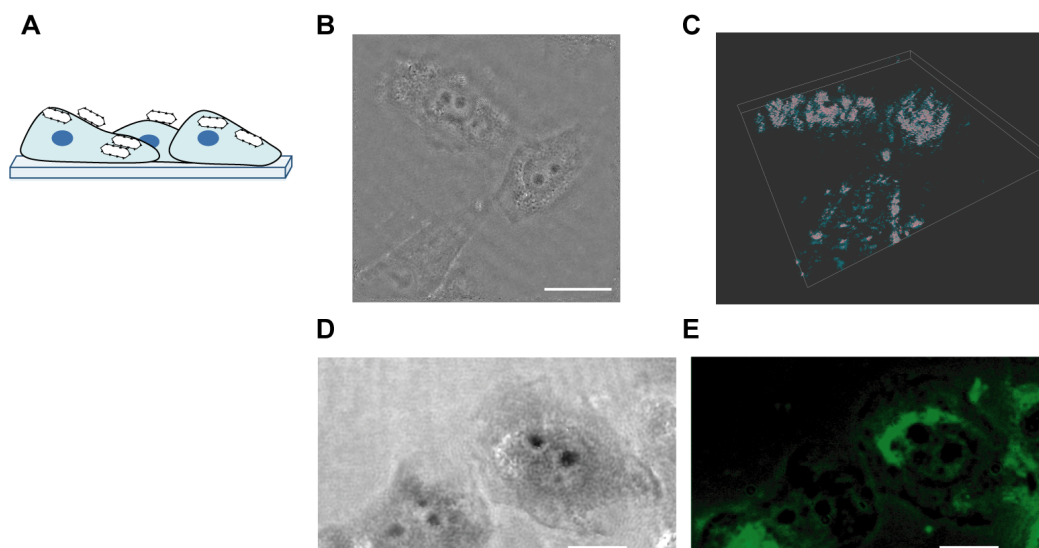


Figure 6.3 – DHM imaging of mammalian cells labelled with engineered gas vesicles. (A) The surface of gas vesicles can be genetically decorated with R8 peptides to label mammalian cells. (B) Chinese hamster ovary (CHO) cells labelled with polyarginine modified-gas vesicles and imaged using DHM. Scale bar represents $25\ \mu\text{m}$. (C) Pseudocolored 3D rendering of gas vesicles decorating CHO cells. See Appendix C for more information. (D) Phase image (scale bar represents $25\ \mu\text{m}$) of CHO cells transfected with GFP labeled GVVs under the high power DHM showing positive phase contrast in correspondence with (E) a high power fluorescence image (scale bar represents $25\ \mu\text{m}$) of the identical CHO cells.

(Figures 6.3B & 6.3C). GVVs were fluorescently labelled to confirm the location of GVV-labelling on the cells (Figure 6.3D and 6.3E).

GVVs as genetically expressed contrast agents in *Salmonella typhimurium*

Following the characterization of GVVs as DHM contrast agents, we tested the ability of genetically encoded GVVs to act as phase contrast agents in living bacteria. A recently developed GVV hybrid gene cluster, made by combining genes from *Anabaena flos-aquae* and *Bacillus megaterium* [23], was placed under the control of the acyl homoserine lactone- (N-(β -ketocaproyl)-L-homoserine lactone; AHL) mediated quorum sensing luxI promoter and used to heterologously express gas vesicles in *Salmonella typhimurium* (Figure 6.4A). In the presence of AHL, *Salmonella* expressed numerous GVVs, which were visualized under transmission electron microscopy and seen to typically cluster in two distinct subcellular regions (Figure 6.2B). We used this observed pattern to simulate the wavefront perturbations expected as light passes through a gas vesicle-expressing *Salmonella* cell. Simulated

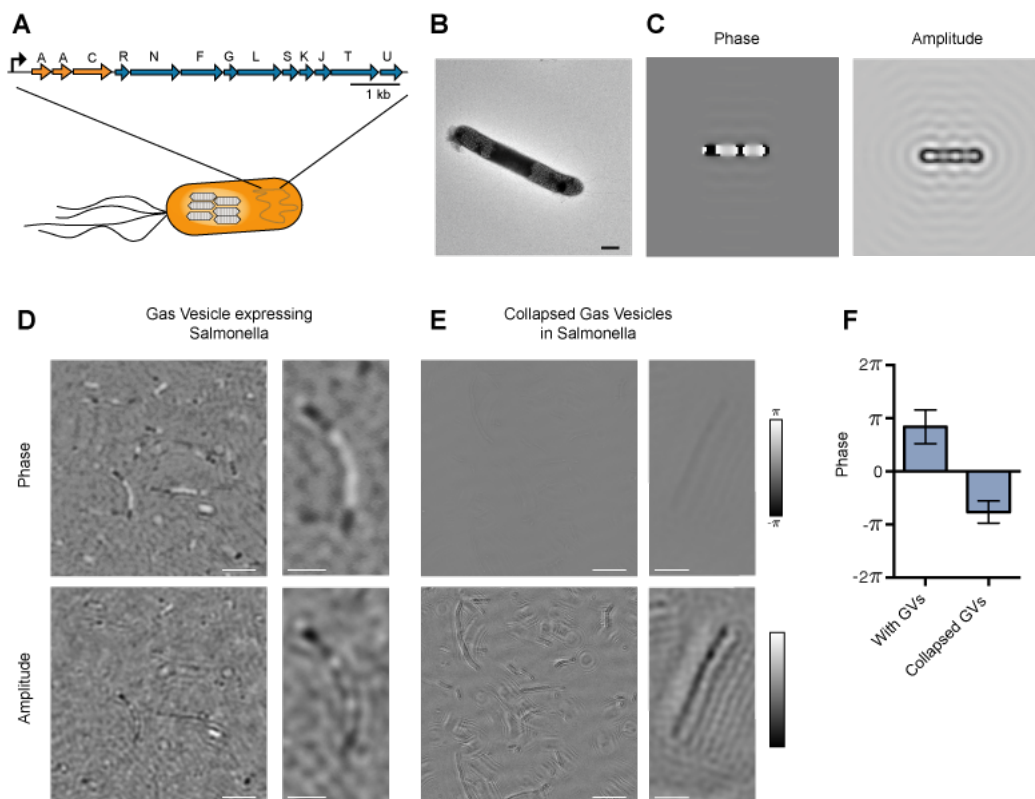


Figure 6.4 – GVs as genetically encoded phase contrast agents in *Salmonella*. (A) Schematic of engineered gas vesicle gene cluster comprising genes from *Anabaena flos-aquae* (orange genes) and *Bacillus megaterium* (blue genes) that enable heterologous expression of gas vesicles in *Salmonella typhimurium*. (B) Representative transmission electron micrograph of *S. typhimurium* expressing gas vesicles. Scale bar represents 1 μm. (C) Numerical simulation of phase and amplitude images of a GV-expressing *Salmonella* cell. (D) Representative phase and amplitude images of gas vesicles-expressing *S. typhimurium* cells under DHM. Example zoomed-in images are illustrated on the right. Scale bars for full field of view are 25 μm and 5 μm for the zoomed-in images. (E) Representative phase and amplitude images of GV-expressing *S. typhimurium* cells after collapsing GVs using 1.2 MPa of hydrostatic pressure. Scale bars for full field of view are 25 μm and 5 μm for the zoomed-in images. (F) Quantified average phase contrast from *S. typhimurium* cells with intact gas vesicles compared with collapsed gas vesicles ($n = 88$).

holograms were reconstructed into amplitude and phase images, showing distinct patterns of light and dark bands (Figure 6.4C).

Under DHM, GV-expressing *Salmonella* displayed similar features to the electron micrographs and simulations in both amplitude and phase. In amplitude images, regions containing GVs appeared darker than the surrounding cell. The correspond-

ing phase images showed lighter areas corresponding to the two subcellular regions of high GV concentration, with an observed phase signal within GV expressing Salmonella cells of 1.32 ± 1.00 radians (95% C.I.) (Figures 6.4D & 6.4F).

A convenient internal control was provided by collapsing the GVs within GV expressing Salmonella cells by exposing cells to hydrostatic pressure, which opens up the protein shell and allows the gas core to rapidly dissolve in the solution [72]. Upon collapse of gas vesicles, the positive phase contrast disappeared, resulting in a phase signal within GV expressing Salmonella cells after exposure to hydrostatic pressure of -1.13 ± 0.57 radians (95% C.I.) (Figure 6.4E & 6.4F).

By comparing phase images of GV expressing Salmonella cells before and after collapsing GVs, it was observed that GVs increase the average SNR of Salmonella cells in phase images by more than three times.

Concluding Remarks

Our results demonstrate that GVs may be used as contrast agents for QPI due to their large difference in index of refraction compared with water and cytoplasm. The gaseous core of GVs results in a phase difference that is in the opposite direction to typical organelles or minerals, resulting in positive phase contrast. This is especially beneficial for studying small samples such as microorganisms or subcellular features. Using the rapid volumetric image reconstruction of DHM, we have demonstrated the ability to robustly identify and track gas vesicles in a mixed solution containing alumina beads of a similar size. In addition, the modular protein make-up of gas vesicles enables protein engineering to confer novel properties for use as phase imaging nanoscale reporters. We have demonstrated that GVs fused to a cell-penetrating peptide confer subcellular phase contrast in cultured CHO cells. This may allow for rapid studies of cellular-nanoparticle interactions, or tracking of membrane dynamics and trafficking by tagging membrane proteins. Lastly, by introducing a newly developed heterologous hybrid gas vesicle gene cluster to bacteria, we can obtain genetically encoded phase contrast. These studies result in a QPI toolkit that will permit specific labeling in a large number of situations.

The methods and materials used for sample preparation and data processing for this section are described in detail in Appendix C

*Chapter 7***FIELD EXPERIMENTATION**

In order to validate the DHM field instrument (orangeBox), it was used in multiple field campaigns to various remote environments. These field campaigns to remote environments served multiple purposes. First, it provided a field campaign with remote and rough terrain that was a physical test of the field instrument. The field testing of technology is a large step in advancing a technology towards flight qualification for space travel. Secondly, the field sites visited represent extreme environments for life as we know it. Learning from life in these extreme environments not only sheds light on the robust nature of life, but helps advance the human race's understanding of fundamental biology.

Many parameters can cause an environment to be extreme for life as we know it. These factors include salinity, pH, temperature, pressure, liquid water availability, as well as oxygen concentrations. Table 7.1 summarizes the various parameters that can make an environment extreme as well as low/high thresholds for what would constitute an extreme environment. It is important to note that the specific values reported here are highly subjective and are meant only to provide qualitative and contextual understanding of what life as we know it might find to be extreme.

Environments with extreme concentrations of saline represent an extreme environment for life due to the fact that cells utilize various flavors of ion-gated channels across their membrane, which can become compromised in extreme concentrations of sodium [1]. Not only can salinity affect cellular ion-gated channel function, but extreme salinity can cause cell damage or death by plasmolysis and endosmosis due to high and low concentrations of sodium, respectively.

Environments with extreme pH represent an extreme environment for life due to the fact that environments of extreme pH (high or low) cause proteins denaturation. This prevents many cellular functions from functioning properly and can eventually lead to cell death.

Environments with extreme temperatures represent an extreme environment for life due to the fact that many chemical processes are temperature dependent. Many cellular functions rely on chemical diffusion to transport chemicals and nutrients throughout the volume of the cell. The time scales for these diffusive chemical

transport phenomena change dramatically as a function of temperature. Furthermore, temperature can affect the fluidity and permeability of cell membranes which can lead to cell damage and/or death [99].

Environments with extreme pressures represent an extreme environment for life due to the extreme physical stresses that can overcome the structural integrity of the phospholipid bilayers that compose the membrane of cells. Both extremely high and low pressures can cause cell damage by either causing the cell to collapse into itself or for the cell membrane to be torn apart.

Environments with no liquid water availability represent an extreme environment because virtually any biological process that has been studied thus far in human history has required the presence of liquid water to facilitate and or participate in the chemical reactions or biological processes that constitute life. Furthermore, we have come to realize that any place on Earth with available liquid water harbors life [53, 99, 105].

The known processes of cellular respiration all have one major thing in common: they involve the movement of electrons through some process which allows for the creation of a molecule that can be used as cellular energy. A common terminal electron acceptor in cellular respiration is oxygen. Other anaerobic metabolic pathways exist, but are far less energetically favorable, and thus environments with scarce amounts of oxygen represent an extreme environment due to the energetic limits it places on cellular respiration.

It is difficult to locate an environment on Earth that meets all of these criteria for an extreme environment. In addition, any such environment would be extremely dangerous for the scientists who intend to investigate it. Because of these and other logistical reasons, only a select few field sites have been visited in order to investigate the prevalence of microbial life and motility in extreme environments. Figure 7.1 shows the geographic locations that the DHM field instrument has been used to measure *in situ* microbial motility. The locations denoted with a red star are the locations that will be discussed in detail here.

The contents of this chapter are intended for publication along with results from other field campaigns. The field sites discussed in this thesis are sites that I was directly responsible for as I prepared for, attended, as well as collected and analyzed the data from these field campaigns.

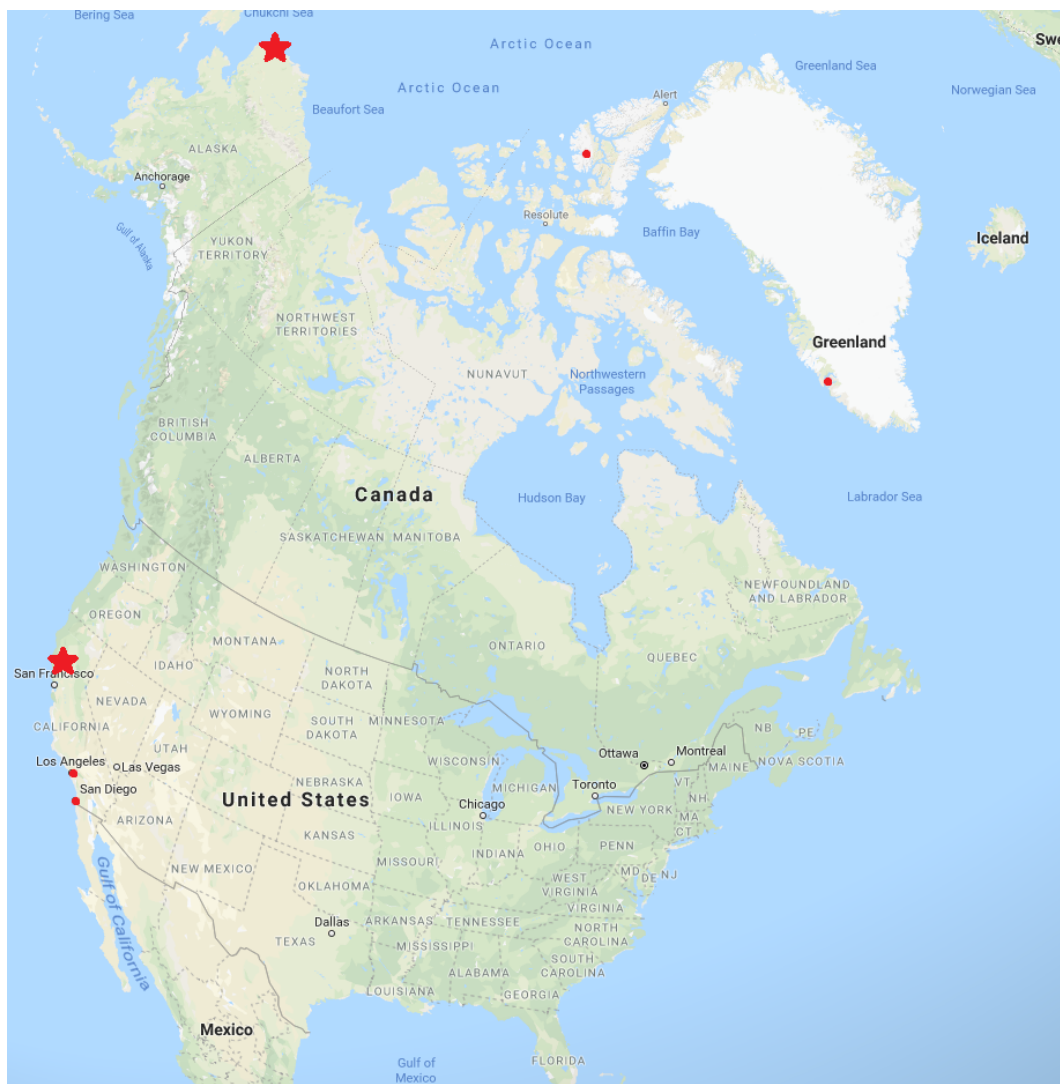


Figure 7.1 – Geographic locations that have been visited by the DHM field instrument

Table 7.1 – Conditions that would constitute an extreme environment

Environmental Parameter	Low Threshold	High Threshold
<i>Salinity</i>	<0.9%	>3.5%
<i>pH</i>	<5	>9
<i>Temperature</i>	<4°C	>40°C
<i>Pressure</i>	-	>200 atm
<i>Liquid water availability</i>	no liquid water	-
<i>Oxygen concentration</i>	≈1 ppm	-

7.1 Utqiagvik (Barrow), Alaska, USA

Utqiagvik (formerly Barrow), Alaska is the most northern point of continental North America as there exists no land mass in the continent above this point. This site represents an extreme environment for both the DHM field instrument as well as the microbial life there. Due to logistical difficulties related to travel to and from this location, the field instrument and all associated scientific equipment must have been shipped prior to the field campaign. This presented a large risk as the shipping process by a commercial freight company could cause irreparable damage to the components of any instrument by the mishandling of the package. Furthermore, the ambient temperature in Utqiagvik during the field campaign was approximately -5°C , which caused all polymeric components to become brittle. This exacerbated the fragility of all instruments involved with the field campaign, not only the DHM.

The conditions in Utqiagvik also present an extreme environment for microbial life due to temperature and salinity. During the field campaign, a total of three field samples were analyzed:

1. Sea ice brine
2. Seawater from the ice/ocean interface
3. Cryopeg brine

Sea ice brine is high salinity ($\approx 8.7\%$) liquid water that is trapped in micro-channels throughout sea ice. As seawater (salinity $\approx 3.5\%$) freezes, the crystalline structure of ice that forms causes the nearby remaining liquid water to increase in solute concentration. This concentration increase causes freezing point depression in the remaining liquid, which keeps it in its liquid state [75]. The sampled sea ice brine was at a temperature of -4.0°C . For a detailed description on the sampling method of these brine micro-channels see Appendix D. Sea ice brine represents an extreme environment for life due to its higher salinity than that of seawater as well as its sub-zero temperatures.

The ice/ocean interface was accessed via ice core drilling. Using sterile sampling procedures, liquid seawater (salinity $\approx 3.5\%$) from the interface was obtained. For a detailed description on the sampling method of seawater see Appendix D. Arctic seawater represents an extreme environment for life due to its cold temperatures.

Cryopegs are volumes of liquid water that have been encapsulated by permafrost when it was formed [32]. In much the same way as the sea ice brine micro-channels

are formed, as permafrost formed, smaller volumes of high salinity water remained, which were able to remain in the liquid state indefinitely due to their high salinity ($\approx 14.0\%$). The cryopeg sampled here was accessed via the Barrow permafrost tunnel (coordinates: 71.2944°N , 156.7153°W) and the brine was measured to be at -4.3°C . For a detailed description on the sampling methods of cryopeg brines, see Appendix D. Cryopeg brine represents an extreme environment for life due to its high salinity, low temperature, and complete isolation from any source of nutrients.

In these extreme environments, it was estimated that *in situ* active motility would be scarce, but present. As a result, sea ice brine samples were subjected to a salinity gradient in an attempt to induce microbial motility. These samples were subjected to a salinity gradient because the motility of marine bacteria are known to be a function of salt concentration [39]. In fact, levels of motility have been seen to increase as salt concentrations decrease. By establishing a salinity gradient such that a point source acts as a chemical sink, the local salt concentration within the field of view of the DHM can be decreased, thus inducing motility in the microorganisms present in the sample. Cryopeg samples were subjected to salinity gradients as well as thermal gradients in an attempt to induce motility. The thermal gradient experimental setup is detailed in Appendix C. In the following sections, only select data will be presented for brevity, however all data and associated images and videos can be found on the GitHub repository under the 'fieldData' directory [82].

Sea ice brine showed a wide variety of microbial life at low biomasses comprised of mostly prokaryotic cells. This low biomass is to be expected from an environment that is not only cold but at high salt concentrations. Even with the low biomass of the sea ice brine samples, motile eukaryotes were observed. Of the roughly 10^2 particles in the field of view of the instrument at any given time, less than 1 cell per data set was observed to exhibit motile characteristics. Of these motile cells, the average motility speed was observed to be $4.4 \mu\text{m/s}$.

By analyzing the organism's turning angle as a function of time, the frequency of reorientation of the organism was found. Two regimes of reorientation were quantified. The first being for turning angles between 45° and 135° , and the second being for turning angles between 135° and 180° . For more information on the method and implementation of quantifying reorientation time scales, see Appendix B. The timescale of reorientation for $45^\circ \leq \theta < 135^\circ$ is 2.10 seconds. Reorientations between 135° and 180° occurred once every 1.34 seconds on average.

Figure 7.2 shows a select trajectory of a motile microorganism found in sea ice brine

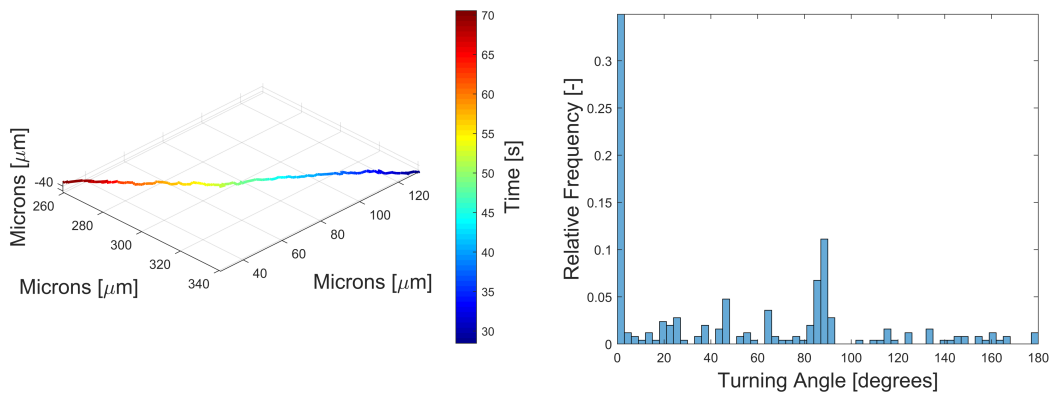


Figure 7.2 – Select trajectory plot (left) and histogram of turning angles from sea ice brine samples

samples as well as a histogram of its turning angles. From the visual inspection of the trajectory plot, it can be seen that the organisms exhibit sprinting characteristics where they swim in a single direction without drastic changes in direction, suggesting that this organism has a single polar flagellum.

Halotaxis experiments were performed on samples of sea ice brine by placing low salinity (3.5%) sterile agarose into a needle and allowing the formation of a salinity gradient within a sample of sea ice brine. A sufficiently dense agarose was used to allow the diffusion of sodium ions while preventing organisms from swimming into the needle, where imaging is not possible. No motile characteristics were seen throughout these experiments. Time-lapse data also showed no net aggregation or dispersion of biomass towards or away from the salinity gradient, respectively. It was the hypothesis of this experiment that a decrease in salinity near the needle tip would cause a measurable change in the motility of the microorganisms. The results of this experiment do not support this hypothesis, however, as no measurable change in motility was observed as a result of a local salinity gradient.

Liquid samples of seawater taken at the ice/ocean interface showed a much higher biomass and diversity of microbial life. These liquid samples contained both prokaryotic and eukaryotic microbial life. Motile single celled eukaryotes were observed with roughly spherical and ellipsoidal shapes with an average diameter on the order of 10-20 μm with an average motility speed of 19.7 $\mu\text{m/s}$. Prokaryotic motility was also observed in the ice/ocean samples. These cells were roughly spherical with an average diameter of approximately 1 μm and an average swimming speed of 106.3 $\mu\text{m/s}$. Figure 7.3 shows select trajectories of the heterogeneous

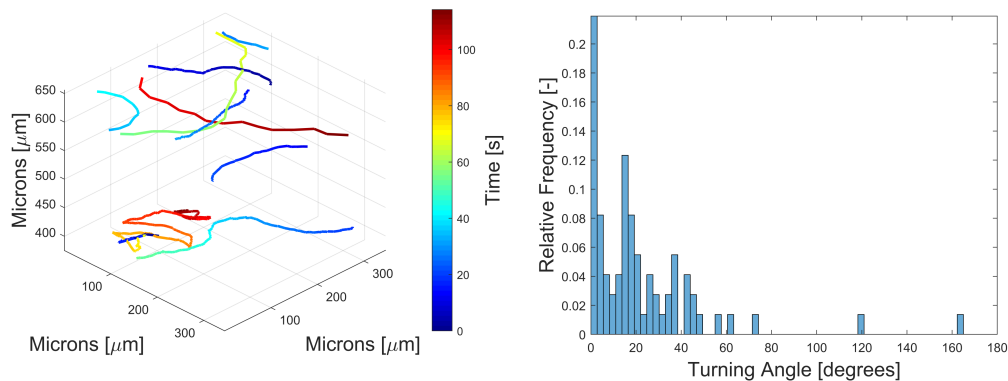


Figure 7.3 – Select trajectory plots of motile eukaryotic cells (left) and a histogram of turning angles of these cells (right) imaged from the ice/ocean interface

population of cells imaged from the ice/ocean interface.

A distinct difference was found in the motility characteristics of prokaryotic and eukaryotic organisms within the seawater samples with regards to their frequency of reorientation. Prokaryotes were seen to reorient themselves on timescales ranging between 5.16 to 5.87 seconds for angles between 45° and 135° , and between 6.67 and 9.82 seconds for angles between 135° and 180° . Eukaryotes, however, exhibited no detected reorientation. All eukaryotes were observed to swim in single directions with only minor changes in their direction of travel.

Samples taken from cryopeg brines were imaged directly after sampling, but no evidence of active motility was seen whatsoever throughout the eighteen data sets that were recorded over a total of four different samples. Each of the eighteen data sets consisted of a total of one minute of data captured at a camera frame rate of 15 fps. Samples were taken back to the laboratory in order to attempt to induce motility, but to no avail. Samples of cryopeg brine were subject to linear temperature gradients from 4.0°C to 32.0°C for approximately one hour. Discrete sections of the sample chamber were imaged corresponding to temperatures of 4.0°C , 7.5°C , 17.0°C , and 32.0°C . None of these temperatures showed any evidence of motility in the cryopeg brine sample.

Cryopeg brine samples were subjected to a salinity gradient by a point source of low salinity solution. A needle tip filled with low salinity (3.5%) sterile agarose was used to establish and maintain a salinity gradient within the field of view of the DHM while imaging took place. This caused no change in the observed motility characteristics of the cryopeg brine sample. Time-lapse data also showed no net

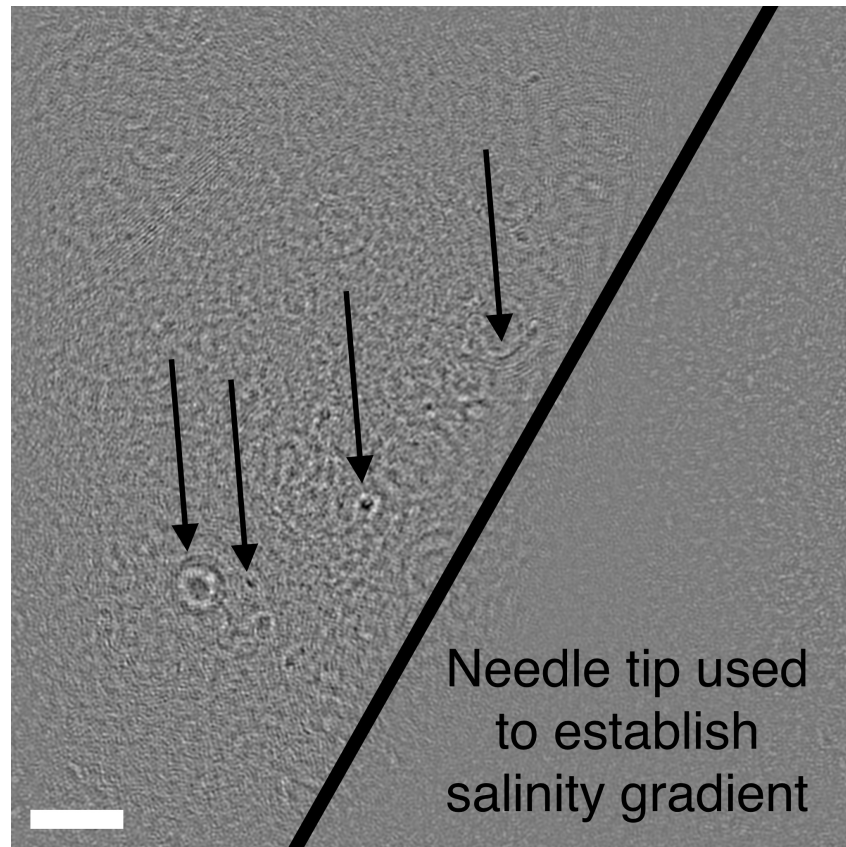


Figure 7.4 – Amplitude image of cryopeg brine showing a cylindrical object as well as three other non-spherical objects. Scale bar represents 20 μm .

aggregation or dispersion of biomass towards or away from the salinity gradient, respectively. However, due to the large salinity gradient, osmotic driven flow was established which brought multiple particles in the field of view that were roughly cylindrical, with one particle in particular having a diameter of roughly 1 μm and length of approximately 20 μm . This object, along with three other objects that were non-spherical, appear to have similar morphology to many cylindrical prokaryotic organisms and can possibly be a sign of life within the cryopeg (extant or extinct), even though no active motility was seen. Figure 7.4 show these potentially biological particles seen in the cryopeg brine.

Figure 7.5 provides a succinct summary of the scientific yield from the field campaign discussed in this section. Figure 7.5A shows a select trajectory of a motile microorganism found in sea ice brine samples. This image is a composite image rendered by the minimum pixel intensity projection of multiple images. The projected images show the organism's trajectory over 5 seconds. 7.5B shows select trajectory

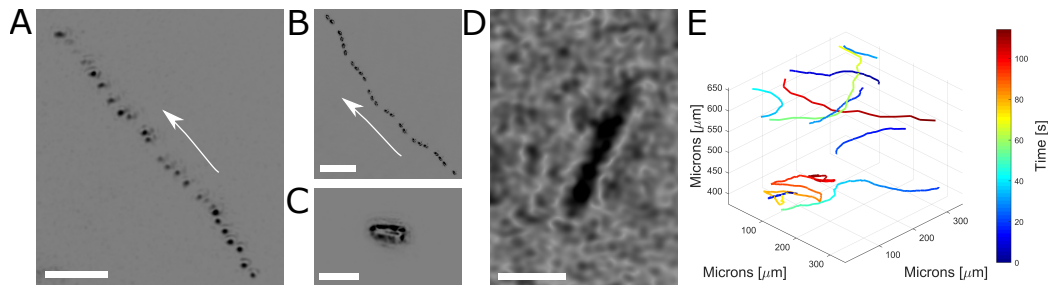


Figure 7.5 – *In situ* results from various field sites visited in Utqiagvik (Barrow), Alaska. (A) Select trajectory of a motile microorganism found in the sea ice brine sample. This image is a composite image rendered by the minimum pixel intensity projection of 5 seconds of data. Scale bar represents $10\ \mu\text{m}$. (B) Select trajectory of a motile microorganism found in the ice/ocean interface sample. This image is a composite image rendered by the minimum pixel intensity projection of 5 seconds of data. Scale bar represents $50\ \mu\text{m}$. (C) A single plane intensity reconstruction showing a select microorganism observed at the ice/ocean interface sample. Scale bar represents $10\ \mu\text{m}$. (D) A single plane intensity reconstruction of a particle that exhibits lifelike morphological features observed in the cryopeg brine sample. Scale bar represents $10\ \mu\text{m}$. (E) Trajectories of the heterogeneous *in situ* sample taken from the ice/ocean interface. This plot shows trajectories of multiple organisms within the field of view of the DHM instrument and is color-coded with respect to time.

of a cell imaged from the ice/ocean interface. This image is a composite image rendered by the minimum pixel intensity projection of multiple images. The projected images show the organism's trajectory over 5 seconds. Figure 7.5C shows a still intensity reconstruction of an organism found to be within the ice/ocean interface sample. Figure 7.5E shows trajectories of the heterogeneous *in situ* sample taken from the ice/ocean interface. Figure 7.5D shows a typical potentially biological particle observed in the cryopeg brine.

The work presented in this section not only represents the first time that I, or any of the DHM team visited Utqiagvik, but also the very first time that a sample of cryopeg brine has been imaged on the micron scale. The goal of this deployment was to further test the physical robustness of the orangeBox DHM instrument as well as to investigate the prevalence of microbial motility in extreme cold and saline environments. Samples from three field sites yielded positive measurements of motility from two of the three sites. Sea ice brine and seawater from the ice/ocean interface contained many motile microorganisms of various sizes, shapes, and motile characteristics. Cryopeg brine, being the most extreme of environments sampled

Table 7.2 – Field deployment summary from Utqiagvik 2017

<i>Sample Origin</i>	<i>Experiment Type</i>	<i>Temperature [°C]</i>	<i>Salinity [‰]</i>	<i>Motility [$\mu\text{m/s}$]</i>	<i>Number of Motile Cells</i>	<i>Number of Data Sets</i>
<i>Sea Ice Brine</i>	<i>in situ</i>	-4.0	8.7	(4.4, 9.5)	2	5
	Halotaxis	-1.0*	(3.5-8.7)^	-	-	3
<i>Seawater</i>	<i>in situ</i>	0.0	3.5	(13.1-165.9)	14	5
<i>Cryopeg Brine</i>	<i>in situ</i>	-4.3	14.0	-	-	18
	Thermotaxis	(4.0-32.0)^	14.0	-	-	3
	Halotaxis	-6.0*	(3.5-14.0)^	-	-	3

*Experiment conducted in temperature-controlled environment

^Taxis experiment. Values ranged between extremas

throughout this field deployment, showed no sign of active motility. There were objects that were imaged that morphologically resembled either extant or extinct life, but this cannot be considered a definite biosignature as some non-organic structures have been observed to self assemble into bio mimetic structures [49]. Table 7.2 summarizes the scientific results of the field deployment to Utqiagvik, AK in May of 2017.

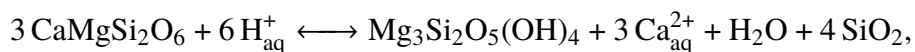
7.2 The Cedars, California, USA

The Cedars is an active serpentinization site in coastal Northern California, north of San Francisco. Serpentinization is a process in which water reacts with ultramafic minerals such as olivine and pyroxene, in order to produce other minerals such as serpentine, magnetite, as well as hydrogen gas and alkaline liquids [47, 113, 118]. The spring waters that emerge from this site have an extremely high pH (≈ 11.5), low redox potential (≈ -550 mV), and low ionic concentrations [118]. The high pH in addition to the low ionic concentration make this an exceptionally extreme environment for life. Even with these challenges, there is great macro- and microscale diversity within these ultrabasic springs. A multi-year study of liquid samples from three sites in The Cedars showed that even with varying geochemical factors from the three sites, there was sufficient bio-stability to conclude that these environments are capable of sustaining life [118].

This site has many factors that make it a very scientifically significant location. First, The Cedars is one of the few known land-based serpentinization sites in the world. Because this serpentinization site is fed by fresh spring water that is not of marine origin, it has a low salinity and sulfate concentration. Alkaliphiles are known to have the ability to use sodium ions instead of protons (hydrogen ions) as well as use sodium based ATPase in the generation of ATP [39, 118]. Due to the lack of sodium ions in the springs of The Cedars, an unknown mechanism are used by the microbial population in ATP generation.

Secondly, the low sulfate concentration results in a lack of electron acceptors in a liquid with a low redox potential. Electron acceptors (such as oxygen) play a key role in the process of cellular respiration, and in the Cedars it remains unclear what electron acceptors is used for this purpose.

Lastly, the spring water from the Cedars has a high pH due to the fact that it is a serpentinization site. At the Cedars, the particular serpentinization reaction has been investigated and characterized in [88] and found to be of the following general form:



where there are multiple intermediary reactions that are not shown.

This results in almost all free protons in the water to be used in the reaction. This lack of hydrogen ions in the resulting water causes the pH to increase dramatically. The known mechanisms of motility in non-marine prokaryotic life require the presence of free protons. This well-studied mechanism for prokaryotic motility, involves establishing and maintaining a proton gradient across their cell membrane which allows them to exploit the proton motive force as a means of conducting mechanical work (oscillate or rotate flagella). The lack of protons in the spring water from The Cedars makes the presence of motility in prokaryotic life of extreme significance and interest. Furthermore, only a select few marine bacteria are known to be able to use ions other than protons for the purposes of motility [4, 7, 62]. The known ion used by marine bacteria is sodium (Na⁺) [39], which is also scarce in the ultrabasic springs of The Cedars, hinting that the prokaryotic life in these ultrabasic springs utilize a potentially novel chemical pathway to facilitate motility.

Studies of *in situ* motility from spring water had not been done prior to this work due in part to: 1) the remote environment of The Cedars and 2) the very low biomass in the springs.

The DHM field instrument (orangeBox) was deployed to The Cedars in a multi-year field campaign, first in September of 2017 and second in October of 2018. The first field campaign was with the intentions of a general survey campaign. This being the first time any instrument has been used for the *in situ* investigation of motility at The Cedars, the goal was to shed light on whether microbial life native to these ultrabasic springs exhibited *in situ* motility or not. The following year's field campaign aimed at quantifying the particle concentrations within these springs. Using a modified experimental technique based on the work that was developed and published in

Astrobiology and the *Journal of Visualized Experiments (JoVE)* [11, 12], flow was established and maintained through the sample chamber of the DHM field instrument and subsequent images were recorded at a constant camera frame rate. With the statistical model that was developed, the particle concentrations of various springs were estimated. For more information on the experimental technique employed during this field campaign, see Appendix C. In the following sections, only select data will be presented for brevity, however references to all field data can be found on the GitHub repository under the 'fieldData' directory [82].

2017: General Survey

When conducting a general survey of samples from The Cedars in 2017, a total of two ultrabasic water springs were sampled at various locations. These springs are the Barns Spring 5 (BS5) (pH 11.5) and the Grotto Pool Spring (GPS) (pH 11.9).

Of the samples taken from these springs, this initial field deployment was able to image active microbial motility in BS5 as well as GPS samples. Prior to deployment, it was known that the expected biomass of these springs is to be low [118], which would make it difficult to image *in situ* motility in a short period of time. The unique advantage of DHM to conduct instantaneous volumetric imaging made imaging motility in low biomass samples possible.

At BS5, samples were taken directly from the spring, collected using pre-sterilized tubing. Among the samples taken directly from BS5, the biomass was extremely low made evident by the lack of particles in the field of view of the DHM instrument. The organisms that were seen to exhibit active motility characteristics were of sizes slightly below 1 μm in their longest dimension. These microorganisms exhibited motility speeds averaging $4.4 \pm 0.9 \mu\text{m/s}$.

Samples from BS5 exhibited a wide range of reorientation frequencies. By analyzing each organism's turning angle as a function of time, timescales were quantified which describe how often the organism turns with a certain angle range. Samples from BS5 exhibited timescales of reorientation with angles between 45° and 135° of 1.33 to 1.83 seconds. Timescales of reorientation between 135° and 180° varied between 2.60 and 7.82 seconds.

Figure 7.6 shows the trajectories of select organisms from the direct BS5 samples as well as a histogram of the turn angles of the organisms. This histogram of the turning angles as well as the trajectory plot shows the 'run and tumble' motility characteristics of the microorganisms.

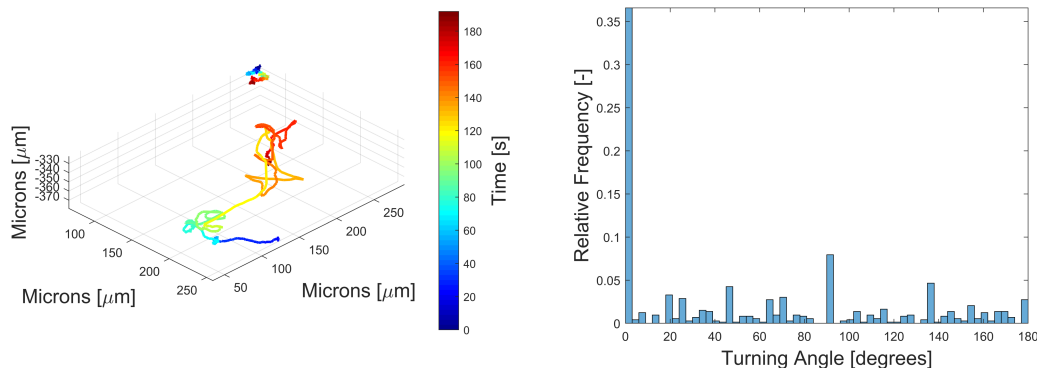


Figure 7.6 – Select microbial trajectories (left) and histogram of turning angles (right) of microorganisms from samples taken directly from BS5 (Top Pool).

At GPS, multiple samples were taken directly from the spring as well as from neighboring pools at the air/water interface. As with BS5, the samples taken directly from GPS exhibited very low biomass. Nevertheless, *in situ* motility was observed. The organisms observed to exhibit motile characteristics were all roughly spherical in shape and of sizes slightly below $1\ \mu\text{m}$ in their longest dimension. These microorganisms exhibited an average swimming speed of $3.2\pm 0.9\ \mu\text{m/s}$.

Samples from GPS exhibited a wide range of reorientation frequencies. By analyzing each organism's turning angle as a function of time, timescales were quantified which describe how often the organism turns with a certain angle range. Samples from BS5 exhibited timescales of reorientation with angles between 45° and 135° of 1.36 to 3.54 seconds. Timescales of reorientation between 135° and 180° varied between 3.72 and 18.68 seconds.

Figure 7.7 shows the trajectories of select organisms from GPS samples as well as a histogram of the turn angles of the organisms. This histogram of the turning angles as well as the trajectory plot shows the 'run and tumble' motility characteristics of the microorganism.

Samples were also taken from a neighboring pool to GPS referred to as the White Calcite Pool. A context image of the White Calcite Pool is shown in Figure 7.8.

This pool, contained large amounts of calcification due to its proximity to the spring as well as the fact that it is near the air/water interface. By absorbing carbon dioxide from the atmosphere, it is able to form calcium carbonate deposits. Samples from this pool exhibited more diverse motility characteristics. Run and tumble motility was seen as well as a single organism that exhibited a corkscrew motility pattern.

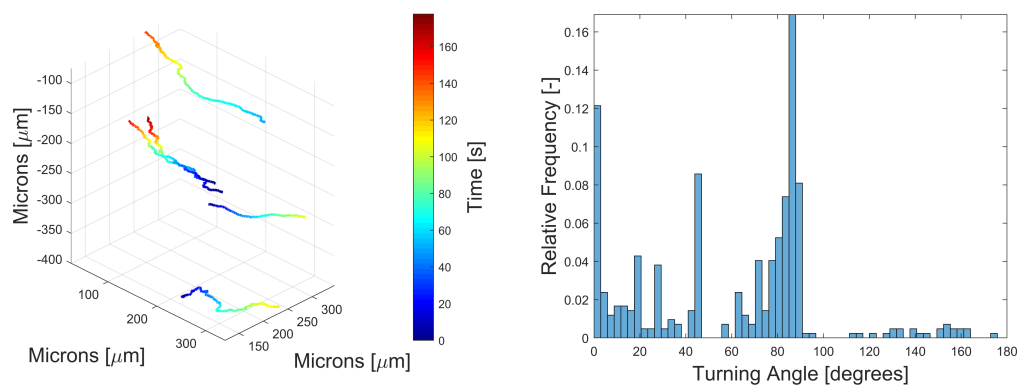


Figure 7.7 – Select microbial trajectories (left) and histogram of turning angles (right) of microorganisms from samples taken directly from GPS.



Figure 7.8 – Sample location near GPS called 'White Calcite Pool'

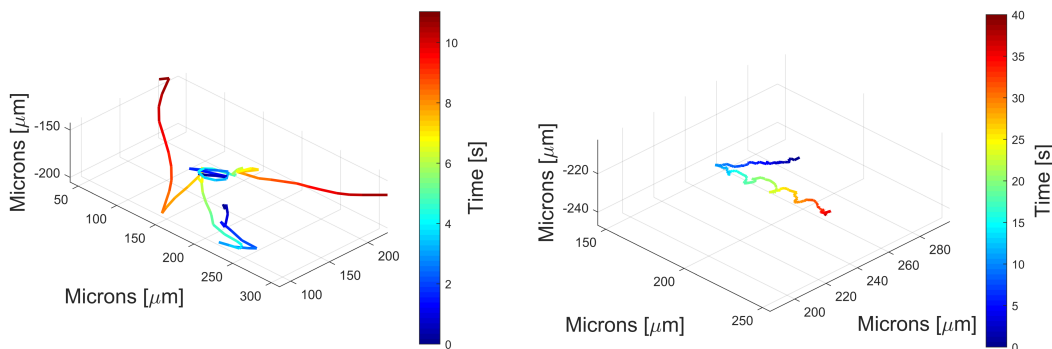


Figure 7.9 – Select microbial trajectories from the White Calcite Pool

Samples from WCP exhibited a range of reorientation frequencies. By analyzing each organism's turning angle as a function of time, timescales were quantified which describe how often the organism turns with a certain angle range. Samples from BS5 exhibited timescales of reorientation with angles between 45° and 135° of 1.09 to 2.03 seconds. Timescales of reorientation between 135° and 180° varied between 1.56 and 2.99 seconds.

Figure 7.9 shows trajectories of select microorganisms from the White Calcite Pool. The average swimming speed of the organisms in the White Calcite Pool was $27.4 \mu\text{m/s}$ with the range of organisms swimming at 4.0 to $56.4 \mu\text{m/s}$.

Another neighboring pool to GPS was sampled and referred to as the Orange Calcite Pool. Figure 7.10 shows a context image of the Orange Calcite Pool.

This pool did not exhibit the same levels of diversity in the types of motility present as the White Calcite Pool, however showed very active motility by the average motility speeds of the organisms being $62.0 \mu\text{m/s}$, with the fastest organism averaging speeds of $201.2 \mu\text{m/s}$.

Samples from OCP exhibited less diversity in the timescales for reorientation than samples from BS5, GPS, or WCP. By analyzing each organism's turning angle as a function of time, timescales were quantified which describe how often the organism turns with a certain angle range. Samples from BS5 exhibited timescales of reorientation with angles between 45° and 135° of 0.75 to 1.05 seconds. Timescales of reorientation between 135° and 180° varied between 1.55 and 2.33 seconds.

Figure 7.11 shows select trajectories of organisms from the Orange Calcite Pool sample as well as a histogram of turning angles, which shows the abundance of 'run and tumble' organisms in the sample.



Figure 7.10 – Sample location near GPS called ‘Orange Calcite Pool’

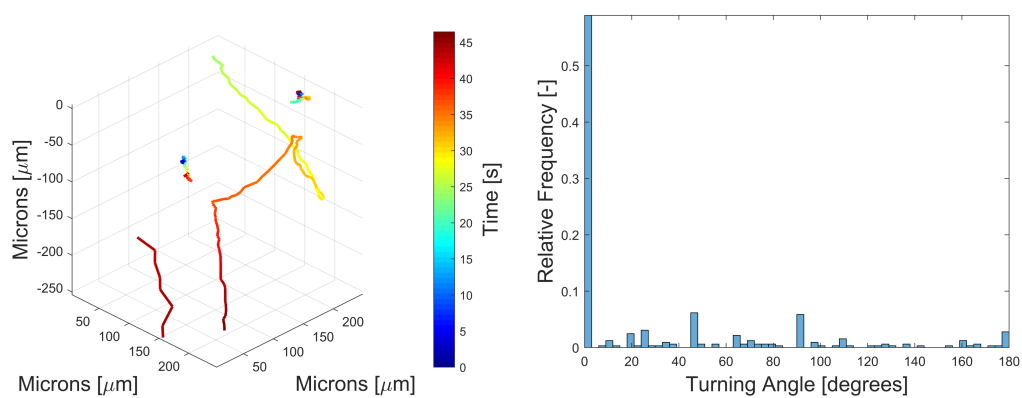


Figure 7.11 – Select trajectory plot (left) and histogram of turning angles (right) of microorganisms from samples taken from the Orange Calcite Pool

Table 7.3 – Field deployment summary from The Cedars General Survey 2017

<i>Sample Origin</i>	pH	Temperature [°C]	Motility [$\mu\text{m/s}$]	Number of Motile Cells	Number of Data Sets
Barns Spring 5	11.5	-	(3.3-8.7)	2	7
Grotto Pool Spring	11.9	-	(2.1-4.8)	6	9
White Calcite Pool	n/a	-	(4.0-56.4)	10	3
Orange Calcite Pool	n/a	-	(4.4-201.2)	4	1

Figure 7.12 provides a succinct summary of the scientific yield from this preliminary field campaign to The Cedars in 2017. Figure 7.12A shows an intensity reconstruction of select organism from the direct BS5 sample. Figure 7.12B shows the trajectories of select organisms from GPS samples. This image is a composite image rendered by the minimum pixel intensity projection of multiple images. The projected images show the organism's trajectory over 7 seconds. Figure 7.12C and 7.12D show trajectories of the heterogeneous *in situ* sample taken from the WCP. The average swimming speed of the organisms in the WCP was $27.4 \mu\text{m/s}$ with the range of organisms swimming at 4.0 to $56.4 \mu\text{m/s}$. Figure 7.12E shows select trajectories of organisms from the *in situ* OCP sample.

From the initial visit to The Cedars in the late summer of 2017, two ultrabasic springs were sampled: Barns Spring 5 and the Grotto Pool Spring. Both of these springs showed evidence of *in situ* active motility. Motility was observed in these samples without any sort of stimuli. Furthermore, the extremely low biomass of these springs did not prevent the orangeBox DHM from being able to successfully observe *in situ* active motility, which further shows its capability as a tool for the investigation of motility in extreme aquatic environments. Table 7.3 summarizes the scientific results of the field deployment to The Cedars, CA in September of 2017.

2018: Concentration Measurements

Following the general survey field campaign of 2017 to The Cedars, a return to the same location one calendar year later in 2018 was aimed at quantifying the concentration of microbial life in the ultrabasic springs of The Cedars.

Three springs were sampled and their respective cell densities were quantified. These three springs were the Grotto Pool Spring (GPS), Barns Spring 5 (BS5), and Mortar Bed Spring (MBS). The technique that was employed during this field campaign was inspired by the technique described in Chapter 4.3 as well as in the peer-reviewed journal *JoVE* [11]. This technique was altered slightly to accommodate the use of a peristaltic pump rather than a syringe pump. This change in the experimental

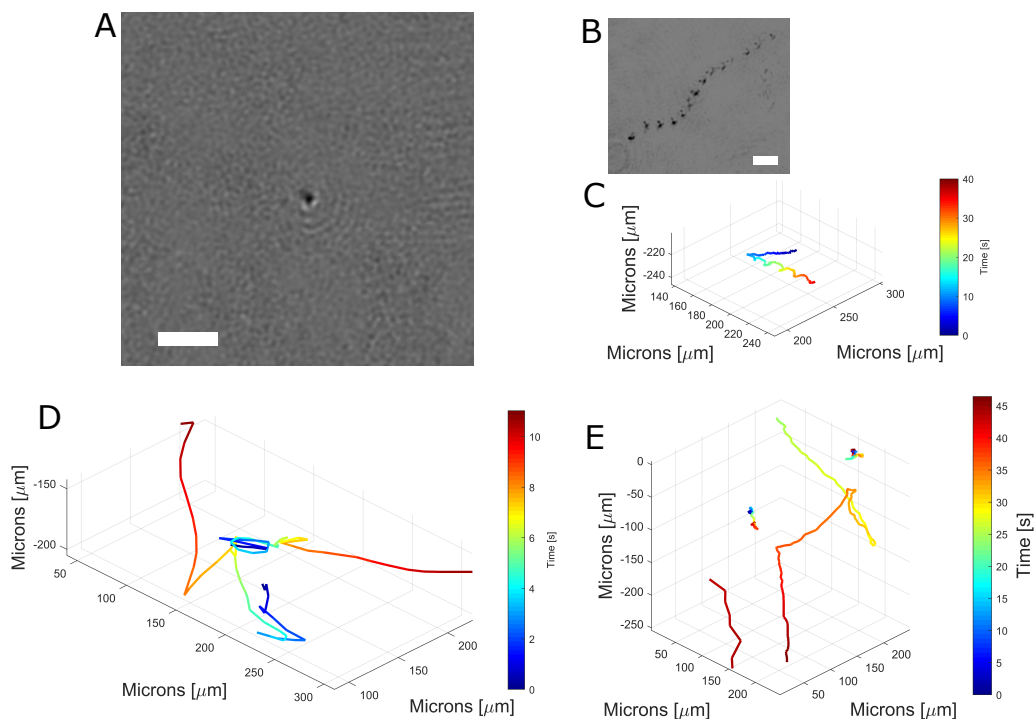


Figure 7.12 – *In situ* results from various field sites visited in The Cedars, California. (A) A single plane intensity reconstruction of a select micron-sized organism from the BS5 spring sample. Scale bar represents 10 μm . (B) Select trajectory of a motile microorganism found in the direct GPS spring sample. This image is a composite image rendered by the minimum pixel intensity projection of 7 seconds of data. Scale bar represents 10 μm . (C) A single trajectory of a micron-sized organism from the White Calcite Pool, which was volumetrically tracked through time. The plot shown is color-coded with respect to time. (D) Trajectories of the heterogeneous *in situ* sample taken from the White Calcite Pool. This plot shows trajectories of multiple organisms within the field of view of the DHM instrument and is color-coded with respect to time. (E) Trajectories of the heterogeneous *in situ* sample taken from the Orange Calcite Pool. This plot shows trajectories of multiple organisms within the field of view of the DHM instrument and is color-coded with respect to time.

Table 7.4 – Measured cell densities of ultrabasic springs at The Cedars

<i>Location</i>	Cell Density [cells/mL] (95% C.I.)	Flow Rate [mL/min]	Reynolds Number	Dean Number	Number of Replicates
<i>Grotto Pool Spring (GPS)</i>	257±69	0.46	5.48	0.93	7
<i>Barns Spring 5 (BS5)</i>	871±515	0.48	5.71	0.97	7
<i>Mortar Bed Spring (MBS)</i>	391±199	0.43	5.12	0.87	7

technique necessitated the use of a deformable reservoir that was plumbed less than ten pipe diameters after the peristaltic pump in order to attenuate the pulsations in flow introduced by the peristaltic pump. The use of a deformable reservoir is to absorb the excess momentum of the flow by converting that energy to strain energy in the deformation of the reservoir, which results in a steadier flow out of the reservoir. This technique was inspired by my undergraduate thesis where I was part of a team that worked with Blacoh Fluid Control, Inc., a company located in Riverside, CA that designs and manufactures pulsation dampener devices that are meant to attenuate unsteady flow that is caused by peristaltic pumps. My undergraduate thesis was aimed at designing an automated failure detection system for a specific model of pulsation dampener which involved the use of a deformable diaphragm. The resulting design of my undergraduate thesis was adopted by Blacoh Fluid Controls, Inc. and was used in the subsequent model of that particular pulsation dampener. For more information about the experimental technique developed for this field campaign, see Appendix C. My undergraduate thesis is available electronically in the GitHub repository under the ‘underGradThesis’ directory [82].

Each spring was imaged at an appropriate camera frame rate at 60 second intervals. Each spring was imaged a total of seven times resulting in roughly 6,000 holograms per spring, equating to roughly seven minutes of real time data per spring.

The measured cell densities of each of the three springs is tabulated in Table 7.4. From this table, it can be seen that the cell density measurements from BS5 are not nearly as constant as the other springs. This was noticed at the time of data collection because it was seen that there would be discrete bursts of cells passing through the field of view of the DHM instrument followed by a period of far less cells passing through the field of view. This can be due to many unverified factors. A possible explanation is that the bursts of cells passing through the DHM are cells that become dislodged from a biofilm that is growing at some location deeper in the spring.

The cell densities measured at the three springs are in very close agreement to the work that was done, not only during the general survey work of 2017, but from the previous years of work done by other institutions and research groups. This is based on qualitative comparisons, however, as no other research team has attempted to quantify the cell densities in the ultrabasic springs of The Cedars.

The cell concentrations of the three springs, being on the order of 10^2 cells/mL present further validation of DHM's usefulness in the investigation of *in situ* motility in extreme aquatic samples, by not only being a useful tool for investigating motility, but also being capable of extracting relevant sample information such as cell concentrations in a short period of time without the need for traditional culture methods. Traditional methods of cell quantification of field samples are difficult because plate cultures are only capable of counting microbial concentrations in units of culture forming units (CFU) per mL. This implies that the microbial population in the sample is culturable in the first place, which is not necessarily true for extreme field samples as the nutrients required by field samples in order to form cultures are often unknown.

Concluding Remarks

Throughout the course of this thesis, development and analysis of DHM instruments has been presented. Much attention has been paid to the design of an instrument that would be capable of investigating *in situ* microbial motility in extreme aquatic environments. This chapter discussed the deployment of the orangeBox DHM field instrument to two extreme locations in North America. These extreme locations are Utqiagvik, Alaska and The Cedars, California. Although the orangeBox DHM has been deployed to many other extreme environments around the world, only these two locations were discussed here because these were field sites I was directly involved with. Other locations visited with the orangeBox DHM include: Nuuk, Greenland, Death Valley, CA, Ireland, and Axel Heiberg Island, Canada.

A total of three field samples were collected from Utqiagvik including sea ice brine, seawater from the ice/ocean interfaces, as well as cryopeg brine. These samples represent extreme environments for life due to the cold temperatures and high salt concentrations of the samples. Active *in situ* motility was observed in both sea ice brine as well as seawater from the ice ocean interface. Experiments were performed in an attempt to increase levels of motility in sea ice brine by establishing and maintaining salinity gradients, but showed no measurable change in levels of motil-

ity. Samples of cryopeg brine showed no evidence of *in situ* motility whatsoever. Experiments were performed in an attempt to induce motility in cryopeg brine samples with salinity and temperature gradients, but to no avail. Multiple objects were observed from cryopeg samples that had morphological features consistent with microorganisms, but morphology alone is not a sufficient biosignature for detecting extant or extinct life.

The Cedars CA, was visited twice in a multiyear field campaign to survey and quantify bacterial populations of multiple ultrabasic springs. This site represents an extreme environment because of the low sulfate concentration, low redox potential, and ultra high pH of the spring. First, in 2017 a general field survey shed light on the prevalence of microbial motility in ultrabasic fresh water springs. Of two springs that were sampled (BS5 and GPS), active *in situ* motility was observed from both springs. Samples were also taken by the nearby pools of GPS at the air/water interface. From these pool samples, a higher biodiversity was observed as well as larger percentage of motile organisms, including larger eukaryotic cells. Second, in 2018 a return trip to The Cedars shed light on the concentrations of microscopic life from the ultrabasic springs of The Cedars. Three springs were analyzed during the 2018 field deployment: Barns Spring 5, Grotto Pool Spring, and Mortar Bed Spring. The quantification of biomass in these springs showed that each spring contains concentration on the order of 10^2 cells/mL. These low levels of biomass are consistent with other field deployments where iterative sample filtering was required in order to collect enough biomass for subsequent analysis such as genomic analysis.

The Cedars represents a highly relevant astrobiological analogue site due to its extreme environment. Due to the particular conditions at this field location, microbiologists involved with investigating this site expect to find novel metabolic pathways in the life that resides in these ultrabasic springs. Current work is being devoted to the incubation of direct field samples with various chemical enrichments in order to understand biological influences on the microbial population found in the ultrabasic springs. Enrichments with various amino acids, nucleic acids, carbon substrates, and electron acceptors will shed light on the chemical processes employed by the bacteria found in the ultrabasic springs. DHM will be used to image these various enrichments to investigate motility as a function of chemical enrichment. In addition to targeted experiments on field samples, chemotactic experiments using calcium, sodium, and potassium ions on bacterial isolates from The

Cedars can shed light on the fundamental mechanisms employed by the bacteria in order to be motile. This work will not only expand our understanding of life, but further demonstrate DHM's capabilities as a tool for targeted research in the field of microbiology.

Chapter 8

CONCLUSIONS

"It is not enough to be busy. So are the ants. The question is: What are we busy about?"

- Henry David Thoreau

Throughout the course of one's thesis, it is not uncommon to become consumed by the immediate work at hand, spending every waking moment on a new data analysis algorithm or perfecting an experimental technique. It can be difficult to force oneself to take a step back and ask, 'Why am I doing this?'

I often found myself wondering why I'm undertaking such a demanding program as a Ph.D., and I have time and time again been pleased (and relieved) to have a satisfactory answer. These satisfactory answers came in the form of potential fields of study and applications for off-axis DHM.

This thesis described the development of both hardware and software techniques for an off-axis digital holographic microscope in order to accomplish the high-level goal of one day being used in the search for extraterrestrial life, but also explored more immediate Earth-based applications as a microbiological scientific tool to conduct sophisticated and targeted experimentation. First, an in-depth analysis of the problem that is to be addressed was presented as well as a survey of the current state of the art in instruments that can shed light on this problem. The solution as developed in this thesis was then introduced with explicit definitions of the expected scientific and engineering capabilities of the instrument. The instrument was described in detail including the theoretical operating principle, hardware and software development, as well as the experimental verification of its performance. Next, laboratory experiments were introduced with the instrument involving the development of a novel optical phase contrast agent for the targeted increase in optical phase contrast of samples. Lastly, field experimentation with the instrument were introduced where the instrument was used for the *in situ* study of liquid samples in multiple remote and extreme environments. The development of this instrument as well as development of novel laboratory and field experimentation techniques have open the doors to a wide range of potential applications of DHM that are all very exciting and emerging fields.

In the years of development of this project, I have kept a list of possible applications and ideas for the devices and technologies developed in this thesis. These ideas, among other reasons, are what give my thesis, and my years of hard work, purpose to me.

The application of this work that I see as the most impactful to our way of life is its potential use in the medical field. As an instrument that has proven itself to have sub-micron resolution so that it can readily resolve bacteria as well as be much more sensitive than traditional optical microscopy, a DHM can be used as a rapid and autonomous means of identification of infectious disease in the human body. Furthermore, the development of a machine learning-based identification algorithm shows possibility of not only detecting bacteria in the human body, but also possibly being able to classify them.

The work presented in this thesis related to the use of gas vesicles (GV) as a phase contrast agent shows the potential use of DHM in addition to GVs to be a much more biocompatible contrast agent for diagnostic imaging. Quantitative phase imaging (QPI) is still a developing, but rapidly growing, field. The use of GVs in conjunction with DHM shows promise as a seminal work in the development of targeted optical phase contrast agents.

The DHM field instrument, as well as its use in remote and extreme environments such as The Cedars CA to quantify particle concentrations shows the potential for its use as a device that can actively monitor the water quality of various bodies of water. Using the low-level particle detection algorithm to rapidly detect particles, this can provide real time as well as high temporal resolution data on bacterial concentrations in fresh water reserves and other bodies of water, on the time scales of days, weeks, months, and even years.

Extending out of the medical or biological fields entirely, the technological developments related to DHM and described in this thesis can be applied to fundamental research related to fluid flow visualization on both the micro and macro scale. This thesis has shown that off-axis DHM is capable of tracking near-resolution-limit-sized objects, such as GV clusters and alumina beads across a very large depth of field. If these objects were subjected to a flow, the tracks can be used to reconstruct the flow field through the field of view of the DHM. This can be kept on the micron spatial scale by directly using the instruments described in this thesis, or these techniques can be applied to larger scale instruments to visualize flows on a much larger spatial scale (e.g. wind tunnels). Furthermore, the high sensitivity of the DHM allows for

its application as a quality control device in commercial manufacturing facilities that process liquids. For example, the pharmaceutical industry relies heavily on sterile and particulate free water in the manufacturing of certain chemicals. DHM can be used as an in-line and real-time method of monitoring water quality at such facilities.

These potential applications are not without their share of obstacles, however. There are many areas of work that must still be addressed in order to develop these ideas further. The theoretical analysis of phase noise as well as the experimental analysis of the effects of sample chamber design and substrate type on holographic image quality has shed light on not only the sources of noise in a typical hologram, but also the degree to which they affect the quality of a holographic image. Development into the attenuation of these sources of error can lead to high SNRs which will allow the use of lower computational overhead algorithms to accomplish particle identification and tracking. Furthermore, the high image quality will make DHM a more attractive imaging modality to the microbiological research and medical communities. In addition, efforts in the application of GVs as an optical phase contrast agent represents a seminal work, as a result further development and even cross-validation is necessary to confirm and develop its use as a contrast agent.

Lastly, the preliminary research that has been conducted with the DHM field instrument has shed light on just how little we know about the *in situ* behavior of bacteria and other microscopic organisms in extreme environments. This instrument, as well as the development and use of this instrument in more sophisticated and targeted laboratory experimentation can not only shed light on the behaviors of microscopic life but also help us understand various fundamental mechanisms of cellular respiration and motility.

BIBLIOGRAPHY

- [1] William S Agnew. Voltage-regulated sodium channel molecules. *Annual review of physiology*, 46(1):517–530, 1984.
- [2] Tanvir Ahmed, Thomas S Shimizu, and Roman Stocker. Bacterial chemotaxis in linear and nonlinear steady microfluidic gradients. *Nano letters*, 10(9):3379–3385, 2010.
- [3] Milka Atanasova, Galina Yordanova, Ruska Nenkova, Yavor Ivanov, Tzonka Godjevargova, and Dinko Dinev. Brewing yeast viability measured using a novel fluorescent dye and image cytometer. *Biotechnology & Biotechnological Equipment*, pages 1–11, 2019.
- [4] Tatsuo Atsumi, Linda McCartert, and Yasuo Imae. Polar and lateral flagellar motors of marine vibrio are driven by different ion-motive forces. *Nature*, 355(6356):182, 1992.
- [5] Yoon-Sung Bae, Jong-In Song, and Dug Young Kim. Volumetric reconstruction of brownian motion of a micrometer-size bead in water. *Optics Communications*, 309:291–297, 2013.
- [6] Corien Bakermans, Alexandre I Tsapin, Virginia Souza-Egipsy, David A Gilichinsky, and Kenneth H Nealson. Reproduction and metabolism at -10 °C of bacteria isolated from siberian permafrost. *Environmental Microbiology*, 5(4):321–326, 2003.
- [7] Sonia L Bardy, Sandy YM Ng, and Ken F Jarrell. Prokaryotic motility structures. *Microbiology*, 149(2):295–304, 2003.
- [8] P Baudoz, Y Rabbia, and J Gay. Achromatic interfero coronagraphy-i. theoretical capabilities for ground-based observations. *Astronomy and Astrophysics Supplement Series*, 141(2):319–329, 2000.
- [9] P Baudoz, Y Rabbia, J Gay, R Burg, L Petro, P Bely, B Fleury, P-Y Madec, and F Charbonnier. Achromatic interfero coronagraphy-ii. effective performance on the sky. *Astronomy and Astrophysics Supplement Series*, 145(2):341–350, 2000.
- [10] Manuel Bedrossian, Edmond Taslakian, George Eckert, and Kameron Johnson. *Dampener Charge Monitoring and Control System: Final Design Report*. Department of Mechanical Engineering, University of California Riverside, 2015.
- [11] Manuel Bedrossian, Casey Barr, Chris A Lindensmith, Kenneth Nealson, and Jay L Nadeau. Quantifying microorganisms at low concentrations using

- digital holographic microscopy (dhm). *JoVE (Journal of Visualized Experiments)*, (129):e56343, 2017.
- [12] Manuel Bedrossian, Chris Lindensmith, and Jay L Nadeau. Digital holographic microscopy, a method for detection of microorganisms in plume samples from enceladus and other icy worlds. *Astrobiology*, 17(9):913–925, 2017.
- [13] Manuel Bedrossian, Jody W Deming, and Jay Nadeau. Methods for collection and characterization of samples from icy environments. In *Methods in Microbiology*, volume 45, pages 293–321. Elsevier, 2018.
- [14] Manuel Bedrossian, J. Kent Wallace, Eugene Serabyn, Lindensmith Christian, and Jay Nadeau. Enhancing final image contrast in off-axis digital holography using residual fringes. *Submitted to Optics Express*, 2020.
- [15] Charles R Bentley and Bruce R Koci. Drilling to the beds of the greenland and antarctic ice sheets: a review. *Annals of glaciology*, 47:1–9, 2007.
- [16] Waheb Bishara, Uzair Sikora, Onur Mudanyali, Ting-Wei Su, Oguzhan Yaglidere, Shirley Luckhart, and Aydogan Ozcan. Holographic pixel super-resolution in portable lensless on-chip microscopy using a fiber-optic array. *Lab on a Chip*, 11(7):1276–1279, 2011.
- [17] Boris K Biskaborn, Jean-Pierre Lanckman, Hugues Lantuit, Kirsten Elger, Streletskiy Dmitry, Cable William, and Romanovsky Vladimir. The new database of the global terrestrial network for permafrost (gtn-p). *Earth System Science Data*, 7:245–259, 2015.
- [18] Space Studies Board, National Research Council, et al. *Signs of life: A report based on the April 2000 Workshop on Life Detection Techniques*. National Academies Press, 2002.
- [19] Max Born and Emil Wolf. *Principles of optics: electromagnetic theory of propagation, interference and diffraction of light*, pages 333–335, 415, 424. Elsevier, 2013.
- [20] Max Born and Emil Wolf. *Principles of optics: electromagnetic theory of propagation, interference and diffraction of light*, pages 256–260. Elsevier, 2013.
- [21] Max Born, Emil Wolf, Avadh Behari Bhatia, PC Clemmow, et al. *Principles of optics: electromagnetic theory of propagation, interference and diffraction of light*, volume 4. Pergamon press Oxford, 1970.
- [22] Raymond W Bourdeau, Audrey Lee-Gosselin, Anupama Lakshmanan, Arash Farhadi, Sripriya Ravindra Kumar, Suchita P Nety, and Mikhail G Shapiro. Acoustic reporter genes for noninvasive imaging of microorganisms in mammalian hosts. *Nature*, 553(7686):86, 2018.

- [23] Raymond W Bourdeau, Audrey Lee-Gosselin, Anupama Lakshmanan, Arash Farhadi, Sripriya Ravindra Kumar, Suchita P Nety, and Mikhail G Shapiro. Acoustic reporter genes for noninvasive imaging of microorganisms in mammalian hosts. *Nature*, 553(7686):86, 2018.
- [24] Robert W Boyd. Intuitive explanation of the phase anomaly of focused light beams. *JOSA*, 70(7):877–880, 1980.
- [25] GF Brand. A new millimeter wave geometric phase demonstration. *International Journal of Infrared and Millimeter Waves*, 21(4):505–518, 2000.
- [26] Roland Brock. The uptake of arginine-rich cell-penetrating peptides: putting the puzzle together. *Bioconjugate chemistry*, 25(5):863–868, 2014.
- [27] Anwar Chengala, Miki Hondzo, and Jian Sheng. Microalga propels along vorticity direction in a shear flow. *Physical Review E*, 87(5):052704, 2013.
- [28] Nicolas Chenouard, Ihor Smal, Fabrice De Chaumont, Martin Maška, Ivo F Sbalzarini, Yuanhao Gong, Janick Cardinale, Craig Carthel, Stefano Coraluppi, Mark Winter, et al. Objective comparison of particle tracking methods. *Nature methods*, 11(3):281, 2014.
- [29] Fook Chiong Cheong, Bhaskar Jyoti Krishnatreya, and David G Grier. Strategies for three-dimensional particle tracking with holographic video microscopy. *Optics express*, 18(13):13563–13573, 2010.
- [30] Lusik Cherkezyan, Hariharan Subramanian, Valentina Stoyneva, Jeremy D Rogers, Seungmoo Yang, Dhwanil Damania, Allen Taflove, and Vadim Backman. Targeted alteration of real and imaginary refractive index of biological cells by histological staining. *Optics letters*, 37(10):1601–1603, 2012.
- [31] David Cohoe, Iulian Hanczarek, J Kent Wallace, and Jay Nadeau. Multi-wavelength digital holographic imaging and phase unwrapping of protozoa using custom fiji plug-ins. *Frontiers in Physics*, 7:94, 2019.
- [32] J Colangelo-Lillis, H Eicken, SD Carpenter, and JW Deming. Evidence for marine origin and microbial-viral habitability of sub-zero hypersaline aqueous inclusions within permafrost near barrow, alaska. *FEMS microbiology ecology*, 92(5):fiw053, 2016.
- [33] Katherine Creath. Phase-measurement interferometry techniques. *Progress in optics*, 26:349–393, 1988.
- [34] Etienne Cuche, Pierre Marquet, and Christian Depeursinge. Spatial filtering for zero-order and twin-image elimination in digital off-axis holography. *Applied optics*, 39(23):4070–4075, 2000.
- [35] IG Da Paz, PL Saldanha, MC Nemes, and JG Peixoto de Faria. Experimental proposal for measuring the gouy phase of matter waves. *New Journal of Physics*, 13(12):125005, 2011.

- [36] Peter Debye. Das verhalten von lichtwellen in der nähe eines brennpunktes oder einer brennlinie. *Annalen der Physik*, 335(14):755–776, 1909.
- [37] Winfried Denk, James H Strickler, and Watt W Webb. Two-photon laser scanning fluorescence microscopy. *Science*, 248(4951):73–76, 1990.
- [38] Dino Di Carlo, Jon F Edd, Katherine J Humphry, Howard A Stone, and Mehmet Toner. Particle segregation and dynamics in confined flows. *Physical review letters*, 102(9):094503, 2009.
- [39] PA Dibrov, VA Kostyrko, RL Lazarova, VP Skulachev, and IA Smirnova. The sodium cycle. i. na⁺-dependent motility and modes of membrane energization in the marine alkalotolerant vibrio alginolyticus. *Biochimica et Biophysica Acta (BBA)-Bioenergetics*, 850(3):449–457, 1986.
- [40] Shawn D Domagal-Goldman, Katherine E Wright, Katarzyna Adamala, Leigh Arina de la Rubia, Jade Bond, Lewis R Dartnell, Aaron D Goldman, Kennda Lynch, Marie-Eve Naud, Ivan G Paulino-Lima, et al. The astrobiology primer v2. 0. *Astrobiology*, 16(8):561–653, 2016.
- [41] Frank Dubois, Catherine Yourassowsky, Olivier Monnom, J-C Legros, Olivier Debeir, Philippe Van Ham, Robert Kiss, and Christine Decaestecker. Digital holographic microscopy for the three-dimensional dynamic analysis of in vitro cancer cell migration. *Journal of biomedical optics*, 11(5):054032, 2006.
- [42] Hajo Eicken and Maya Salganek. *Field techniques for Sea-ice Research*. University of Alaska Press, 2010.
- [43] Arash Farhadi, Gabrielle Ho, Martin Kunth, Bill Ling, Anupama Lakshmanan, George J Lu, Raymond W Bourdeau, Leif Schröder, and Mikhail G Shapiro. Recombinantly expressed gas vesicles as nanoscale contrast agents for ultrasound and hyperpolarized mri. *AIChE Journal*, 64(8):2927–2933, 2018.
- [44] John F Federici, Robert L Wample, David Rodriguez, and Suman Mukherjee. Application of terahertz gouy phase shift from curved surfaces for estimation of crop yield. *Applied Optics*, 48(7):1382–1388, 2009.
- [45] Simin Feng and Herbert G Winful. Physical origin of the gouy phase shift. *Optics letters*, 26(8):485–487, 2001.
- [46] Lars Friedrich and Alexander Rohrbach. Tuning the detection sensitivity: a model for axial backfocal plane interferometric tracking. *Optics letters*, 37(11):2109–2111, 2012.
- [47] B Ronald Frost and James S Beard. On silica activity and serpentization. *Journal of petrology*, 48(7):1351–1368, 2007.

- [48] Adolfas K Gaigalas, Steven Choquette, and Yu-Zhong Zhang. Measurement of scattering and absorption cross sections of dyed microspheres. *Journal of research of the National Institute of Standards and Technology*, 118:15, 2013.
- [49] Juan Manuel García-Ruiz, Elias Nakouzi, Electra Kotopoulou, Leonardo Tamborrino, and Oliver Steinbock. Biomimetic mineral self-organization from silica-rich spring waters. *Science advances*, 3(3):e1602285, 2017.
- [50] Frederick Gittes and Christoph F Schmidt. Interference model for back-focal-plane displacement detection in optical tweezers. *Optics letters*, 23(1):7–9, 1998.
- [51] Carl Giuffre, Peter Hinow, Ryan Vogel, Tanvir Ahmed, Roman Stocker, Thomas R Consi, and J Rudi Strickler. The ciliate paramecium shows higher motility in non-uniform chemical landscapes. *PloS one*, 6(4):e15274, 2011.
- [52] Louis Georges Gouy. Sur la propagation anormale des ondes. *Compt. Rendue Acad. Sci. Paris*, 111:33, 1890.
- [53] William D Grant and Koki Horikoshi. *Extremophiles: microbial life in extreme environments*, volume 28. Wiley-Liss New York, 1998.
- [54] Steven JM Habraken and Gerard Nienhuis. Geometric phases in astigmatic optical modes of arbitrary order. *Journal of Mathematical Physics*, 51(8):082702, 2010.
- [55] Kevin P Hand, Murray A.E., Garvin J.B., Brinckerhoff W.B., Christner B.C., Edgett K.S., Ehlmann B.L., German C.R., Hayes A.G., Hoehler T.M., Horst S.M., Lunin E J.I., Nealson K.H., Paranicas C., Schmidt B.E., Smith D.E, Rhoden A.R., Russel M.J., Templeton A.S., Willis P.A., Yingst R.A., Phillips C.B., Cable M.L, Craft K.L, Hofmann A.E., Nordheim T.A., Pappalardo R.P, and the Project Engineering Team (2017). *Report of the Europa Lander science definition team*. National Aeronautics and Space Administration, 2017.
- [56] A. Hanslmeier, S. Kempe, and J Seckbach. Life on earth and other planetary bodies. cellular origin, life in extreme habitats and astrobiology. *Springer*, 24, 2012.
- [57] P Hariharan and PA Robinson. The gouy phase shift as a geometrical quantum effect. *Journal of Modern Optics*, 43(2):219–221, 1996.
- [58] David W Hosmer Jr, Stanley Lemeshow, and Rodney X Sturdivant. *Applied logistic regression*, volume 398. John Wiley & Sons, 2013.
- [59] Gui Huang, Wenzhang Tian, Meng Qi, Xiangjun Gong, and Guangzhao Zhang. Improving axial resolution for holographic tracking of colloids and bacteria over a wide depth of field by optimizing different factors. *Optics express*, 26(8):9920–9930, 2018.

- [60] Pascal Jourdain, Nicolas Pavillon, Corinne Moratal, Daniel Boss, Benjamin Rappaz, Christian Depeursinge, Pierre Marquet, and Pierre J Magistretti. Determination of transmembrane water fluxes in neurons elicited by glutamate ionotropic receptors and by the cotransporters *kcc2* and *nkcc1*: a digital holographic microscopy study. *Journal of Neuroscience*, 31(33):11846–11854, 2011.
- [61] Karen Junge, Hajo Eicken, and Jody W Deming. Motility of *colwellia psycherythraea* strain 34h at subzero temperatures. *Applied and environmental microbiology*, 69(7):4282–4284, 2003.
- [62] Ikuro Kawagishi, Yukiyo Maekawa, Tatsuo Atsumi, Michio Homma, and Yasuo Imae. Isolation of the polar and lateral flagellum-defective mutants in *vibrio alginolyticus* and identification of their flagellar driving energy sources. *Journal of Bacteriology*, 177(17):5158–5160, 1995.
- [63] Björn Kemper, Daniel D Carl, Jürgen Schnekenburger, Ilona Bredebusch, Marcus Schäfer, Wolfram Domschke, and Gert von Bally. Investigation of living pancreas tumor cells by digital holographic microscopy. *Journal of biomedical optics*, 11(3):034005, 2006.
- [64] Myun-Sik Kim, Toralf Scharf, Carsten Rockstuhl, and Hans Peter Herzig. Phase anomalies in micro-optics. In *Progress in Optics*, volume 58, pages 115–197. Elsevier, 2013.
- [65] Myung K Kim. *Digital holographic microscopy*, page 152. Springer, 2011.
- [66] Myung K Kim. *Digital holographic microscopy*, pages 49–51. Springer, 2011.
- [67] Myung K Kim. *Digital holographic microscopy*, pages 29–34. Springer, 2011.
- [68] Taewoo Kim, Renjie Zhou, Mustafa Mir, S Derin Babacan, P Scott Carney, Lynford L Goddard, and Gabriel Popescu. White-light diffraction tomography of unlabelled live cells. *Nature Photonics*, 8(3):256, 2014.
- [69] Gordon S Kino and Timothy R Corle. *Confocal scanning optical microscopy and related imaging systems*. Academic Press, 1996.
- [70] Herwig Kogelnik and Tingye Li. Laser beams and resonators. *Applied optics*, 5(10):1550–1567, 1966.
- [71] Jonas Kühn, Bimochan Niraula, Kurt Liewer, J Kent Wallace, Eugene Serabyn, Emilio Graff, Christian Lindensmith, and Jay L Nadeau. A mach-zender digital holographic microscope with sub-micrometer resolution for imaging and tracking of marine micro-organisms. *Review of Scientific Instruments*, 85(12):123113, 2014.

- [72] Anupama Lakshmanan, Arash Farhadi, Suchita P Nety, Audrey Lee-Gosselin, Raymond W Bourdeau, David Maresca, and Mikhail G Shapiro. Molecular engineering of acoustic protein nanostructures. *ACS nano*, 10(8):7314–7322, 2016.
- [73] Anupama Lakshmanan, George J Lu, Arash Farhadi, Suchita P Nety, Martin Kunth, Audrey Lee-Gosselin, David Maresca, Raymond W Bourdeau, Melissa Yin, Judy Yan, et al. Preparation of biogenic gas vesicle nanostructures for use as contrast agents for ultrasound and mri. *Nature protocols*, 12(10):2050, 2017.
- [74] Guy Lamouche, Marc L Dufour, Bruno Gauthier, and Jean-Pierre Monchalain. Gouy phase anomaly in optical coherence tomography. *Optics communications*, 239(4-6):297–301, 2004.
- [75] Christian A Lindensmith, Stephanie Rider, Manuel Bedrossian, J Kent Wallace, Eugene Serabyn, G Max Showalter, Jody W Deming, and Jay L Nadeau. A submersible, off-axis holographic microscope for detection of microbial motility and morphology in aqueous and icy environments. *PloS one*, 11(1):e0147700, 2016.
- [76] EH Linfoot and E Wolf. Phase distribution near focus in an aberration-free diffraction image. *Proceedings of the Physical Society. Section B*, 69(8):823, 1956.
- [77] PY Liu, LK Chin, W Ser, HF Chen, C-M Hsieh, C-H Lee, K-B Sung, TC Ayi, PH Yap, B Liedberg, et al. Cell refractive index for cell biology and disease diagnosis: past, present and future. *Lab on a Chip*, 16(4):634–644, 2016.
- [78] James E Lovelock. A physical basis for life detection experiments. *Nature*, 207(997):568–570, 1965.
- [79] George J Lu, Arash Farhadi, Jerzy O Szablowski, Audrey Lee-Gosselin, Samuel R Barnes, Anupama Lakshmanan, Raymond W Bourdeau, and Mikhail G Shapiro. Acoustically modulated magnetic resonance imaging of gas-filled protein nanostructures. *Nature materials*, 17(5):456, 2018.
- [80] Wuwu LV, Tang Gao, Shuanglian Wang, Jing Hou, Mian Liu, Jiu Yang, Tao Du, Zhikang Chen, Zihua Chen, Xueping Feng, et al. Long-term tracking of cancer cell nucleus and identification of colorectal cancer with an aggregation-induced emission-based fluorescent probe. *Journal of biomedical nanotechnology*, 15(5):1033–1042, 2019.
- [81] EW Maas, AM Simpson, A Martin, S Thompson, EY Koh, SK Davy, KG Ryan, and RF O’Toole. Phylogenetic analyses of bacteria in sea ice at cape hallett, antarctica. *New Zealand Journal of Marine and Freshwater Research*, 46(1):3–12, 2012.

- [82] Bedrossian. Manuel. Manuel bedrossian phd digital library. https://github.com/mbedross/mmb_PhD_Thesis, 2019.
- [83] Joseph M Martel and Mehmet Toner. Inertial focusing in microfluidics. *Annual review of biomedical engineering*, 16:371–396, 2014.
- [84] Hanno Meyer, Lutz Schirrmeister, Andrei Andreev, Dirk Wagner, Hans-W Hubberten, Kenji Yoshikawa, Anatoly Bobrov, Sebastian Wetterich, Thomas Opel, Evgeniya Kandiano, et al. Lateglacial and holocene isotopic and environmental history of northern coastal alaska—results from a buried ice-wedge system at barrow. *Quaternary Science Reviews*, 29(27-28):3720–3735, 2010.
- [85] Maria Falck Miniotis, Anthonny Mukwaya, and Anette Gjørloff Wingren. Digital holographic microscopy for non-invasive monitoring of cell cycle arrest in 1929 cells. *PloS one*, 9(9):e106546, 2014.
- [86] Mehdi Molaei and Jian Sheng. Imaging bacterial 3d motion using digital in-line holographic microscopy and correlation-based de-noising algorithm. *Optics express*, 22(26):32119–32137, 2014.
- [87] Mehdi Molaei, Michael Barry, Roman Stocker, and Jian Sheng. Failed escape: solid surfaces prevent tumbling of escherichia coli. *Physical review letters*, 113(6):068103, 2014.
- [88] Penny L Morrill, J Gijs Kuenen, Orion J Johnson, Shino Suzuki, Amanda Rietze, Alex L Sessions, Marilyn L Fogel, and Kenneth H Nealson. Geochemistry and geobiology of a present-day serpentinization site in california: The cedars. *Geochimica et Cosmochimica Acta*, 109:222–240, 2013.
- [89] Jay L Nadeau, Yong Bin Cho, and Christian A Lindensmith. Use of dyes to increase phase contrast for biological holographic microscopy. *Optics letters*, 40(17):4114–4117, 2015.
- [90] Jay L Nadeau, Yong Bin Cho, Jonas Kühn, and Kurt Liewer. Improved tracking and resolution of bacteria in holographic microscopy using dye and fluorescent protein labeling. *Frontiers in chemistry*, 4:17, 2016.
- [91] Julian Papadopoulos and Thomas JJ Müller. Rapid synthesis of 4-alkynyl coumarins and tunable electronic properties of emission solvatochromic fluorophores. *Dyes and Pigments*, 2019.
- [92] Nicolas Pavillon, Jonas Kühn, Corinne Moratal, Pascal Jourdain, Christian Depeursinge, Pierre J Magistretti, and Pierre Marquet. Early cell death detection with digital holographic microscopy. *PloS one*, 7(1):e30912, 2012.
- [93] Felicitas Pfeifer. Distribution, formation and regulation of gas vesicles. *Nature Reviews Microbiology*, 10(10):705, 2012.

- [94] Anh-Hoang Phan, Jae-Hyeung Park, and Nam Kim. Super-resolution digital holographic microscopy for three dimensional sample using multipoint light source illumination. *Japanese Journal of Applied Physics*, 50(9R):092503, 2011.
- [95] Benjamin Rappaz, Florian Charrière, Christian Depeursinge, Pierre J Magistretti, and Pierre Marquet. Simultaneous cell morphometry and refractive index measurement with dual-wavelength digital holographic microscopy and dye-enhanced dispersion of perfusion medium. *Optics letters*, 33(7):744–746, 2008.
- [96] Benjamin Rappaz, Billy Breton, Etienne Shaffer, and Gerardo Turcatti. Digital holographic microscopy: a quantitative label-free microscopy technique for phenotypic screening. *Combinatorial chemistry & high throughput screening*, 17(1):80–88, 2014.
- [97] Lord Rayleigh. Xxxi. investigations in optics, with special reference to the spectroscope. *The London, Edinburgh, and Dublin Philosophical Magazine and Journal of Science*, 8(49):261–274, 1879.
- [98] Scott O Rogers, Vincent Theraisnathan, LJ Ma, Y Zhao, G Zhang, S-G Shin, JD Castello, and WT Starmer. Comparisons of protocols for decontamination of environmental ice samples for biological and molecular examinations. *Appl. Environ. Microbiol.*, 70(4):2540–2544, 2004.
- [99] Lynn J Rothschild and Rocco L Mancinelli. Life in extreme environments. *Nature*, 409(6823):1092, 2001.
- [100] Basudev Roy, Sambit Bikas Pal, Arijit Haldar, Ratnesh Kumar Gupta, Nirmalya Ghosh, and Ayan Banerjee. Probing the dynamics of an optically trapped particle by phase sensitive back focal plane interferometry. *Optics express*, 20(8):8317–8328, 2012.
- [101] A Rubinowicz. On the anomalous propagation of phase in the focus. *Physical Review*, 54(11):931, 1938.
- [102] Johannes Schindelin, Ignacio Arganda-Carreras, Erwin Frise, Verena Kaynig, Mark Longair, Tobias Pietzsch, Stephan Preibisch, Curtis Rueden, Stephan Saalfeld, Benjamin Schmid, et al. Fiji: an open-source platform for biological-image analysis. *Nature methods*, 9(7):676, 2012.
- [103] Hermann Schlichting and Klaus Gersten. *Boundary-layer theory*. Springer, 2016.
- [104] Ulf Schnars and Werner PO Jüptner. Digital recording and numerical reconstruction of holograms. *Measurement science and technology*, 13(9):R85, 2002.

- [105] Joseph Seckbach. *Journey to diverse microbial worlds: adaptation to exotic environments*, volume 2. Springer Science & Business Media, 2000.
- [106] Mikhail G Shapiro, Patrick W Goodwill, Arkosnato Neogy, Melissa Yin, F Stuart Foster, David V Schaffer, and Steven M Conolly. Biogenic gas nanostructures as ultrasonic molecular reporters. *Nature nanotechnology*, 9(4):311, 2014.
- [107] Mikhail G Shapiro, R Matthew Ramirez, Lindsay J Sperling, George Sun, Jinny Sun, Alexander Pines, David V Schaffer, and Vikram S Bajaj. Genetically encoded reporters for hyperpolarized xenon magnetic resonance imaging. *Nature chemistry*, 6(7):629, 2014.
- [108] Derek Shaw. *Fourier transform NMR spectroscopy*, volume 4. Elsevier Amsterdam, 1984.
- [109] Jian Sheng, Edwin Malkiel, Joseph Katz, Jason Adolf, Robert Belas, and Allen R Place. Digital holographic microscopy reveals prey-induced changes in swimming behavior of predatory dinoflagellates. *Proceedings of the National Academy of Sciences*, 104(44):17512–17517, 2007.
- [110] Jian Sheng, Edwin Malkiel, Joseph Katz, Jason E Adolf, and Allen R Place. A dinoflagellate exploits toxins to immobilize prey prior to ingestion. *Proceedings of the National Academy of Sciences*, 107(5):2082–2087, 2010.
- [111] A. E Siegman. Lasers /. pages 682–685. URL <http://caltech.tind.io/record/539696>.
- [112] R Simon and N Mukunda. Bargmann invariant and the geometry of the güoy effect. *Physical review letters*, 70(7):880, 1993.
- [113] NH Sleep, A Meibom, Th Fridriksson, RG Coleman, and DK Bird. H₂-rich fluids from serpentinization: geochemical and biotic implications. *Proceedings of the National Academy of Sciences*, 101(35):12818–12823, 2004.
- [114] Lars H Smedsrud and Ragnheid Skogseth. Field measurements of arctic grease ice properties and processes. *Cold Regions Science and Technology*, 44(3):171–183, 2006.
- [115] Todd M Squires and Stephen R Quake. Microfluidics: Fluid physics at the nanoliter scale. *Reviews of modern physics*, 77(3):977, 2005.
- [116] Roman Stocker. Reverse and flick: Hybrid locomotion in bacteria. *Proceedings of the National Academy of Sciences*, 108(7):2635–2636, 2011.
- [117] D Subbarao. Topological phase in gaussian beam optics. *Optics letters*, 20(21):2162–2164, 1995.

- [118] Shino Suzuki, Shun'ichi Ishii, Angela Wu, Andrea Cheung, Aaron Tenney, Greg Wanger, J Gijs Kuenen, and Kenneth H Neilson. Microbial diversity in the cedars, an ultrabasic, ultrareducing, and low salinity serpentinizing ecosystem. *Proceedings of the National Academy of Sciences*, 110(38): 15336–15341, 2013.
- [119] KM Taute, S Gude, SJ Tans, and TS Shimizu. High-throughput 3d tracking of bacteria on a standard phase contrast microscope. *Nature communications*, 6:8776, 2015.
- [120] CA Taylor. Fourier transforms and their physical applications by dc champagne. *Acta Crystallographica Section A: Crystal Physics, Diffraction, Theoretical and General Crystallography*, 30(1):126–126, 1974.
- [121] Jean-Yves Tinevez. Simple tracker. *MATLAB File Exchange*, 2016.
- [122] Svenja M Vater, John Finlay, Maureen E Callow, James A Callow, Thomas Ederth, Bo Liedberg, Michael Grunze, and Axel Rosenhahn. Holographic microscopy provides new insights into the settlement of zoospores of the green alga *Ulva linza* on cationic oligopeptide surfaces. *Biofouling*, 31(2): 229–239, 2015.
- [123] J Kent Wallace, Stephanie Rider, Eugene Serabyn, Jonas Kühn, Kurt Liewer, Jody Deming, Gordon Showalter, Chris Lindensmith, and Jay Nadeau. Robust, compact implementation of an off-axis digital holographic microscope. *Optics Express*, 23(13):17367–17378, 2015.
- [124] J Kent Wallace, Eugene Serabyn, Chris Lindensmith, Stephanie Rider, and Jay Nadeau. A multiwavelength, common-mode architecture for a digital holographic microscope. In *Digital Holography and Three-Dimensional Imaging*, pages W2B–6. Optical Society of America, 2019.
- [125] Anthony E Walsby. Gas vesicles. *Microbiology and Molecular Biology Reviews*, 58(1):94–144, 1994.
- [126] George A Wistreich. Microbiology laboratory. *Fundamentals and applications*, 2:139–256, 1997.
- [127] Wenbo Xu, MH Jericho, IA Meinertzhagen, and HJ Kreuzer. Digital in-line holography of microspheres. *Applied optics*, 41(25):5367–5375, 2002.
- [128] Jianpeng Xue, Zeqing Li, Hanmei Xu, and Yang Pu. A novel fluorescent gold nanoparticle inhibiting migration and invasion of tumor cells. In *Reporters, Markers, Dyes, Nanoparticles, and Molecular Probes for Biomedical Applications XI*, volume 10893, page 108930S. International Society for Optics and Photonics, 2019.

- [129] Caojin Yuan, Guohai Situ, Giancarlo Pedrini, Jun Ma, and Wolfgang Osten. Resolution improvement in digital holography by angular and polarization multiplexing. *Applied optics*, 50(7):B6–B11, 2011.
- [130] Wenqi Zhu, Amit Agrawal, and Ajay Nahata. Direct measurement of the gouy phase shift for surface plasmon-polaritons. *Optics express*, 15(16): 9995–10001, 2007.

Appendix A

REFERENCE EQUATIONS AND DERIVATIONS

Reference Equations

This section lists reference equations that were useful in the design and implementation of the devices and experiments discussed in the thesis. These reference equations have been divided into three sections for convenience: 1) Optics, 2) Fluid Mechanics, and 3) Miscellaneous.

Optics

— **Numerical Aperture**

$$NA = n \sin(\theta)$$

where n is the index of refraction of the lens and θ is the maximum convergence half angle of the lens.

— **F-Number**

$$F = \frac{f}{D}$$

where f is the focal length of the lens and D is the diameter of the entrance pupil of the lens.

— **Lens-Maker's Equation**

$$\frac{1}{f} = \Delta n \left(\frac{1}{r_1} - \frac{1}{r_2} + \frac{\Delta n d}{n_2 r_1 r_2} \right)$$

where f is the focal length of the lens, $\Delta n = n_2 - n_1$ is the difference in index of refraction between the lens and its surrounding medium, r_1 and r_2 are the radii of curvature of the lens, and d is the thickness of the lens.

— **Lens-Maker's Equation with thin lens approximation**

$$\frac{1}{f} = \Delta n \left(\frac{1}{r_1} - \frac{1}{r_2} \right)$$

where f is the focal length of the lens, $\Delta n = n_2 - n_1$ is the difference in index of refraction between the lens and its surrounding medium, and r_1 and r_2 are the radii of curvature of the lens.

— **Diffraction Limited Lateral Resolution Limit (Rayleigh)**

$$r_{(x,y)} = \frac{1.22\lambda}{2NA}$$

where λ is the illumination wavelength and NA is the numerical aperture of the instrument.

— **Diffraction Limited Axial Resolution Limit (Abbe)**

$$r_z = \frac{2\lambda}{\text{NA}^2}$$

where λ is the illumination wavelength and NA is the numerical aperture of the instrument.

— **Optical Path Length Difference**

$$\Delta\mathcal{L} = n\Delta s$$

where n is the index of refraction of the propagation medium and Δs is the physical path length difference.

— **Optical Phase Difference**

$$\Delta\phi = \frac{2\pi}{\lambda}\Delta s\Delta n = \frac{2\pi}{\lambda}\Delta\mathcal{L}$$

where λ is the illumination wavelength, Δs is the physical path length difference, and Δn is the difference in refractive index.

— **Fringe Spacing**

$$x = \frac{a\lambda_0}{nd}$$

where a is the distance from the two point sources of the interferometer, λ_0 is the illumination wavelength, n is the refractive index of the propagation media, and d is the distance of separation between the two point sources. See Figure 2.1.

— **Fringe Visibility**

$$V = \frac{2\sqrt{I_1 I_2}}{I_1 + I_2} = \frac{I_{\max} - I_{\min}}{I_{\max} + I_{\min}}$$

where I_1 and I_2 are the intensities of the two beams of the interferometer. I_{\max} and I_{\min} are the maximum and minimum intensities of a pixel neighborhood where fringe visibility is to be calculated.

— **Static Interferogram**

$$I(x, y) = I_1 + I_2 + 2\sqrt{I_1 I_2} \cos(\Delta\phi)$$

where I_1 and I_2 are the intensities of the two coherent beams of the interferometer and $\Delta\phi$ is the phase difference between the two beams.

— **Displacement Function of an Electromagnetic Wave**

$$\psi(x, y, t) = A(x, y)e^{i(\phi(x, y) - \omega t)}$$

where A is the amplitude of the EM wave, ϕ is the phase, and ω is the angular frequency of the wave.

— **Intensity of Electromagnetic Wave**

$$I(x, y) = \int_{t_1}^{t_2} \Psi\Psi^* dt$$

where Ψ is the displacement function of the electromagnetic wave and Ψ^* is its complex conjugate.

— **Complex Wavefront (Holographic Reconstruction)**

$$\Gamma(\xi, \eta) = \mathfrak{F}^{-1}[\mathfrak{F}(I(x, y) \cdot R) * G]$$

where $I(x, y)$ is the hologram, G is the free space propagation term, \mathfrak{F} is the Fourier Transform operator, and R is a ‘phase adjustment’ term that is used to remove tilt and other unwanted artifacts from the phase reconstructions.

— **Transfer Function of Free Space**

$$G(m, n) = \exp\left(\frac{-2\pi zi}{\lambda} \sqrt{1 - \lambda^2 f_x^2 - \lambda^2 f_y^2}\right)$$

where z is the focal plane, λ is the wavelength of the illuminating light source, and F_x and f_y are spatial frequency variables in the x and y directions, respectively.

— **Phase of a Complex Wavefront**

$$\phi(x, y) = \arctan\left(\frac{\Im(\Gamma)}{\Re(\Gamma)}\right)$$

where $\Gamma = \rho + \omega j$ is a complex number with real and imaginary parts ρ and ω , respectively.

Fluids

— **Hydraulic Diameter of a Rectangular Pipe**

$$D_h = \frac{2ab}{(a+b)}$$

where a and b are the dimensions of the channel’s cross-sectional area.

— **Reynolds Number**

$$Re = \frac{\rho u L}{\mu}$$

where ρ is the density of the fluid, u is the velocity of the fluid, L is the characteristic length scale of the flow, and μ is the dynamic viscosity of the fluid.

— **Deans Number**

$$De = Re \sqrt{\frac{D_h}{2R_c}}$$

where Re is the Reynolds Number, D_h is the hydraulic diameter, and R_c is the radius of curvature of the bend in the pipe.

— **Boundary Layer Thickness (Blasius solution)**

$$\delta \approx \frac{4.91x}{\sqrt{Re_x}}$$

where x is the distance along the pipe and Re_x is the Reynolds Number at that point.

— **Entrance Length for Fully Developed Flow**

$$L \approx \frac{D_h Re}{9.82}$$

where D_h is the hydraulic diameter of the pipe and Re is the Reynolds Number.

— **Fully Developed Velocity Profile**

$$v(x) = v_{\max} \left(1 - \left(\frac{x}{L}\right)^2\right)$$

where v_{\max} is the maximum velocity of the fluid (at the center of the pipe), x is the position along the pipe's cross-section, and L is the hydraulic radius of the pipe.

— **Average Flow Velocity in a Fully Developed Flow**

$$\bar{v} = \frac{1}{2L} \int_{-L}^L v_{\max} \left(1 - \left(\frac{x}{L}\right)^2\right) dx = \frac{2}{3} v_{\max}$$

where v_{\max} is the maximum velocity of the fluid (at the center of the pipe), x is the position along the pipe's cross-section, and L is the hydraulic radius of the pipe.

— **Average Volumetric Flow Rate**

$$Q = \iint_A \mathbf{v} \cdot d\mathbf{A} = A\bar{v}$$

where A is the pipe's cross-sectional area and \bar{v} is the average flow velocity. This is assuming that the velocity is completely normal across the area.

Miscellaneous

— **Radial Averaging**

$$\bar{I}_r(\omega_r) = \frac{\int_0^{2\pi} I(\omega_r, \omega_\theta) d\theta}{\int_0^{2\pi} \omega_r d\theta}$$

where $I(\omega_r, \omega_\theta)$ is the 2D matrix that is to be radially averaged expressed in polar coordinates.

— **Power Spectra Density Function (PSD)**

$$P = \frac{|\mathfrak{F}(S)|^2}{f_s \prod_{i=1}^m N_i}$$

where \mathfrak{F} is the Fourier Transform operator, S is the signal, f_s is the sampling frequency of the signal, N is the number of samples of that signal, and m is the number of dimensions of the signal S .

— **Signal Variance**

$$\sigma^2 = 2 \int_0^{\omega_m} P(\omega) d\omega$$

where ω_m is the maximum sample frequency, dictated by the Nyquist-Shannon sampling theorem, and $P(\omega)$ is the PSD of the signal.

— **Signal to Noise Ratio (SNR)**

$$\text{SNR} = \frac{S}{\sigma}$$

where S is the signal being measured, and σ is the standard deviation of the signal.

— **Propagation of Error**

$$\delta\phi^2 = \sum_{i=1}^n \left(\frac{\partial\phi}{\partial I_i} \right)^2 \delta I_i^2$$

where $\delta\phi^2$ is the variance in the calculated value, ϕ , I_i is i^{th} measured signal used to calculate ϕ , and δI_i^2 is the variance in that measured signal.

— **Discrete Definition of Velocity**

$$v_j^i(\tau) = \frac{\Delta j}{\Delta t} = \frac{j^i(\tau+1) - j^i(\tau)}{t(\tau+1) - t(\tau)}$$

where $v_j^i(\tau)$ is the j -component velocity at time point τ of the i^{th} particle.

Derivations

The Gouy Phase Anomaly

Beginning with the wave equation, which is defined as

$$\nabla^2 u + k^2 u = 0, \quad (\text{A.1})$$

where u is the displacement function and k is the wave number.

There exists an approximate solution for a beam of Gaussian cross-section [70]

$$u(r, z) = \frac{\omega_0}{\omega(z)} \exp \left(i(kz - \Phi(z)) - r^2 \left(\frac{1}{\omega^2(z)} - \frac{ik}{2R(z)} \right) \right), \quad (\text{A.2})$$

where r is the radial coordinate in a plane perpendicular to the optical axis (z), $k = 2\pi/\lambda$ is the wave number, the function $\omega(z)$ is the beam radius and is defined as

$$\omega^2(z) = \omega_0^2 \left(1 + \left(\frac{\lambda z}{\pi \omega_0^2} \right)^2 \right), \quad (\text{A.3})$$

where $\omega_0 \triangleq \omega(z = 0)$.

This equation defines the beam radius as a hyperbolic function. Therefore, the effective convergence/divergence angle can be calculated as

$$\theta_{\text{eff}} = \frac{\lambda}{\pi \omega_0}. \quad (\text{A.4})$$

The function $R(z)$ defines the radius of curvature of the light's wavefront at any point along the optical axis. This function is defined as

$$R(z) = z \left(1 + \left(\frac{\pi \omega_0^2}{\lambda z} \right)^2 \right). \quad (\text{A.5})$$

The function $\Phi(z)$ describes the phase of the wave of light along the optical axis and is defined as

$$\Phi(z) = \arctan\left(\frac{\lambda z}{\pi\omega_0^2}\right). \quad (\text{A.6})$$

Phase Noise

The Four Bucket/Step Method

According to Equation 2.3, the intensities of the electric field at each of the four sample points are:

$$I_a = I_1 + I_2 + 2\sqrt{I_1 I_2} \cos \phi, \quad (\text{A.7a})$$

$$I_b = I_1 + I_2 + 2\sqrt{I_1 I_2} \cos(\phi + \pi/2) = I_1 + I_2 - 2\sqrt{I_1 I_2} \sin \phi, \quad (\text{A.7b})$$

$$I_c = I_1 + I_2 + 2\sqrt{I_1 I_2} \cos(\phi + \pi) = I_1 + I_2 - 2\sqrt{I_1 I_2} \cos \phi, \quad (\text{A.7c})$$

$$I_d = I_1 + I_2 + 2\sqrt{I_1 I_2} \cos(\phi + 3\pi/2) = I_1 + I_2 + 2\sqrt{I_1 I_2} \sin \phi. \quad (\text{A.7d})$$

With these equations describing the electric fields of the incident light, phase (ϕ) becomes

$$\phi = \arctan\left(\frac{\sin \phi}{\cos \phi}\right) = \arctan\left(\frac{I_d - I_b}{I_a - I_c}\right). \quad (\text{A.8})$$

Beginning with the equations for the electric field intensities at four points along a fringe in Equation A.7, and its resulting equation for phase in Equation A.8, we apply the equation for the propagation of error. The equation for phase variance is

$$\delta\phi^2 = \sum_{i=1}^n \left(\frac{\partial\phi}{\partial I_i}\right)^2 \delta I_i^2. \quad (\text{A.9})$$

where n is the number of fringe measurements made in the particular technique (i.e. $n = 4$).

The partial derivatives of phase with respect to each intensity function are

$$\frac{\partial \phi}{\partial I_a} = -\frac{\partial \phi}{\partial I_c} = \frac{I_b - I_d}{(I_a - I_c)^2 + (I_d - I_b)^2}, \quad (\text{A.10a})$$

$$\frac{\partial \phi}{\partial I_b} = -\frac{\partial \phi}{\partial I_d} = \frac{I_c - I_a}{(I_a - I_c)^2 + (I_d - I_b)^2}. \quad (\text{A.10b})$$

Combining Equations A.8, A.10, and 4.6, yields a phase variance of

$$\delta\phi^2 = \frac{I_1 + I_2 + (\Delta t \delta D)^2 + M(\delta R)^2 + \frac{L_{\text{SB}}^2}{12}}{4I_1 I_2}. \quad (\text{A.11})$$

Introducing a variable for the composite electric field intensity $\bar{I} = I_1 + I_2$, as well as fringe visibility $V = \frac{2\sqrt{I_1 I_2}}{I_1 + I_2}$, the above expression can be rewritten such that the phase errors introduced by the Four Bucket/Step Method are

$$\delta\phi = \sqrt{\frac{1}{2V^2 \bar{I}} + \frac{(\Delta t \delta D)^2 + M(\delta R)^2 + \frac{L_{\text{SB}}^2}{12}}{2V^2 \bar{I}^2}}. \quad (\text{A.12})$$

The Three Bucket/Step Method

According to Equation 2.3, the intensities of the electric field at each of the three sample points are

$$I_a = I_1 + I_2 + 2\sqrt{I_1 I_2} \cos \phi, \quad (\text{A.13a})$$

$$I_b = I_1 + I_2 + 2\sqrt{I_1 I_2} \cos(\phi + \pi/2) = I_1 + I_2 - 2\sqrt{I_1 I_2} \sin \phi, \quad (\text{A.13b})$$

$$I_c = I_1 + I_2 + 2\sqrt{I_1 I_2} \cos(\phi + \pi) = I_1 + I_2 - 2\sqrt{I_1 I_2} \cos \phi. \quad (\text{A.13c})$$

With these equations describing the electric fields of the incident light, phase (ϕ) becomes

$$\phi = \arctan\left(\frac{\sin \phi}{\cos \phi}\right) = \arctan\left(\frac{I_c - I_b}{I_a - I_b}\right). \quad (\text{A.14})$$

The partial derivatives of phase with respect to the three intensity functions in Equation A.13 are

$$\frac{\partial \phi}{\partial I_a} = \frac{I_b - I_c}{(I_a - I_c)^2 + (I_c - I_b)^2}, \quad (\text{A.15a})$$

$$\frac{\partial \phi}{\partial I_b} = \frac{I_c - I_a}{(I_a - I_c)^2 + (I_c - I_b)^2}, \quad (\text{A.15b})$$

$$\frac{\partial \phi}{\partial I_c} = \frac{I_a - I_b}{(I_a - I_c)^2 + (I_c - I_b)^2}. \quad (\text{A.15c})$$

Combining the above partial derivatives with Equation A.9, as well as the definitions of average electric field intensity and fringe visibility, the phase error due to the Three Bucket/Step Method is

$$\delta \phi = \sqrt{\frac{1 + 2 \cos^2 \phi - 2V \sin \phi \cos^2 \phi}{4V^2 \bar{I}} + \frac{3 \left((\Delta t \delta D)^2 + M(\delta R)^2 + \frac{L_{SB}^2}{12} \right) (1 - \sin 2\phi)}{16V^2 \bar{I}^2}}. \quad (\text{A.16})$$

where $\bar{I} = I_1 + I_2$ is the composite electric field intensity, and V is the fringe visibility.

The Carré Method

The Carré Method allows for phase calculations where the phase offset, or fringe sample spacing between exposures can vary linearly. This requires four measurements along the length of an interference pattern, each with a phase offset of α between each sample, where $\alpha \in (0, \pi]$. The four resulting intensities can be expressed as

$$I_a = I_1 + I_2 + 2\sqrt{I_1 I_2} \cos(\phi - 3\alpha/2), \quad (\text{A.17a})$$

$$I_b = I_1 + I_2 + 2\sqrt{I_1 I_2} \cos(\phi - \alpha/2), \quad (\text{A.17b})$$

$$I_c = I_1 + I_2 + 2\sqrt{I_1 I_2} \cos(\phi + \alpha/2), \quad (\text{A.17c})$$

$$I_d = I_1 + I_2 + 2\sqrt{I_1 I_2} \cos(\phi + 3\alpha/2). \quad (\text{A.17d})$$

The unknown phase offset, α , can be solved for as

$$\alpha = 2 \arctan \left(\sqrt{\frac{3(I_b - I_c) - (I_a - I_c)}{(I_b + I_c) + (I_a + I_d)}} \right). \quad (\text{A.18})$$

With the phase shift between exposures known, the phase of the incident light may be expressed as

$$\phi = \arctan \left(\frac{\sin \phi}{\cos \phi} \right) = \arctan \left(\frac{\sqrt{3(I_b - I_c)(I_a - I_c)}}{(I_b + I_c) - (I_a + I_d)} \right). \quad (\text{A.19})$$

The partial derivatives of phase with respect to the four intensity functions in Equation A.17 are

$$\frac{\partial \phi}{\partial I_a} = -\frac{\partial \phi}{\partial I_d} = \frac{\frac{3(I_b^2 - I_c^2) - (I_a + I_d)}{2\sqrt{3(I_b - I_c)(I_a - I_d)}} + \sqrt{3(I_b - I_c)(I_a - I_d)}}{((I_b + I_c) - (I_a + I_d))^2 + 3(I_b - I_c)(I_a - I_d)}, \quad (\text{A.20a})$$

$$\frac{\partial \phi}{\partial I_b} = -\frac{\partial \phi}{\partial I_c} = \frac{\frac{3(I_a - I_d)(I_b + I_c) - (I_a + I_d)}{2\sqrt{3(I_b - I_c)(I_a - I_d)}} + \sqrt{3(I_b - I_c)(I_a - I_d)}}{((I_b + I_c) - (I_a + I_d))^2 + 3(I_b - I_c)(I_a - I_d)}. \quad (\text{A.20b})$$

Combining the above partial derivatives with Equation A.9, the phase variance due to the Carré Method is

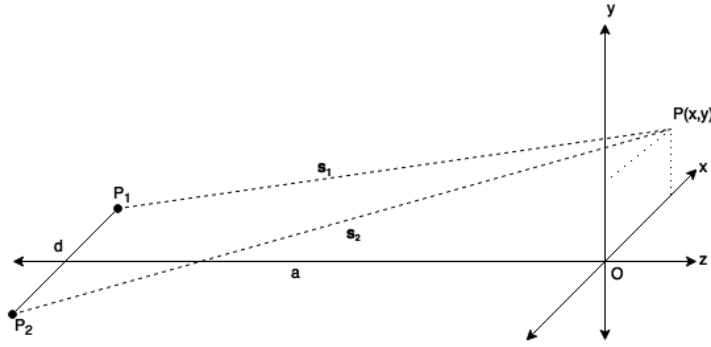
$$\delta \phi^2 = \frac{A \left(\frac{3D(B-A)}{2\sqrt{3CD}} + \sqrt{3CD} \right) + B \left(\frac{3C(B-A)}{2\sqrt{3CD}} + \sqrt{3CD} \right)}{(B-A)^2 + 3CD} + 2\delta I_i^2 \left(\frac{(3D(B-A) + 6CD)^2 + (3C(B-A) + 6CD)^2}{12CD((B-A) + 6CD)^2} \right), \quad (\text{A.21})$$

where

$$A = I_a + I_d, \quad (\text{A.22a})$$

$$B = I_b + I_c, \quad (\text{A.22b})$$

$$C = I_a - I_d, \quad (\text{A.22c})$$



$$D = I_b - I_c, \quad (\text{A.22d})$$

and δI_i is defined in Equation 4.6.

Young's Double Slit Experiment

P_1 and P_2 are the two 'pinholes' of the double slit setup, d is the distance between them, a is the distance along the optical axis between the two light sources and the observation plane where the interference pattern is created, and $P(x, y)$ is an arbitrary point on the observation plane at coordinate $(x, y, z = 0)$.

The magnitude of vectors s_1 and s_2 are

$$s_1 = \sqrt{a^2 + y^2 + \left(x - \frac{d}{2}\right)^2}, \quad (\text{A.23a})$$

$$s_2 = \sqrt{a^2 + y^2 + \left(x + \frac{d}{2}\right)^2}. \quad (\text{A.23b})$$

The physical difference between the distances s_1 and s_2 is:

$$\Delta s = s_2 - s_1 = \frac{(s_2 + s_1)(s_2 - s_1)}{s_2 + s_1} = \frac{s_2^2 - s_1^2}{s_2 + s_1} = \frac{2xd}{s_2 + s_1}. \quad (\text{A.24})$$

Here, we assume that $a \gg d$, such that we can approximate $s_1 \approx s_2 \approx a$, such that $s_2 + s_1 \approx 2a$. Thus,

$$\Delta s = \frac{xd}{a}. \quad (\text{A.25})$$

The optical path length difference between the two light sources is

$$\Delta\mathcal{L} = n\Delta s = \frac{nx d}{a}, \quad (\text{A.26})$$

where n is the index of refraction of the medium through which the light is propagating. The phase difference between the two light sources at this point is

$$\phi = \frac{2\pi}{\lambda_0} \left(\frac{nx d}{a} \right), \quad (\text{A.27})$$

where λ_0 is the nominal illumination wavelength.

Recall that for an interference pattern created by two light sources, the intensity at the observation plane can be expressed as

$$I(x, y) = I_1 + I_2 + 2\sqrt{I_1 I_2} \cos \phi. \quad (\text{A.28})$$

From Equation A.28, it can be seen that there are maxima and minima of $I(x, y)$, that is dependent of the value of ϕ . The values of x that cause $\phi = 2\pi p$, $p = 0, 1, 2, \dots$ are

$$x = \frac{ma\lambda_0}{nd}; m = 0, 1, 2, \dots \quad (\text{A.29})$$

The distance between peak-peak values in the interference pattern (fringe spacing) at the observation plane, close to the optical axis is

$$x = \frac{a\lambda_0}{nd}. \quad (\text{A.30})$$

One-Dimensional Random Walk

Assuming that a bacterium takes a step every second, the net distance traveled by a bacterium can be expressed as

$$\mathbf{d} = v \sum_{i=1}^k S_i, \quad (\text{A.31})$$

where v is the magnitude of the distance traveled by the bacterium per step (in μm per step), and $S_i \in \{-1, 1\}$ corresponding to a step backwards or forwards over a

total of k steps. From the possible values of S_i , the expected value of any S_n^2 is $E(S_n^2) = 1$.

Because the bacterium has an equal probability of going forward or backward, $\lim_{k \rightarrow \infty} \mathbf{d} = 0$, but for a finite number of steps, the magnitude of the net distance traveled by the bacterium is

$$\begin{aligned}
 |\mathbf{d}| = \sqrt{\mathbf{d}^2} &= \sqrt{v^2 \left(\sum_{i=1}^k S_i \right) \left(\sum_{j=1}^k S_j \right)} \\
 &= v \sqrt{\sum_{i=1}^k \sum_{j=1}^k S_i S_j} = v \sqrt{k},
 \end{aligned}
 \tag{A.32}$$

resulting in a net distance on the order of $|\mathbf{d}| = v\sqrt{k}$ over k seconds.

Table A.1 – Common Mode instrument parameters

Property	Value	Unit	Note
<i>Operating wavelength</i>	405	nm	Single-mode fiber-coupled laser
<i>Objective focal length</i>	7.6	mm	Aspheric Singlet
<i>Objective numerical aperture</i>	0.30	-	
<i>Relay lens focal length</i>	150	mm	Achromatic doublet
<i>System magnification</i>	19.7	-	
<i>Lateral resolution</i>	0.7	μm	
<i>CCD pixel size</i>	3.45×3.45	$\mu\text{m}\times\mu\text{m}$	2448 by 2048 (4Mpx) sensor
<i>Sample imaging volume</i>	360×360×>600	$\mu\text{m}\times\mu\text{m}\times\mu\text{m}$	
<i>Sample rate</i>	15	frames per second	
<i>Instrument length</i>	400	mm	Input fiber to back of CCD

Table A.2 – Mach-Zehnder instrument parameters

Property	Value	Unit	Note
<i>Operating wavelength</i>	405	nm	Single-mode fiber-coupled laser
<i>Objective focal length</i>	4	mm	
<i>Objective working distance</i>	13	mm	Mitutoyo (50x, NA0.55) Long Working Distance Objective
<i>Objective numerical aperture</i>	0.55	-	
<i>System magnification</i>	50	-	
<i>Lateral resolution</i>	0.4	μm	
<i>CCD pixel size</i>	3.45×3.45	$\mu\text{m}\times\mu\text{m}$	2448 by 2048 (4Mpx) sensor
<i>Sample rate</i>	15	frames per second	

Table A.3 – Sensor parameters used in error simulations

Sensor	Sensor Type	Dark Noise [e^-/s]	Read Noise [$e^-/read$]	Well Depth [$e^-/pixel$]	Bit Depth
Sony ICX625	CCD	8.73	0.003	5903	8

Table A.4 – Physical properties of GV clusters, aluminum oxide, and water

Property	GV Cluster (air)	Aluminum Oxide	Water
<i>Density (kg/m^3)</i>	1.2	2700	1000
<i>Dynamic Viscosity ($\text{N}\cdot\text{s}/\text{m}^2$)</i>	-	-	8.9×10^{-4}

*Appendix B***DATA PROCESSING AND HANDLING**

This section describes the data structure of the holographic data collected throughout this thesis, as well as all data analysis code used. Data analysis was conducted on both closed and open source applications, namely KOALA (by Lencee Tec), MATLAB (MathWorks), and imageJ. All code that is referenced in this section is linked to an external GitHub repository where the digital source files are available for use [82].

Data and File Structure

The directory where all data is stored for a particular acquisition sequence is a time stamp of the date and time of day it was recorded in the form of ‘YYYY.MM.DD hh-mm’ (e.g. a data set acquired at 2:34 pm on December 3, 2016 would be in a directory named ‘2016.12.03 14-34’). Within this main directory are sub-directories containing the raw holograms called ‘Holograms’ numerically reconstructed data, called ‘Stack’ and a metadata file called ‘timestamps.txt.’

Holograms are named sequentially as zero-indexed five-digit numbers starting at 00000 with a suffix of ‘_holo.tif.’ For example, the 76th hologram would be named ‘00075_holo.tif’. Hologram files are unsigned 8-bit images that are saved as TIFF files. These files have a width and height of 2048 by 2048 pixels, although they do not necessarily need to have these dimensions.

Numerical reconstructions are separated into two sub-directories within the ‘Stack’ folder. These two sub-directories are ‘Amplitude’ and ‘Phase’ based on whether it is an amplitude and/or phase reconstruction. Whether the amplitude or phase sub-directory, the reconstructions are all structured in the same way. Within the folder of the particular reconstruction type are sub-directories corresponding to the various focal planes where reconstructions have been done.

Each focal plane contains all time points where reconstruction has occurred. Because of the reconstruction software used to generate these files, the numerical values assigned to focal plane directories do not directly correspond to units of physical length. The conversion from the naming scheme of the sub-directories to units of

physical distance in the sample volume is

$$1.00 \text{ [A.U.]} = \frac{1}{m^2} \text{ [cm]}, \quad (\text{B.1})$$

where A.U. are ‘arbitrary units,’ m is the magnification of the system, and cm are units of centimeters. For example, in the common mode instrument, which has a magnification of $m = 20$, one A.U. used in the naming scheme of the reconstruction directory is equal to 0.0025 cm or 25 μm .

The metadata is stored in ‘timestamps.txt’ and is structured into 4 columns. First, the file’s name (e.g. 00000, 00001, etc.), second the time (‘hh:mm:ss.sss’), third the date (‘YYYY.MM.DD’), and lastly the elapsed time since the first hologram was recorded in milliseconds.

Numerical Reconstruction with KOALA

Data acquisition is accomplished through the software KOALA. Logging into this software requires a user name and password, which are as follows:

- **User Name:** admin
- **Password:** holo2000

Once logged in, a configuration setting must be selected. Table B.1 provides a comprehensive list of all configurations currently installed on Koala.

The commonly used configuration files are numbers 163 and 170, corresponding to the Mach-Zehnder and common mode instruments, respectively. Make sure to take note of the configuration file used when acquiring data, as this information will be necessary for reconstruction later.

This section discusses the procedure of using the software KOALA, as well as a custom written MATLAB script to conduct multiple reconstructions of a single holographic data set. MATLAB code for this is provide in the GitHub repository under the ‘numericalReconstruction’ directory [82].

Below are the steps required to numerically reconstruct a series of holograms at multiple focal planes using KOALA and MATLAB.

1. Open MATLAB and KOALA, and load the configuration file that was used to acquire the data that is to be reconstructed (refer to Table B.1)

Table B.1 – List of configuration files in KOALA

Conf. #	Name	Description
127	2.5 x 1	
137	SHAMU 1024 BIO	
138	SHAMU 1024 USAF	
139	SHMAU 1024 USAF reverse	
140	SHAMU 1024 USAF BACKUP	DO NOT USE - Jonas
141	SHAMU 2048 USAF reverse	
142	SHAMU 2048 USAF BACKUP	DO NOT USE - Jonas
143	SHAMU 1024 BIO BACKUP	DO NOT USE !
144	SHAMU 1024 BIO v2	
145	SHAMU 1024 BIO Bcopy	Copy for trial
146	Sequence Biceps 20140520	
147	Sequence Ecoli 20140428	
148	Jay sample dense	
149	SHAMU 1024 BIO bonded side-ch-side	
150	SHAMU 1024 BIO fixed chambers - 1024	
151	Emilio	
152	1024 BIO v3	
153	Romans new PDMS	
154	SHMAU 1024 BIO B - 675 laser	
155	1024 Bcopy 675b	
156	SHAMU 2048 JONAS	
157	SHAMU Bcopy 2 (dist 0.3)	
158	SHAMU 2048 Bcopy	
159	2048 USAF Bcopy	
160	trial 1024 USAF	
161	CommonMode 2048	Kent's common mode setup
162	SHAMU 1024-Blanck July 2014	
163	SHAMU 2048 Gene	
164	SHAMU 20x 4MPx	Jonas mag tuneup to 20x-07/16/14
165	SHAMU 20x 1MPx	Upgrade to 20x 07/14/14
166	SHAMU 20x 4MPx biocopy	
167	SHAMU 20x 4MPx bio2	
168	SHAMU 20x 4MPx bio_agar	reset ref hologram for every use
169	Common-mode 4MPx BIO	
170	Common-mode 4MPx BIO local	
171	High-Res MZ 60x 4MPx	Jonas, Jan 2015
172	lensless	
173	chubby bunny	
174	CommonModeField	
175	CM_2lambda_Laser 1	
176	HighResColwellia	
177	HighRes 100x	

2. With the configuration loaded from the KOALA drop down menu, navigate to 'Mode»Hologram' to open a previously recorded hologram. A dialog box will appear. Navigate to the desired hologram file path and open the first hologram (e.g. '00000_holo.tif').
3. Display the desired views (Fourier, Amplitude, and/or Phase). With these open, adjust the reconstruction/focal plane settings and Fourier mask to a desired state and save the configuration.
4. Close configuration windows (hologram, Fourier, etc.)
5. Put KOALA into 'production' mode by selecting 'Mode»Production' in the drop down menu
6. From MATLAB, run the reconstruction script named 'koalaReconstruction.m'
7. When prompted, specify which configuration number was used through Koala (refer to Table B.1)
8. Select the file path for the holograms that are to be reconstructed (i.e. 'YYYY.MM.DD hh-mm')
9. When prompted with 'Do you want to compensate for tilt?', click yes if you wish to compensate for tilt
10. When prompted with 'Add to profile?', select 'no' and allow the reconstruction process to take place
11. Once reconstruction has occurred, append the parent directory's name to include '_r' to indicate that it has been reconstructed (e.g. 'YYYY.MM.DD hh-mm_r').

koalaReconstruction.m

This section discusses the user inputs for the MATLAB script used in reconstruction. Much of the user inputs for the reconstruction script are in the first section of the code, which is as follows:

```

1 %%
2 % Declare global object variable
3 global obj
4
5 % Choose which type of reconstruction to do (1 = yes, 0 = no)
6 phaseRecon = 1;      % Phase Reconstructions
7 ampRecon = 1;       % Amplitude Reconstructions

```

```

8
9 online = false;
10 % online = false;    % Ask user to open a hologram
11 % online = true;     % Perform an aquisition
12 % buffer = 'E:\remote_buffer_directory\';
13
14 Number_wavelength_default = 1;
15
16 % User desired inputs
17 nominal_d = 0;           % Default working distance
18 range_d = 10;           % Plus/minus range_d around ...
    nominal_d in cm
19 delta_d = 0.1;         % Step of reconstruction distance cm
20 degtorad = 0.0174532925; % Conversion factor
21
22 % Reconstruction bounds
23 d_actual = nominal_d;
24 d_min=d_actual-range_d;
25 d_max=d_actual+range_d;
26
27 % Define phase modulo
28 dynrangemin = -pi();
29 dynrangemax = pi();

```

From the above, lines 6, 7, and 18 through 20 are the only user-dependent variables. ‘range_d’ specifies the focus distance desired around the focal plane of interest (‘nominal_d’). ‘delta_d’ specifies the increments of reconstruction in terms of plane distance. Refer to Equation B.1 for more information on the physical meaning of these values.

At times, it is desired to reconstruct multiple focal planes for certain time intervals. In order to do this, a for loop must be modified in the reconstruction script. The segment of code that must be modified is as follows:

```

183 %% Begin Reconstruction
184
185 for x = 1 : length(times)    % Reconstruct all time points
186 %for x = 1 : 132            % For building stacks of ...
    only a range of t
187     Load_xth_holo(formatSequence, seqholo, width, height, ...

```

```

        times(x), SequenceDir);
188     for dist = d_min : delta_d : d_max
189         obj.SetRecDistCM(dist);
190         obj.OnDistanceChange();
191         if phaseRecon
192             dirPhase = strcat(SequenceDir, '\Stack\Phase\', ...
                sprintf('%.2f',dist), '\');
193             if ((exist(dirPhase, 'dir')) ≠ 7)
194                 mkdir(dirPhase);
195             end
196             phasePath = strcat(dirPhase, ...
                sprintf('%05d',times(x)), '.tiff');
197             Phase = GetPhaseImg('lambda1');
198             I8bit = uint8(Phase); %convert data type to bytes
199             imwrite(I8bit, phasePath);
200         end
201         if ampRecon
202             dirAmp = strcat(SequenceDir, ...
                '\Stack\Amplitude\', sprintf('%.2f',dist), '\');
203             if ((exist(dirAmp, 'dir')) ≠ 7)
204                 mkdir(dirAmp);
205             end
206             ampPath = strcat(dirAmp, ...
                sprintf('%05d',times(x)), '.tiff');
207             Amp = GetAmpImg('lambda1');
208             I8bit = uint8(Amp); %convert data type to bytes
209             imwrite(I8bit, ampPath);
210         end
211     end
212 end

```

This loop begins on line 185 of the original reconstruction script. The initial for loop with index ‘*x*’ is the loop that dictates the hologram used for reconstruction, while the nested for loop with index ‘*dist*’ dictates the focal plane of reconstruction. One can modify these two loops’ indices instead of ‘range_d’ and ‘delta_d’ earlier in the code. Editing the bounds of the index variable *x* will give the user control over which hologram(s) are reconstructed. To reconstruct through non-uniform depths (not through $dist \pm \delta_d$), modify the index variable *dist* in the nested loop with appropriate bounds.

The reconstruction process creates a subdirectory ‘YYYY.MM.DD hh-mm/Stack’

where the reconstructed .tiff files are organized and stored.

Image Processing/De-Noising

This section will discuss the image processing steps involved in the work of this thesis. These image processing techniques include mean subtraction as well as spatial frequency filtering. The process of mean subtraction was introduced in the Low-Level Object Detection subsection of Section 5.2.

Mean subtraction is used to attenuate temporally static artifacts from a time series of images. This technique is commonly used in image processing and can be implemented in a variety of ways to a variety of data types.

First, mean subtraction can be implemented using a custom macro in the open source image processing software imageJ or FIJI (Fiji Is Just ImageJ). The macro for doing so is

```
macro MeanSubtract{
  avi = getImageID;
  run("32-bit");
  run("Z Project...", "projection=Mean");
  mean = getImageID;
  imageCalculator("Subtract stack", avi, mean);
}
```

This macro can be used on any arbitrary data sequence that is concatenated to a ‘z-stack’ in imageJ. This includes, but is not limited to, holograms, and amplitude or phase reconstructions.

This same algorithm can be implemented in MATLAB and is done so in a more user friendly manner as part of the machine learning tracking algorithm, which is discussed in Section 5.1. The code for this algorithm is available in the GitHub repository under the ‘automatedTracking’ directory [82].

The implementation of the image processing as part of the machine learning tracking algorithm is more robust than the macro for imageJ and is intended to run on a series of z-plane reconstruction for amplitude and/or phase images. This image processing algorithm involves not only the mean subtraction of each z-plane of the reconstructed stack, but also the spatial frequency filtering of these stacks. Mean subtraction is done as a rolling mean with a predefined window (batch) size. This is because it

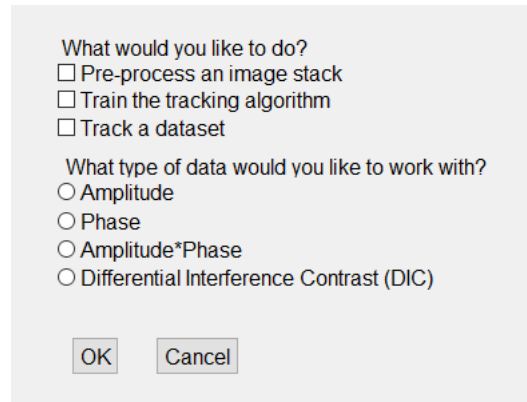


Figure B.1 – Initial dialog box of the automated tracking software suite

was found as a result of the experimentation throughout this thesis, that there is a timescale involved with fringe stability and thus an upper limit exists on the time scale at which mean subtraction can be conducted while yielding acceptable results. For this reason, the batch size can be modified on line 66 of the ‘MAIN.m’ file. Furthermore, the spatial cut-off frequencies can be modified in the code and are located in lines 111-114 of the same file.

The file ‘MAIN.m’ is intended to be the only code that the user must interact with. No inputs are needed to run the script. Simply running the script will display a dialog box in which a user can choose their desired course of action. Figure B.1 shows this dialog box.

To process a series of images (amplitude and/or phase reconstructions), select ‘Pre-process an image stack’ under the question ‘What would you like to do?’, and under the question ‘What type of data would you like to work with?’, select ‘Amplitude’ and/or ‘Phase.’ Other options exist, as seen in Figure B.1, but are not discussed here as they are experimental methods to increase image contrast.

Once the appropriate selections have been made, a navigation pane will appear asking the user to specify the file path of data wished to be processed. Select the parent directory of the data (‘/YYY.MM.DD hh-mm’). Once selected, the process will begin and run to completion.

SNR Calculation

Throughout this thesis, the SNR has often been quantified, but not necessarily reported as a result in a publication or plot. The SNR of an image is a useful metric in analyzing the contrast and image quality of an image. This section presents the

code used in quantifying the SNR of select points in an image. This code can be found in the GitHub repository under the ‘SNRcalculation’ directory [82].

This code expects as an input a variable (I) which is a two-dimensional matrix of the image. The user input parameters are the first two variables of the code in which the line width of the SNR plot line is specified as well as whether the SNR is to be calculated with respect to a ‘bright’ or ‘dark’ object. This code only searches for the absolute maximum of the pixel values in the pixel neighborhood defined by the line width variable. Other more sophisticated curve fitting or peak detection techniques were not employed to maintain the simplicity of the algorithm and stay congruent with other SNR calculation schemes.

Power Spectra Density Function Calculation

When quantifying the optical quality of various substrates in phase reconstruction of the common mode DHM, radial averaging as well as power spectra density (PSD) function calculations were done to quantify the noise levels present at various spatial frequencies of the resulting image. This section presents the MATLAB code used to conduct these calculations. The code for these calculations are available on the GitHub repository in the ‘PSDcalculation’ directory [82].

The MATLAB code ‘PSDmain.m’ was written as a wrapper function that would analyze multiple data sets at once. The contents of this code contain the algorithm used to calculate the radially averaged PSD of a series of images. Within this code, subroutines are called which conduct the radial averaging and PSD calculation ‘radialavg.m’ and ‘PSD.m’, respectively.

‘PSD.m’ expects as an input a two-dimensional matrix corresponding to the pixel values of an image. It calculates the PSD function as defined in the body of the thesis in Equation 3.1.

‘radialavg.m’ expects as an input the PSD matrix that is to be radially averaged as well as the desired number of bins for the output of the radial averaging. The bins are necessary due to the discrete nature of digital images.

Automated Tracking

The code for the machine learning-based automated tracking algorithm is located in the GitHub repository under the ‘automatedTracking’ directory [82].

To implement the automated tracking routine, which was described in detail in Section 5.1 as well as in [5], simply run the MATLAB script ‘MAIN.m.’

A dialog box will appear asking for user inputs and is shown in Figure B.1.

If training the machine learning (ML) algorithm on a new dataset, select ‘Train the tracking algorithm’ as well as the type of data wished to be trained on. If it is desired to track the same data set after training, then select ‘Track a dataset’ as well.

The next navigation pane to appear will ask the file path for the data to be trained and/or tracked. Navigate to the data set’s parent directory (‘YYYY.MM.dd hh-mm’). Next, a navigation pane will ask you where you would like to save the ML model once it has been trained on that particular data set. After this, an image will appear of the data. You will be able to select (using the cursor) all in-focus particles. Once all in-focus particles have been selected, press ‘ENTER’ or ‘RETURN’ to be shown a new z-plane. Repeat this process multiple times. Once the algorithm has received enough data points, the training process will begin. Once trained, the ML model will be saved to the desired location with the desired file name.

If it was desired to track data after training, the algorithm will begin tracking the data immediately after saving the ML model.

During the tracking process, because it can take such a long time, it saves status variables all along the way. In the event of a computer crash, unexpected power failure, or anything that would disrupt the process, simply re-running ‘MAIN.m,’ selecting ‘Track a dataset,’ and following the resulting instructions will begin tracking precisely where the code left off. This prevents the loss of potentially hours’ worth of computation.

Manual Tracking

The machine learning-based automated tracking algorithm, however effective, is only effective for homogeneous samples of a single type of bacteria or particle. Heterogeneous samples, such as environmental samples from the field sites described in Chapter 7, require manual tracking. This is done using either the Manual Tracking plugin in FIJI (Fiji is just imageJ) or a custom written MATLAB script.

In tracking using FIJI, the output is a comma separated values (CSV) file. This file contains many columns pertaining to the (x, y, t) locations of the selected particles. It is possible to conduct depth tracking with this plugin, but the computational requirements are often very high (require many GB’s of RAM). Because of this, z-tracking can be done plane-by-plane, in imageJ or through MATLAB using a custom written MATLAB script.

Z-Tracking with FIJI

Tracking in the z direction can be done on a plane-by-plane basis, but the z -values for a particle at particular points in time must be manually entered in the CSV file.

With the manually entered z information of the sample, the CSV file is complete with the (x, y, z, t) trajectories of a particle. The units of the (x, y) coordinates are in pixels, the units of z are in the arbitrary units of the z -stack naming convention, and the time units are in frame number. A MATLAB script has been written to import the data in these CSV files into a MATLAB workspace variable and convert it to consistent and physically relevant units in order to allow for other downstream analysis.

In order to do this, the CSV files from the FIJI plugin must be imported into MATLAB. The code to do this is in the GitHub repository under the ‘manualTracking/imageJonly’ directory [82].

The main function is ‘importDataCSV.m.’ This script expects as an input a string variable of the file path to the holographic data set (‘./YYYY.MM.DD hh-mm’). This script will import the CSV file, convert all units to either microns or seconds for each tracked particle, calculate turning angles at each time step, calculate velocities of each particles at each time step, and save this data to a ‘.MAT’ file in the parent directory specified at the start of the script. Two common variables that should be paid attention to are on lines 33-34, where the (x, y) field of view are specified in terms of pixel pitch in microns and the z conversion ratio is specified in microns per A.U. (Equation B.1). In this same GitHub repository sub-directory, there are other example data analysis and visualization scripts that can be used and/or customized to fit specific needs.

Z-Tracking with MATLAB

Manual tracking in the z dimension can also be done in MATLAB via a custom written script. Here, (x, y) tracking is done in FIJI similar to the previous section, however, the MATLAB script is used to visualize the data in a streamlined manner to allow for easier tracking in the z dimension. The code to conduct this manual tracking scheme is provided in the GitHub repository under the ‘/manualTracking/matlabANDimageJ’ directory [82]. It is important to note that in this scheme, at least one z -track must be made in the CSV files for each particle. This is to tell the MATLAB script the general z location of the particle.

With the generated CSV files from the Manual Tracking plugin of FIJI, the main

MATLAB script ‘manualTrackingMain.m’ will import the data of each particle that has been tracked and begin tracking in the z direction one at a time. This main script expects as an input the file path to the holographic data’s parent directory (‘./YYYY.MM.DD hh-mm’) as well as a string variable specifying the type of reconstruction wished to be tracked (e.g. ‘Amplitude’).

The MATLAB script will proceed to import the CSV files and display the first particle tracked at the first time point as an XZ slice. This will show the diffraction pattern of the object. By looking for the ‘waist’ of this diffraction pattern, the precise z location can be obtained. Follow the on-screen instructions to continue tracking the particle through time. Once finished with a particular particle, the next particle will be shown and the process can be repeated.

After each particle has been tracked, the workspace variables are saved to avoid loss of data as a result of a program crash or power failure. The data will be saved in physical units of microns and seconds for other downstream analysis and data visualization.

Tracking with MATLAB Only

Lastly, a custom written MATLAB script was written to conduct tracking without the use of imageJ altogether. This script, along with all of its dependant sub-routines can be found in the GitHub repository under the ‘manualTracking/matlabOnly’ directory [82].

The main script, ‘manualTrackingMain.m’, expects as an input the file path to the parent directory of the holographic data set to be tracked (‘./YYYY.MM.DD hh-mm’) as well as a string variable specifying the type of reconstruction desired to be tracked (e.g. ‘Amplitude’).

This script functions much like the Manual Tracking plugin in the sense that it presents the user with a particle z -plane of data and asks the user to begin tracking a particle. If no particle exists in focus at that particular z -plane, press ‘ENTER’ or ‘RETURN’ to be shown a new z -plane. Once a particle is found, simply click on the location of the particle and press ‘ENTER’ or ‘RETURN,’ the next time point will be shown, and the process will be repeated. After each particle is tracked in the (x, y) dimensions, XZ slices of each location of that particle through time will be displayed for the user to track in the z direction. This step is identical to what was described in the previous section.

After each particle has been tracked, the workspace variables are saved to avoid

loss of data as a result of a program crash or power failure. The data will be saved in physical units of microns and seconds for other downstream analysis and data visualization.

Reorientation Frequency Analysis

The result of the various tracking methods discussed earlier are CSV files containing spatio-temporal information of various tracked organisms. From these (x, y, z, t) coordinates, various statistical analyses are possible. One statistical metric of interest for the analysis of bacterial motility is the temporal frequency of reorientation. As a bacterium swims, various phenomena can cause the bacterium to reorient itself and to begin swimming in a different direction. The timescale of this reorientation can shed light on the type of organism that is tracked.

This analysis is accomplished by analyzing the turning angle of each tracked organism as a function of time. Figure B.2 shows a typical plot of a tracked organism's turning angle as a function of time. From this plot, with the use of a standard peak detection algorithm, we can find the timescales between local maxima in various ranges of turning angles. Code for the analysis of timescales of reorientation for three angle ranges are provided in the MATLAB code 'importDataCSV.m', which is included in the GitHub repository for this thesis [82]. The three angle intervals are angles between:

1. $0^\circ \leq \theta \leq 45^\circ$
2. $45^\circ < \theta \leq 135^\circ$
3. $135^\circ < \theta \leq 180^\circ$

Residual Fringe Visibility as a Means of Enhanced Image Contrast

This section describes the use and implementation of the residual fringe visibility section. The code discussed in this section is available in the 'residualFringeVisibility' directory of the GitHub repository [82].

The main function for this algorithm is called 'residualFringe.m.' This MATLAB routine does not expect any inputs as the only input that is needed is received via GUI. This GUI automatically launches when the file is run and asks the user to navigate to the data set of interest. There are a few user defined variables that must be set prior to running the code, however. These variables include:

- Image batch size *bSize* (in units of numbers of holograms)

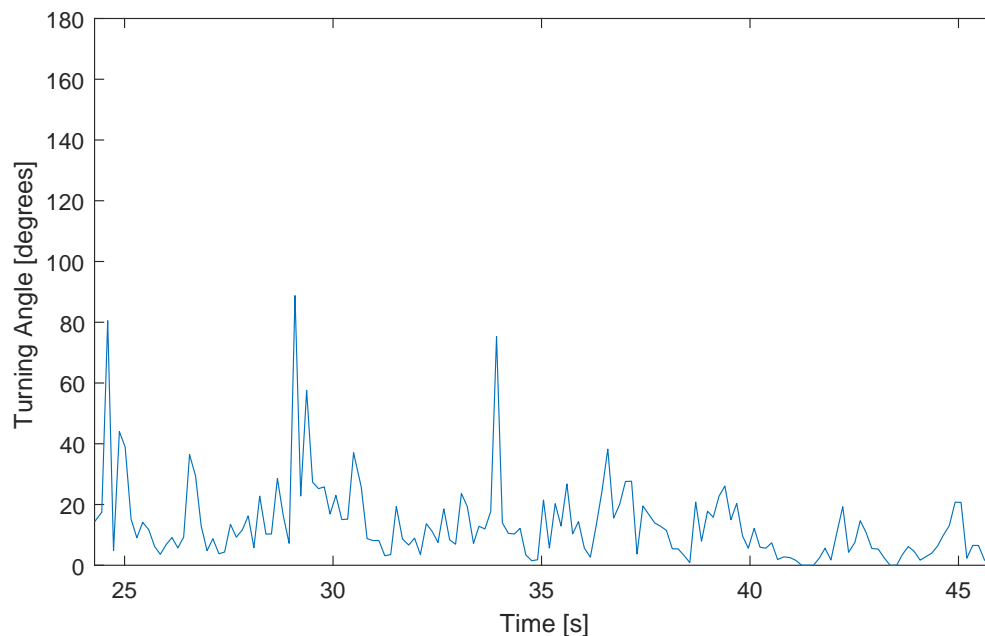


Figure B.2 – Plot of turning angles as a function of time.

- Use 'Box Car' average scheme? *boxCar* (1=yes, 0=no)
- Search for and remove duplicate holograms? *removeDupes* (1=yes, 0=no)

The *bSize* variable dictates the number of holograms to use when conducting background subtraction. This number is closely related to the number of frames that were experimentally found to correspond to the fringe stability of the DHM system, see 5.2.

The *boxCar* variable decides whether the 'Box Car' average scheme is used for background subtraction. This involves the calculation of a temporally averaged hologram while using a sliding window of size *bSize*. This scheme is useful for smaller data sets where RAM capacity is not an issue. For larger data sets, *boxCar* should be set to 0 as the regular mean subtraction algorithm was specifically written to handle larger data sets.

The *removeDupes* variable decides whether to search for and remove duplicate holograms from the mean calculation. Throughout the use of the commercially available data acquisition software KOALA, it was seen that running the camera at its nominal rate of 15 frames per second would result in about a 30% loss of data. The software would make up for this loss of data by rewriting the last frame acquired as a new frame without notifying the user of the lost frame(s). Because

of the duplicated holograms, this results in a skewed temporally average hologram calculation as the duplicated holograms become falsely weighted in the average calculation. The removal of duplicate frames is a lengthy process depending on the data set size, and in addition, other DAQ methods have been developed without this issue. Because of this, the user is presented with the option to bypass the duplicate removal step.

With these variables, the code then proceeds to process all holograms in the data by background subtraction. This background subtraction routine is outlined in Chapter 5.2.

Once processed, the holograms are then saved to a separate directory within the main directory of the data set using the same naming convention of the raw holograms.

This program ends at this stage in order to allow for different types of downstream analysis.

Off-Axis Hologram Simulations

The code to generate simulated off-axis holograms is available on the GitHub repository under the directory 'hologramSimulation'[82].

The optical theory used in the MATLAB code discussed in this document are well reviewed by Ulf Schnars, et al. [104]. The main function ('OAhologramSimulator.m') expects two variables as an input. The first is called 'waveFront.' This is a complex matrix of the size of the final image. This matrix describes the normalized amplitude and phase of the electric field of the sample we wish to simulate. For the purposes of this manuscript, the variable 'waveFront' is provided in the file 'waveFront.mat.' The second input variable is 'desiredFileName,' which is the desired file path and name of the output. The output is the final 8-bit TIFF hologram.

The variable 'waveFront' is generated by creating two three-dimensional matrices of the electric field attenuation and the index of refraction of light that passes through a cylindrical simulated 'salmonella cell' with the morphology as shown in the main manuscript. With the two 3D matrices, a series of radon transforms are used to project a collimated beam of light through the object. These projections are then used to calculate the resultant wavefront as a result of the projected electric field attenuation and phase delay (introduced by the index of refraction matrix). The hologram simulation code can be separated and described in eight sections.

DHM Parameters

This section establishes the optical performance parameters of the DHM instrument that is to be simulated. In this implementation, the off-axis holograms that are being simulated are of the ‘low-power’ instrument and have the appropriate performance parameters for that instrument.

Note that the numerical aperture of the objective lenses is not necessary because the geometric properties of the objective lens is inputted as ‘fl’ and ‘DiaLens’ (lens focal length and lens diameter, respectively).

Create the undisturbed reference beam

This section creates the reference wave. The reference wave by definition is undisturbed and un-attenuated, thus the reference wave is a simple matrix of ones.

Propagate target and ref to lens object focal plane

This section takes the input variable ‘waveFront’ and the newly created reference wave front ‘U2ref’ and propagates the two waves to the focal plane of the objective lens. The propagation of the two waves is conducted using the Angular Spectrum Method (ASM) as described in Schnars, et al. The propagation is done by calling an external function ‘ang_spec_prop.m.’ The output of this section are the variables ‘U3’ and ‘U3ref’ corresponding to the propagated wave front of the sample (U3) and reference (U3ref).

Propagate to the lens

This section takes the output from the previous section and propagates the two wave fronts to the objective lens. This section uses the same external function as the previous section. The outputs are ‘U4’ and ‘U4ref’.

Simulate the phase delay introduced by the lens

This section models an ideal objective lens that introduces a phase delay into light as it travels through the lens. This simulates an ideal lens because it introduces no wave front aberrations or electric field attenuation.

In addition to simulating the phase delay caused by the objective lens, it applies this phase delay to ‘U4’ and U4ref.’ The output of this section is ‘Alens’ and ‘Alensref.’

Propagate to the focal plane

This section takes the output of the previous section and propagates the two wave fronts to the back focal plane of the objective lens. The output of this section are the variables 'U5' and 'U5ref.'

Combine wavefront with reference wave

This section acts as the relay lens of the 'low-power' instrument by recombining the object wave front (U5) with the reference wave front (U5ref) as well as introducing a tilt angle between them so that they create interference patterns at the 'detector.' The output of this section becomes a single complex wave front 'Uccd.'

Generate and save the hologram

Because optical detectors such as CCD's only image electric field intensities, the intensity of 'Uccd' is calculated and saved as an 8-bit TIFF image with the file path and location inputted at the very beginning of this routine.

*Appendix C***EXPERIMENTAL TECHNIQUES**

Throughout this thesis, sophisticated laboratory methods and materials were employed in order to conduct the experimentation presented. In addition, novel experimental techniques were developed and employed during field campaigns to conduct sophisticated experimentation in remote and extreme environments. This Appendix describes, in detail, the methods and materials used in the development of gas vesicles as an optical phase contrast agent (discussed in Chapter 6). This Appendix also discusses the novel experimental techniques developed and employed on the field campaigns to Utqiagvik (Barrow), AK and The Cedars, CA.

Methods and Materials Regarding Chapter 6**Author Contributions**

Arash Farhadi (AF), Manuel Bedrossian (MB), Mikhail G. Shapiro (MGS), and Jay Nadeau (JN) conceived and planned the research. AF, JL, and GH prepared the biological samples. MB and JN conducted the DHM data collection and reconstruction with help from AF. MB carried out the generation and analysis of the salmonella hologram simulations as well as the analysis particle and salmonella image reconstruction and data analysis. MB performed the processing and rendering of the 3D pseudo-colored phase image of CHO cells. AF, MB, MGS and JN analyzed the results, and wrote the manuscript with input from all authors. MGS, and JN supervised the research.

Anabaena gas vesicle expression, purification and clustering

Anabaena flos-aquae (CCAP strain 1403/13F) was cultured for ≈ 2 weeks in Gorham's media supplemented with BG-11 solution (Sigma) and 10 mM NaHCO₃ at 25 °C, 100 rpm under 1% CO₂ and a 14:10 hour light/dark cycle. At confluency, the buoyant cell fraction was isolated by floating to the top of a separating funnel over a 48h period, after which the supernatant was discarded. The collected cells were then lysed using 500 mM sorbitol and 10% Solulyse solution (Genlantis). Gas vesicles were purified through repeated rounds of isolating the buoyant fraction through centrifugation and resuspension in phosphate-buffered saline.

Gas vesicle clusters were synthesized by first biotinylating purified GVs with 105

molar excess of EZ-Link Sulfo-NHS-LC-biotin (Thermo Scientific) in PBS buffer for 4-hours. Afterwards, the sample underwent 2 rounds of overnight dialysis in PBS buffer. The biotinylated GVs were then clustered by incubation with streptavidin (Geno Technology) for 30-minutes at room temperature.

Dynamic Light Scattering (DLS)

The hydrodynamic size of the gas vesicles, gas vesicle clusters, and alumina beads were measured in 50 μL samples at $\text{OD}_{500} = 0.2$ using a Zeta-PALS analyzer (Brookhaven Instruments). Samples were mixed thoroughly and measured five times for each reported hydrodynamic diameter.

Engineered gas vesicles for cell labelling

The process of genetically engineering the surface of gas vesicles for cell labeling has been previously describe [72]. In brief, gas vesicle protein C gene sequence from *Anabaena flos-aquae* was codon-optimized for E. coli expression and cloned into a pET28a(+) plasmid (Novagen) with an N-terminal hexahistidine-tag and C-terminal GSGRRRRRRRR sequence. Plasmids were transformed into BL21(DE3) cells (Invitrogen) and expressed for recombinant polyarginine modified-gas vesicle protein C after 6-hour expression at 30°C. Polyarginine modified-gas vesicle protein C in the form of inclusion bodies was purified by lysing the cells using 10% Solu-lyse supplemented with DNaseI (10 $\mu\text{g}/\text{mL}$) and lysozyme (400 $\mu\text{g}/\text{mL}$) at room temperature. Inclusion bodies were recovered by centrifugation at 27,000 g for 15 minutes in an ultracentrifuge. The inclusion body pellets were resuspended in 20 mM Tris-HCl buffer with 500 mM sodium chloride and 6 M urea (pH 8.0) and incubated with Ni-NTA resin (Qiagen, Valencia, CA) for 2h at 4°C. After washing, proteins were eluted using 250 mM imidazole.

Purified GVs were treated with 6 M urea and 20 mM Tris-HCl (pH = 8.0) to remove their wild-type gas vesicle protein C. The stripped gas vesicles were isolated with two rounds of centrifugally assisted buoyancy purification in urea. Purified polyarginine modified-gas vesicle protein C was then added according to the formula $2 \times \text{optical density} \times 198 \text{ nM} \times \text{liters GVs} = \text{nmol of recombinant gas vesicle protein C}$ and dialyzed in PBS for 8 hours. 105 molar excess of Alexa Fluor 488 NHS was then added to the GVs and incubated at room temperature for 4 hours under gentle rotation, before being quenched with 20 mM Tris-HCl (pH = 8.0), and dialyzed in PBS again to remove excess dyes.

Cell culture and GV labeling

Chinese hamster ovary (CHO-K1; ATCC) cells were cultured in DMEM with 10% FBS and penicillin/streptomycin. Coverslips (18x18 mm) were sterilized with 70% ethanol and washed twice in PBS and placed in 6-well plates. Fibronectin (Sigma) was diluted 1:20 in PBS and 200 μL was added to each well over the entire surface of the coverslip and incubated for 1 hour at room temperature. Excess solution was aspirated and CHO-K1 cells were seeded on the coverslips and grown to 75% confluency.

For GV labeling, a 6-well plate was coated with paraffin and UV sterilized. Then, 300 μL of 37°C DMEM media and 300 μL of 114 pM ($\text{OD}_{500} = 1$) of R8-gas vesicles was added to the bottom of the well and mixed. The cells cultured on coverslips were inverted onto the DMEM and gas vesicle mixture, so the cells were facing the bottom of the plate. The coverslips and gas vesicles were incubated at 37°C. Following incubation, the cells were washed three times with 200 μL of PBS and fixed with 1 mL of formaldehyde for 30 minutes. The coverslips were mounted using Diamond Antifade mountant (Thermo Fisher) and sealed using clear nail polish.

Fluorescence imaging

Fluorescence images were taken on an Olympus IX-71 inverted microscope using Hg lamp illumination through a 1.4 NA oil immersion objective and using the enhanced green fluorescent protein (EGFP) filter set (Chroma). To register fluorescence image with phase images, a 1 μm tip glass pipette was secured to the specimen and cells were imaged in the vicinity of the tip across the two instruments.

Gas Vesicle Expression in Salmonella

Gas vesicle expression in *Salmonella typhimurium* (strain ELH1301) cells has been described previously [23]. Briefly, the gene cluster encoding a hybrid gas vesicle variant was cloned in pTD103 (gift from Jeff Hasty) and transformed into *S. typhimurium* cells and cells from an individual colonies cryostocked. Cells containing the gas vesicle gene were grown in 5 mL of 2xYT media with 50 $\mu\text{g}/\text{ml}$ kanamycin for 16 hours at 37°C, 250 rpm. Cultures in 50 mL 2xYT media with 50 $\mu\text{g}/\text{ml}$ kanamycin were then inoculated with 500 μL of the starter culture and grown on the shaker at 37°C until $\text{OD}_{600} = 0.4-0.6$. These cultures were induced with 3 nM N-(β -ketocaproyl)-L-homoserine lactone (AHL), and then grown for 22 hours at 30°C, 250 rpm. Cells were then harvested by spinning at 300 g at 30°C for 2 hours. The buoyant cell fraction was transferred into clean tubes. To collapse the

gas vesicles inside cells, gas vesicle-expressing salmonella were placed in a quartz cuvette (Hellma Analytics) connected to a N₂ cylinder through a pressure controller (Alicat Scientific) set to 1.2 MPa.

TEM sample preparation and imaging

Electron microscopy was performed in the Beckman Institute Resource Center for Transmission Electron Microscopy at Caltech. Purified gas vesicles were diluted to $OD_{500} = 0.2$ in 10 mM HEPES buffer and Salmonella cells were diluted to $OD_{600} \approx 0.2$ in 10 mM HEPES buffer or PBS. Samples were then spotted on Formvar/Carbon 200 mesh grids (Ted Pella), which were rendered hydrophilic by glow discharging (Emitek K100X). Purified gas vesicle samples were stained with 2% uranyl acetate while cells were imaged unstained. Image acquisition was performed using a Tecnai T12 Lab6 120 kV transmission electron microscope equipped with a Gatan Ultrascan 2k x 2k CCD camera.

Holographic Simulations

Holograms were simulated with MATLAB (R2017b) using a custom hologram simulation routine. First, a two-dimensional projection image was created using a series of Radon Transforms, modeling a typical gas vesicle expressing Salmonella cell as a cylinder, with a diameter of 1 μm and a length of 5 μm , with bands of lower refractive index corresponding to areas dense in gas vesicles as seen in TEM images. This projection is then downsampled, via bicubic interpolation, in order to accommodate and emulate the diffraction limited resolution of the common mode DHM instrument. Within this projection, gas vesicles were simulated using index of refraction of 1.00. Other intracellular areas were simulated using an index of refraction of 1.37. The index of refraction used to simulate the cell's surrounding medium is 1.33.

The wavefront perturbations as a result of a collimated plane wave passing through the simulated cell is then propagated using the Angular Spectrum Method [104]. The resulting diffracted wavefront is numerically propagated and recombined with a reference (undisturbed) plane wave in order to simulate an off-axis hologram. Code for the simulator is provided in Appendix B. The simulated holograms were reconstructed into amplitude and phase images using the commercially available software KOALA (LynceeTec). No image noise was added to the simulation besides quantization noise when the holograms were saved as 8-bit image files whereas in reality there are numerous sources of noise including, but not limited to, photon

'shot' noise, temporal and spatial noise due to changes in the coherence of the illumination laser, as well as various sources of noise introduced by the digital CCD used to record the holograms.

Throughout this thesis, two custom experimental techniques were developed and used in field experimentation. This appendix provides information and verification of these experimental techniques.

3D Pseudo-Colored CHO Image Rendering

The 3D rendering was generated using the commercially available software ARIVIS Vision4D. This software allows the import of a multidimensional image that is to be visualized in a variety of ways. The 2D images that comprise the 3D image stack used in ARIVIS were first processed using the methods described in the Image Processing & Handling section of this document. These processed images were then thresholded using a user defined threshold. Next, the magnitude of the image gradient was calculated and stored as a separate stack of 2D images. The two 3D image stacks were then imported to ARIVIS Vision4D. The pixel values were plotted using a pseudo-colored lookup table. The opacity of each pixel was plotted as a weighted function of the magnitude of the image gradient at that pixel. This was done to highlight areas of large changes in phase signal within the cell.

Thermal Gradient Generator

In the investigation of the effects of temperature on the motility characteristics of arctic liquid samples, a custom thermal gradient generator was constructed that would establish and maintain a quantifiable thermal gradient in a liquid sample.

This temperature gradient is established using a commercially available temperature controller (Thorlabs TC200) with an adhesive backed heating element with embedded temperature sensor. With the closed loop of the embedded temperature sensor, this controller can maintain constant temperature of a surface using a standard PID control loop. This heating element is attached to a thin metallic surface such that there is sufficient thermal contact. The metallic surface is then thermally insulated in all directions except for a single surface. This surface is the surface on which the sample chamber will rest. The heating element provides a heat source, while a free end, at the other side of the sample chamber, acts as the heat sink. This heat sink is open to ambient temperature. By constraining the flow of thermal energy to only this surface, it can be assumed that thermal dissipation can only happen through conduction, which results in a linear thermal gradient. Of course, convection occurs

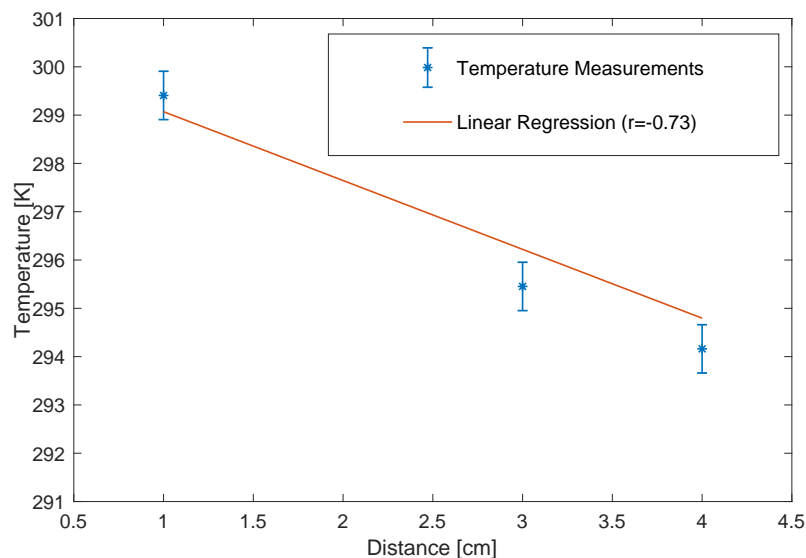


Figure C.1 – The temperature along the thermal gradient generator with a linear correlation of $r = -0.73$

as well, which introduces non-linearity to the temperature gradient, but as will be seen, these effects are negligible as the measured gradient has a high degree of linear correlation.

To verify the design and linearity of this experimental technique, the temperature controller was used to establish a thermal gradient on a metallic plate. Sufficient time was allotted for this plate to reach thermal equilibrium and temperatures were measured at various points along the plate. Figure C.1 shows a typical thermal gradient established with this method. With a linear correlation coefficient of $r = -0.73$ showing a strong linear correlation in temperature as a function of distance along the plate, it can be assumed that this experimental technique is capable of establishing a steady and quasi-linear temperature gradient.

Pulsatile Flow Dampener

In the quantification of particle concentrations of field samples from sources such as the ultrabasic springs of The Cedars in Northern California, a peristaltic pump is often used to continuously sample from the spring. For the quantification scheme used with the DHM instrument, the pulsating nature of a peristaltic pump is undesirable and can introduce errors in the concentration calculation scheme. Because a steady flow is needed, an experimental technique was developed which was inspired by my undergraduate thesis project [10] involving the development of a failure

detection method for a pulsation dampener. These pulsation dampeners are used in conjunction with peristaltic pumps in order to attenuate pressure spikes in the flow which can lead to water hammer and other undesirable effects. The basis for these pulsation dampeners is that by exposing the flow to a gas-filled bladder with a deformable membrane, momentum from the flow can be taken and converted to mechanical energy, which compresses the gas-filled bladder. This can attenuate the pulsatile flow characteristics of a peristaltic pump by multiple orders of magnitude.

In this implementation, a sterile deformable container was used in parallel to a peristaltic pump which would absorb the pulsations introduced by the pump so that the flow outward toward the sample chamber of the DHM would be uniform and steady. Figure C.2 shows an in-field image of the experimental setup. Right after the exit of the sample chamber, a pinch valve was used to regulate the flow through the sample chamber.

Care was taken in the design of the sample chambers for this experiment as well. In this technique, we are concerned with imaging cells as they flow through the field of view of the DHM. In order to do this, we must have a sufficient camera frame rate as to be able to image every cell that passes through the FOV. If the camera frame rate is too slow, a cell can potentially pass through the FOV of the DHM without being imaged. Furthermore, we would want the flow through the DHM to be in a single direction. These two constraints cause the Reynolds Number and Dean Number to be of importance in the design process. These two dimensionless numbers can shed light on the maximum expected velocity of the fluid through the sample chamber as well as if there are any secondary flow effects introduced by curvature in the flow. Appendix E discusses this further. A custom written Microsoft Excel worksheet was written for convenient in-field calculation of these metrics and is provided electronically in the GitHub repository under the main directory [82].

The volumetric flow rate through the sample chamber was measured using a 5 mL graduated cylinder. Flow rates were quantified by measuring the total amount of liquid dispensed from the sample chamber of three-minute intervals done in triplicate.



Figure C.2 – Experimental setup of the in-field pulsation dampener

*Appendix D***BIO-SAFETY AND MICROBIOLOGY PROTOCOLS**

This Appendix is intended to discuss the microbiological concerns and considerations that must be made when conducting biological research in the laboratory or field. Many factors must be considered when conducting biological work regardless of where the work may take place. These considerations include, but are not limited to, general laboratory rules and regulations, safety precautions, personal protective equipment, culture/sample handling procedures, and sterilization techniques. Many resources exist, including the safety officer in charge of any given laboratory. For more information about these considerations, a well-documented book on these techniques is written by Wistreich and can prove to be a useful guide [126].

This appendix will focus mostly on the sample collection and handling of field samples. In the course of data collection in Utqiagvik (Barrow), AK I along with Jay Nadeau (professor of Physics at Portland State University and member of this PhD committee) and Jody Deming (professor of Oceanography and Ocean Microbiology at the University of Washington, Seattle), were invited to write a chapter in the textbook 'Methods in Microbiology' on our sample collection and analysis technique. This book chapter can be found here [13]. The following sections are excerpts from the book chapter that are related to sample handling and preliminary analysis. The excerpts shown here were predominantly written by myself, although Dr. Nadeau and Dr. Deming provided tremendous support and editorial comment.

Metadata and Sample Labeling

Samples should be identified with all appropriate metadata. Metadata may be included directly in the publications or deposited in data repositories. Repositories may be specific to the journals published by a particular society, such as the Geological Society of America data repository, or more general and available to authors in any journal.

At minimum, metadata should include:

- Latitude and longitude
- Date and time

- Liquid samples: temperature, salinity, pH
- Weather conditions, including air temperature, cloud fraction, wind speed and direction, and contact information for complete meteorological data from a nearby ship or station
- Water depth (as appropriate)
- Ice samples: ice texture, density; depth in the core, measured from the top
- Estimates of snow or melt-pond coverage and measurements of their depths on the surface of the ice
- Sample description. For sea ice, include approximate age (whether multi-year or first-year ice, and for young ice, an estimate of time since initial ice formation), thickness, freeboard, and texture; for ice core sections, include temperature and bulk salinity. Eicken et al. [42] contain excellent descriptions of how to collect these metadata. For glacier ice, the Ice Cores Working Group has defined sets of metadata as Essential, Recommended, and Desired from the point of view of palaeoclimate research. Essential metadata include age scale and dating points, any melt in transport, depth of any melt layers, depth of any ash layers, and whether the core was taken in discrete intervals or continuously. For permafrost, important metadata include thickness of the active layer and borehole temperature. The Global Terrestrial Network for Permafrost (GTP-N) maintains a database of permafrost data [17].

Collection Methods

The key aspect in microbiological studies is to keep the sample in as close to *in situ* conditions as possible before analysis. This means preventing contamination and shifts in temperature or salinity (causing thermal or osmotic shock), and maintaining *in situ* light conditions (the latter can be crucial for photosynthetic organisms). In addition to avoiding shocks to the ice-adapted inhabitants, even slight warming should be avoided as some microorganisms dormant in the sample under *in situ* conditions may begin to grow under altered conditions.

Samples from cold liquid environments, such as seawater or cold springs, may be collected as from any (warmer) liquid environment, subject to the caveats discussed earlier. Sampling of frozen environments poses specific challenges as discussed in the following sections. Any low-biomass samples that will be evaluated for microbial counts and/or activity need to be protected scrupulously from contamination. This means handling them with ethanol-rinsed gloved hands and sterilized tools in the

field, and manipulating them inside laminar flow cabinets on sterilized surfaces in the laboratory. Such concerns are of lesser importance for high biomass samples such as biofilms or bacteria adherent to minerals (as in permafrost), unless highly sensitive techniques such as quantitative PCR are to be applied. Nevertheless, proper sterile technique should be kept in mind at all times.

Bulk Ice

For any bulk ice sample, the primary challenges are (1) collecting the sample without contamination and (2) processing the sample without losing or destroying the cells. The first challenge is to collect and process the ice without introducing contaminants from the surrounding environment including any soil or water, the investigators' hands and tools, or even the air. The equipment typically needed to sample bulk sea ice, for example, includes: clean core extractor, ethanol-rinsed hand saw for ice sectioning, and sterilized foil and plastic for wrapping/containing core sections until later processing. Ethanol (for sea ice) or sodium hypochlorite (bleach, for glacial ice) can be used with care for decontamination.

For both sea and glacier ice, coring is the standard approach, using a core extractor. Some of the most common drilling kits for glacier ice include the IDDO Auger kit, the PICO Auger kit, the Mark II coring system, and the SIPRE auger kit [15]. Also needed are a T handle (for manual coring) or an electric drill adaptor (for use with an electric drill), an electric drill (if desired), and core retrieval tongs. A typical ice-coring barrel consists of four components: a cutting blade, hollow cylindrical barrel, rifled barrel flutes to evacuate ice chips, and a connector hub to attach a T handle or electric drill.

Because the hole depth of a typical sea ice core is more than 10 times that of the bore diameter, an interrupted drilling technique is often used in coring sea ice. By periodically lifting the coring barrel, though stopping short of removing it from the bore hole, the ice chips and possible liquid that have accumulated around the barrel flutes can be removed for more effective continued coring. Most ice core barrels also have internal carbide "teeth" that are intended to catch ice cores once drilled all the way through the ice (to underlying seawater). This feature allows retrieval of full ice cores. Cores are frequently, but not always, sectioned and bagged on site. If such on-site work is not possible, full cores can be placed into sterilized plastic sleeves and transported to the laboratory before sectioning and processing [81]. Black plastic sleeves can be used to protect against exposure to light during

transport.

Ice core sections may be prepared in the field by placing the ice core onto a cutting board, first ethanol-rinsed or covered by autoclaved foil, and slicing with an ethanol-rinsed saw. These actions should be taken quickly, especially in the case of highly porous ice, in order to minimize loss of interstitial fluid by drainage. The thickness of the core sections may vary, but parameters are best analyzed on sections of comparable thickness. Equivalent sections from multiple cores may be pooled during (or after) melting to increase the available volume, provided that information on horizontal heterogeneity is not needed.

Samples should be kept as close to the *in situ* temperature as possible during sawing and later melting, to prevent thermal or osmotic shock to the microorganisms, and light exposure needs to be minimized during transport and storage to limit growth, light shock, and photochemical degradation.

The outer surface of a glacial ice core must be decontaminated to prevent surface organisms from being represented in the sample. A 2004 study carefully compared chemical and physical methods of decontamination and found that only 5% sodium hypochlorite killed all external organisms with little effect on internal organisms [98]. This procedure has been adopted as a standard protocol for glacial ice. The core is immersed into 5% sodium hypochlorite for 10 s, then rinsed three times with sterile water. Core sections are melted and then treated like any other liquid sample.

For sea ice, cores are usually sectioned from the bottom to limit brine loss from more channelized or permeable parts of the ice. Decontamination is not standard because of the higher organism concentration in sea ice cores. Sea ice in early stages of formation presents particular challenges of both access and sampling because it cannot bear a load. It may be sampled from a small boat or by reaching out from the safety of shore while tethered to a fixed object (Figure D.1). When thin enough, it may be sampled with a (sterilized) trowel or bottle. When thicker but still unconsolidated, a “frazil sampler” may be used. This is simply a transparent plastic tube with a rubber stopper on the end. The tube is submerged and then the end is closed. A ruler or calibration mark permits measurement of ice depth [114].

Sea Ice Brine

In order to access a significant volume of sea ice brine, a hole can be drilled into the ice cover (without penetrating to seawater below) and left to collect brine as it drains into the hole from the exposed brine channels and veins in the surrounding ice

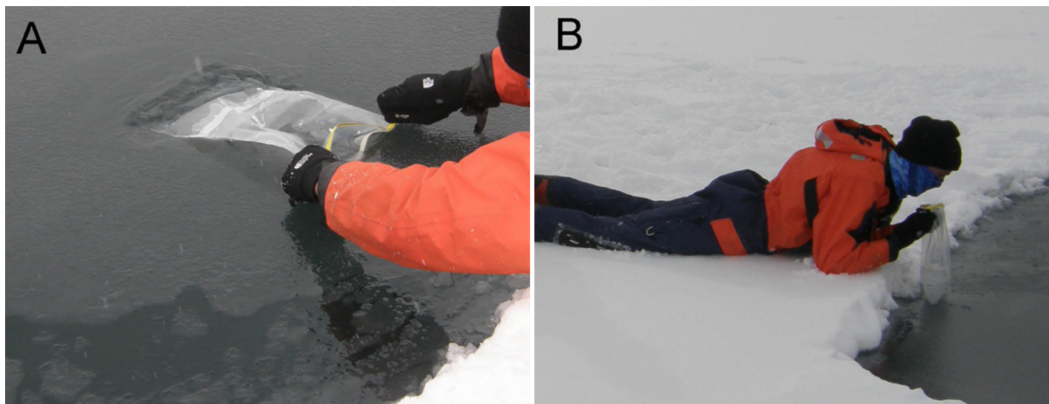


Figure D.1 – Sampling new sea ice. (A) Using a sterile bag to collect new (hour-old) “grease ice” as it forms on the surface of freezing seawater at the edge (lower right) of young (month-old) sea ice. Ethanol-rinsed latex gloves should be worn when the sample is intended for microbiological analysis. (B) Young sea ice can support the weight of a researcher, but safety precautions include wearing an immersion suit, as shown, and a harness with tethering rope to a secure position.

walls. This “sackhole” collection approach is most effective in the warmer sea ice seasons. First, it is necessary to measure the ice thickness near the location where sea ice brine is to be collected. Using an ice augur or the ice core barrel, a hole is drilled all the way through the ice to seawater, about 1 m away from the intended sample collection site, after clearing any snow cover. The thickness of the ice is then measured using a weighted depth gauge indicator. Once the approximate ice thickness is known, the same interrupted drilling method is used at the collection site to drill to the desired depth, for example, 50%–70% of the ice thickness. Once at this depth, the ice core is removed, leaving a cylindrical hole in the sea ice that does not penetrate to underlying seawater. The hole is covered to prevent aerial inputs and simulate snow cover, if light is an important factor in the study, and sufficient time is allotted for brine to accumulate in the hole. Expected sample yields, depending on the temperature (and thus position in the ice cover and season), can be in the hundreds of milliliters over the course of an hour or two (Figure D.2).

Cryopeg Brines

Cryopegs are unfrozen soils within permafrost that contain “lenses” of brine remaining liquid at the *in situ* temperatures of 6°C to 11°C due to high salt concentrations. These marine cryopegs have also been called “cryosaline water” or “overcooled brine” [56]. They are unique among Earth’s hydrogeological systems in being isolated from external factors for tens to hundreds of thousands of years and perma-



Figure D.2 – Ice coring in Utqiagvik (formerly Barrow), Alaska. (A) The interrupted coring technique is used to drill into sea ice, while another team member clears ice chips from the drill site. A third team member has completed the process of clearing the snow cover from the planned coring area. (B) Using a weighted depth gauge to measure the sea ice thickness through a borehole drilled through the ice to underlying seawater; the gauge is designed to anchor to the underside of the ice for a taught pull upwards. (C) Using core retrieval tongs to pull a partial ice core out of the sea ice cover and establish a “sackhole” for the accumulation of sea ice brine. Photos courtesy of Anders Torstensson.

nently below 0°C [6]. Although radar suggests they are common in Arctic coastal permafrost, they are not well studied microbiologically because identifying, locating, and sampling them without contamination all present formidable challenges. Of those published, most studies have derived from Siberian locations, with only two from Alaskan locations, in one case [32] from the fortuitous existence of the Barrow Permafrost Tunnel, excavated in the 1960’s by the US Army Cold Regions Research and Engineering Laboratory (CRREL) for geological purposes. This tunnel permits researchers to access a horizontal excavation 10 m long and 6–8 m below surface, where in 2004 geophysical methods indicated the presence of brines 1.3 m below the tunnel floor [84]. Polyvinylchloride tubes were inserted through narrow boreholes into the cryopeg layer at different locations and left capped for future access. Using a hand pump, vacuum flasks, and sterile tubing, brine was later collected into sterile containers, placed in coolers, and quickly transported to the laboratory for processing [32].

*Appendix E***TECHNICAL INFORMATION**

This Appendix contains all technical information referenced throughout the thesis. This includes a list of all objective lenses that were successfully tested on the Mach-Zehnder DHM instrument, as well as descriptions and technical drawings, with references to digital CAD files, for the designs that were discussed throughout this thesis. First, information on the objective lenses used on the Mach-Zehnder instrument will be introduced, followed by a discussion of the design principles used in the design and fabrication of all sample chambers. This includes the designs for field instrument sample chambers, as well as the mold designs that were used to manufacture them. Next, the evolution of the sample chambers' manufacturing to more repeatable/scalable methods are introduced. The design and schematics for the electronics package of the miniaturized DHM field instrument will also be discussed. This includes digital prototype PCB designs with references to the digital file in the GitHub repository under the 'fieldInstrumentPCB' directory.

Both the design and manufacturing techniques of the DHM sample chambers have iteratively evolved throughout the time of this project. These iterations can be separated into two main categories: 1) Reusable sample chambers and 2) Disposable sample chambers.

Objective Lenses for Mach-Zehnder DHM

The four tested objective lenses that have been implemented on the Mach-Zehnder DHM have all been of the same product line, the Mitutoyo infinity corrected long working distance objective lenses. These objective lenses come in a variety of magnifications and numerical aperture. The lenses of this series that have been tested are:

1. 10x NA0.28
2. 50x NA0.55
3. 50x NA0.75
4. 100x NA0.70

The depth of field is proportional to the inverse square of the numerical aperture (NA) of the lens. In addition, the magnification is relative to the focal length of the relay lens used to create the image at the detector. All magnifications reported here are assuming a relay lens with a 200 mm focal length.

Flow Considerations of Sample Chamber Design

Typical sample chamber dimensions for the common mode instrument are two separate fluidic channels separated (center to center) by 6 mm. Each channel is roughly 2 mm wide, 0.8 mm thick, and roughly 10 mm in length. Flow rates of sample in and out of the sample chamber are typically low, but vary depending on the type of experiment. In an experiment where a sample is to be introduced into the chamber and imaged under no flow conditions, the sample is typically injected at relatively higher flow rates on the order of 1 mL/min. In other experimental techniques (described in detail in Section 4.3), imaging occurs while the sample is being flowed through the field of view of the instrument. In data acquisition schemes of this nature, flow rates are much lower, on the order of 0.1 mL/min.

Due to the relatively small fluid volumes necessary for DHM, along with the relatively low flow rates expected in this system, we can assume that all flow physics pertaining to the design of the sample chambers will be in the laminar regime ($Re \approx 5$, see Table 7.4). The dimensionless number used to describe this flow regime is the Reynolds Number (Re), which is defined as

$$Re = \frac{\rho u L}{\mu}, \quad (\text{E.1})$$

where ρ is the density of the fluid, u is the velocity of the fluid, L is the characteristic length scale of the flow, and μ is the dynamic viscosity of the fluid. For the scope of flow physics discussed here, all flow is internal, so the characteristic length scale is defined as the microfluidic channel's hydraulic diameter. For a rectangular flow channel, the hydraulic diameter is defined as

$$D_h = \frac{2ab}{(a + b)}, \quad (\text{E.2})$$

where a and b are the dimensions of the channel's cross-sectional area. The sample chambers used in this work are of rectangular cross-section with an aspect ratio of $\approx 1:2$. For purposes of simplicity, a hydraulic diameter is used to reduce this no

symmetric geometry to a symmetric one. This assumption can introduce errors as will be discussed.

A flow phenomenon that must be considered is caused by the change in the fluid's mean direction of movement due to a curvature in the pipe. Any pipe flow that is subject to a curvature in the pipe experiences an adverse pressure gradient along the curve. This adverse pressure gradient causes a decrease in flow velocity along the convex edge of the curve (inner wall of the pipe), as well as an increase in flow velocity along the concave edge of the curve (outer wall of the pipe). This adverse pressure gradient occurs under the assumption that there is no lateral variation in the pressure change before and after the curve (i.e. Δp is constant across the pipe's cross section). This velocity gradient as a result of the curve introduces a secondary flow in the fluid that are known as Dean Vortices [115]. The prevalence of Dean Vortices in a flow as a result to a curvature of the pipe is quantified by a dimensionless number called the Dean Number (De), which compares inertial and centripetal forces with viscous forces. The Dean Number is defined as

$$De = Re \sqrt{\frac{D_h}{2R_c}}, \quad (\text{E.3})$$

where R_c is the radius of curvature of the bend in the pipe.

This phenomenon is of concern during various types of experiments conducted using the DHM instrument such as the experiments described in Section 4.3. In the detection of bacteria in sparse samples, where the concentration of bacteria is so low that there are statistically fewer than one bacteria in the field of view of the instrument at any one time, flow is used to continually image sample as it flows through the FOV. The introduction of secondary flow artifacts as the sample is being imaged causes deleterious effects in accuracy and sensitivity of the DHM instrument. For this reason, the Dean number is relevant because it can be used to ensure that these secondary flows are not prominent in the microfluidic device.

Furthermore, as flow is established through a pipe, the flow velocity takes on a parabolic profile. For the experiments described in Section 4.3, where particles are imaged as they flow through the FOV of the instrument, it is important to account for this parabolic flow profile as some particles will flow through the FOV faster than others depending on their position along the pipe's cross-section. Assuming that the flow velocity is symmetric through the pipe, the velocity profile of a fully

developed internal flow is described by

$$v(x) = v_{\max} \left(1 - \left(\frac{x}{L} \right)^2 \right), \quad (\text{E.4})$$

where v_{\max} is the maximum velocity of the fluid (at the center of the pipe), x is the position along the pipe's cross-section, and L is the total length of the pipe's cross-section. No analytical solution exists for the flow profile through a rectangular cross-section. Flow in the corner regions of a rectangular pipe can lead to recirculation currents, which make a flow profile difficult to analyze. Here, we neglect these effects as imaging is done far from these corners.

In an idealized system with an incompressible fluid and rigid pipe, we know that the volumetric flow rate (Q) is equal to the integral of the velocity profile across the cross sectional area of the pipe ($Q = \iint_A \mathbf{v} \cdot d\mathbf{A} = A\bar{v}$, where \bar{v} is the average flow rate). With the integral definition of an average as well as the velocity profile from Equation E.4, the maximum flow velocity can be estimated as

$$v_{\max} = \frac{3}{2}\bar{v}. \quad (\text{E.5})$$

This can serve as an overestimate of the maximum velocity of a particle subjected to flow. This is an overestimate as any particle will have mass and drag associated with it, thus slowing the particle down from the theoretical maximum velocity of an infinitesimal fluid parcel.

With this, for any flow through a microfluidic channel of known dimensions and volumetric flow rate, the maximum velocity of any particle in the flow can be calculated [115]. Flow can become parabolic and is referred to as 'fully developed' flow, but there exists a region known as the 'entrance' region of the flow where this parabolic velocity profile is in the process of developing. In the calculation of the maximum and mean velocity of the flow at any point in the sample chamber, it is important to know whether the flow is developing or fully developed at that point. This is done by estimating the thickness of the momentum boundary layer at that point. If the pipe is assumed to behave as two opposing flat plates, the momentum boundary layer grows as a function of the Reynolds Number and the length of the pipe at that point [103]. If the boundary layer thickness is defined as the distance

from the pipe wall to where the flow reaches 99% of the free-stream velocity, the Blasius solution for the boundary layer thickness yields

$$\delta \approx \frac{4.91x}{\sqrt{Re_x}}, \quad (\text{E.6})$$

where x is the distance along the pipe and Re_x is the Reynolds Number at that point.

The flow is considered developed when the boundary layer thickness is equal to half of the pipe's hydraulic diameter.

Of course, these are very basic and general considerations that must be made when designing or using sample chambers for the DHM instrument, but other more sophisticated flow characteristics must be considered when conducting other experiments. Depending on the experimental conditions, effects such as inertial focusing[38, 83] or gradient induced flow (e.g. thermal or chemical gradients) should be consider.

Practical Considerations of Sample Chamber Design

This section involves a qualitative discussion of the practical implementation of sample chamber design and manufacturing techniques. As discussed, many optical considerations must be made in the sourcing of materials for the sample chamber; in addition, much attention must be paid to the design of the sample chamber itself when considering flow characteristics. In the practical use of these sample chambers, one must also weigh the pros and cons of using high optical quality glass, which is usually very expensive and is not often readily available from distributors, or using less expensive, but much lower quality glass.

Throughout the experimentation conducted for this thesis, it was realized that both types of sample chambers are necessary. It is advantageous to have inexpensive and disposable sample chambers of low optical quality as well as reusable sample chambers of high optical quality. The reason becomes apparent when looking at the typical workflow involved with imaging a particular biological sample. In the case of bacteria, a master stock is grown in growth media overnight. This master stock is often too high of a microbial concentration to be imaged under DHM. Because of this, iterative dilution steps are required to converge on a sample concentration that suits the experimenter's desires. This requires diluting the master stock and iteratively imaging a sample of the dilution until the desired concentration is reached. For these iterative steps, using expensive and high optical quality glass is

not necessary. At this step of the experimental procedure, identical sample chambers with low optical quality components will suffice. Once the target concentration is reached, using a high optical quality sample chamber is beneficial as this will ensure high quality data that is publication worthy. Something of importance to note is that the sample chamber design between the low and high quality sample chambers must be identical in order to accurately represent the final publication worthy data (i.e sample chamber depth and optical thicknesses of the glass must be identical). If the sample chamber depth is not identical between the low and high quality sample chambers, then the apparent concentration will not be consistent from one sample chamber to the other (See Section 4.3).

Later in this Appendix, all technical drawings for all sample chamber designs used throughout this thesis as well as references to digital CAD files for each technical drawing are provided. The digital CAD files are in STEP file format to allow for cross platform distribution. The sample chamber designs developed throughout this work have been categorized into two sections: 1) Reusable sample chambers and 2) Disposable sample chambers.

Reusable Sample Chambers

The reusable sample chamber design consists of four main components. 1) A PDMS gasket, which establishes the flow channel geometry, 2) substrate glass, which seals the PDMS ‘gasket,’ 3) the dispensing needles which provide plumbing for fluid transport in and out of the sample chamber, and 4) the metal frames which provide the mechanical compression needed to maintain a sealed system while offering mechanical integrity and robustness. The fully assembled device can be seen in Figures E.1, as well as an exploded CAD model view in Figure E.2.

A schematic of the plumbing of the device can be seen in Figure E.3. Note that due to the fact that this device was developed for an off-axis holographic system, two channels are present. One channel is for the sample being investigated and the other serves as the reference, which is necessary to create interference patterns at the CCD plane. In addition, it is important to note that the sample chamber depicted in Figure E.3 features dispensing needles that are perpendicular to the high optical quality flow section and has sub-millimeter channel dimensions, but this does not have to be the case. The dispensing needle angles and size of the flow channels were designed in this way for the specific application of a DHM system in the orangeBox field instrument. In fact, in early development, sample chambers were designed



Figure E.1 – Fully assembled sample chamber

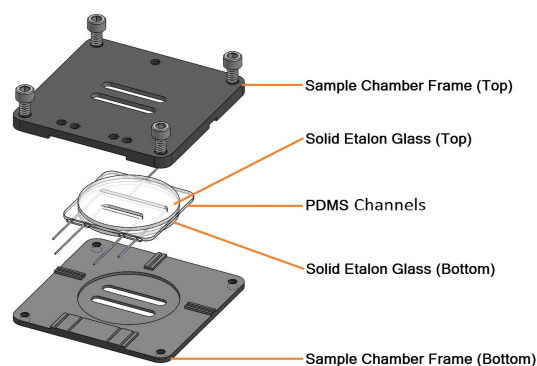


Figure E.2 – Exploded CAD view of sample chamber

with parallel flow cells that varied in size as well, allowing steady and laminar flow through the fluidic chamber with little perturbation of the fluid.

PDMS Gasket and Fabrication Methods

The PDMS gasket is made by the soft lithography of Dow Corning SYLGARD®184 silicone elastomer prepared at a mixing ratio of 10:1 (elastomer base:curing agent). Because soft lithography involves the use of an elastomeric mold, a negative mold is designed and fabricated using 6061-T6 aluminum. Other hardware components are also made for the molding process that help ensure repeatable production as well as controlled thicknesses from mold to mold. The complete mold assembly can be seen in Figure E.4.

The curing process of the PDMS is done with cylindrical tubes in place in order

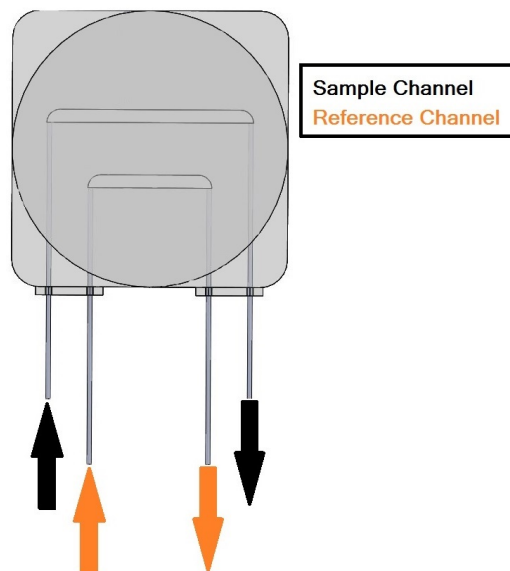


Figure E.3 – Schematic of sample chamber

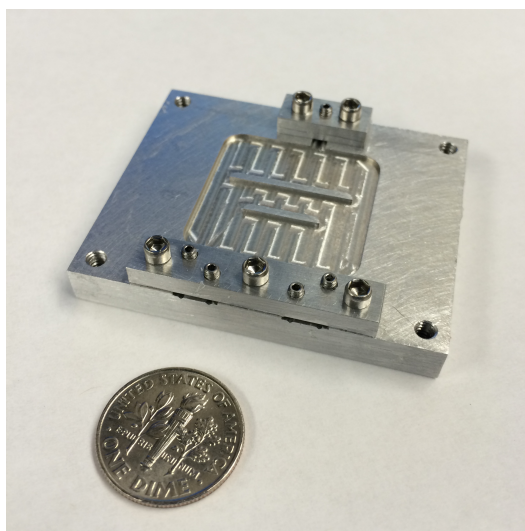


Figure E.4 – Mold assembly used for soft lithography of sample chambers

Table E.1 – Specifications of Etalon Glass

Type	Solid Etalon
Material	UV-grade fused silica
Diameter	25.4 mm
Thickness	1 mm
Wavefront Error	$\lambda/2$
Wedge	≤ 5 arc min
Clear Aperture	$\geq 85\%$

to create pilot holes for the dispensing needles when final assembly occurs. The reason for this is the fact that hollow tube dispensing needles become plugged when uncured PDMS is allowed to cure inside the interior of the tube. Using set screws to hold the tubes in place and installing the top acrylic plate to maintain uniform thickness, the PDMS is allowed to cure for an appropriate amount of time. Once cured and removed from the mold, a positive mold of the sample chamber geometry is attained. The careful removal of the solid tubes and trimming of excess PDMS and ‘flashing’ allows for the insertion of dispensing needles.

Solid Etalon Glass

The glass used for the development of this design was provided by CVI Laser, LLC. The specifications of the etalon glass used are tabulated in Table E.1. Also, throughout the development of this design, anti-reflective coated glass was also used and showed promise for an even higher SNR than non-AR coated glass. The DHM system used in these experiments had an emission wavelength of 405 nm, so the AR coated glass had an AR coating with a narrow bandstop wavelength of 405 nm.

Using the aforementioned glass, the assembled PDMS gasket is set atop a solid etalon, with a second solid etalon placed over the gasket. With the sample channels fully enclosed by glass, the final sample chamber is ready for assembly.

Sample Chamber Frame

The sample chamber frames consist of two 6061-T6 aluminum plates that were black Type-II anodized for longevity. These frames provide compressive sealing of the glass-PDMS-glass flow channel assembly. Through experimental testing, it was determined that a 5-10% compression of PDMS is appropriate to achieve sealing without collapsing the flow channels due to the compliance of PDMS. The frames

also include set screw locations to fix the dispensing needles as a method of strain relief to the PDMS gasket.

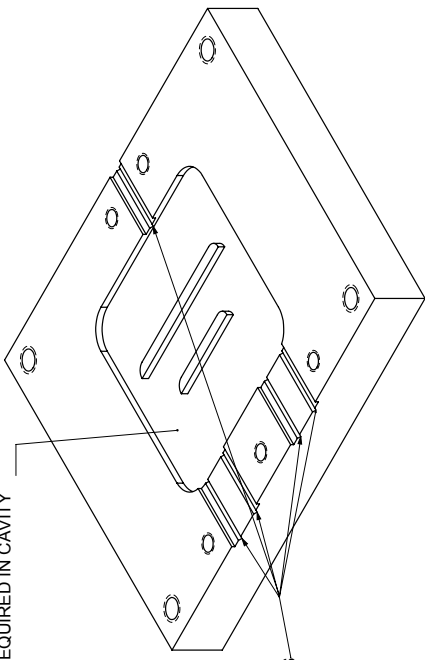
These designs, although allow for the use of high optical quality glass, are cumbersome to deal with, from a user experience standpoint. The disassembly, cleaning, and re-assembly process is difficult and requires a great deal of time. From what was learned by the substrate analysis presented in this thesis, transitioning to lower optical quality glass drastically decreased the cost of the sample chamber while providing easier and more repeatable use and performance.

The following technical drawings are related to the sample chamber mold and frame designs shown here. All digital 3D CAD models and PDF technical drawings have the identical file names as seen on the technical drawings.

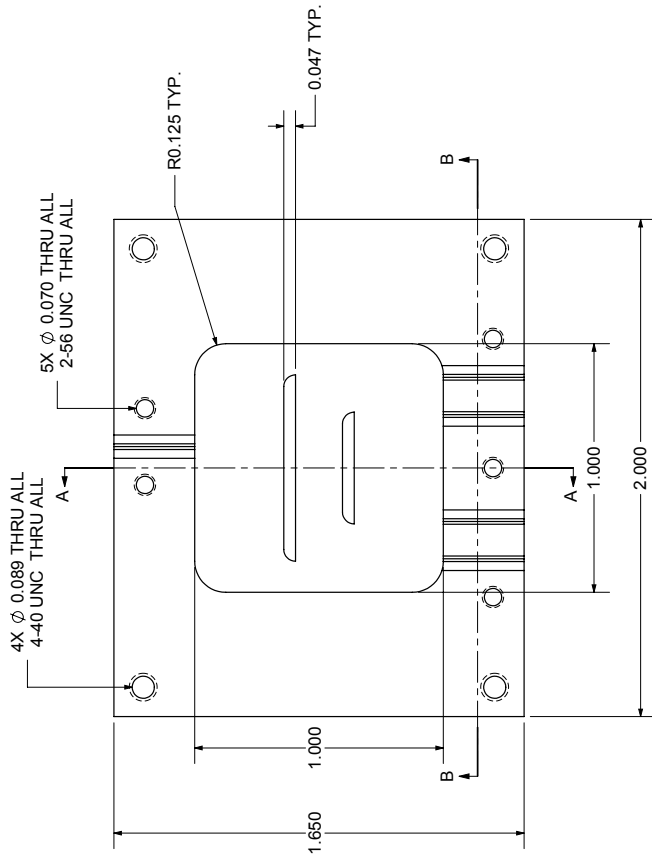
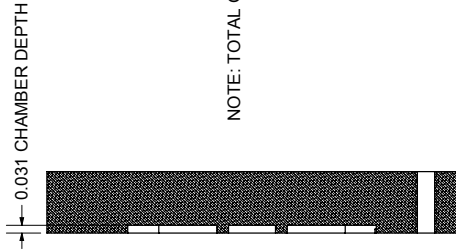
In the next section, efforts in designing and manufacturing disposable sample chambers are discussed. The general design morphology remains the same, however, and only adjustments to the materials and manufacturing methods are required.

The data in this document incorporate proprietary rights of the California Institute of Technology. Any party accepting this document does so in confidence and agrees that it shall not be duplicated in whole or in part, nor disclosed to others, without the consent of the California Institute of Technology.

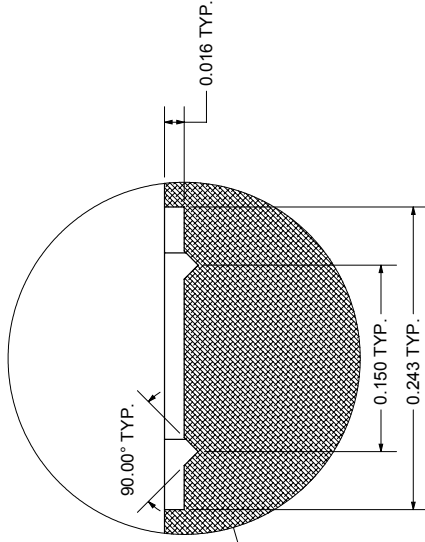
NOTE: SURFACE ROUGHNESS OF 32 MICRO INCHES REQUIRED IN CAVITY



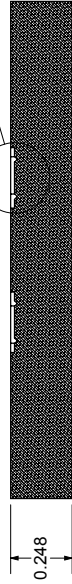
NOTE: TOTAL OF 5 V-GROOVES



SECTION A-A



DETAIL C



SECTION B-B

NOTE: FOR ALL OTHER GEOMETRIES, REFER TO CAD MODEL

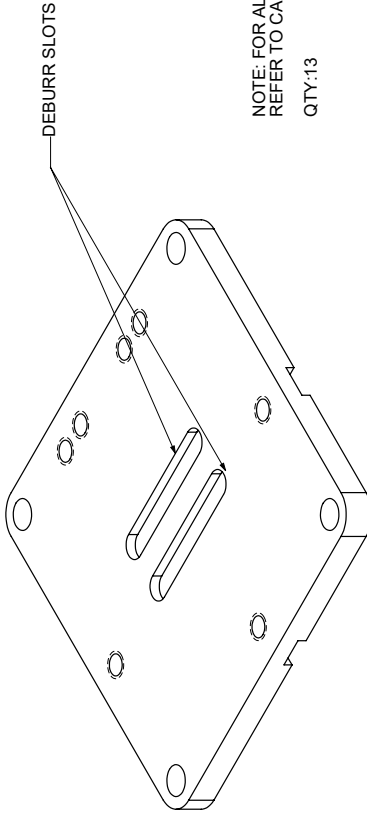
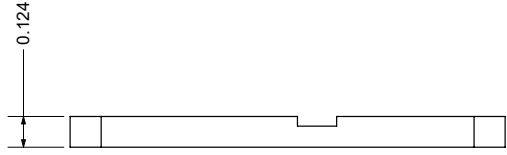
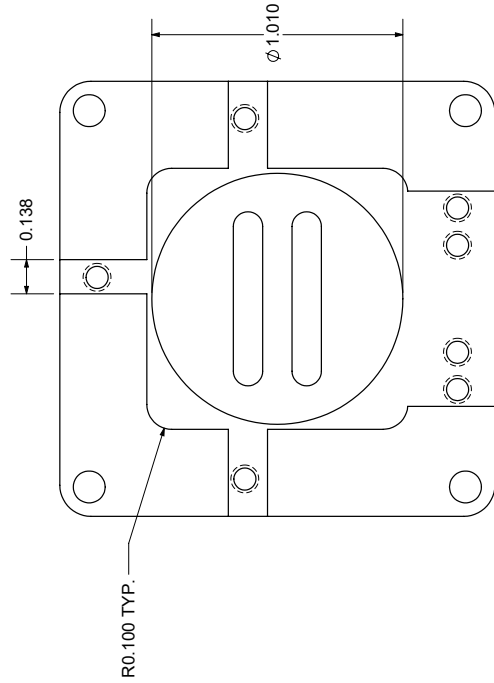
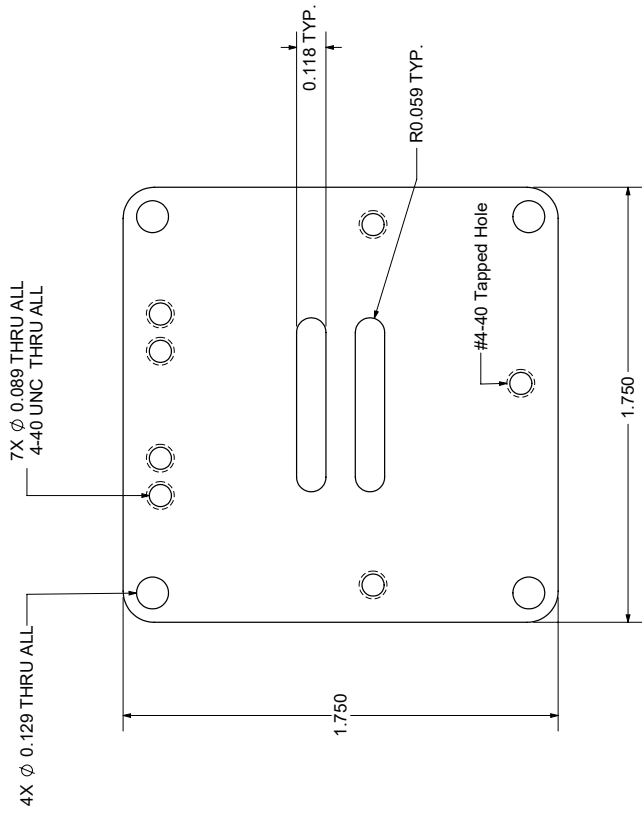
NEEDED QTY: 5

REV. A	DESCRIPTION INITIAL RELEASE	DATE 2/25/2015
DIMENSIONS IN INCHES (MM)		
SHAMU CM2 SAMPLE CHAMBER		
TOLERANCES (EXCEPT AS NOTED)		
DECIMAL	FRACTIONAL	ANGULAR
.XX = ±.010	XXXX = ±.001	MMB 2/25/2015
.XXX = ±.005	NONE	DRAWING NUMBER
.XXXX = ±.001	NONE	1 OF 1
ANGULAR: ±0.5°	SHEET	
TYP EDGE BREAK: .005-.015	DRAWING NUMBER	
	CM-02T-01-A	

Caltech

Manuel Bedrossian
Lucas Bedrossian
mbedr@caltech.edu
626 395 4794
MC 205-46
1200 E California Blvd,
Pasadena, CA 91125
©2011. ALL RIGHTS RESERVED

The data in this document incorporate proprietary rights of the California Institute of Technology. Any party accepting this document does so in confidence and agrees that it shall not be duplicated in whole or in part, nor disclosed to others, without the consent of the California Institute of Technology.



NOTE: FOR ALL OTHER GEOMETRIES
 REFER TO CAD MODEL
 QTY: 13

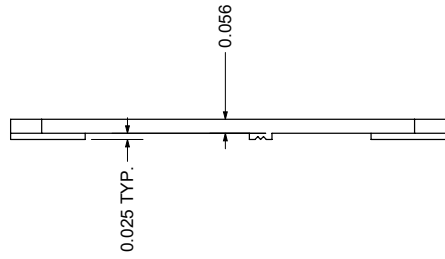
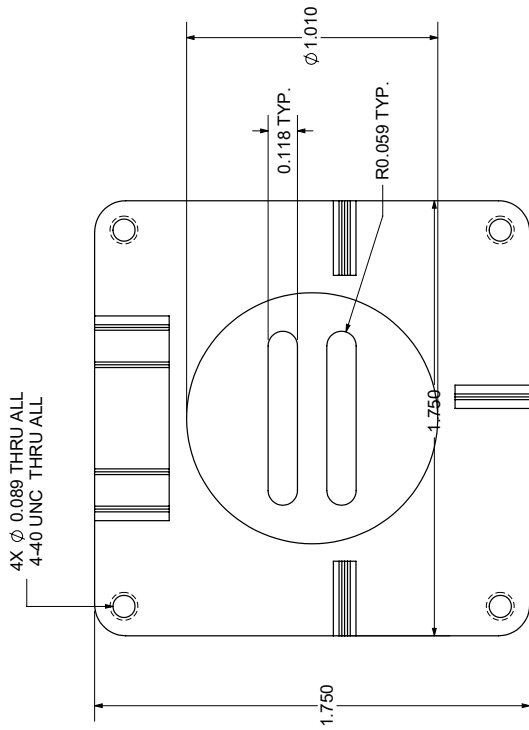
REV.	DESCRIPTION	DATE
A	INITIAL RELEASE	3/10/2015

DIMENSIONS IN INCHES [MM]	SHAMU
TOLERANCES (EXCEPT AS NOTED)	SMAPLE CHAMBER BOTTOM FRAME
DECIMAL	6001-T6 (SS)
.xx = ±0.010	
.xxx = ±0.005	
.xxxx = ±0.001	
FINISH	NONE
DRAWN BY	MMB
CHECKED BY	
DATE	3/10/2015
DRAWING NUMBER	
SHEET	
ANGULAR: 40.5°	
TYP EDGE BREAK:	
	.005-.015

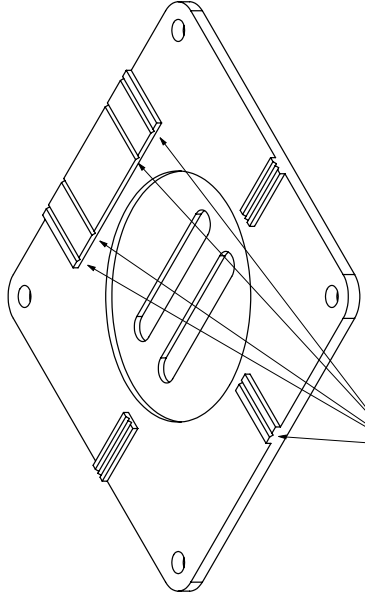
Caltech
 Manuel Badrosian
 Lucas A. Madsen
 mbehr@caltech.edu
 626.385.4794
 MC 205-46
 1200 E California Blvd.
 Pasadena, CA 91125
 ©2011. ALL RIGHTS RESERVED

1 OF CM-SC2-FRMB-A

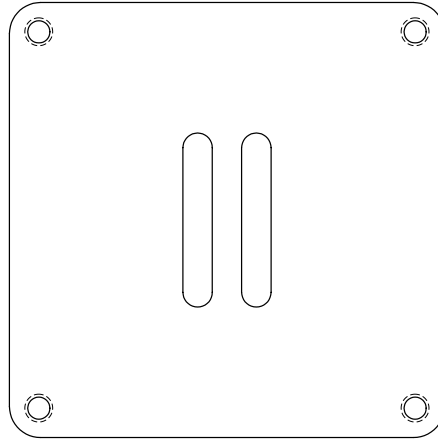
The data in this document incorporate proprietary rights of the California Institute of Technology. Any party accepting this document does so in confidence and agrees that it shall not be duplicated in whole or in part, nor disclosed to others, without the consent of the California Institute of Technology.



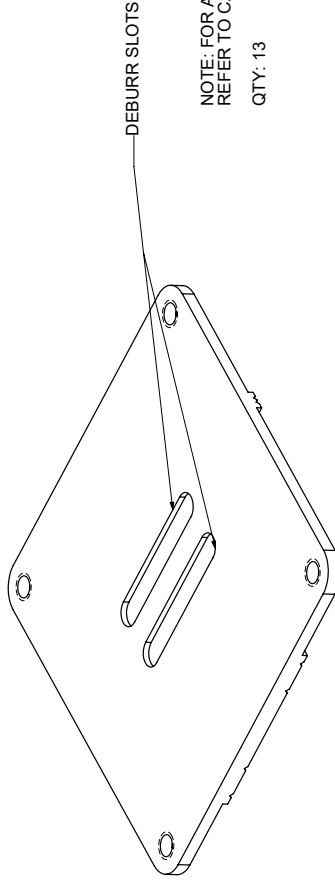
SIDE VIEW



TOTAL OF 5 V-GROOVES



BACK VIEW



NOTE: FOR ALL OTHER GEOMETRIES
REFER TO CAD MODEL

QTY: 13

REV.	DESCRIPTION	DATE
A	INITIAL RELEASE	3/10/2015

DIMENSIONS IN INCHES [MM]	
TOLERANCES (EXCEPT AS NOTED)	
DECIMAL	XX = ±.010
	XXX = ±.005
	.XXX = ±.001
ANGULAR	40.5°
TYP EDGE BREAK .005-.015	

REVISED BY	DATE
MMMB	3/10/2015

DRAWING NUMBER	
NONE	
SHEET	
1 OF CM-SC2-FRMA-A	

PRODUCT	
SHAMU	
DRAWING TITLE	
SAMPLE CHAMBER TOP FRAME	
PART NUMBER	
6061-T6 (SS)	
SHEET	
B	

Caltech
 Manuel Bedrossian
 Lucas Bedrossian
 mbedr@caltech.edu
 626 395 4794

MC 205-46
 1200 E California Blvd.
 Pasadena, CA 91125

©2011. ALL RIGHTS RESERVED



Figure E.5 – A laser cut plastic shim with double-sided adhesive tape

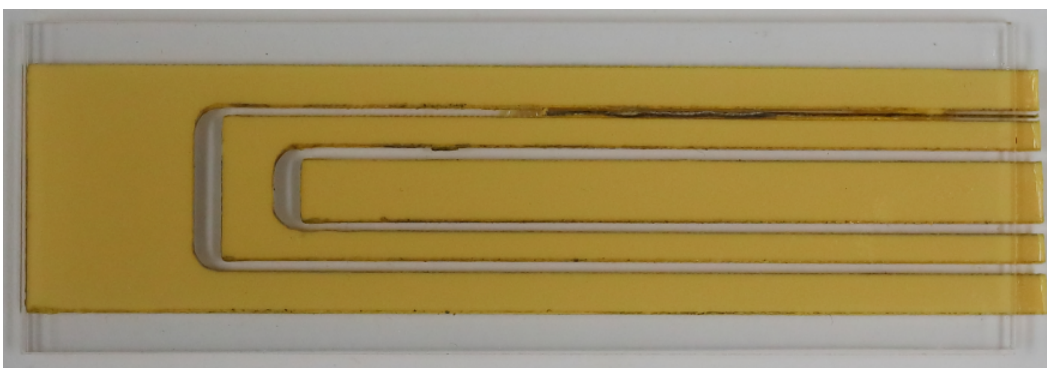


Figure E.6 – Plastic shim stock after being compressed between glass substrates

Disposable Sample Chambers

For increased repeatability in the manufacturing of sample chambers as well as a decrease in cost per sample chamber, a more scalable manufacturing method is introduced here. This design replaces the molded PDMS gasket of the reusable design with a rigid plastic shim that is either laser cut or machined to the designed gasket shape.

Prior to laser cutting or machining, the plastic shim is covered with double-sided adhesive tape on both sides. This is so that it can be permanently attached to both glass substrates upon assembly. In addition, the double-sided adhesive tape is applied prior to laser cutting or machining so that the tape is cut along the channel geometries as well. This ensures a clear optical path through the imaging volume of the sample chamber.

With the plastic shim stock laser cut or machined to the desired sample chamber gasket geometry, it is then compressed between two pieces of low to medium optical quality glass. Once secured, hypodermic needles (blunt tipped) are inserted into the channel cavities and epoxied in place. See Figures E.5, E.6, and E.7 for the manufacturing process described here.

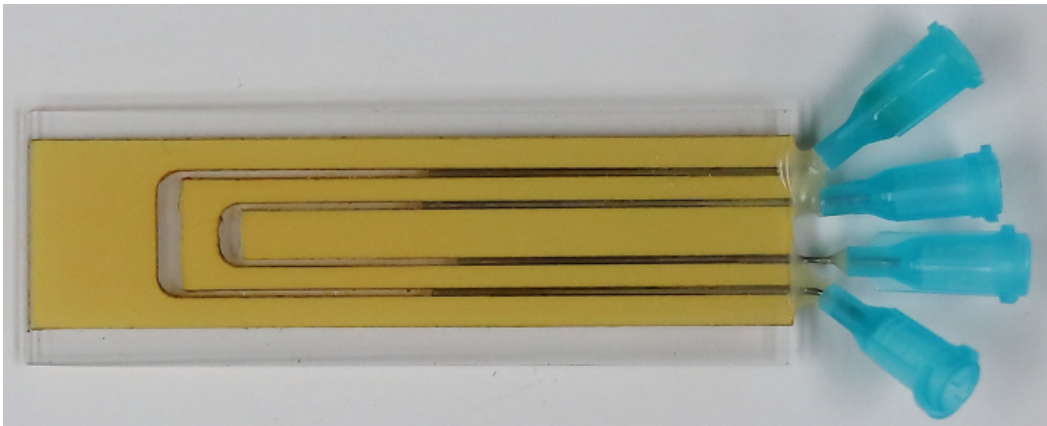


Figure E.7 – A fully assembled disposable sample chamber

These sample chambers are relatively easy to design and manufacture, while being much more cost effective than the reusable sample chamber described in the previous section. This manufacturing method allows for the easy modification of the sample chamber geometry as well as the substrate material.

Miniaturized Field Instrument Electronics Package

As discussed in the body of the thesis, the miniaturized DHM instrument has been equipped with many peripheral electronic devices as well as a processor that is capable of communicating with and controlling these peripheral devices. Using the commercially available software EAGLE Editor, a custom printed circuit board (PCB) was designed in order to interface the main processor of the miniaturized field instrument (UDOO x86 ULTRA) with all peripheral devices. This PCB served two main purposes. It allowed for the miniaturization of the electronics as much of the connections are now made on a board level rather than soldered wire, as well as allowing for the electronics to become more robust against physical vibration. As the PCB requires less soldered wire, physical vibrations are less likely to break soldered joints and cause damage to the instrument. Figure E.8 shows the electronic schematic developed for the miniaturized DHM field instrument. This design includes a total of 3 TTL controlled relay circuits, laser optical power control, monitoring capabilities for the laser as well as temperature and moisture sensors. The files associated with this design are provided in the GitHub repository under the 'fieldInstrumentPCB' directory [82].

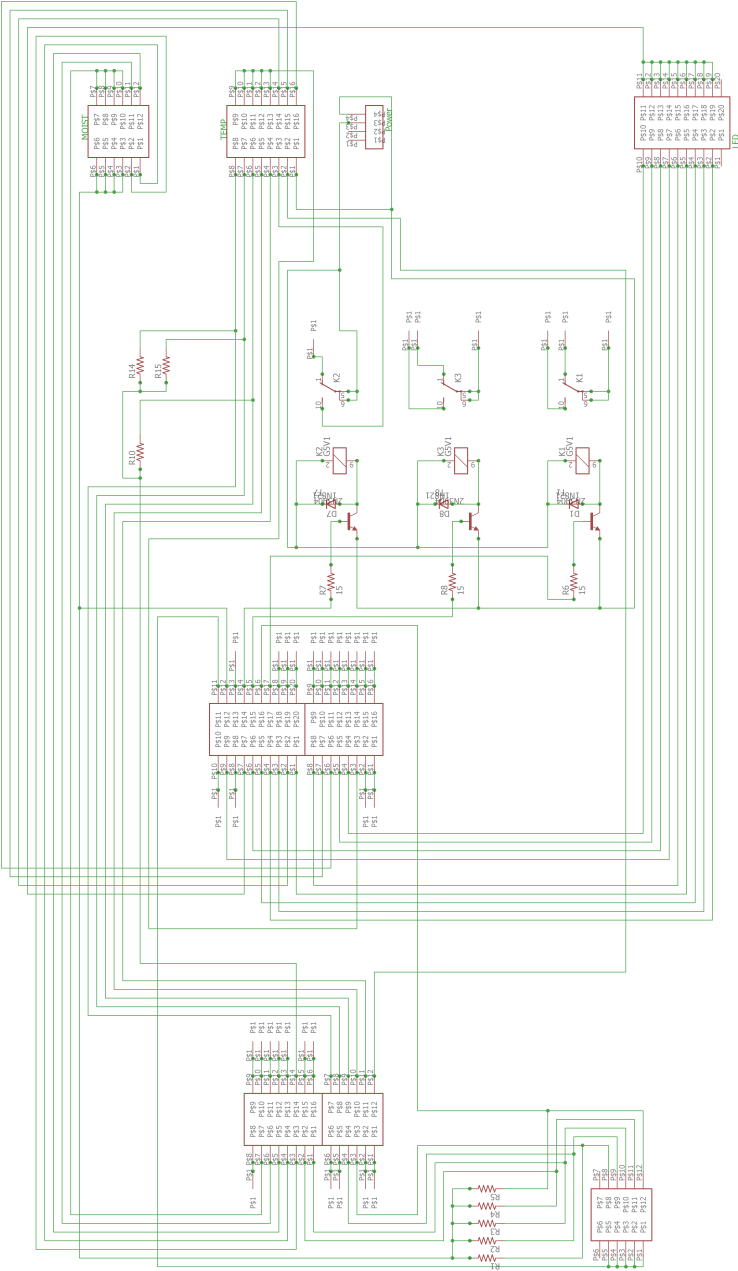


Figure E.8 – Electronic schematic for the miniaturized DHM field instrument

*Appendix F***ACCESSING GITHUB AND DATA BACKUPS**

This Appendix provides information on how to access the GitHub repository where all referenced code and technical drawings are available for public download. In addition to this, all data that is referenced throughout this thesis is backed up on a locally managed data server known as the 'Motility Server.' Information on requesting access to this server is provided as well.

The GitHub repository is located at https://github.com/mbedross/mmb_PhD_Thesis. Due to the nature of this repository, all access to committing changes is prohibited. Users are only able to download files.

All software also has an accompanying DOI number for easy public access. The software and associate DOI numbers are as follows:

- automatedTracking: DOI 10.22002/D1.1408
- axialResolution: DOI 10.22002/D1.1409
- fieldInstrumentPCB: DOI 10.22002/D1.1410
- hologramSimulation: DOI 10.22002/D1.1411
- manualTracking: DOI 10.22002/D1.1412
- numericalReconstruction: DOI 10.22002/D1.1413
- PSDcalculation: DOI 10.22002/D1.1414
- residualFringeVisibility: DOI 10.22002/D1.1415
- SNRcalculation: DOI 10.22002/D1.1416
- underGradThesis: DOI 10.22002/D1.1417

The data presented in this thesis is backed up and stored on a private server. The size of the data sets total on the order of hundreds of GBs, so a online system such as GitHub is not an appropriate location for such files. The server where all data is stored is called the 'Motility Server' and is located at the IP address: 131.215.99.205. This server can be accessed through any web browser as well as third party softwares such as FileZilla. Prior to this, an account must be created for you. Please contact Jay Nadeau for help with setting this up (nadeau@pdx.edu).

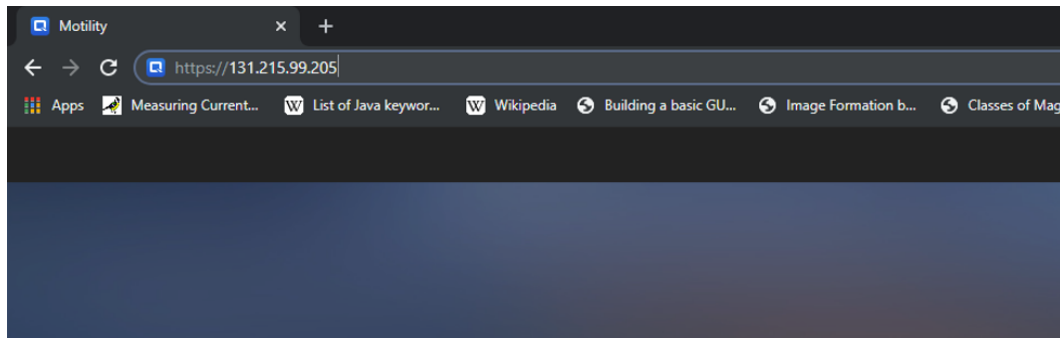


Figure F.1 – Navigating the server IP address via internet browser

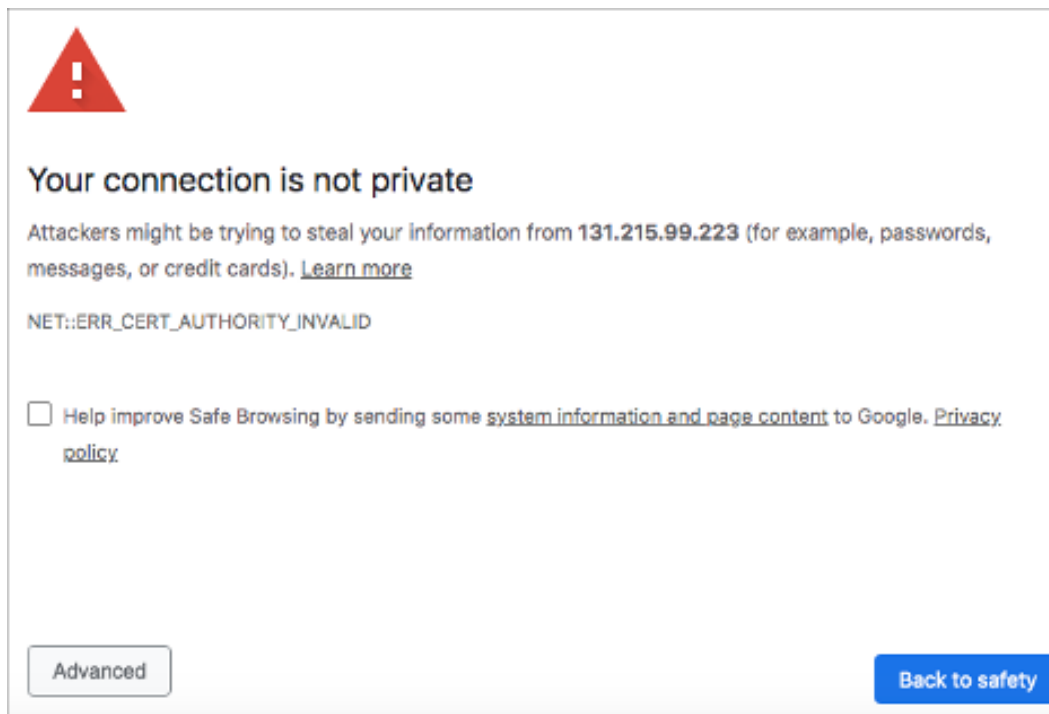


Figure F.2 – Typical warning message given by Google Chrome

Logging On

Navigate to the IP address (shown above) using the internet browser of your choice. This tutorial shows examples using Safari (Mac) and Google Chrome.

Typically, because you are navigating to a server and not a typical webpage, the browser will display a warning message that the site you are about to enter is unsecure. This message will allow you to continue to the website under the 'Advanced' tab (Google Chrome) or the 'Show Details' tab (Safari).

Clicking the appropriate button to continue to the server webpage, will get you to

This server could not prove that it is **131.215.99.223**; its security certificate is not trusted by your computer's operating system. This may be caused by a misconfiguration or an attacker intercepting your connection.

[Proceed to 131.215.99.223 \(unsafe\)](#)

Figure F.3 – Expanded view allowing access to the server IP address. Click ‘Proceed to 131.215.99.223 (unsafe)’ for Google Chrome, or ‘visit this website’ for Safari.

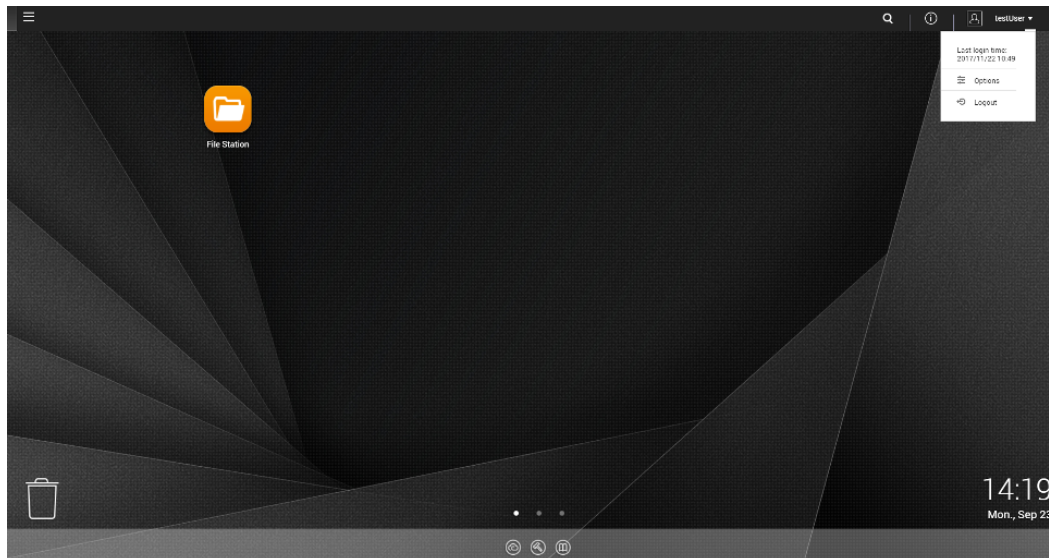


Figure F.4 – Server dashboard (note the ‘Options’ tab at the top right after clicking the dropdown menu attached to the username)

the Motility Server’s main login page. Here, you can enter your log in credentials and navigate to the server dashboard.

Changing Your Password

Once at your server dashboard, click on your username at the top right hand of the web browser and select ‘Options.’

On the dialog box that appears, navigate to the ‘Change Password’ tab. Here, you will be asked to enter your old password (for security reasons) as well as the new password you would like to implement. Click ‘Apply’ when you’re done, and the password on your account will be changed.

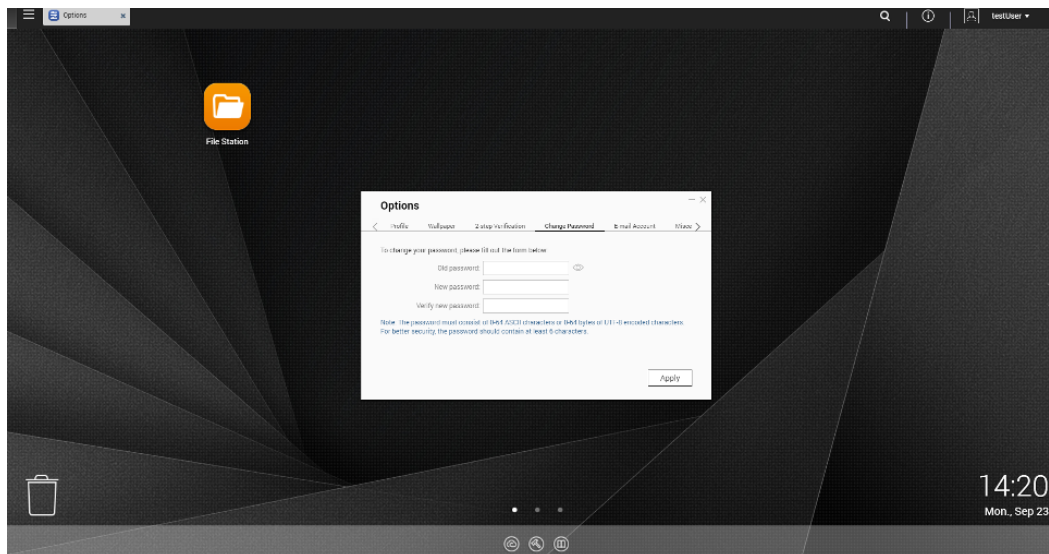


Figure F.5 – The ‘Options’ dialog box where you can change account information, including your password

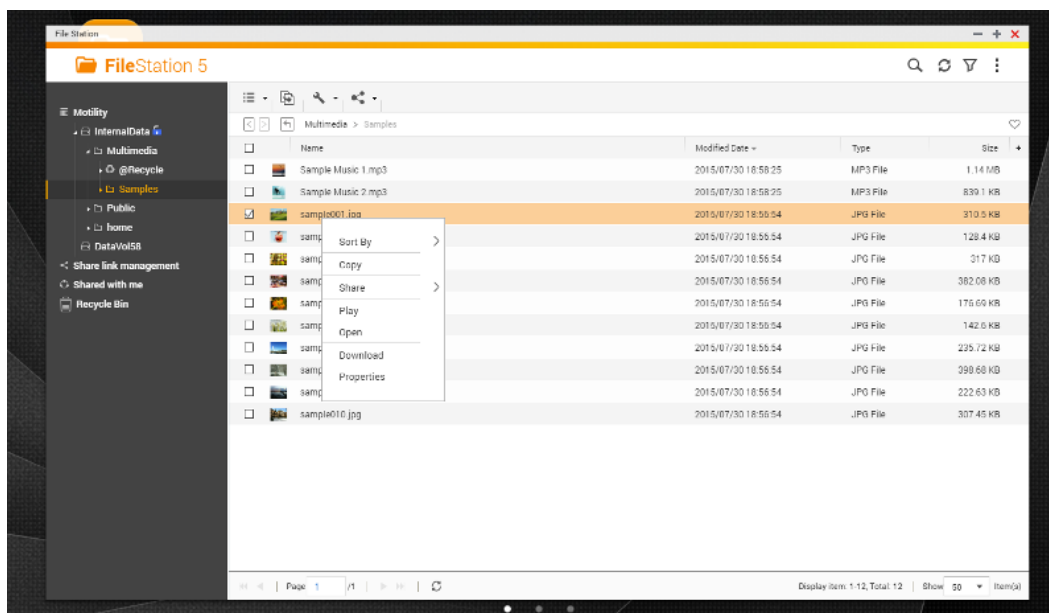


Figure F.6 – File Station dialog box

Using the File Station

The file station is fairly self-explanatory. It is your web-based portal to the data that is on the Motility server. Here, upload and download files to/from the folders that you have access to. The folder containing the data related to this thesis is called ‘Backups/MBedrossian_Thesis_Data/.’